CHARACTERIZATION OF MORPHOLOGY, NANOSTRUCTURE AND OXIDATION KINETICS OF BIOFUEL PARTICULATE MATTERS

PARK WATANAWONGSKORN

A THESIS REPORT SUBMITTED IN PARTIAL FULFILLMENT
OF THE REQUIREMENTS FOR THE DEGREE OF
MASTER OF ENGINEERING IN AUTOMOTIVE ENGINEERING
INTERNATIONAL COLLEGE
KING MONGKUT'S INSTITUTE OF TECHNOLOGY LADKRABANG
ACADEMIC YEAR 2017
KMITL-2017-IC-M-004-002

This material is reserved for educational use only, not allowed for commercial use.
Forbidden to modify the content, and cite the document when use.

COPYRIGHT 2017

INTERNATIONAL COLLEGE

KING MONGKUT'S INSTITUTE OF TECHNOLOGY LADKRABANG

This material is reserved for educational use only, not allowed for commercial use.

Forbidden to modify the content, and cite the document when use.

Thesis Title	Characterization of Morphology, Nanostructure, and Oxidation Kinetics of Biofuel Particulate Matters
Student	Mr. Park Watanawongskorn
Student ID	58610001
Degree	Master of Engineering
Program	Automotive Engineering
Advisor	Asst.Prof.Dr. Preechar Karin
Co-advisor	Dr. Nuwong Chollacoop
Co-advisor	Prof.Dr. Katsunori Hanamura

ABSTRACT

It is well known that diesel engines have highest thermal efficiency at same load conditions compared with other internal combustion engines. However, one of their disadvantages is Particulate Matter (PM) emission. Since particulate matters can be harmful to human health, it is necessary to be removed from exhaust gas before emitted to atmosphere. This research is divided into two main parts. The first part is related to effects of combustion characteristics of Biodiesel and Ethanol-blended fuel on particulate matter emission. Experimental results show that ethanol-blended fuel contributes further reduction of particulate emission by 58.6% compared with base biodiesel. The second part focuses on characteristics of particulate matters emitted from combustion. Relationships of PM's morphology, nanostructure, and oxidation kinetics were investigated. Application of Scanning Electron Microscope (SEM), Transmission Electron Microscope (TEM), and Thermo-Gravimetric Analysis (TGA) was adopted in the analysis. Experimental results reveal that soot particles from the ethanol-blended fuel consist of smaller carbon fringe structure with average size of 0.93 nm which have strong relationship with the reduced activation energy of 78.7 kJ/mol in soot oxidation. That means functional groups in the ethanol fuel molecules play an important role in soot oxidation. Results of this research are expected as useful information for further research in fields of biofuel especially ethanol related particulate matters.

Keywords: Particulate Matter (PM), Diesel Engine, Ethanol, Biodiesel,

This material is reserved for educational use only, not allowed for commercial use.
Forbidden to modify the content, and cite the document when use.

ACKNOWLEDGEMENT

I would like to express my sincere gratitude to following persons and agencies for kind support and advice during my thesis period.

Asst. Prof. Dr. Preechar – thank you for good advices and discussion for my whole thesis. Dr. Nuwong and Prof. Dr. Hanamura – thank you for being my great co-advisor.

I would like to thank KMITL friends for their sincere support. Mr.Komkla AE7 - my senior who guided me a lot in fields of PM and Soot. Mr. Jiramed and Mr.Pop-Paul AE8 - my buddy during the experiment. They are very supportive in equipment setup. Mr. Sombat and Mr. Veerayut AE9 – friends who can be good advisors for everything in KMITL. Dr. Prathan - I am deeply appreciated for his excellent equipment in the Lab.

Ms. Wannipha, international college official - She always support me in every general affairs especially regarding financial documents.

AE9 friends - Mr. Kontorn, Mr. Tripoom, Mr. Piyawat, Mr. Warawut, Ms.Bongkotchaporn, Mr. Kritin, Ms. Benjaporn, Ms. Onnalin, and Mr. Apiroon. Thanks for good friendships in the Master course and hope we will keep in touch.

I also would like to thank to KMITL Automotive Laboratory for the facilities during the experiment, KMITL and TGIST scholarships for funding support, NSTDA and KMITL for international conference funding support, and Focus Lab for fuel test support.

Finally, I would like to express my deep appreciation to my great family and my girlfriend who understand me well and support me during the hard time. Lastly, thanks to my PC for supporting this research.

This material is reserved for educational use only, not allowed for commercial use.
Forbidden to modify the content, and cite the document when use.

TABLE OF CONTENTS

CHAPTER **PAGE**

This material is reserved for educational use only, not allowed for commercial use.

Forbidden to modify the content, and cite the document when use.

This material is reserved for educational use only, not allowed for commercial use.
Forbidden to modify the content, and cite the document when use.

This material is reserved for educational use only, not allowed for commercial use.
Forbidden to modify the content, and cite the document when use.

LIST OF TABLES

Table **Page**

This material is reserved for educational use only, not allowed for commercial use.
Forbidden to modify the content, and cite the document when use.

LIST OF FIGURES

Figure **Page**

This material is reserved for educational use only, not allowed for commercial use.

Forbidden to modify the content, and cite the document when use.

This material is reserved for educational use only, not allowed for commercial use.
Forbidden to modify the content, and cite the document when use.

This material is reserved for educational use only, not allowed for commercial use.
Forbidden to modify the content, and cite the document when use.

This material is reserved for educational use only, not allowed for commercial use.
Forbidden to modify the content, and cite the document when use.

This material is reserved for educational use only, not allowed for commercial use.
Forbidden to modify the content, and cite the document when use.

King Mongkut's Institute of Technology Ladkrabang

This material is reserved for educational use only, not allowed for commercial use.
Forbidden to modify the content, and cite the document when use.

CHAPTER 1

INTRODUCTION

1.1 Research Background

Transportation uses a huge amount of energy [1]. According to the reference case of the International Energy Outlook 2016 (IEO2016), transportation sector delivered energy consumption increases since 2012 at an annual average rate of 1.4% until 2040. Petroleum and other liquid fuels are the dominant source of transportation energy. World transportation sector liquid fuels consumption grows by 36 quadrillion Btu in the reference case projection, with diesel (including biodiesel) showing the largest gain (13 quadrillion Btu), jet fuel consumption increasing by 10 quadrillion Btu, and motor gasoline (including ethanol blends) increasing by 9 quadrillion Btu as shown in Fig. 1.1.

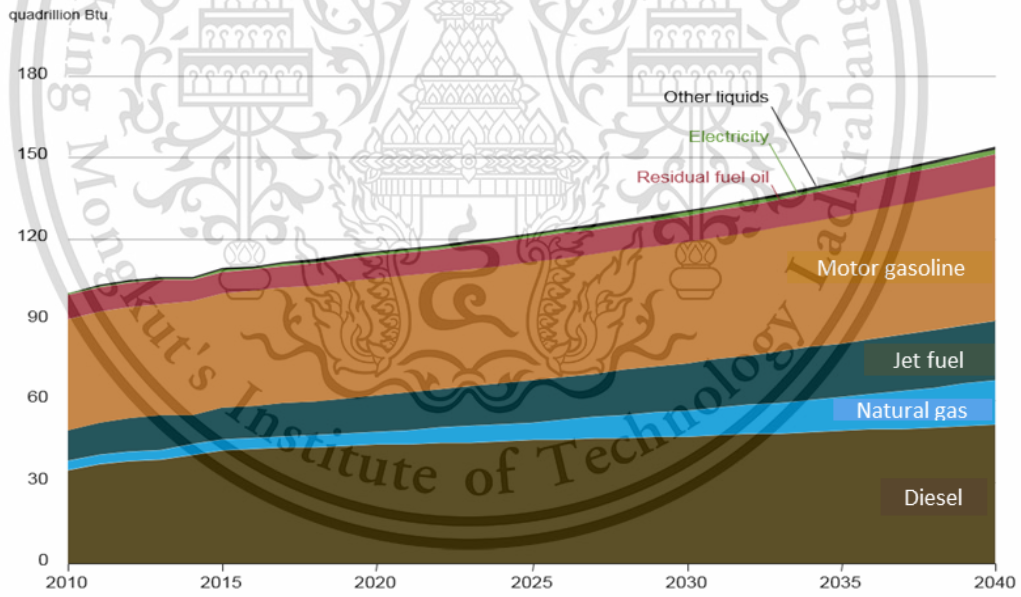

Figure 1.1 World transportation sector delivered energy consumption by energy source, 2010-2040 [2]

It is well known that diesel engines have high thermal efficiency mainly due to high compression ratio compared with other internal combustion engines at the same load. Applying diesel vehicles in transportation sector is an alternative to increase efficiency of limited liquid fossil fuel in the world. However, main pollutants

This material is reserved for educational use only, not allowed for commercial use.
Forbidden to modify the content, and cite the document when use.

from diesel engines are solid particles (Particulate Matter or PM) and nitrogen oxide (NO_x) [3]. Pollutants should be removed from exhaust gas because of their effects on environment and human health, such as lung cancer. Hence, regulations of pollution standard for diesel emission are proper way to control the emission to atmosphere.

Since 2012, Thai government has adopted Thailand Industrial Standard of level 7 (TIS 2160-2543) for small diesel engine vehicles which is equivalent to Euro 4 emission standard in order to control exhaust gas emission from diesel engines especially particulate matter. Figure 1.2 shows EU emission standard for diesel's passenger vehicles. Euro 4 restricts Particulate Matter (PM) emission at less than 0.025 g/km. However, trends of pollutant control in Thailand are going to be more severe in the near future (Euro 5 or Euro 6).

Stage	Date	CO	HC	HC+NOx	NOx	PM	PN
		g/km					#/km
Compression Ignition (Diesel)							
Euro 1†	1992.07	2.72 (3.16)	-	0.97 (1.13)	-	0.14 (0.18)	-
Euro 2, IDI	1996.01	1.0	-	0.7	-	0.08	-
Euro 2, DI	1996.01[a]	1.0	-	0.9	-	0.10	-
Euro 3	2000.01	0.64	-	0.56	0.50	0.05	-
Euro 4	2005.01	0.50	-	0.30	0.25	0.025	-
Euro 5a	2009.09[b]	0.50	-	0.23	0.18	0.005[f]	-
Euro 5b	2011.09[c]	0.50	-	0.23	0.18	0.005[f]	6.0×10^{11}
Euro 6	2014.09	0.50	-	0.17	0.08	0.005[f]	6.0×10^{11}

Figure 1.2 EU Emission Standards for Diesel passenger cars [4]

The biofuel such as biodiesel or bioethanol have been often discussed as alternatives for diesel fuel replacement since they are obtained from renewable sources and can be re-produced faster than fossil fuel. Biodiesel consists of alkyl monoesters of fatty acids are derived from vegetable oil or animal fats. Since its similar physical properties to diesel fuel, there is no need to modify the engine when the engine is fueled with the blends [5-7]. Regarding biodiesel situation in Thailand, Thai government are promoting usage of biodiesel in transportation sectors since it can be produced with domestic agriculture product of palm oil, jatropha oil, and etc.

Another benefit of biodiesel in diesel replacement is emission reduction. Biodiesel has low sulfur and aromatic hydrocarbon content. Besides, biodiesel has oxygen atoms in fuel molecules and also acts like environmental friendly fuel. Oxygen content in biodiesel fuel promotes more complete combustion than fossil

This material is reserved for educational use only, not allowed for commercial use.
Forbidden to modify the content, and cite the document when use.

fuel; that means it emits low amount of particulate matter. Referred from KMITL previous researches, they conform with above statement that biodiesel contribute less particulate matter emission. Figure 1.3 and Figure 1.4 show that use of biodiesel can substantially produce less smoke emission compared with diesel.

Bioethanol or ethanol is a low cost oxygenated fuel with comparatively high oxygen content. It is composed of the homogeneous chemical compound (C_2H_5OH) whether it is produced from sugar-based feedstock or from agricultural residues [8]. Ethanol is a high-octane fuel. So, it obviously cannot be replaced with diesel. However, it can be applied in forms of blend, dual injection, or ethanol fumigation into the intake port. In terms of emission reduction, especially particulate matter, high oxygen content is being considered to bring some PM reduction [9].

From above advantages of biofuels regarding emission reduction, this research aimed to study effects of ethanol on further reduction of particulate matter from biodiesel usage in order to deal with more severe emission control standard.

This material is reserved for educational use only, not allowed for commercial use.
Forbidden to modify the content, and cite the document when use.

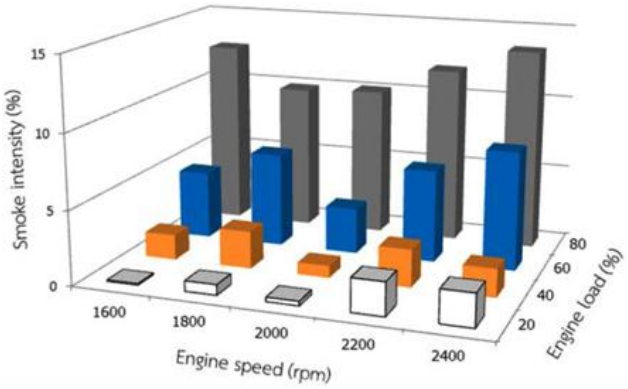

(a) Diesel engine's particulate matters

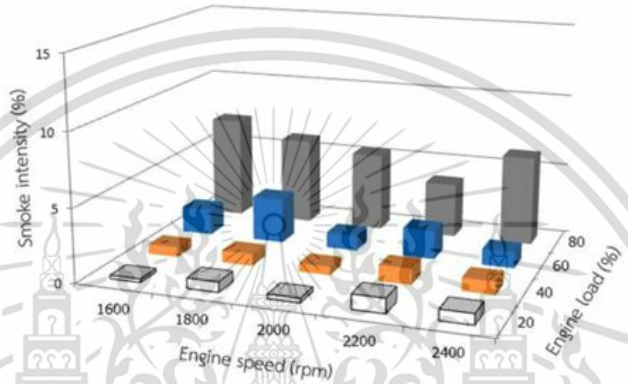

(b) Biodiesel engine's particulate matters

Figure 1.3 Quantity of (a) Diesel engine's PMs and (b) Biodiesel engine's PMs using opacity smoke meter in each engine load and engine speed operation condition [10]

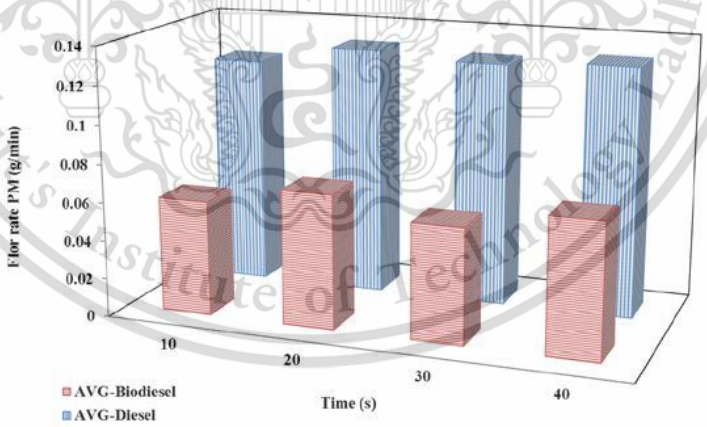

Figure 1.4 Average particulate matter flow rate of diesel (blue) and biodiesel (red) [11]

This material is reserved for educational use only, not allowed for commercial use.
Forbidden to modify the content, and cite the document when use.

1.2 Objectives

- To clarify impact of ethanol on diesel engine's Particulate Matter (PM) emission quantity
- To compare morphology and nanostructure of PM emitted from ethanol-blended biodiesel, biodiesel, and diesel fuel
- To explain relationships between nanostructure and oxidation kinetics of the above PMs

1.3 Scope of work

This research focuses on effects of bio-oxygenated fuel, especially ethanol, on combustion and Particulate Matter (PM) emission characteristics in a small diesel engine. Since unique properties compared with conventional diesel fuel, few percentage of ethanol was blended with palm biodiesel to keep compatibility in fuel properties with biodiesel and diesel fuel. Engine performance and in-cylinder combustion behavior e.g. combustion pressure and heat release rate were investigated. Then, PM analysis was conducted in view of emission quantity and PM morphology. PM morphology was further investigated in detail of nanostructure. In the final part, PM was analyzed by approaches of oxidation kinetics. Highlight of this research is aimed to get an insight of relationships between PM nanostructure and oxidation kinetics i.e. roles of biofuel's PM nanostructure on the oxidation reactivity.

This material is reserved for educational use only, not allowed for commercial use.
Forbidden to modify the content, and cite the document when use.

CHAPTER 2

RESEARCH THEORY AND LITERATURE REVIEW

2.1 Diesel engine

A conventional internal combustion diesel engine works on “Diesel Cycle”. In the simple diesel engines, an injector injects fuel into the combustion chamber above the piston directly. Diesel engines are also commonly known as Compression-Ignition engines; since the diesel is burned due to hot compressed air. The temperature of the air inside the combustion chamber rises to above 400°c to 800°c, which in turn, ignites the diesel which was injected into the combustion chamber. The ‘Diesel Cycle’ does not use an external mechanism such as a spark-plug to ignite the air-fuel mixture. The principle of diesel cycle can be divided in to 4 stoke, as shown in figure2.1.

1. Suction – With pistons moving downwards and opening of the inlet valve creates suction of clean air into the cylinders.

2. Compression – With closing of Inlet valve the area above the piston gets closed. The piston moves up resulting in compression of the air in a confined space under higher compression-ratio.

3. Combustion – At this stage the injector sprays the diesel into the combustion chamber. The rise in temperature of the air caused by its compression; results in instantaneous burning of diesel with in an explosion. This causes heat to release resulting in generation of expanding forces known as power. These forces again push the pistons downwards resulting in their reciprocating motion.

4. Exhaust– On their way up, the pistons push the exhaust gases above them thru’ the exhaust valve which opens during exhaust stroke.

This material is reserved for educational use only, not allowed for commercial use.
Forbidden to modify the content, and cite the document when use.

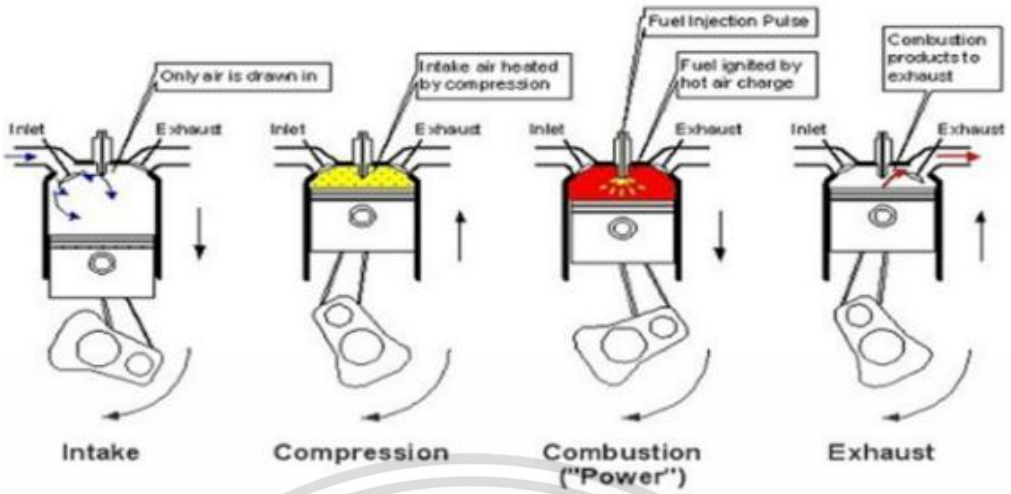

Figure 2.1 Diesel engine cycle [12]

The heat release rate as shown in Fig. 2.2 in the combustion stoke of diesel cycle has 4 stage which consist of ignition delay phase, premixed combustion phase, mixing-controlled combustion phase and late combustion phase. The heat release rate explain the process as

- Ignition Delay Phase, a - b is the time period since the start of fuel injection in the combustion chamber until the fuel ignited.

- Premixed Combustion Phase, b - c is the time duration of the premixed fuel combustion after ignition delay phase which will initiate the rapid auto - ignition and increase heat release rate.

- Diesel Fuel Performance Mixing Combustion Phase, c - d is occurred in combustion chamber after the completely burned of premixed fuel. The combustion rate will be controlled by the formation rate of mixture between air - fuel that ready to be burned.

- Late Combustion Phase, d - e is the period that the heat release rate is low during the exhaust stroke. It is the combustion of the rest of the fuel and carbon residue which previously generated from the rich mixture.

This material is reserved for educational use only, not allowed for commercial use.
Forbidden to modify the content, and cite the document when use.

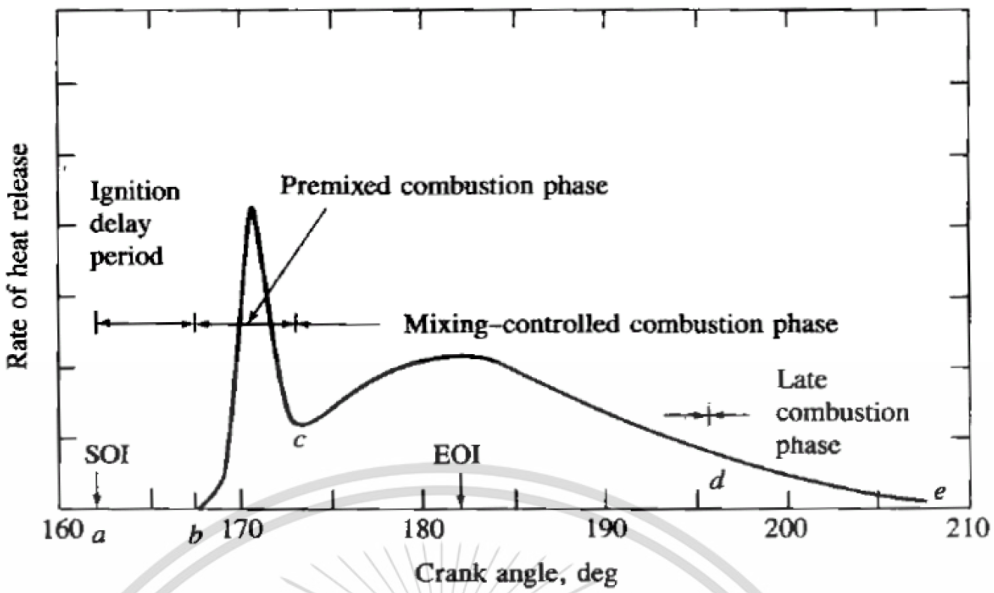

Figure 2.2 Stage of heat release rate [13]

2.2 Emission of diesel engine

Diesel engines convert the chemical energy contained in the fuel into mechanical power. Diesel fuel is injected under pressure into the engine cylinder where it mixes with air and where the combustion occurs. The exhaust gases which are discharged from the engine contain several constituents that are harmful to human health and to the environment. By the emission of diesel engine consist of CO, HC, NOx, SO_2 and particulate matter as shown on eqn. 2.1 [14] and Fig. 2.3 shows the combustion phenomena in combustion chamber.

$$C_xH_y + AIR \rightarrow aCO_2 + bH_2O + cCO + dC_{(s)} + mHC_{(l)} + nNO_x \quad (2.1)$$

This material is reserved for educational use only, not allowed for commercial use.
Forbidden to modify the content, and cite the document when use.

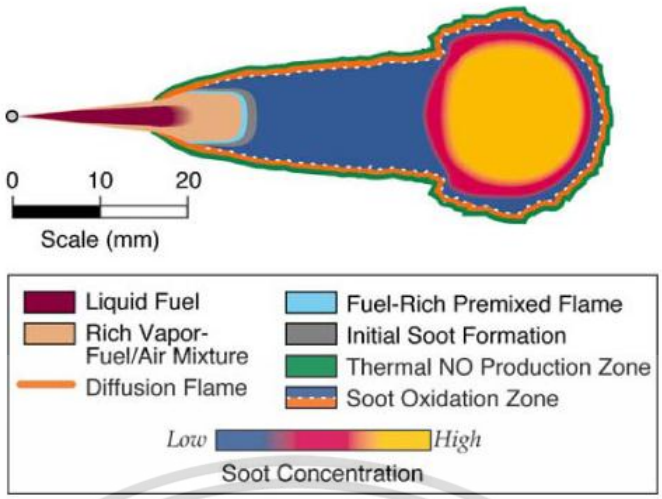

Figure 2.3 Diesel combustion flame zone [14]

Carbon monoxide (CO), hydrocarbons (HC), and aldehydes are generated in the exhaust as the result of incomplete combustion of fuel. A significant portion of exhaust hydrocarbons is also derived from the engine lube oil. When engines operate in enclosed spaces, such as underground mines, buildings under construction, tunnels or warehouses, carbon monoxide can accumulate in the ambient atmosphere and cause headaches, dizziness and lethargy. Under the same conditions, hydrocarbons and aldehydes cause eye irritation and choking sensations. Hydrocarbons and aldehydes are major contributors to the characteristic diesel smell. Hydrocarbons also have a negative environmental effect, being an important component of smog.

Nitrogen oxides (NOx) are generated from nitrogen and oxygen under the high pressure and temperature conditions in the engine cylinder. NOx consist mostly of nitric oxide (NO) and a small fraction of nitrogen dioxide (NO_2). Nitrogen dioxide is very toxic. NOx emissions are also a serious environmental concern because of their role in the smog formation.

Sulfur dioxide (SO_2) is generated from the sulfur present in diesel fuel. The concentration of SO_2 in the exhaust gas depends on the sulfur content of the fuel. Low sulfur fuels of less than 0.05% sulfur are being introduced for most diesel engine applications. Sulfur dioxide is a colorless toxic gas with a characteristic, irritating odor. Oxidation of sulfur dioxide produces sulfur trioxide which is the precursor of sulfuric acid which, in turn, is responsible for the sulfate particulate matter emissions.

This material is reserved for educational use only, not allowed for commercial use.
Forbidden to modify the content, and cite the document when use.

Sulfur oxides have a profound impact on environment being the major cause of acid rains.

Particulate matter (PM) is a complex aggregate of solid and liquid material. Its origin is carbonaceous particles generated in the engine cylinder during combustion. The primary carbon particles form larger agglomerates and combine with several other, both organic and inorganic, components of diesel exhaust.

2.3 Particulate matter

Particulate matter (PM) is the most important characteristics of diesel emissions which is responsible for black smoke traditionally associated with diesel powered vehicles. Diesel particulate matter emission is usually abbreviated as PM or DPM. Size of PM particles can be classified into various categories. Particles normally found in atmosphere can be categorized as PM10, diameter (D) < 10 μm; fine particles, D < 2.5 μm; ultrafine particles, D < 0.10 μm; and nanoparticles, D < 50 nm [15]. Detailed information of particulate matter is to be referred in the literature review session of "**2.6.2 Particulate matter morphology and nanostructure**".

2.4 Alternative fuel

Alternative fuels are derived from sources other than petroleum. Most are produced domestically, reducing our dependence on imported oil. Depletion of petroleum derived fuel and environmental concern has promoted to look over the biofuel as an alternative fuel sources since they are derived from renewable sources and produce less pollution than gasoline or diesel [16]. The two most common types of biofuels are ethanol and biodiesel [17].

2.4.1 Biodiesel

Biodiesel is an alternative fuel for diesel engines that is produced by chemically reacting a vegetable oil or animal fat with an alcohol such as methanol. The reaction requires a catalyst, usually a strong base, such as sodium or potassium hydroxide, and produces new chemical compounds called methyl esters. It is these esters that have come to be known as biodiesel. Because its primary feedstock is a vegetable oil or animal fat, biodiesel is generally considered to be renewable. Since

This material is reserved for educational use only, not allowed for commercial use.
Forbidden to modify the content, and cite the document when use.

the carbon in the oil or fat originated mostly from carbon dioxide in the air, biodiesel is considered to contribute much less to global warming than fossil fuels. Diesel engines operated on biodiesel have lower emissions of carbon monoxide, unburned hydrocarbons, particulate matter, and air toxics than when operated on petroleum-based diesel fuel. Biodiesel is produced through a process known as transesterification, as shown in Fig 2.4. By R1, R2, and R3 are long hydrocarbon chains, sometimes called fatty acid chains. There are only five chains that are most common in soybean oil and animal fats (others are present in small amounts) [18].

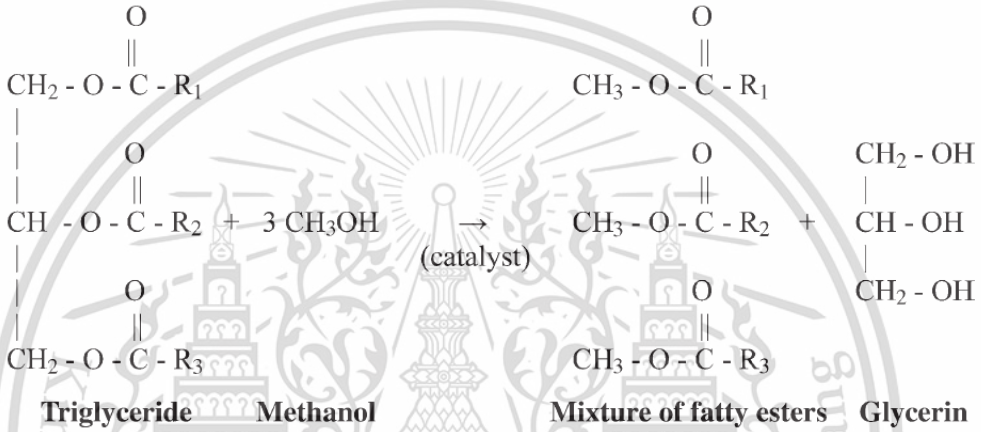

Figure 2.4 Transesterification of Vegetable Oil to Biodiesel [18]

2.4.2 Ethanol

Ethanol is a clear liquid alcohol that is made by the fermentation of different biological materials. This alcohol is known to have many uses, but one in particular is becoming more popular. Ethanol, the most widely used biofuel, is made in a process similar to brewing beer. The ethanol in the end is blended with gasoline to improve vehicle performance and reduce air pollution. Ethanol is the most important member of a large group of organic compounds that are called alcohols. Alcohol is an organic compound that has one or more hydroxyl (OH-) groups attached to a carbon atom. Alcohol is shown as: C-O-H or C-OH. What is attached to the carbon at the three remaining bonds or locations determines the particular kind of alcohol. Ethanol has hydrogen present at two sites while the remaining site holds another carbon atom. This carbon atom, in turn, holds three more hydrogen atoms. It may be shown as Fig.2.5.

This material is reserved for educational use only, not allowed for commercial use.
Forbidden to modify the content, and cite the document when use.

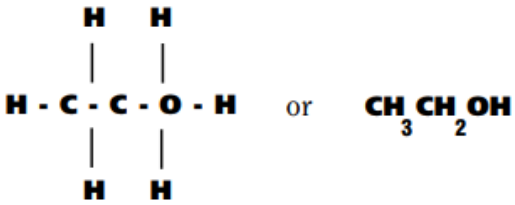

Figure 2.5 Chemical formula of ethanol [19]

2.5 Technical analysis

2.5.1 Scanning electron microscope

The scanning electron microscope (SEM) uses a focused beam of high-energy electrons to generate a variety of signals at the surface of solid specimens. The signals that derive from electron-sample interactions reveal information about the sample including external morphology (texture), chemical composition, and crystalline structure and orientation of materials making up the sample. In most applications, data are collected over a selected area of the surface of the sample, and a 2-dimensional image is generated that displays spatial variations in these properties. Areas ranging from approximately 1 cm to 5 microns in width can be imaged in a scanning mode using conventional SEM techniques (magnification ranging from 20X to approximately 30,000X, spatial resolution of 50 to 100 nm). The main SEM components include: Source of electrons, Column down which electrons travel with electromagnetic lenses, Electron detector, Sample chamber and Computer and display to view the images as shown in Fig. 2.6. Electrons are produced at the top of the column, accelerated down and passed through a combination of lenses and apertures to produce a focused beam of electrons which hits the surface of the sample. The sample is mounted on a stage in the chamber area and, unless the microscope is designed to operate at low vacuums, both the column and the chamber are evacuated by a combination of pumps. The level of the vacuum will depend on the design of the microscope. The position of the electron beam on the sample is controlled by scan coils situated above the objective lens. These coils allow the beam to be scanned over the surface of the sample. This beam scanning, as the name of the microscope suggests, enables information about a defined area on the sample to be collected. As a result of the electron-sample interaction, a number of signals are produced. These signals are then detected by appropriate detectors.

This material is reserved for educational use only, not allowed for commercial use.
Forbidden to modify the content, and cite the document when use.

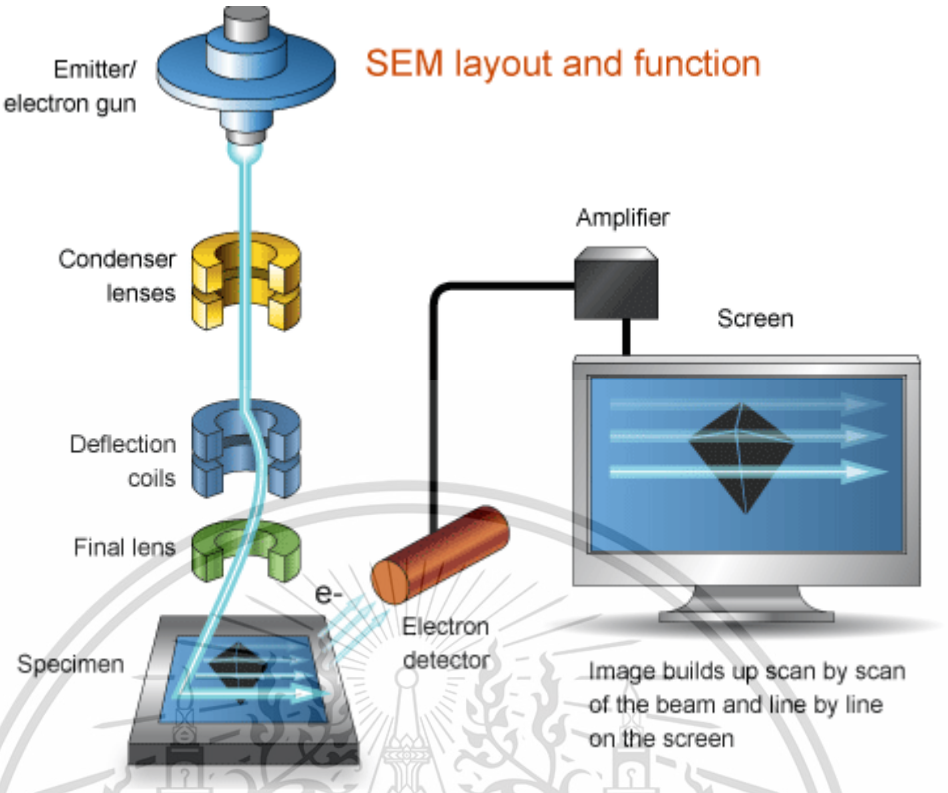

Figure 2.6 Schematics of scanning electron microscopy operation [20]

2.5.2 Transmission electron microscope

The transmission electron microscope (TEM) is a very powerful tool for material science. Figure 2.7 shows schematic of transmission electron microscopy operation by a high energy beam of electrons is shone through a very thin sample, and the interactions between the electrons and the atoms can be used to observe features such as the crystal structure and features in the structure like dislocations and grain boundaries. Chemical analysis can also be performed. TEM can be used to study the growth of layers, their composition and defects in semiconductors. High resolution can be used to analyze the quality, shape, size and density of quantum wells, wires and dots. The TEM operates on the same basic principles as the light microscope but uses electrons instead of light. Because the wavelength of electrons is much smaller than that of light, the optimal resolution attainable for TEM images is many orders of magnitude better than that from a light microscope. Thus, TEMs can reveal the finest details of internal structure - in some cases as small as individual atoms.

This material is reserved for educational use only, not allowed for commercial use.
Forbidden to modify the content, and cite the document when use.

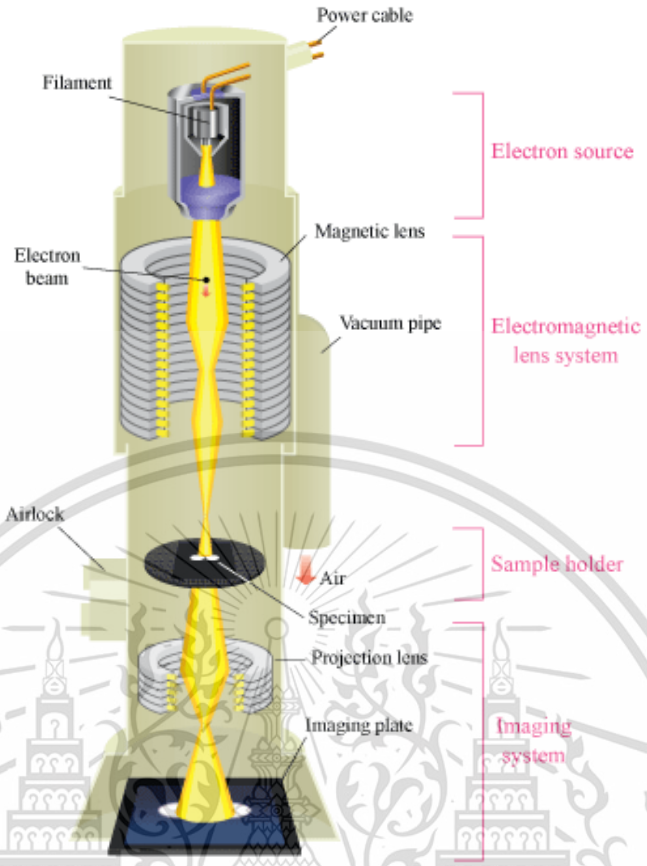

Figure 2.7 Schematics of transmission electron microscopy operation [21]

In the TEM, when a beam of electrons of high energy strikes a thin sample then most of the electrons pass through it. These are called transmitted electrons and include both undeflected and deflected electrons. The beam of electrons which passes through the sample without any deflection from its original direction is focused at the back focal plane (BFP) of the objective lens parallel to the optical axis and is called direct beam as shown in Fig. 2.8 [22]. The other electrons which are scattered at certain angles are focused off-axis at the BFP of the lens and they are called diffracted beams.

In order to form images in the TEM from transmitted electrons, either the central bright spot, or some or all of the scattered electrons can be used. Electrons scattered at a specific angle can thus be selected by inserting an aperture into the BFP of the objective lens. This aperture is called the objective aperture. If the direct beam is selected, the resultant image is called bright-field (BF) image, and if scattered

This material is reserved for educational use only, not allowed for commercial use.
Forbidden to modify the content, and cite the document when use.

electrons are selected then the micrograph is called dark-field (DF) image. Typical magnification ranges of these modes are 25,000x-100,000x.

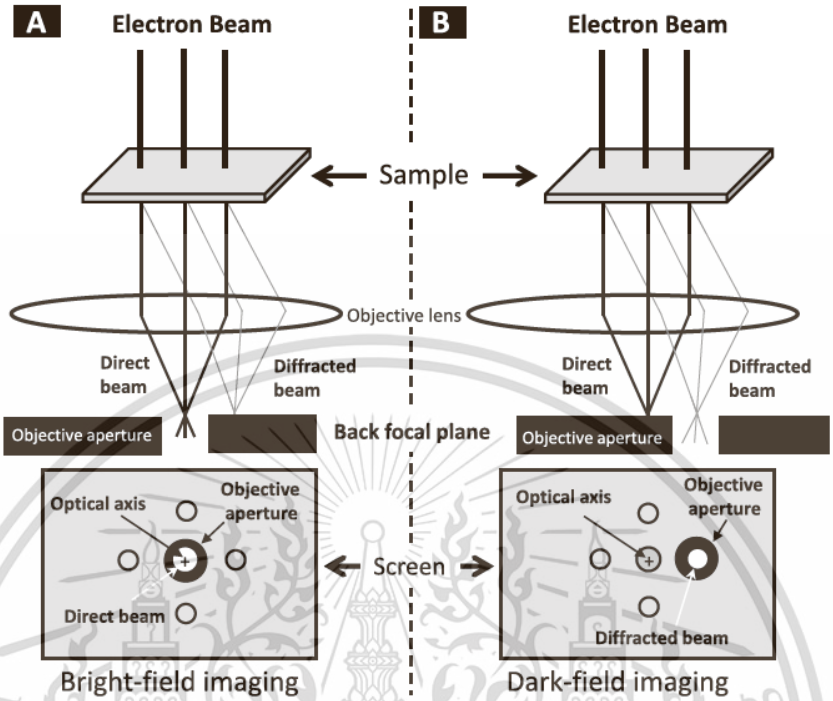

Figure 2.8 Schematics of how the direct and diffracted beams can be selected to form an image on TEM. [22]

2.5.3 Thermogravimetric analysis

Thermogravimetric Analysis or Thermal Gravimetric Analysis (TGA) is a type of testing that is performed on samples to determine changes in weight in relation to change in temperature. Such analysis relies on a high degree of precision in three measurements: weight, temperature, and temperature change. As many weight loss curves look similar, the weight loss curve may require transformation before results may be interpreted. A derivative weight loss curve can be used to tell the point at which weight loss is most apparent. Again, interpretation is limited without further modifications and deconvolution of the overlapping peaks may be required. Typically TGA analysis has 2 types; Isothermal TGA and Non Isothermal TGA. Isothermal TGA works at constant temperature and weight loss is recorded with time, meanwhile Non isothermal TGA performs on continuous increasing temperature with time. Also, weight change is recorded. [23] TGA is commonly employed in research and testing to determine characteristics of materials such as polymers, to determine degradation temperatures, absorbed moisture content of materials, the level of inorganic and

This material is reserved for educational use only, not allowed for commercial use.
Forbidden to modify the content, and cite the document when use.

organic components in materials, decomposition points of explosives, and solvent residues. It is also often used to estimate the corrosion kinetics in high temperature oxidation. Simultaneous TGA-DTA/DSC measures both heat flow and weight changes (TGA) in a material as a function of temperature or time in a controlled atmosphere. Simultaneous measurement of these two material properties not only improves productivity but also simplifies interpretation of the results. The complementary information obtained allows differentiation between endothermic and exothermic events which have no associated weight loss (e.g., melting and crystallization) and those which involve a weight loss (e.g. degradation). Figure 2.9 shows schematics of Thermogravimetric Analysis operation.

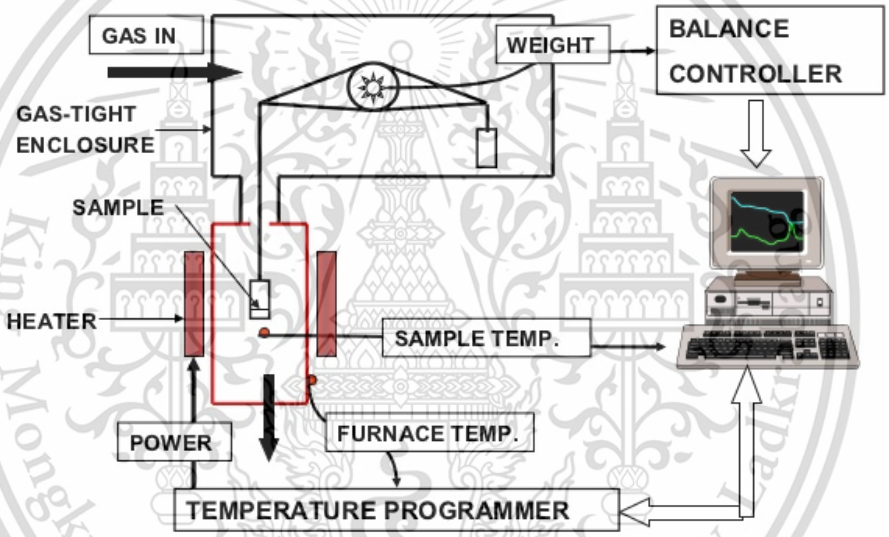

Figure 2.9 Schematics of thermogravimetric analysis operation [24]

This material is reserved for educational use only, not allowed for commercial use.
Forbidden to modify the content, and cite the document when use.

2.6 Literature reviews

2.6.1 Biofuel's effect on diesel engines

Appropriate biofuels which are appropriate for diesel engines in this research field are considered as biodiesel and ethanol. For ethanol, fuel in a form of mixture with conventional diesel as blend might have a concern of miscibility limit. K. Cheenkachorn et al. [25] has researched about miscibility among ethanol, biodiesel, and diesel as following. He explained that miscibility limit occur due to difference in chemical structures and characteristics between ethanol and diesel. Therefore, an effective emulsification technique is necessary for being an emulsion. These two liquid fuels can be efficiently emulsified into a heterogeneous mixture of one micro-particle liquid phase dispersed into another liquid phase by mechanical blending in cooperation with suitable emulsifiers. The emulsifier would reduce the interfacial tension force and increase the affinity between the two liquid phases, leading to emulsion stability [26]. A suitable emulsifier for ethanol and diesel fuel is suggested to contain both lipophilic part (non-polar) for matching with diesel molecules and hydrophilic part (polar) for matching with ethanol molecules in order to obtain an emulsion of diesohol. And such chemical structures can be found in biodiesel, as shown in Fig. 2.10.

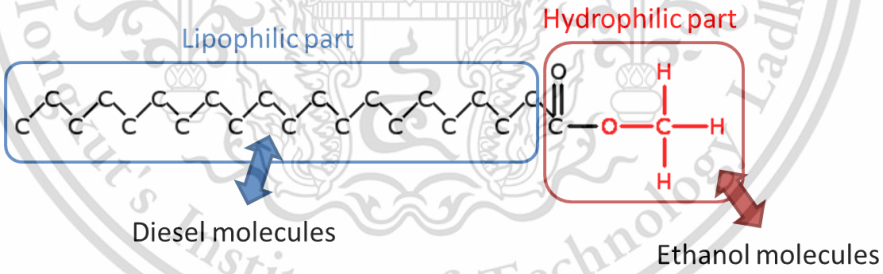

Figure 2.10 Biodiesel chemical structure

According to fuel miscibility, P. Kwanchareon et al. [27] have performed experiments of three phase diagram of diesel - palm biodiesel - ethanol at different conditions of temperature and purity of ethanol. Overall results show that biodiesel could be used as an effective additive for ethanol-diesel emulsions. Intersolubility of the components of diesel–biodiesel–ethanol system decreased with decreasing temperature. However, at temperatures above 20 degree Celsius, there was no

This material is reserved for educational use only, not allowed for commercial use.
Forbidden to modify the content, and cite the document when use.

problem with phase separation. Figure 2.11 shows a three phase diagram of ethanol 99.5%-biodiesel-diesel at 20°C.

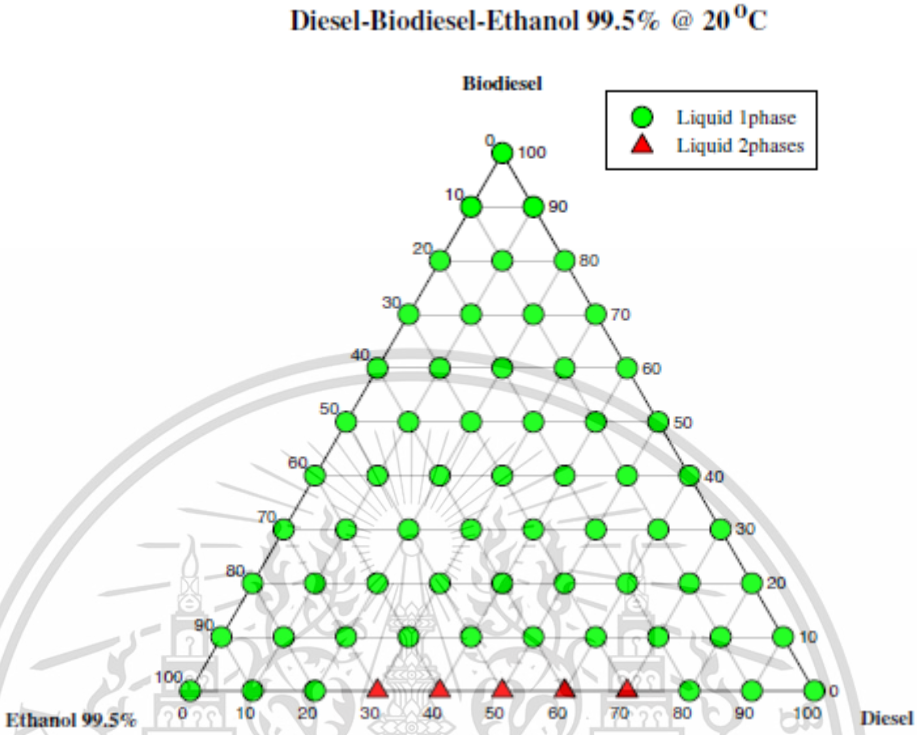

Figure 2.11 Phase behavior of diesel–biodiesel–ethanol 99.5% at 20°C [27]

In terms of engine performance, combustion characteristics, and emission, following researchers have done experiments and discussed in various interesting points.

D. B. Hulwan et al. [28] performed experiments with blended fuels of biodiesel (B), ethanol (E), and diesel (D) with ratio of D70/E20/B10, D70/E30/B20, D50/E40/B10, and D100. Fuels were supplied to a 3-cylinders diesel engine with adjustable injection timing. At low load of 0.2 MPa BMEP, low speed of 1200 RPM, and injection timing of 13 bTDC (timing range from 13 to 21 bTDC), fuel with ethanol content show obvious combustion delay represented as pressure and heat release graphs with respect to crank angle represented as Fig 2.12. In addition, fuel consumption increases as ethanol proportion in the fuel as shown in Fig. 2.13. Regarding emission gas and smoke, smoke reduced remarkably for blends especially at medium and high loads of both speeds and all injection timings. NO emission does not show obvious trend while CO emission is drastically increased at low loads and decreased slightly at high loads for the blends.

This material is reserved for educational use only, not allowed for commercial use.
Forbidden to modify the content, and cite the document when use.

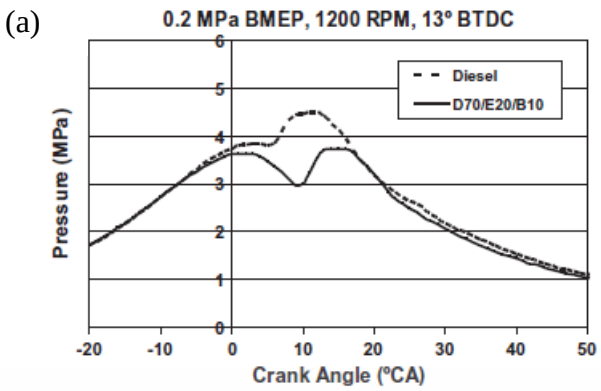

Figure 2.12 (a) Pressure–Crank angle diagram, (b) Net heat release rate at 1200 RPM [28]

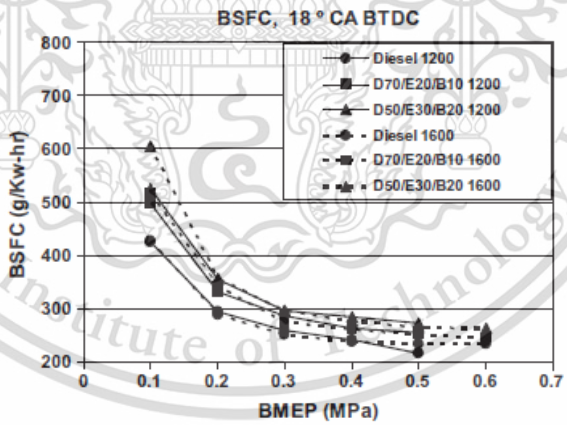

Figure 2.13 Brake specific fuel consumption [28]

W. Tutak et al. [29] compared combustion effect between diesel-ethanol (DE) mixture and biodiesel-ethanol (BE) mixture on a small diesel engine. Compared to the BE blend, diesel engine powered by the DE blend is characterized by higher values of IMEP and thermal efficiency (Fig. 2.14). However, as increasing ethanol content, obvious combustion delay can be observed as represented in Fig. 2.15

This material is reserved for educational use only, not allowed for commercial use.
Forbidden to modify the content, and cite the document when use.

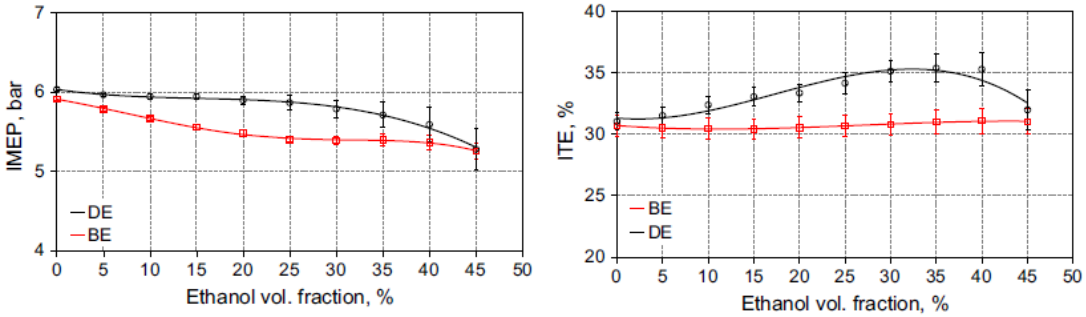

Figure 2.14 Indicated mean effective pressure and indicated thermal efficiency [29]

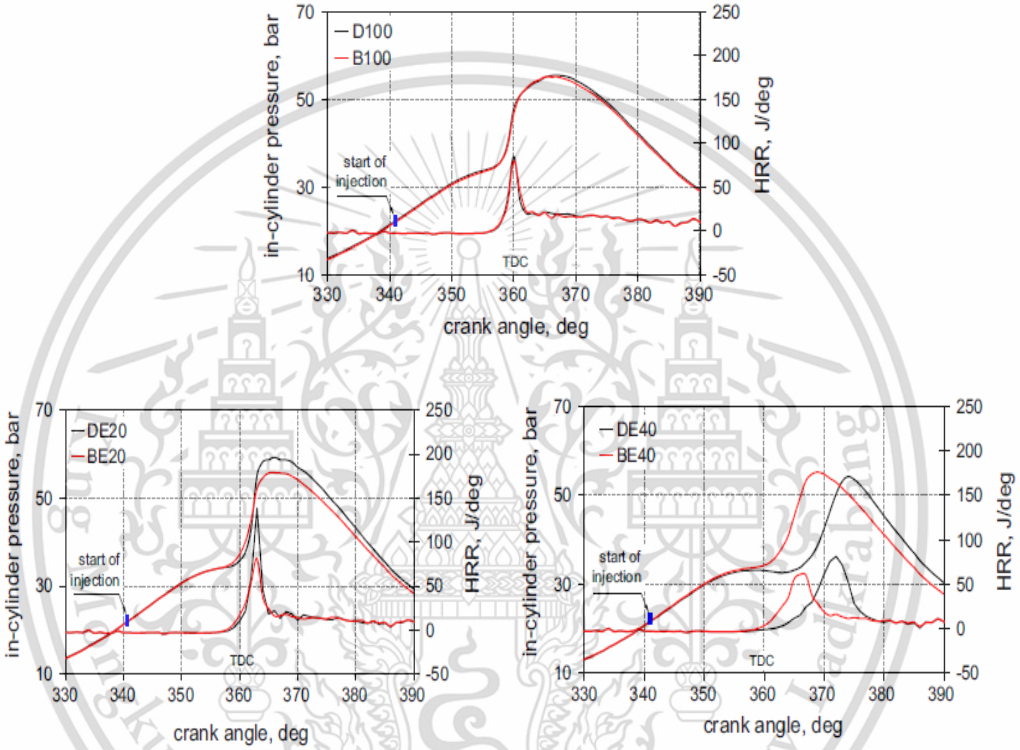

Figure 2.15 Pressure and heat release of engine by diesel-ethanol (DE) and biodiesel-ethanol (BE) at various ethanol ratio [29]

L. Zhu et al. [30] investigated combustion performance and emission characteristics of a DI diesel engine fueled with ethanol–biodiesel blends (BE). Figure2.16 shows results of engine performance which indicate that when compared with Euro V diesel, thermal efficiency of biofuels has improved significantly and BE5 has highest thermal efficiency. On the whole, compared with Euro V diesel fuel, the BE blends could lead to reduction of both NOx and particulate emissions of the diesel engine as shown in Fig 2.17.

This material is reserved for educational use only, not allowed for commercial use.
Forbidden to modify the content, and cite the document when use.

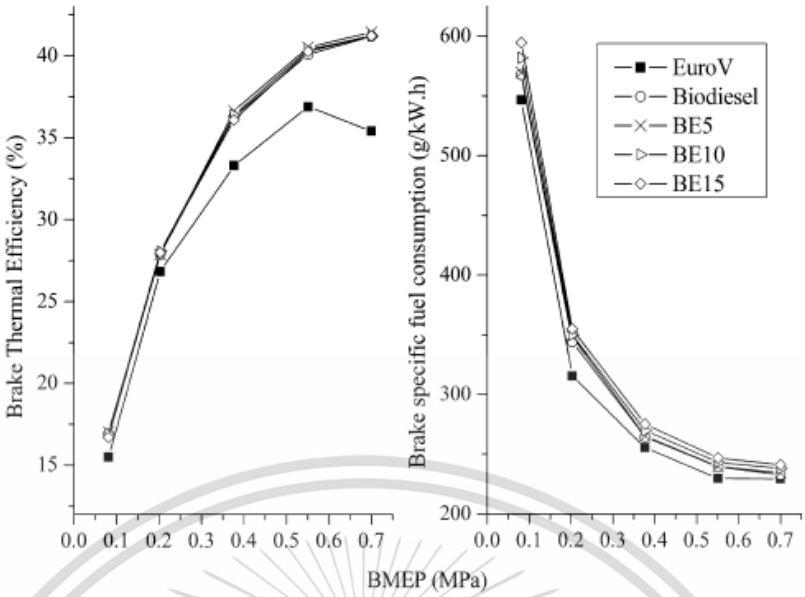

Figure 2.16 Brake thermal efficiency and brake specific fuel consumption [30]

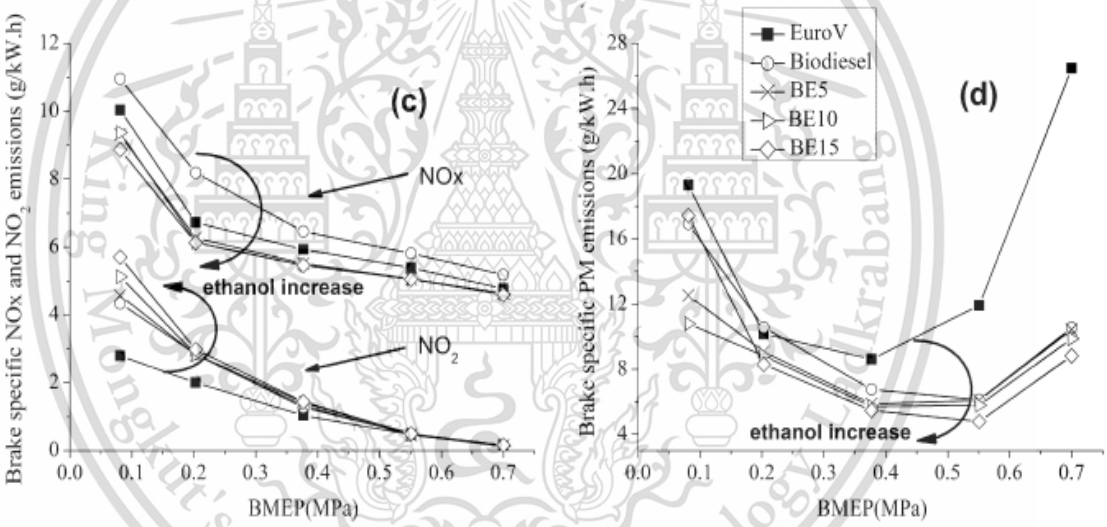

Figure 2.17 Brake specific emissions [30]

2.6.2 Particulate matter's morphology and nanostructures

Particles of particulate matters can be divided into 3 modes of size range according to exhaust stream of a motor vehicle: Nucleation mode, Accumulation mode, and Coarse mode as shown in Fig 2.18 [31]. Nucleation mode is so far obscure. Most researchers suggested that nucleation mode particles consist of volatile material i.e. appear in spherical shapes, while others proclaimed nucleation mode particles are in fact solid.

Accumulation mode particles consist of many **primary particles** or **spherules**. Spherules are porous carbonaceous shells established by pyrolysis of

This material is reserved for educational use only, not allowed for commercial use.
Forbidden to modify the content, and cite the document when use.

gaseous fuels or volatile components of liquid or solid fuels. Size range of spherules is typically 20-50 nm. Agglomerate sizes arbitrarily depend on number of the spherules. Number of the spherules in agglomerate has not been revealed in clear relationship with other factors yet.

Coarse mode is formed at combination of the accumulation and the nucleation mode which particles include abnormal rust and scale. Processes in the coarse mode were reported as random and unpredictable manner.

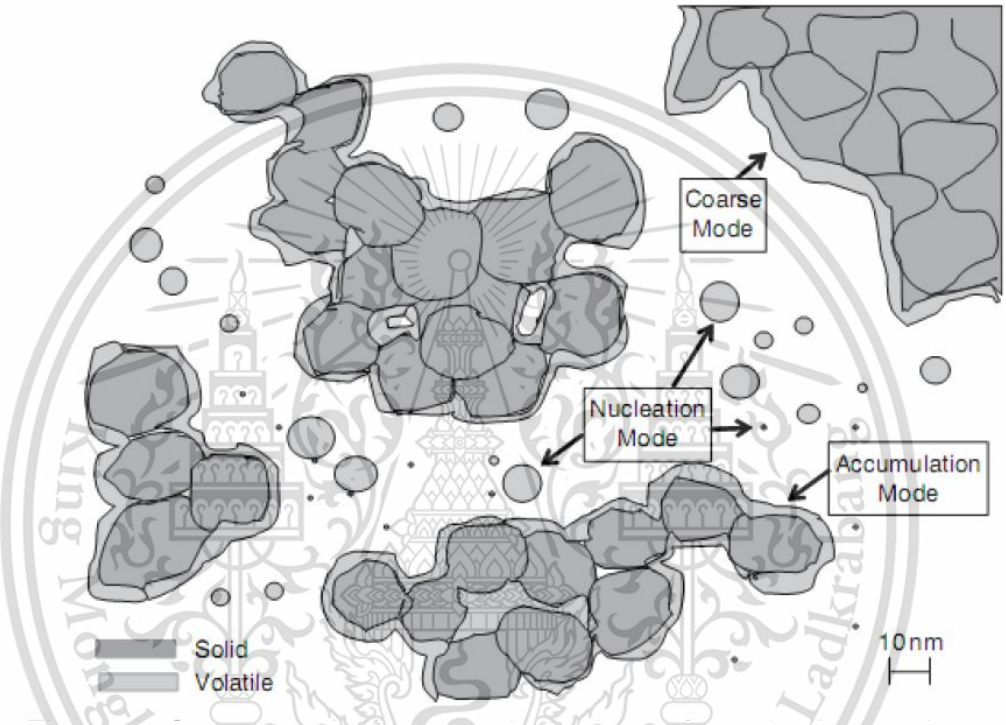

Figure 2.18 Schematic diagram of particles in coarse mode (largest, shown in part), accumulation mode (middling), and nucleation mode (smallest) [31]

M. M. Maricq (2007) [32] proposed characteristics of particulate matters from diesel engine. Figure 2.19 shows that diesel particulate matter consists of two types of particles: (a) fractal-like agglomerates of primary particles 15–30 nm in diameter, composed of carbon and traces of metallic ash, and coated with condensed heavier end organic compounds and sulfate; (b) nucleation particles composed of condensed hydrocarbons and sulfate.

This material is reserved for educational use only, not allowed for commercial use.
Forbidden to modify the content, and cite the document when use.

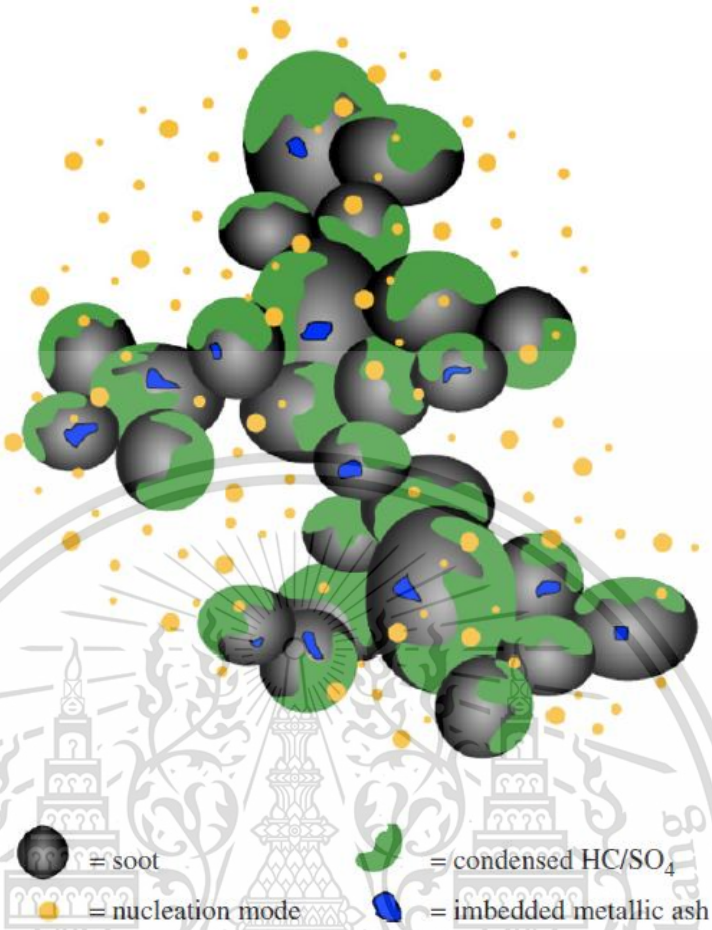

Figure 2.19 Artist's conception of diesel particulate matter [32]

D. B. Kittelson [15] proposes a model of size distributions for typical particles emitted from internal combustion engines as shown in Fig. 2.20. The size distributions were plotted according to 3 measurement aspects: number, area, and mass distribution. For nucleation mode, particles range from few nanometers to less than 50 nm and become larger by accumulation mode in the range of 0.1 – 0.3 micron. Coarse mode which consists of nucleation mode and accumulation mode are further larger.

This material is reserved for educational use only, not allowed for commercial use.
Forbidden to modify the content, and cite the document when use.

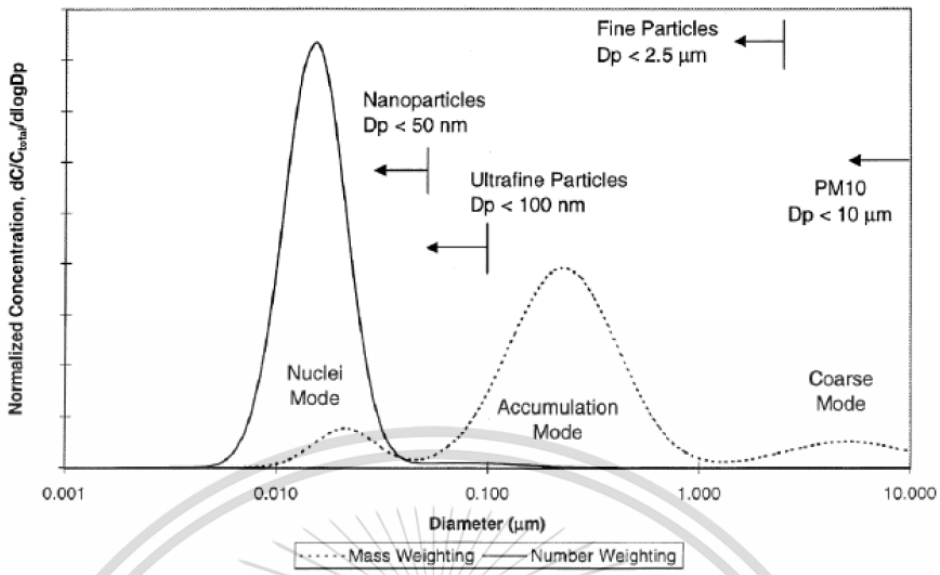

Figure 2.20 Particle size distribution of soot from a diesel engine [15]

Referred from P. Eastwood [31], particulate matters composition can be categorized into 2 main groups as; volatile or soluble group, and non-volatile or insoluble group. **Volatile** matters consist of **sulphate fraction and organic fraction**. **Non-volatile** matters consist of **carbonaceous fraction or "Soot**" in this research, and **ash fraction**. Soot and ash are generated in the engine, while other volatile substances form later. Four main sources of particulate matter's emergence are fuel, lubricant, air, and material breakdown. Fuel contributes mainly to carbonaceous fraction and organic fraction, while other agents contribute to ash and sulphate fraction. Particulate matter formation starts with the earliest process in the combustion chamber. Carbonaceous fraction or soot forms within the engine. Ash fraction probably forms before exhaust valve open depending on the source of emergence. Organic and sulphate fraction which is considered as volatile are suggested to form at final stage, probably at the cold end of the exhaust system.

Since carbonaceous fraction is considered to be the best explanation for the particulate formation, this research focuses on the mechanisms of carbonaceous or **Soot formation**.

Soot formation start with fuel molecules in the combustion chamber with lack of oxygen. At high temperature and low oxygen condition, **pyrolysis** breaks down fuel molecules with high molecular weight into **Soot precursor** molecules as

This material is reserved for educational use only, not allowed for commercial use.
Forbidden to modify the content, and cite the document when use.

represented in Fig. 2.21. Precursor molecules are hold and undergo **Nucleation** to form the first discernable particle or **Nuclei** at less than 3 nm. which Wang H. [33] proclaimed as acetylene (C_2H_2) and polycyclic aromatic hydrocarbons (PAH). Nuclei begin to increase their mass but keep unchanged number of particles in **Surface growth.** At this process, spherules are generated by carbon added but hydrogen is removed so that ratio of C/H reduces and isolated spherule particles are formed with size range of 20 – 50 nm. During this growth, spherules collision due to free movement sticks particles together in **Agglomeration** process. Concurrent surface growth and agglomeration lead to bigger particles with familiar identities. Particle number decreases with mass unchanged in this process. Agglomeration is more physical while nucleation and surface growth is rather chemical process.

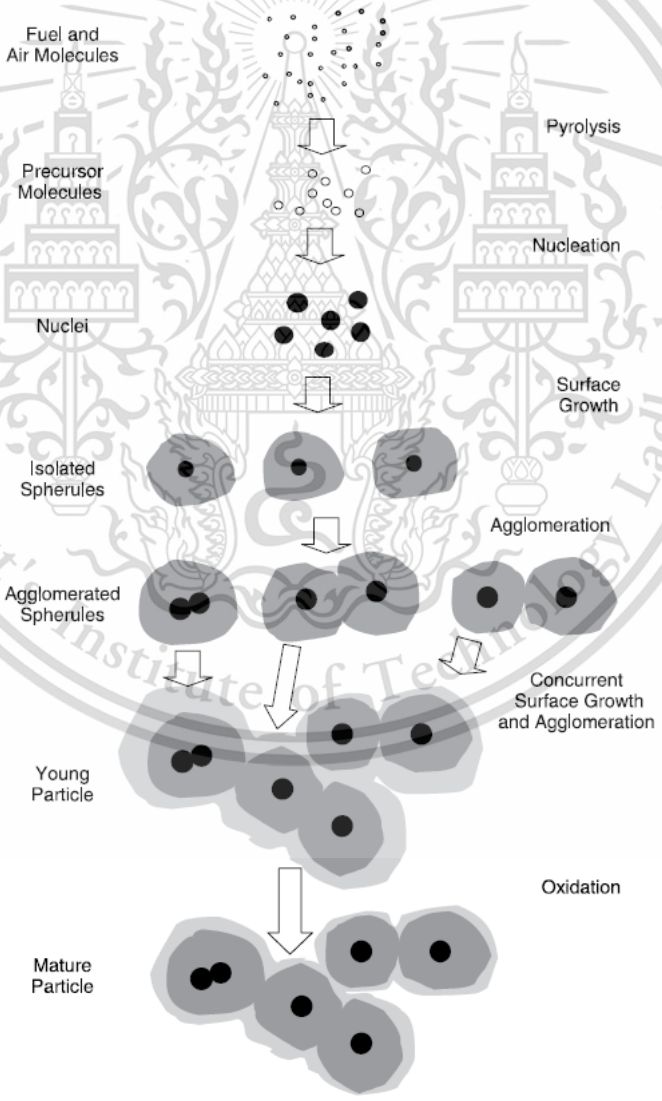

Figure 2.21 Conceptual scheme for soot formation [31]

This material is reserved for educational use only, not allowed for commercial use.
Forbidden to modify the content, and cite the document when use.

Oxidation is a converse process since it reverses the process of soot production and stops the growth in any formation stage. There are two aspects in explanation of restricted spherule diameters even across different combustion. First, common termination of surface growth due to supply of soot precursors is exhausted. Second is oxidation of the spherule surface stops the particle's growth. Oxidation is a chemical rather than physical. Responsible oxidant is suggested as O, OH, H, CO_2, CO, H_2O, and O_2. **Predominant oxidant is proclaimed as OH and O_2** [34]. Clustered morphology tends to be less oxidized than chain. Disorder amorphous structure tends to be more oxidative which take place on surface as expressed as surface recession.

To visualize soot concepts, P. Karin et al. [35] investigated physical characterization of diesel particulate matters by SEM and TEM. Figure2.22 shows SEM image of diesel agglomerated PMs. The agglomerate particle size is about 100 to 600 nm and much amount number of particles is in range of 100 to 300nm.

Figure 2.22 SEM image of fine agglomerated PM from a small diesel engine [35]

Figure 2.23 shows TEM image of diesel fine agglomerated PMs which consist of many primary particles. The particle size was about 20 to 80 nm. The different size of a primary particle might be depends on not only amount of carbon atoms accumulation but also the oxidation of PM's surface during fuel combustion process. Detailed primary particles as shown in Fig.2.24 are nearly spherical shape even though surfaces are not so smooth. The image also shows structure of inner core zone and outer shell zone of PMs. The inner core diameters are approximately 5 to10 nm

This material is reserved for educational use only, not allowed for commercial use.
Forbidden to modify the content, and cite the document when use.

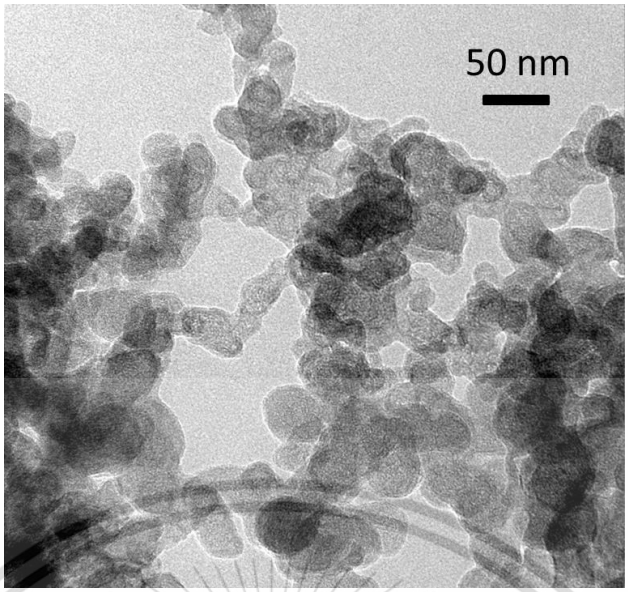

Figure 2.23 TEM image of fine agglomerated PM from a small diesel engine [35]

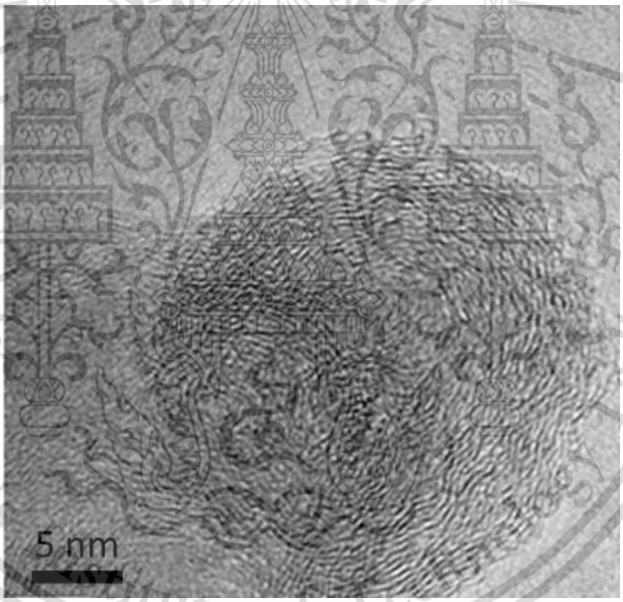

Figure 2.24 TEM image of primary particle PM from a small diesel engine [35]

Since basic structure unit of the carbonaceous fraction is spherule or primary particle, examining particles in nanostructure detail might help to get more insight of soot. Lipkea et al. [36] proposed well-accepted conceptual models of spherule nanostructure as shown in Fig. 2.25. On an ascending dimensional scale, a primary particle's nanostructure components start from carbon atoms arranged in repeating six-membered rings with covalent bond, forming planar hexagonal arrays. Two hexagonal arrays are chemically bonded, forming parallel with 0.35 – 0.36 nm apart,

This material is reserved for educational use only, not allowed for commercial use.
Forbidden to modify the content, and cite the document when use.

face-centered layers or **platelets**. Two to five platelets are stacked, forming commonly oriented **crystallites**. This interlayer bonding is weaker, relying on Van der Waal's forces. Crystallites are stacked in various orientations, forming completed spherules. Naturally, a spherule contains ~10^5 to 10^6 carbon atoms into ~10^3 to 10^4crystallites.

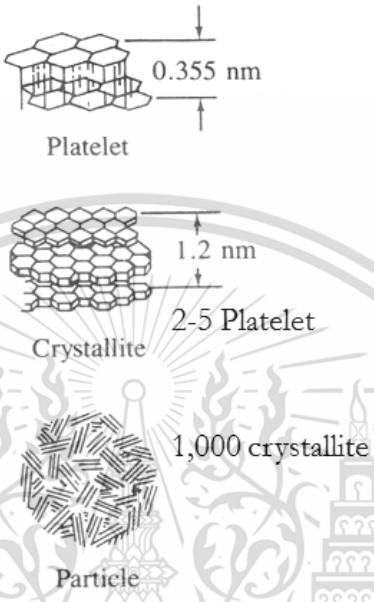

Figure 2.25 Conceptual model of primary particle's nanostructure components [36]

Braun et al. [37] claimed from the experimental observation that hexagonal ordered microstructure can be referred as graphite or the arrays of **graphene sheets**. V. Fernandez-Alos et al. [38] represented soot and char molecular models derived from High Resolution TEM lattice fringe images. Soot images were image-processed to generate the lattice fringe format. It was assumed that each fringe length is as long as it is deep in depth dimension so that a **graphene sheet is formed** in the shape of a hexagon which depend on sizes of polyaromatic hydrocarbon (PAH) molecules. The longer fringes are inferred as larger aromatic structures of varying carbon numbers (numbers of hexagonal rings). Figure 2.26 show schematic diagram of relationships between number of hexagon rings and amount of carbon atoms contained in the graphene sheet.

This material is reserved for educational use only, not allowed for commercial use.
Forbidden to modify the content, and cite the document when use.

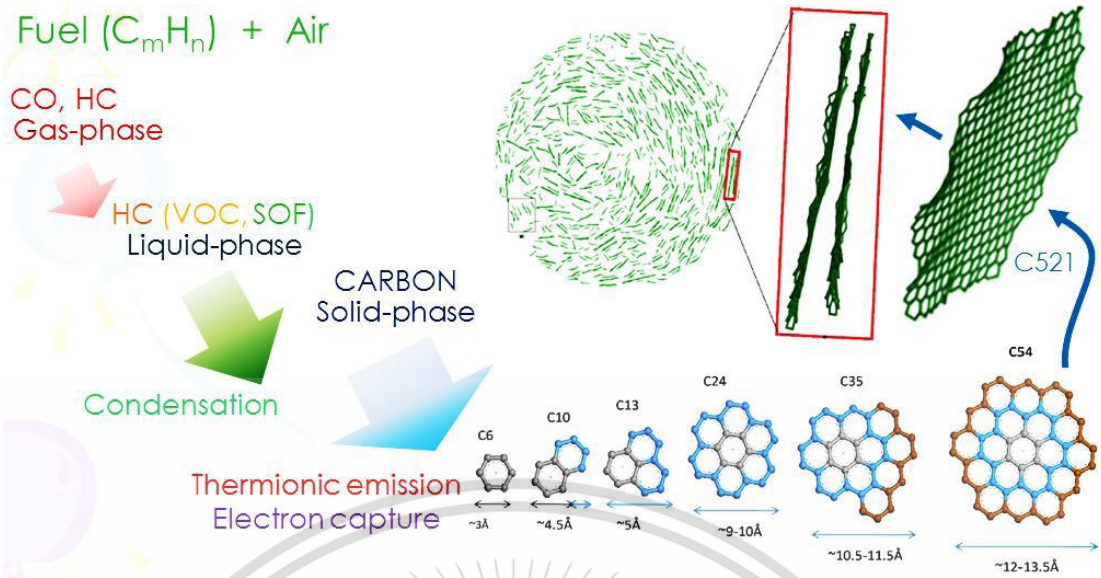

Figure 2.26 Relationship between number of hexagon rings and Carbon atoms in graphene sheet of soot particle [38]

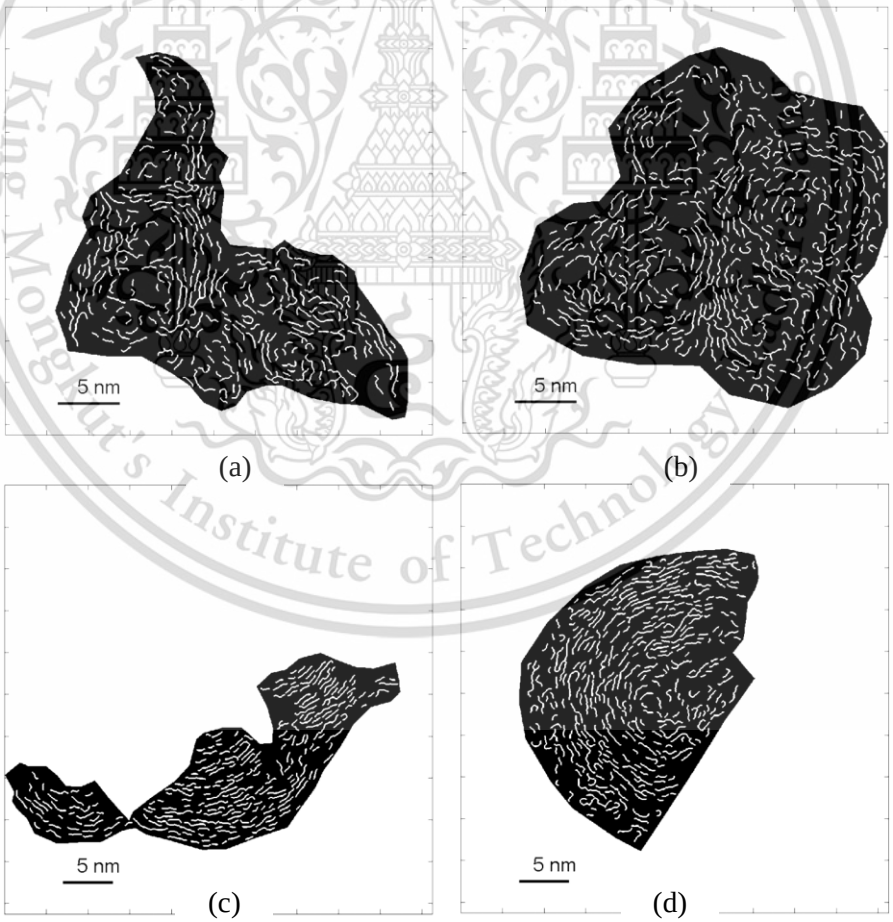

Figure 2.27 Skeletonized images on the selected region of four TEM images of soot (a, b) High-efficiency clean combustion, (c, d) conventional diesel combustion [39]

This material is reserved for educational use only, not allowed for commercial use.
Forbidden to modify the content, and cite the document when use.

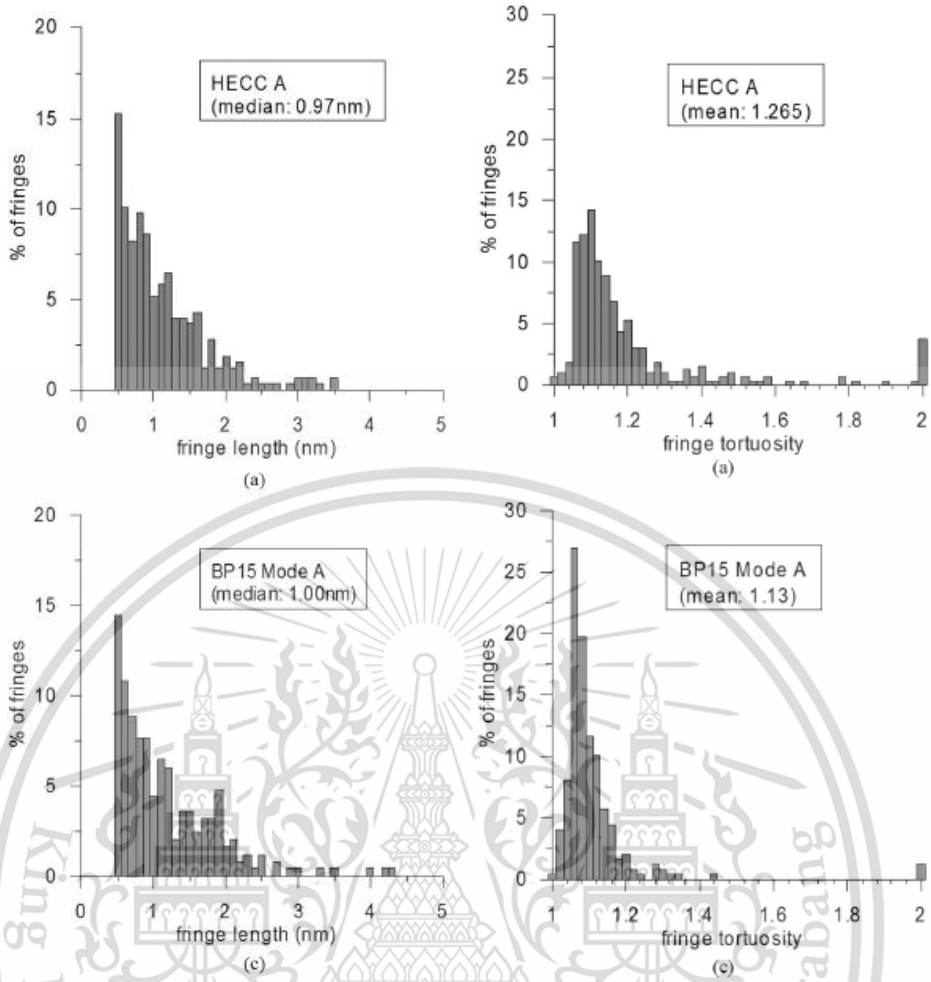

Figure 2.28 Fringe length and tortuosity histograms for (a) high-efficiency clean combustion and (c) conventional diesel combustion condition [39]

K. Yehliu et al. [39] investigated characterization of soot nanostructure generated by a turbo diesel engine in different operating conditions. There is comparison of fringe length and tortuosity. Results on Fig 2.27 and Fig. 2.28 show that conventional diesel combustion condition contributes well-organized soot nanostructure with more portions of long fringe length but low fringe tortuosity compared with high-efficiency clean combustion condition.

As continued investigation of P. Karin [35], they estimated carbon atom density of diesel and biodiesel's PMs with the information of carbon platelet length derived from image processing of soot's TEM images. The estimation applies concepts of "the molecule of carbon-6 (C6) is the possible smallest size" / "there are 3 layers arranged to be a platelet". Results show that PMs contain approximately 600-900 carbon atoms/nm^3.

This material is reserved for educational use only, not allowed for commercial use.
Forbidden to modify the content, and cite the document when use.

2.6.3 Oxidation kinetics

Particulate matter's oxidation kinetics usually applies TGA experimental data for analysis. A. Williams et al. [40] investigated different fuel property effects on particulate matter reactivity. Biodiesel - diesel blend or B20 and decanol ($C_{10}H_{21}OH$) – diesel blend or D23 which have same percent oxygen content were compared in the experiment. From Fig. 2.29, TGA results of soot created by combustion of the B20 and D23 shows that D23's soot are more reactive. They suggested that the oxygen in decanol is more available for incorporation into the soot as reactive surface oxygen.

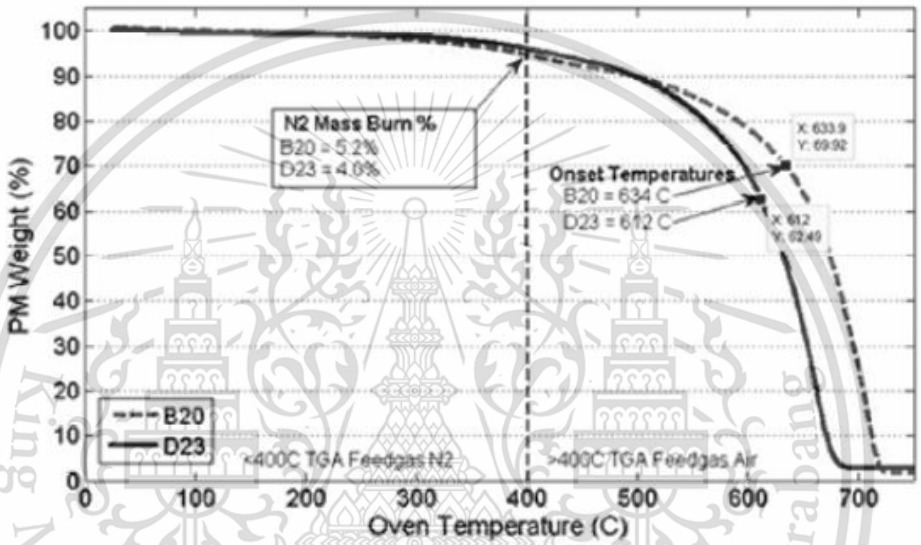

Figure 2.29 Fuel Oxygen Group – TGA Results [40]

J. P. A. Neeft et al. [41] reported on kinetics of the oxidation of diesel soot. They performed TGA experiments on comparison between carbon black soot and diesel soot to determine many oxidation kinetics parameters e.g. reaction rate, reaction order in carbon, reaction order in oxygen, activation energy, and pre-exponential factors. They adopted the oxidation kinetics models as shown in a general form of Eqn. 2.2 to describe the reaction rate of carbonaceous materials

$$r = N_t \cdot k(T) \cdot f(p_{O2}, p_{H2O}, \dots) \tag{2.2}$$

where r is the reaction rate, N_t is the total number of active sites, *k(T)* is a temperature-dependent reaction rate constant, and $f(p_{O2}, p_{H2O}, \dots)$ is a function that describes the dependence of the reaction rate on the partial pressure of the various

This material is reserved for educational use only, not allowed for commercial use.
Forbidden to modify the content, and cite the document when use.

reactants and gas-phase components. The total number of active sites N_t is often described by Eqn. 2.3

$$N_t = \lambda \cdot S_a \tag{2.3}$$

where λ is the surface concentration of active sites and S_a is the specific surface area. As it is generally accepted that the specific surface area S_a is a function of conversion ξ (the fraction of carbon that is oxidized), kinetic models describe the dependence of N_t as a function of conversion. A simple approach is to use an n^{th} order of $(1-\xi)$ as Eqn. 2.4

$$S_a = S_{a,0} \cdot (1-\xi)^{n_\xi} \tag{2.4}$$

where $S_{a,0}$ is the initial surface area (at $\xi = 0$) and n_ξ is the reaction order in carbon. With increasing conversion, the model predicts a decrease in N_t and therefore, in the reaction rate. However, for highly porous carbons, such as soot and activated carbons, S_a can actually increase as a function of conversion, due to pore growth and opening of concluded pore space. Several models have been proposed to account for these phenomena.

The temperature dependence of the reaction rate is usually described by the Arrhenius equation as Eqn. 2.5

$$k(T) = k_0 \cdot \exp(-\frac{E_a}{RT}) \tag{2.5}$$

where T is the absolute temperature, k_0 is the pre-exponential factor, R is the molar gas constant, and E_a is the activation energy.

The function that describes the influence of the partial pressures of the gas-phase components on the reaction rate is usually limited to the influence of the oxygen partial pressure, described by the n_{th} order expression as Eqn. 2.6

$$f(p_{O2}, p_{H2O}, \dots) = p_{O2}^{n_{O2}} \tag{2.6}$$

where p_{O2} is the partial pressure of oxygen and n_{O2} is the order in the oxygen partial pressure.

This material is reserved for educational use only, not allowed for commercial use.
Forbidden to modify the content, and cite the document when use.

P. Karin [42] studied PM oxidation kinetics on conventional cordierite diesel particulate filters (DPF) powders mixed with biodiesel's PM and diesel's PM by TGA. The calculated activation energies of biodiesel's PM in oxidation are lower than that of the diesel engine's PM and carbon black because of unburned oxygenated molecule. The activation energy of biodiesel's PM and diesel's PM on the DPF powders are in the range of 109 ~ 131 kJ/mole and 117 ~ 130 kJ/mole, respectively.

J. Hamada et al. [43] studied effects of engine operating conditions on PM structure and oxidation rate. Different combustion conditions produce soot with different oxygen (O) per carbon (C) ratio. Results show that soot with higher O/C ratio tends to have lower activation energy as shown in Fig. 2.30. The mechanism is assumed that soot has oxygen connected to edge of the graphite crystallite (Fig. 2.31). The smaller graphite structure, more oxygen connected due to more surface area. As a result, Soot with small graphite is easier to oxidize than the bigger graphite which is lack of oxygen at central part.

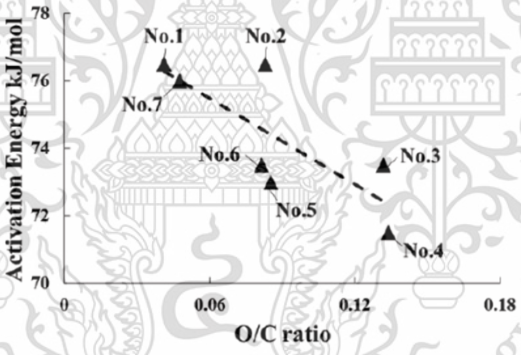

Figure 2.30 Relationships between O/C ratio and activation energy [43]

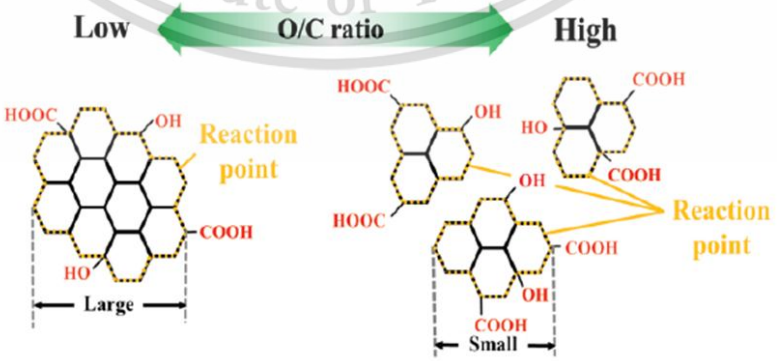

Figure 2.31 Relationships between O/C ratio and graphite crystallite [43]

This material is reserved for educational use only, not allowed for commercial use.
Forbidden to modify the content, and cite the document when use.

CHAPTER 3

RESEARCH METHODOLOGY

3.1 Experimental equipment

3.1.1 Diesel engine specification

There are two small diesel engine used in PM related research as shown in Fig. 3.1. The engine A which was applied in previous research (Biodiesel-Diesel) comes up with single cylinder of 638 cm^3 displacement. The engine B which was applied in present research (Ethanol-Biodiesel) is also a single cylinder engine with 709 cm^3 displacement. Engine specification of both engine are represented in Table 3.1 and Table 3.2.

Table 3.1 "A" engine specification

Items	Details
Engine type	1-cylinder, Natural aspirated, Direct injection, Compression Ignition Engine
Bore x Stroke	92 mm x 96mm
Displacement	638 cm3
Compression ratio	16.1:1
Rated power	7.7 kW @ 2400 rpm
Injection timing	19° CA bTDC
Injection pressure	20 MPa

Table 3.2 "B" engine specification

Items	Details
Engine type	1-cylinder, Natural aspirated, Direct injection, Compression Ignition Engine
Bore x Stroke	97 mm x 96mm
Displacement	709 cm3
Compression ratio	18:1
Rated power	9.2 kW @ 2400 rpm
Injection timing	19° CA bTDC
Injection pressure	22 MPa

This material is reserved for educational use only, not allowed for commercial use.
Forbidden to modify the content, and cite the document when use.

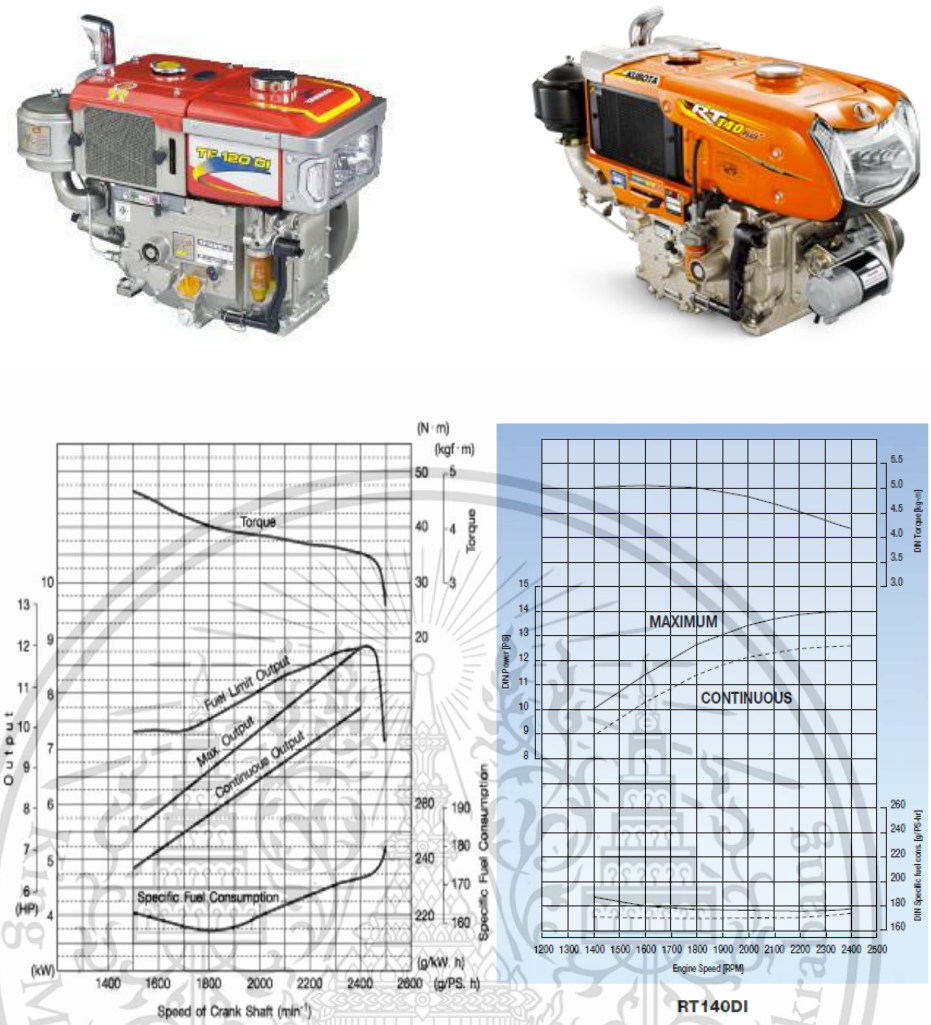

Figure 3.1 Diesel engine A (left) and engine B (right) specification

3.1.2 Eddy Current Engine Dynamometer

The engine dynamometer as shown in Fig. 3.2, Tokyo Plant model ED-60-Horizontal, was used in the experiment for applying a load on the tested engine and also measuring force, moment of force (torque) and power that the tested engine can produce against the load. The type of the engine dynamometer is Eddy current with external water cooling systems. Eddy current dynamometer can provide a quick load change rate for rapid load setting. Eddy current dynamometer consists of an electrically conductive core moving across a magnetic field to produce resistance to movement. The magnetic field is generated by using variable electromagnets that can change the magnetic field strength to control the amount of braking. The electromagnet voltage is control by a desktop computer, using changes in the magnetic field to match the power output.

This material is reserved for educational use only, not allowed for commercial use.
Forbidden to modify the content, and cite the document when use.

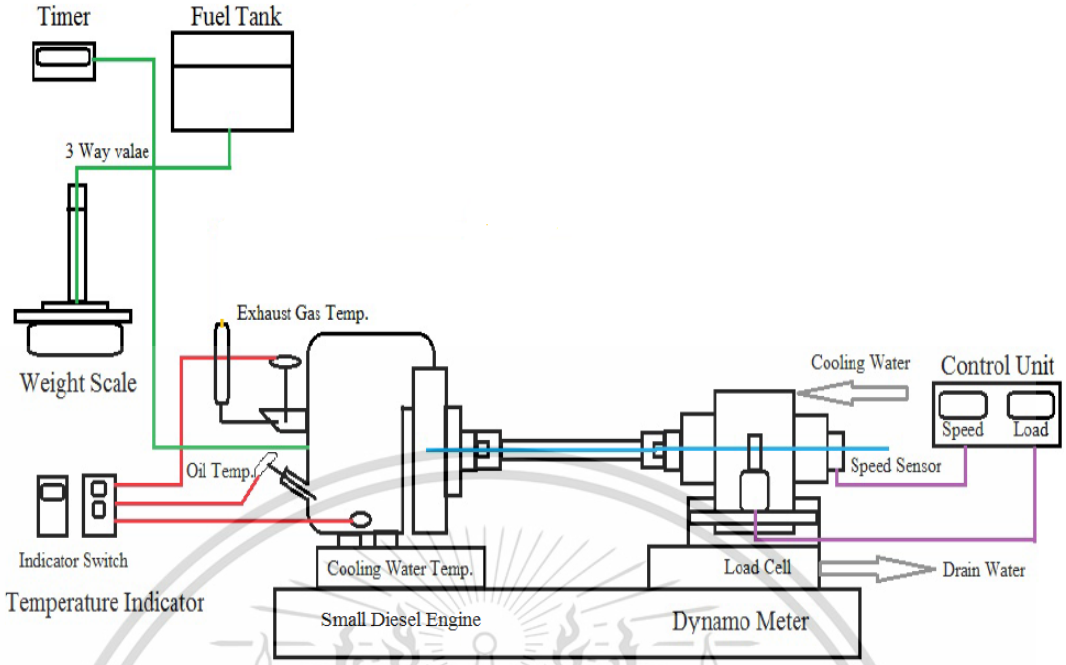

Figure 3.2 Schematic diagram of engine dynamometer

3.1.3 Fuel specification

The fuels used in this experiment are biodiesel (B100) and ethanol-biodiesel blend. The blended fuels contain 10% and 20% by weight of ethanol, and are identified as BE10 and BE20 respectively. The biodiesel was produced from palm-olein (B100-TIS2313-2549). The ethanol was used as anhydrous ethanol 99.8%. For the blended fuel and ethanol, properties of calorific value, heat of vaporization, carbon content, hydrogen content, oxygen content, stoichiometric air-fuel ratio, and density were estimated by interpolation as shown in Table 3.3. Also, Distillation graph of each based fuel is represented in Fig. 3.3.

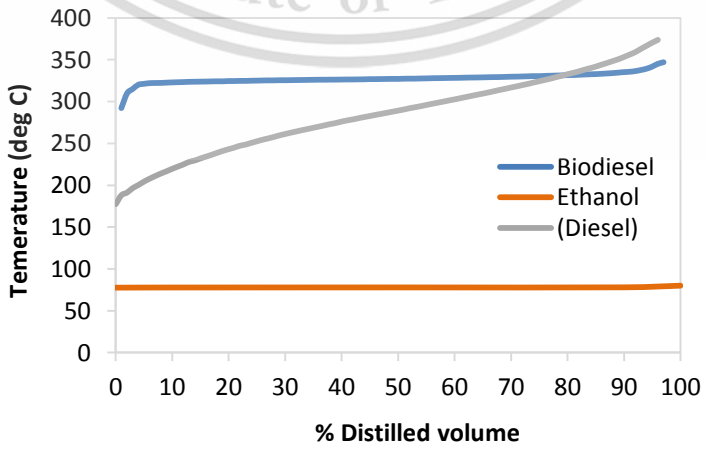

Figure 3.3 Distillation of diesel, biodiesel, and ethanol

This material is reserved for educational use only, not allowed for commercial use.
Forbidden to modify the content, and cite the document when use.

Table 3.3 Fuel properties

Fuel Properties	(Diesel)	Biodiesel	Ethanol	BE10	BE20
Chemical formula	$C_{14.2}H_{28}$	$C_{14.9}H_{29.9}O_{1.9}$	C_2H_6O	-	-
Auto ignition temperature (°C)	288	294	365	-	-
Calorific Value (kJ/kg)	46180	39525	28329	38405	37285
Heat of vaporization (kJ/kg)	250	300	840	354	408
Viscosity @ 40°C (mm^2/s)	3.0	4.5	1.2	-	-
Carbon (% mass)	85.1	74.5	52.2	72.3	70.0
Hydrogen (% mass)	14.0	12.5	13.0	12.5	12.6
Oxygen (% mass)	0.9	13.0	34.8	15.2	17.4
Stoichiometric Air fuel ratio	14.7	12.3	9.0	11.9	11.6
Density @ 25°C (kg/m^3)	844.8	875.3	789.0	866.7	858.0

Figure 3.3 explains about the distillation curve of fuels in this research. Ethanol can be distilled easier at low temperature than biodiesel and diesel because it has much smaller molecule sizes. Diesel which is considered as derived from petroleum has wide range of fuel molecules. Therefore, small-size molecules start to vaporize since less than 180°C whereas bigger molecules eventually vaporize at more than 350°C. For biodiesel, according to production process, it is considered as more homogeneous which can be distilled in narrow range of temperature 300~350°C

3.1.4 Black smoke meter

Particulate matter emitted from engine combustion is measured in black smoke's intensity percentage. The smoke meter is applied to measure particulate matter's concentration between particulate matter in exhaust gas before trapping and after trapping in particulate filter by light emitting method. The 0 percentage black smoke means no particulate matter detected on filter, while 100 percentage means the filter be covered with particulate matter at full scale of intensity. This smoke meter

This material is reserved for educational use only, not allowed for commercial use.
Forbidden to modify the content, and cite the document when use.

percentage can be summarized that the filtration efficiency of particulate filter. The smoke meter for the present research, model : Okuda DSM - 240, is shown in figure3.4 .

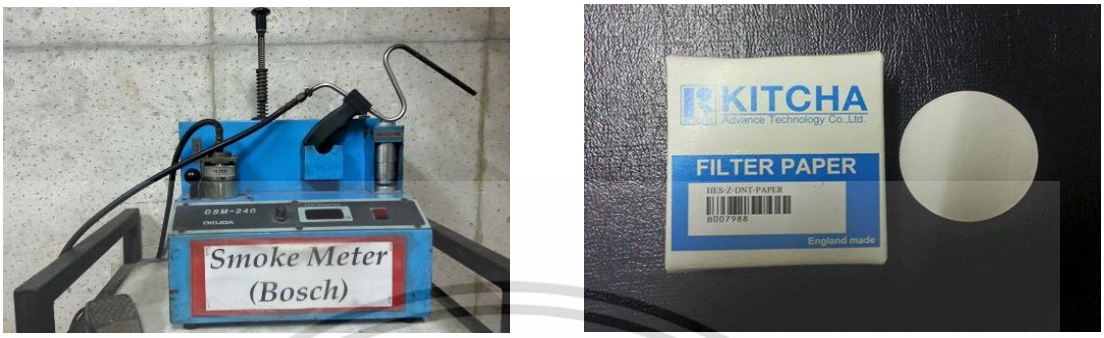

Figure 3.4 Smoke meter

3.1.5 Pressure sensor

Pressure sensor is used to measure pressure variation in the combustion chamber which is the most important parameter to be analyzed in combustion characteristics. The sensor type “Kistler 6052C31-piezoelectric crystal” represented as Fig. 3.5 is mounted on the cylinder head of the engine B.

Figure 3.5 Pressure sensor connect inside cylinder

This material is reserved for educational use only, not allowed for commercial use.
Forbidden to modify the content, and cite the document when use.

3.1.6. Crank angle encoder

Crank angle encoder is used to measure real-time crankshaft position for matching with the pressure parameter as well as to calculate combustion chamber volume. The encoder type “CA-RIE-360” represented as Fig. 3.6 was applied and mounted on the end of dynamometer for serviceability. Resolution of the encoder is 1 degree. The function is based on transmission light principle. An infrared beam is emitted and received at the sensor unit. The customized marker disk (with slits) is mounted in-between the sensors gate. The slits will interrupt the infrared beam; the receiver transforms the light to voltage signal.

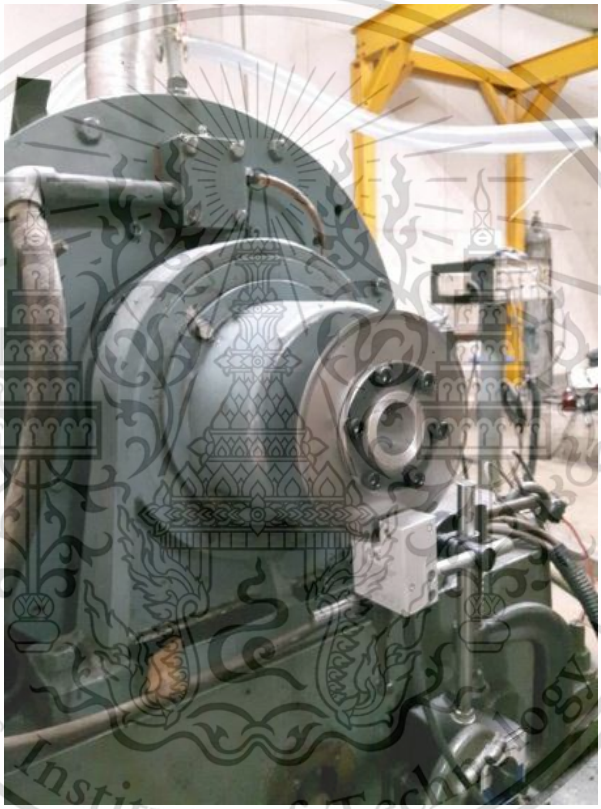

Figure 3.6 Crank angle encoder at end of engine dynamometer

3.1.7. Data acquisition system

Data acquisition system as shown in orange-highlight portion of Fig. 3.7 is used to integrate signals from both pressure sensor and crank angle encoder. Then it processes data based on crank angle domain so that user can obtain results of Pressure-Volume, Pressure-Crank angle, Rate of heat release-Crank angle, Pressure derivative-Crank angle, Cumulative heat release-Crank angle, and etc. Figure 3.8 – Figure 3.10 shows details of the data acquisition unit “DEWESoft SIRIUSi-HS-CA” for this research.

This material is reserved for educational use only, not allowed for commercial use.
Forbidden to modify the content, and cite the document when use.

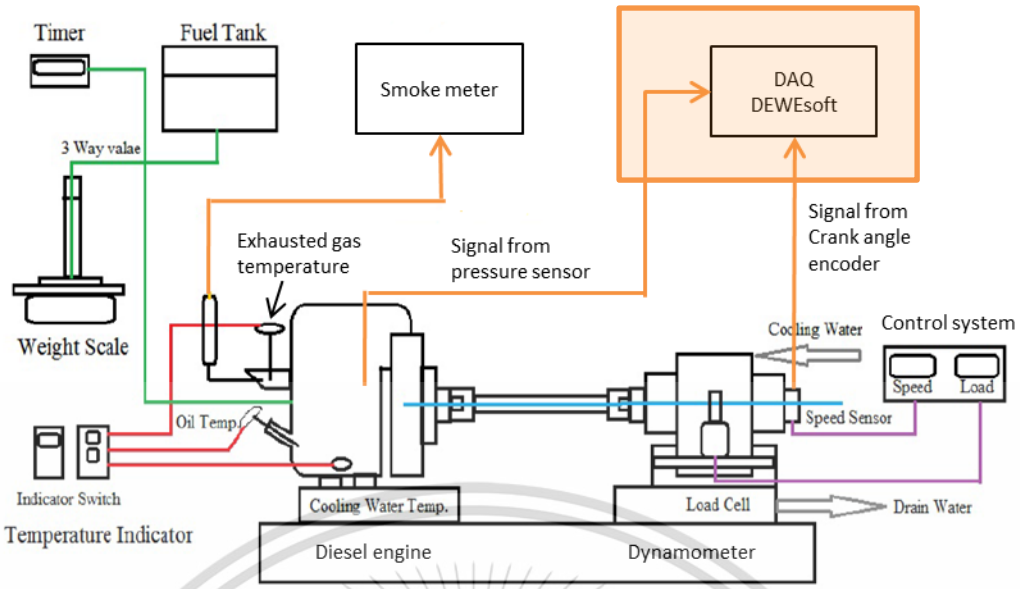

Figure 3.7 Schematic diagram of data acquisition unit connected to Pressure and Crank angle encoder

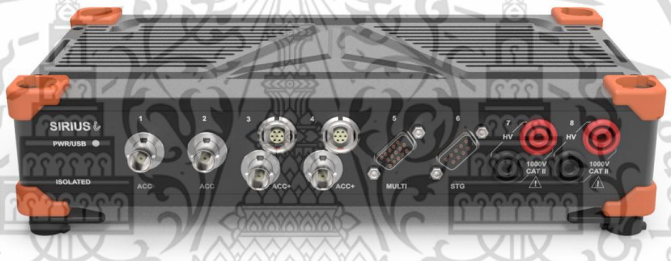

Figure 3.8 Data Acquisition Unit (DAQ) DEWEsoft SIRIUSi-HS-CA

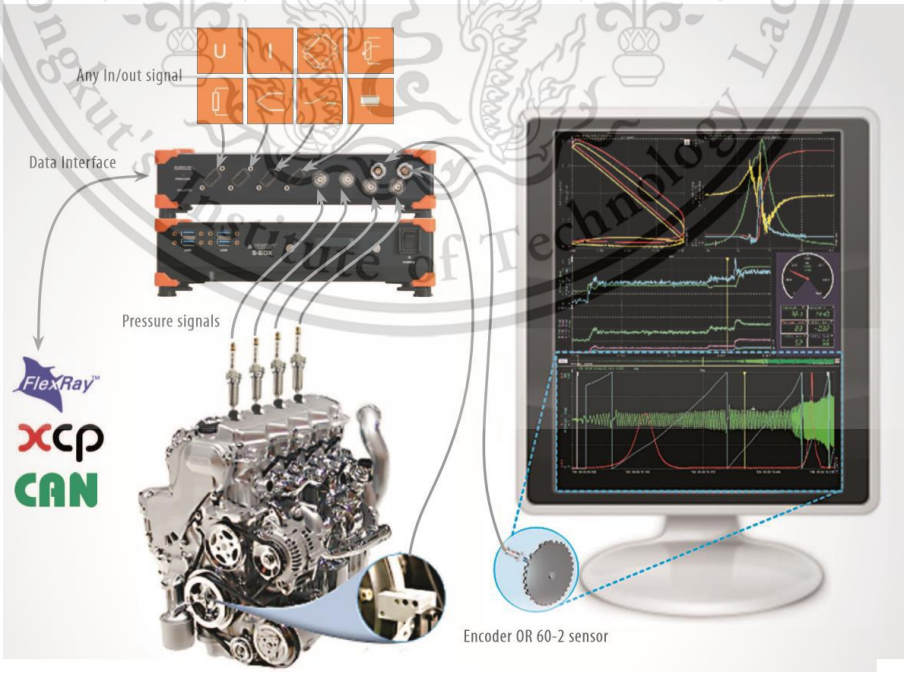

Figure 3.9 Data Acquisition Unit (DAQ) DEWEsoft

This material is reserved for educational use only, not allowed for commercial use.
Forbidden to modify the content, and cite the document when use.

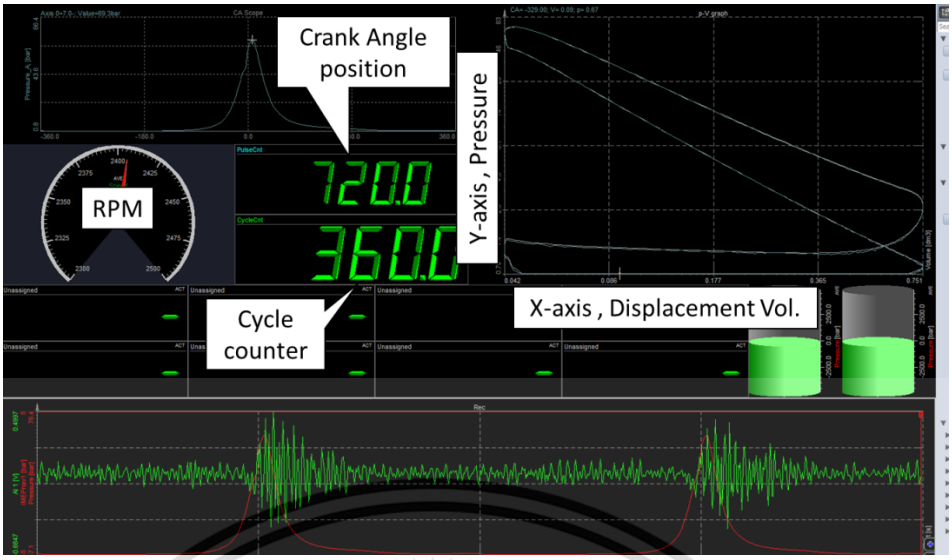

Figure 3.10 Data acquisition interface

3.2 Experimental procedure

This research, biodiesel (B100) and ethanol-blended biodiesel (BE10 and BE20) were supplied in the diesel engine's combustion chamber to produce particulate matter. Combustion characteristics, PM quantity emission, PM morphology, and PM oxidation kinetics will be analyzed through the research.

3.2.1 Combustion characteristics

First, engine performance for each type of fuel was investigated to see overall scope of the experiment. The test was performed at Wide Opened Throttle (WOT) condition varying from 1400 RPM to 2400 RPM. Then, fuel consumption as well as exhaust gas temperature were measured to investigate fuel effect on engine's Brake Thermal Efficiency (BTE). The test was done at constant engine speed of 2000 RPM by varying from no load to 80% load. To be comparable with other research work, load conditions for the combustion analysis were converted to Brake Mean Effective Pressure (BMEP). Then, in-cylinder combustion parameter such as 'Pressure VS Crank angle' and 'Rate of heat release VS Crank angle' were investigated to see combustion characteristics. The test was performed at constant engine speed of 2400 RPM by varying load at 0.2MPa, 0.4MPa, and 0.6MPa of BMEP.

This material is reserved for educational use only, not allowed for commercial use.
Forbidden to modify the content, and cite the document when use.

3.2.2 Particulate matter quantity emission

The particulate matter quantities were investigated by percentage intensity of smoke on filter paper as shown in Fig. 3.11. The particulate matter was trapped by the smoke meter device and filtered while it suspended in exhaust gas in condition. White filter paper was used to trap particulate matter in exhaust gas to be measured by light emitting method. Results of the present research i.e. PM intensity from B100, BE10, and BE20 were compared with the results from previous research (B100 and diesel) in order to see effect of ethanol on PM emission reduction.

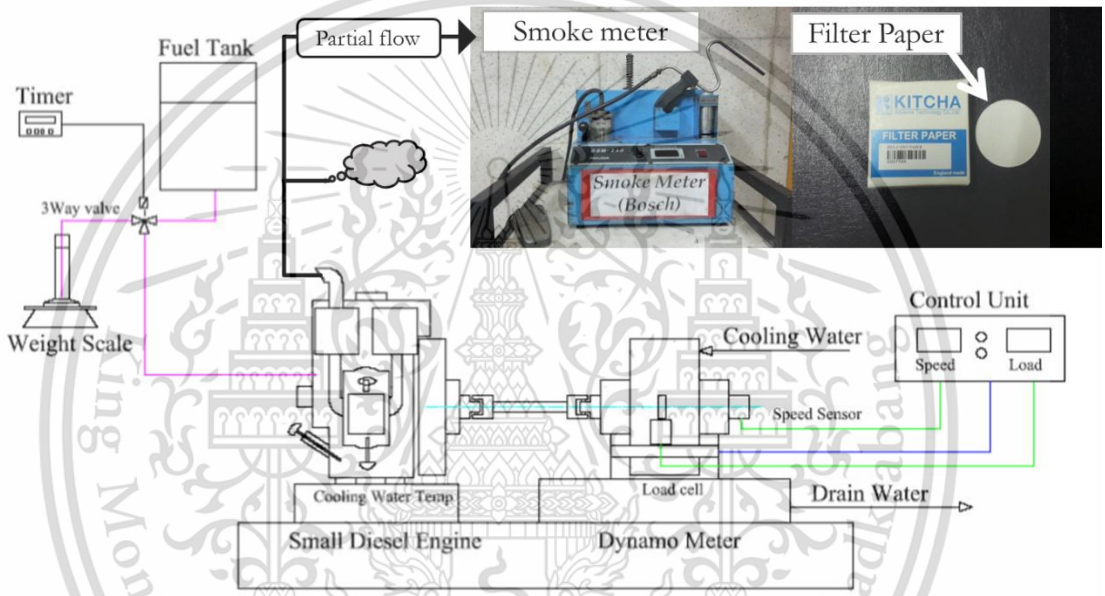

Figure 3.11 Schematic diagram of PM intensity measurement by smoke meter

This material is reserved for educational use only, not allowed for commercial use.
Forbidden to modify the content, and cite the document when use.

3.2.3 Particulate matter morphology and nanostructure

PM emitted from each type of fuel was investigated in viewpoint of morphology. There are two methods for PM collection in this research. First method is PM collection on filter paper which is similar to PM intensity measurement in the section 3.3.2. PM dispersed on filter paper was investigated by Scanning Electron Microscope (SEM) as shown in Fig. 3.12 to see morphology of agglomerated particles. Second method collected PM as powder (trapping equipment is shown as Fig. 3.13). This method, PM was investigated into more detail of morphology by Transmission Electron Microscope (TEM) as shown in Fig. 3.14. Therefore, details of PM nanostructure e.g. primary particle's morphology and of graphite crystallite can be obtained. The engine operating condition for PM collection was controlled at 80% load.

Figure 3.12 Scanning Electron Microscope for agglomerated particle investigation

This material is reserved for educational use only, not allowed for commercial use.
Forbidden to modify the content, and cite the document when use.

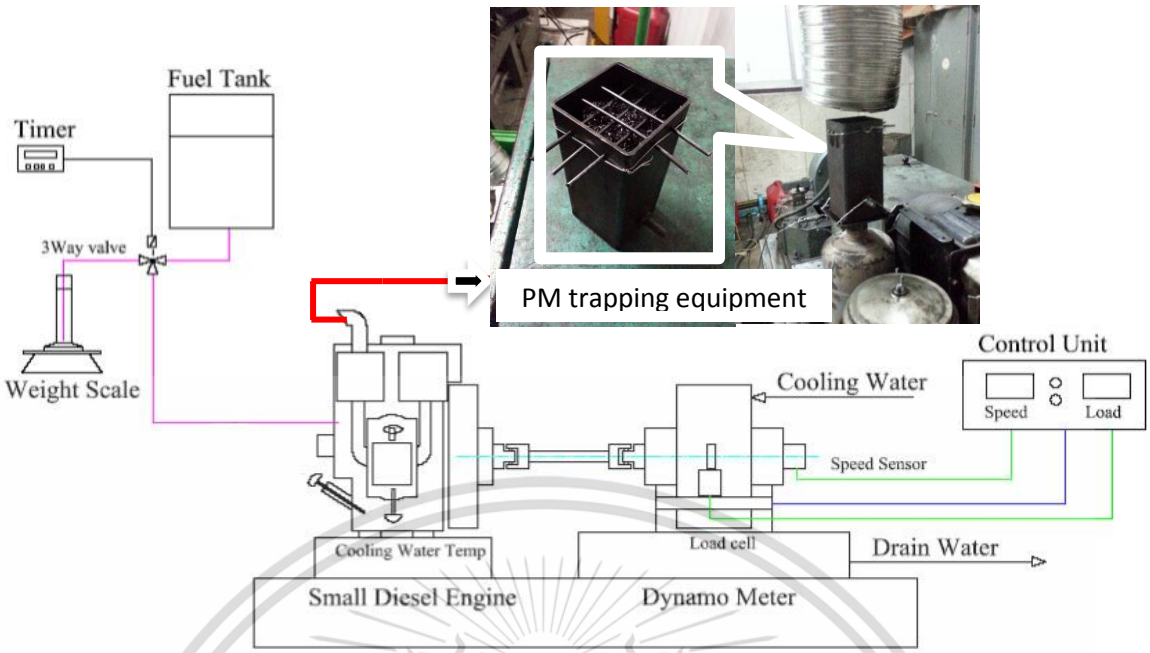

Figure 3.13 Schematic diagram of PM collection for investigation via Transmission Electron Microscope

Figure 3.14 Transmission Electron Microscope for PM nanostructure investigation

This material is reserved for educational use only, not allowed for commercial use.
Forbidden to modify the content, and cite the document when use.

3.2.4 Particulate matter oxidation kinetics

The particulate matter powder from each fuel's combustion in section 3.3.3 was brought to analyze by Thermo Gravimetric Analysis (TGA) with isothermal method. The TGA equipment and PM sample for this research is shown in Fig. 3.15. Mass reduction rate together with temperature results from TGA were investigated into oxidation kinetics and chemical consistent. Isothermal TGA applied in this research has temperature range from 425 ℃ to 625 ℃ depending on sources of PM. Before reaching isothermal stage, temperature of all types of PM sample were controlled with the increment rate of 100 ℃ per minute from room temperature (30 ℃). While the **ramping up from 30 ℃ to isothermal stage, nitrogen gas was released** to prevent the oxidation of particulate matter and after that **air was released to oxidize** with particulate matter. For the chemical consistent, the moisture, unburned hydrocarbon and carbon fraction inside the particulate matter from each type of fuel was determined from the oxidation temperature. Moisture and hydrocarbon are oxidized in first phase at low temperature. Carbon or soot is expected to be oxidized in the isothermal phase.

Figure 3.15 TGA Analyzer and PM sample for oxidation kinetics investigation

This material is reserved for educational use only, not allowed for commercial use.
Forbidden to modify the content, and cite the document when use.

CHAPTER 4

RESULTS AND DISCUSSIONS

4.1 Engine performance

The engine B's performance curve of biodiesel (B100), ethanol blended biodiesel (BE10 and BE20), and diesel (put in parenthesizes as reference from co-researcher) is plotted in Fig. 4.1. Engine load drops as increasing engine speed for all fuels. The ethanol blended fuel (BE10 and BE20) produces lower load due to lower calorific value as well as lower stoichiometric air-fuel ratio i.e. leaner combustion compared with biodiesel and diesel. The engine load shows significant drop at higher speed and more ethanol blended ratio.

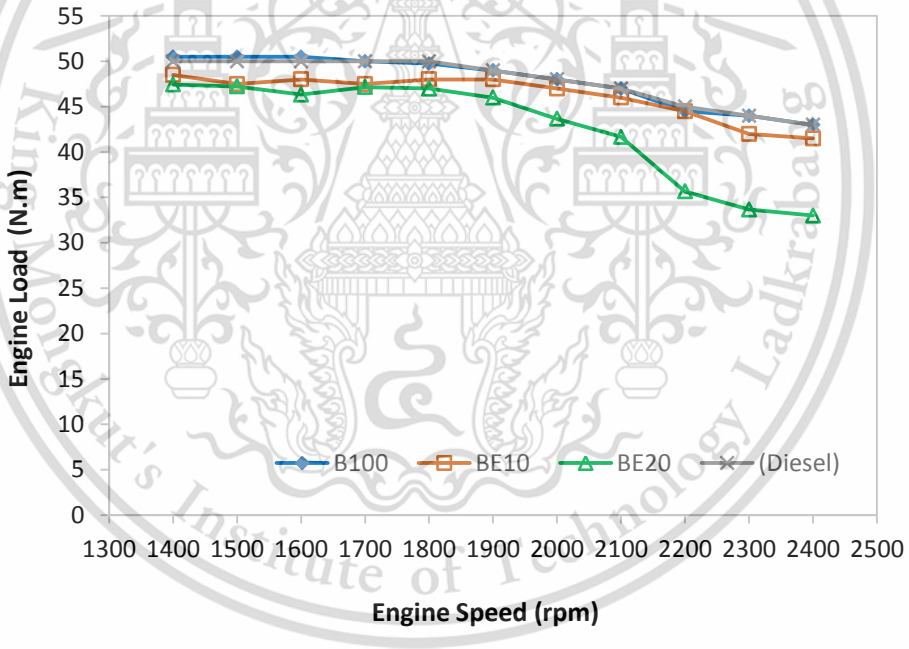

Figure 4.1 Engine performance curve

This material is reserved for educational use only, not allowed for commercial use.
Forbidden to modify the content, and cite the document when use.

4.2 Brake specific fuel consumption (BSFC), Brake thermal efficiency (BTE), and Exhausted gas temperature (EGT)

Brake specific fuel consumption (BSFC), Exhausted gas temperature (EGT), and Brake thermal efficiency (BTE) with respect to engine load are shown in Fig. 4.2, Fig. 4.3, and Fig. 4.4 respectively. BSFC of the ethanol blended fuels, are higher than that of biodiesel at all load conditions due mainly to the lower calorific value of ethanol. (This phenomenon agrees with diesel fuel as well). Thus, the amount of fuel supply into the engine must be greater. The trend shows decrease in the BSFC as the engine load increase. It can be explained as; when the engine load increases, combustion temperature which is implied from the rise of EGT increases as well. Reactivity of fuel and oxygen activates conversion of combustion heat to mechanical work much more than amount of energy from the fuel input. That is why the BSFC decreases as the engine load increases.

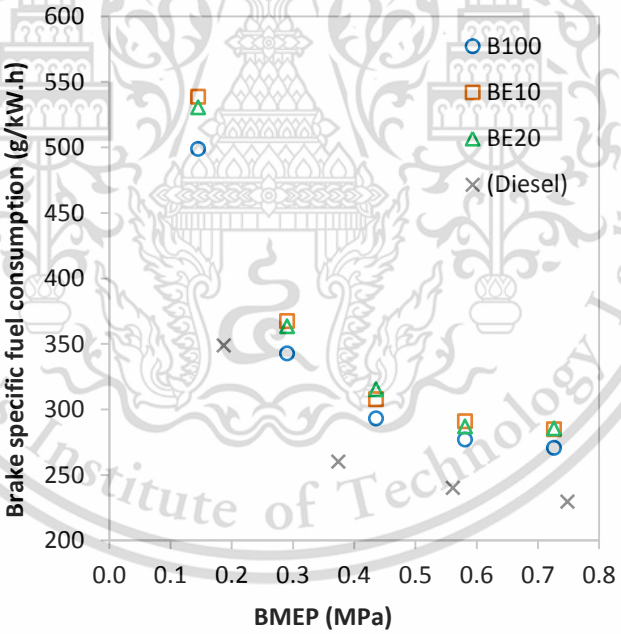

Figure 4.2 Brake specific fuel consumption curve

This material is reserved for educational use only, not allowed for commercial use.
Forbidden to modify the content, and cite the document when use.

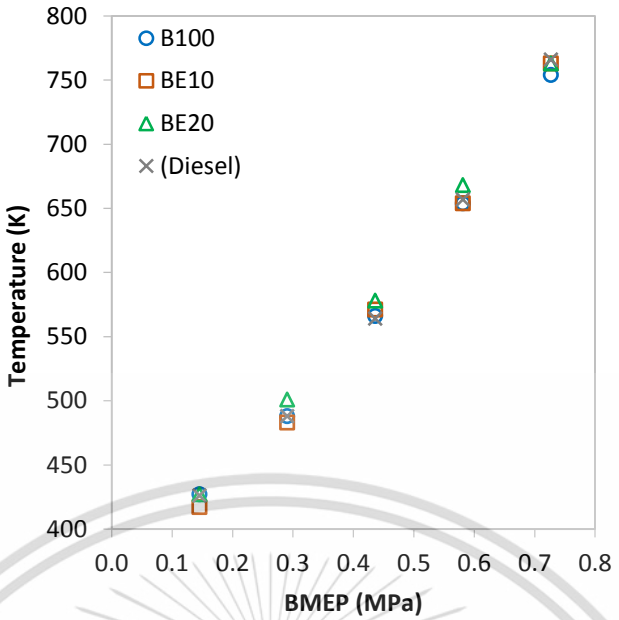

Figure 4.3 Exhausted gas temperature

BTE plots show that as the engine load increases, the engine produces more thermal efficiency for all fuels. BTEs are not significantly different among fuels because fuels with higher BSFC such as BE20 or BE10 compensates their lower calorific values, compared with B100 or diesel.

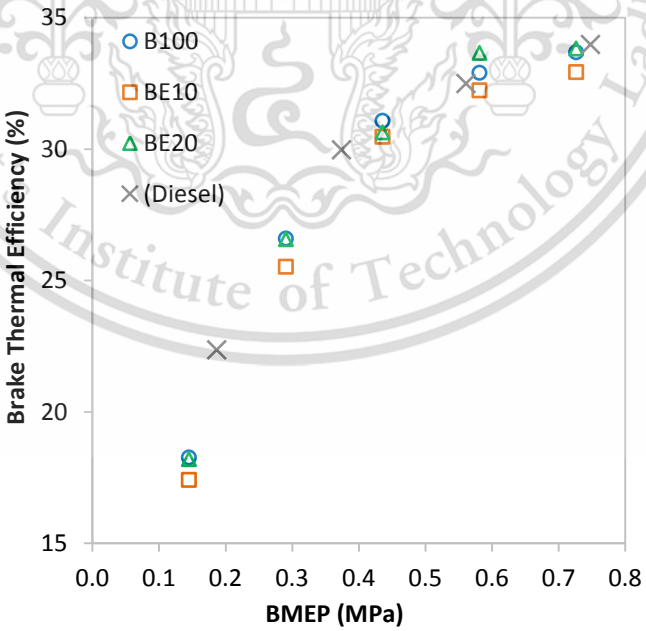

Figure 4.4 Brake thermal efficiency

This material is reserved for educational use only, not allowed for commercial use.
Forbidden to modify the content, and cite the document when use.

4.3 Combustion characteristics

For the engine B's combustion characteristics, in-cylinder pressure variation with respect to crank angle is shown in Fig. 4.5 and heat release rate in Fig. 4.6 for B100, BE10, BE20, and diesel. The engine load was varied in the range of 0.2 MPa, 0.4 MPa, and 0.6 MPa at constant engine speed of 2400 rpm. Peak pressures of all fuels increase with the increasing engine load. Considering at the ethanol blended fuels, at low load of 0.2MPa, the peak pressure occurs after the biodiesel and diesel's peak for 10 to 15 crank angle degrees. At the low load condition, low combustion temperature causes ethanol blended fuel which has higher heat of vaporization as well as high auto ignition temperature start combustion later. At higher engine load, the increment of combustion temperature cause better fuel vaporization. Therefore, the pressure graph of BE10 and BE20 becomes closer to B100 and Diesel.

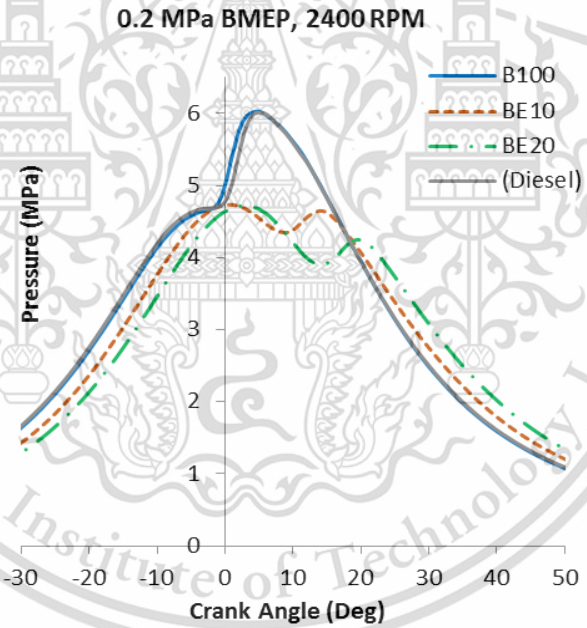

Figure 4.5a In-cylinder pressure versus crank angle at 0.2MPa BMEP and engine speed of 2400 rpm

This material is reserved for educational use only, not allowed for commercial use.
Forbidden to modify the content, and cite the document when use.

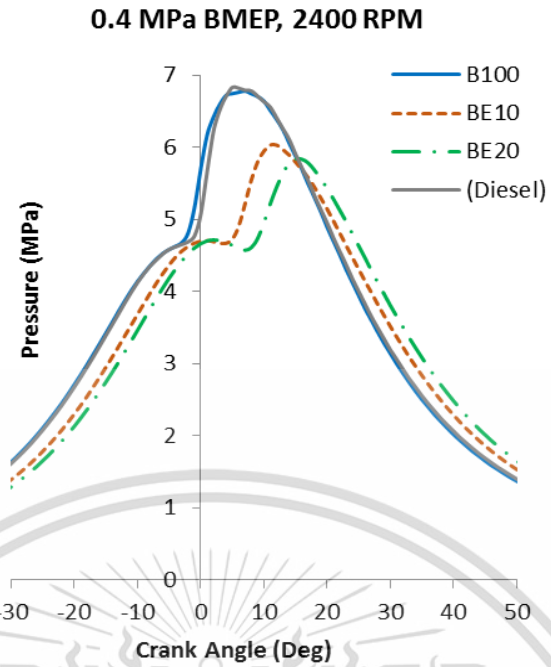

Figure 4.5b In-cylinder pressure versus crank angle at 0.4MPa BMEP and engine speed of 2400 rpm

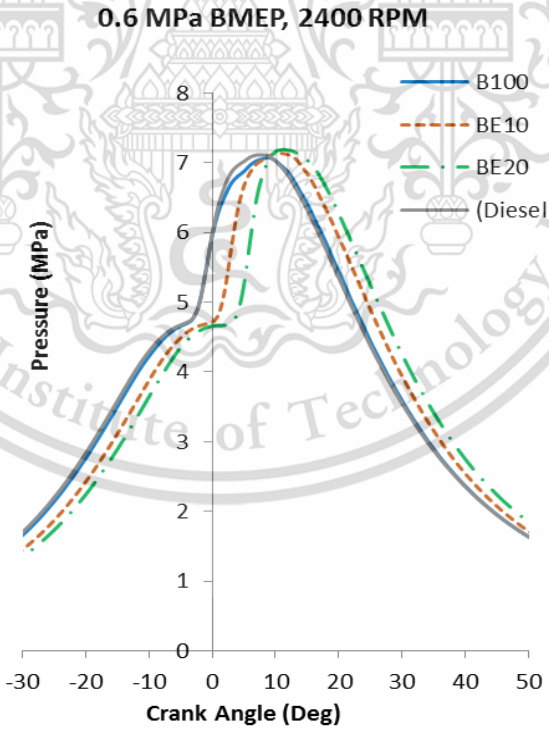

Figure 4.5c In-cylinder pressure versus crank angle at 0.6MPa BMEP and engine speed of 2400 rpm

This material is reserved for educational use only, not allowed for commercial use.
Forbidden to modify the content, and cite the document when use.

Heat release rate plots in Fig. 4.6 show that combustion processes of all fuels start with premixed combustion phase followed by diffusion combustion phase. At low engine load (Fig. 4.6a), the fuel with more ethanol content which is BE20 tends to start combustion after B100 and Diesel, while a higher peak of the heat release can be observed on higher load (Fig. 4.6c). The reason can be explained as; at low temperature in the low load condition, higher heat of vaporization and higher auto ignition temperature of ethanol need more time for fuel atomization. (Nevertheless, lower viscosity should promote easier atomization) After enough fuel atomization and mixing with oxygen, Ethanol fuel tends to promote rapid combustion with producing high peaks of heat release rate. At the higher engine load especially at 0.6 MPa BMEP, higher combustion temperature makes better fuel vaporization and fuel atomization as well. Therefore, the ethanol blended fuels become stronger premixed combustion and lead to higher peak of heat release rate.

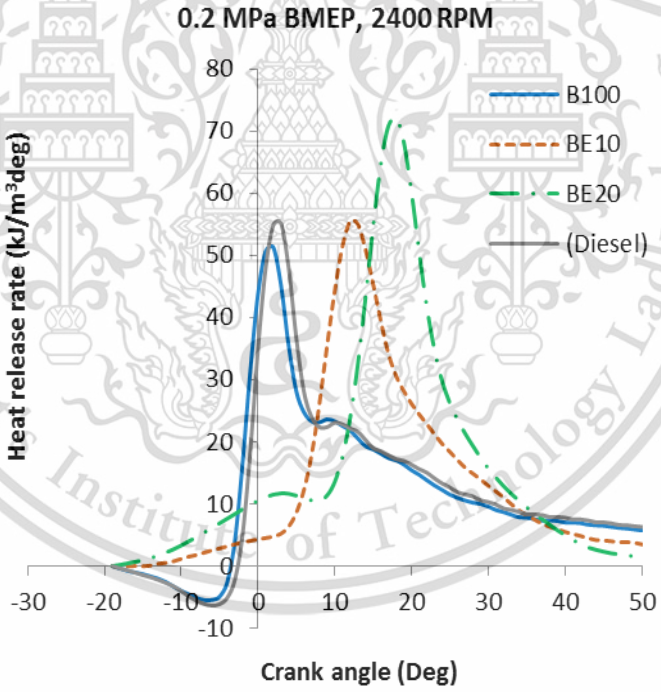

Figure 4.6a Heat release rate versus crank angle at 0.2MPa BMEP and engine speed of 2400 rpm

This material is reserved for educational use only, not allowed for commercial use.
Forbidden to modify the content, and cite the document when use.

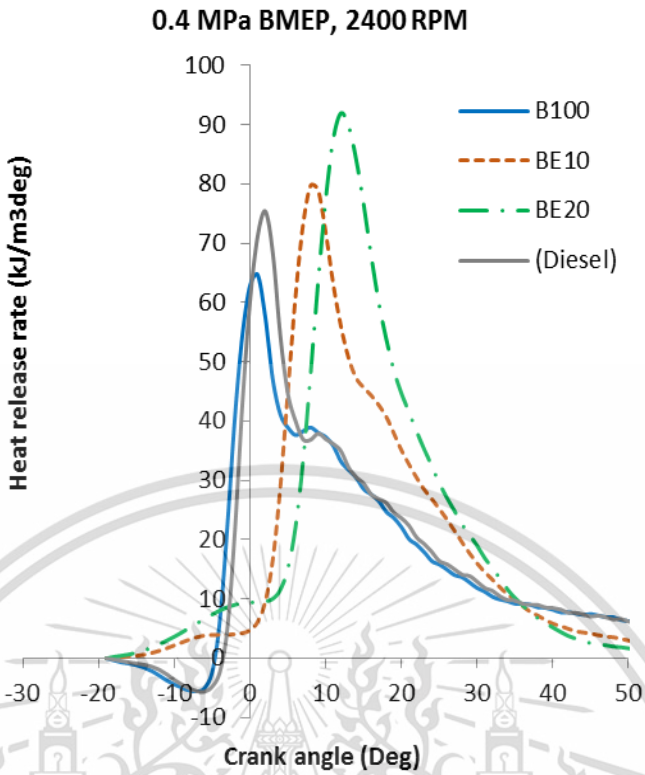

Figure 4.6b Heat release rate versus crank angle at 0.4MPa BMEP and engine speed of 2400 rpm

This material is reserved for educational use only, not allowed for commercial use.
Forbidden to modify the content, and cite the document when use.

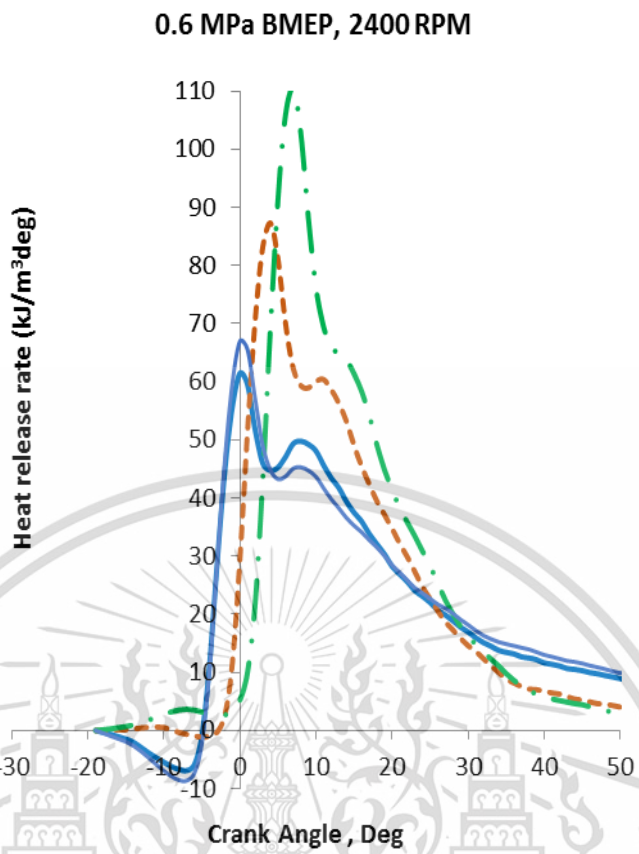

Figure 4.6c Heat release rate versus crank angle at 0.6MPa BMEP and engine speed of 2400 rpm

This material is reserved for educational use only, not allowed for commercial use.
Forbidden to modify the content, and cite the document when use.

4.4 Particulate matter's quantity emission

Figure 4.7a shows a result of the **previous research** in smoke intensity comparison between biodiesel and diesel combustion. The study was found that the intensity be strongly dependent on the engine load. The more engine load, the greater smoke intensity due to more fuel supply for combustion. Biodiesel emits approximately 50% smoke intensity less than diesel combustion in overall operating conditions. The reason was referred as oxygen fraction in biodiesel's fuel molecules which promotes complete combustion. Surely, the smoke intensity measurement can express trends of smoke quantity, however it is difficult to interpret accurate PM's quantity since it is possible that PM covered by colorless volatile or hydrocarbon might not reflect actual measurement result.

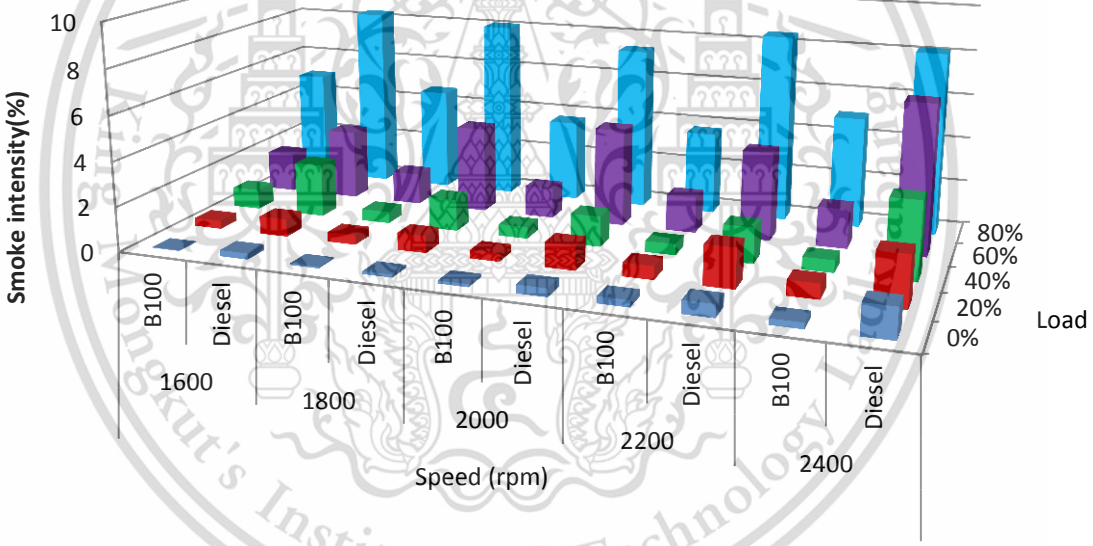

Figure 4.7a Smoke intensity comparison between diesel and biodiesel combustion (**Previous research**)

In the **present research**, comparison of smoke intensity between ethanol blended fuels and biodiesel is shown as Fig. 4.7b aimed to see effects of ethanol on smoke intensity emission. Ethanol blended fuels (BE10 and BE20) produce less smoke at almost all engine operating conditions compared with biodiesel. **Average smoke reduction for BE10 and BE20 is 27.2% and 58.6%** respectively. It can be explained into 2 main aspects. First reason which is similar to the research in Fig. 4.7a

This material is reserved for educational use only, not allowed for commercial use.
Forbidden to modify the content, and cite the document when use.

is that **more oxygen fraction in ethanol plays a key role in promoting complete combustion**. Second, **lower viscosity and higher auto ignition temperature** characteristics of the BE10 and BE20 **provide enough time for better fuel atomization** as well as high p**eak of heat release contributes better fuel-oxygen's reactivity** i.e. more complete combustion.

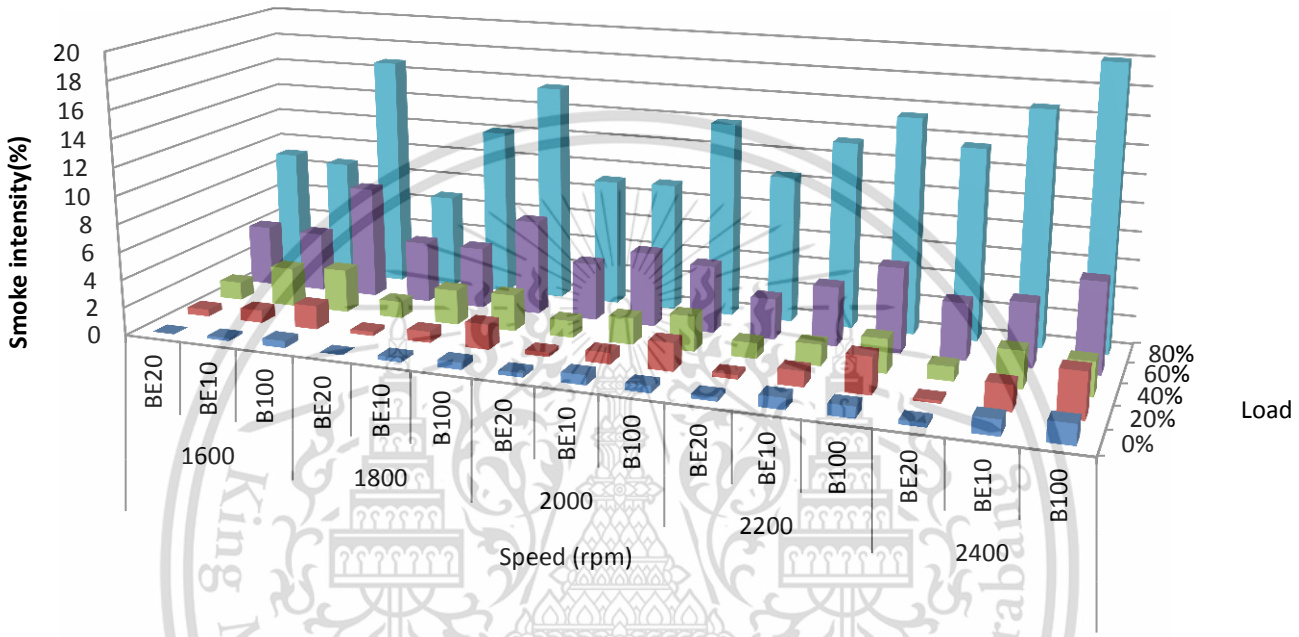

Figure 4.7b Smoke intensity comparison among B100, BE10, and BE20 (**Present research**)

This material is reserved for educational use only, not allowed for commercial use.
Forbidden to modify the content, and cite the document when use.

4.5 Particulate matter's morphology and nanostructure

The particulate matter from **B100 and BE20**'s combustion was investigated for PM morphology and nanostructure **in the present** research. Results were also to be **compared with former research (diesel-biodiesel)**. PM morphology and nanostructure can be analyzed via images derived from modern electron microscopes i.e. Scanning Electron Microscope (SEM) and Transmission Electron Microscope (TEM) techniques.

For SEM images, PMs with a level of **agglomerated particles** can be investigated. Figure 4.8a and Figure 4.8b show samples of SEM images of PM derived from BE20 and B100 respectively. They are composed of groups of agglomerated particles gathered on paper filter. Sizes of these agglomerated particle groups vary from hundreds nanometers to few microns. Fine particles or PM2.5 as shown as red mark on Fig 4.8a can be observed. Bigger groups or PM10 is also shown in the red mark of Fig.4.8b. However, relationships between particle's size, appearance, and combustion of each type of fuel cannot be found in the agglomerated level.

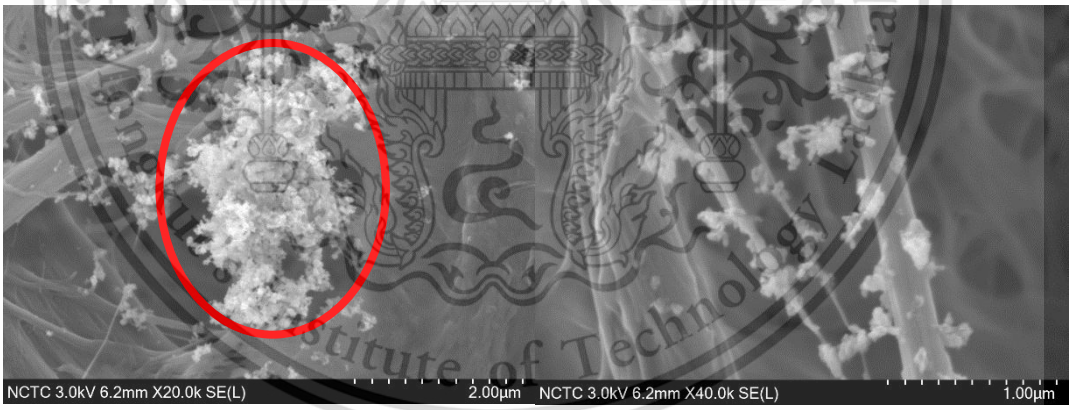

Figure 4.8a SEM images of BE20's particulate matter as agglomerated level

This material is reserved for educational use only, not allowed for commercial use.
Forbidden to modify the content, and cite the document when use.

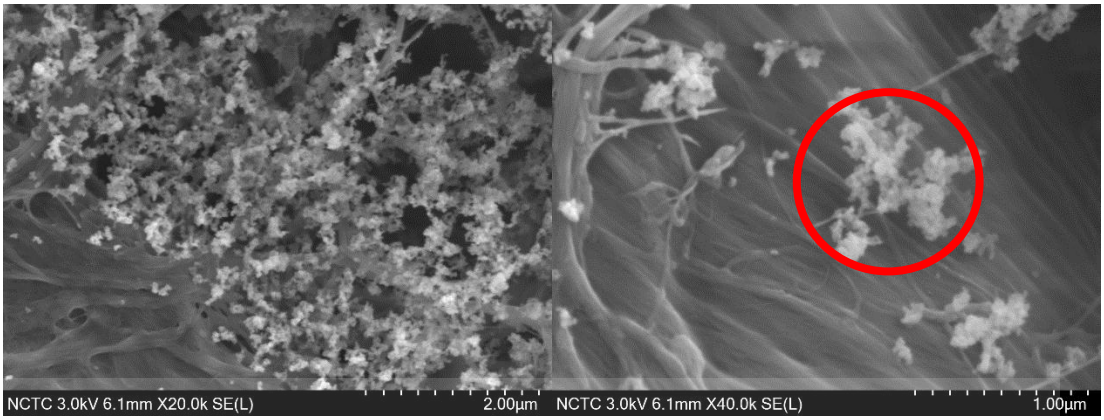

Figure 4.8b SEM images of B100's particulate matter as agglomerated level

To see more detail of the PM, investigation of PM morphology up to Nano scale is necessary. TEM images were applied to show details of agglomerated particles, **single particles or primary particles**, up to level of Carbon fringe structure. Figure 4.9a and Figure 4.9b show TEM images of agglomerated particles from BE20 and B100 respectively. Both of them look similar in appearance. However, detailed morphology and nanostructure were to be analyzed by image processing with software called "**Image J**" to measure quantitative data of particles such as particle's size, particle's surface, or graphitic structure

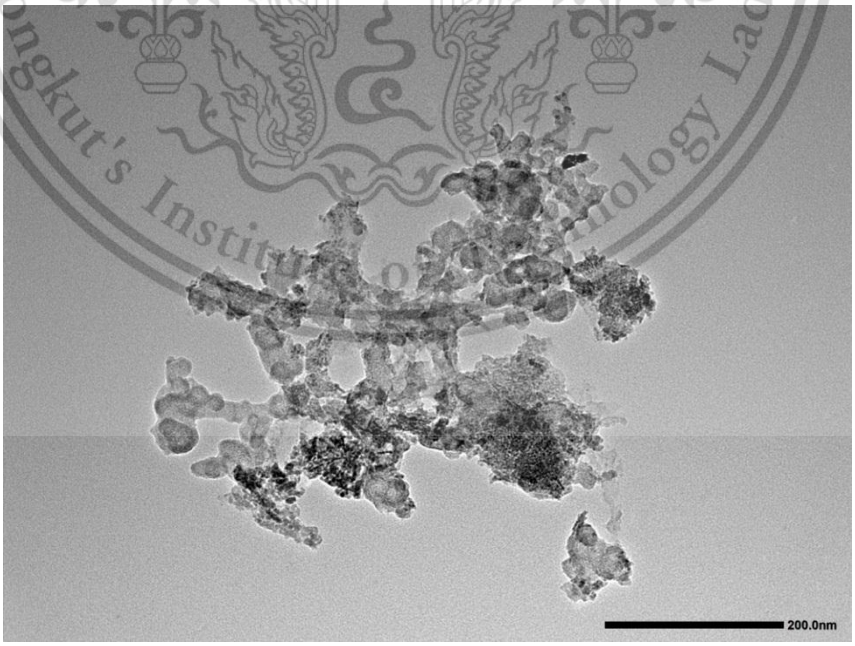

Figure 4.9a TEM image of BE20's agglomerated particle

This material is reserved for educational use only, not allowed for commercial use.
Forbidden to modify the content, and cite the document when use.

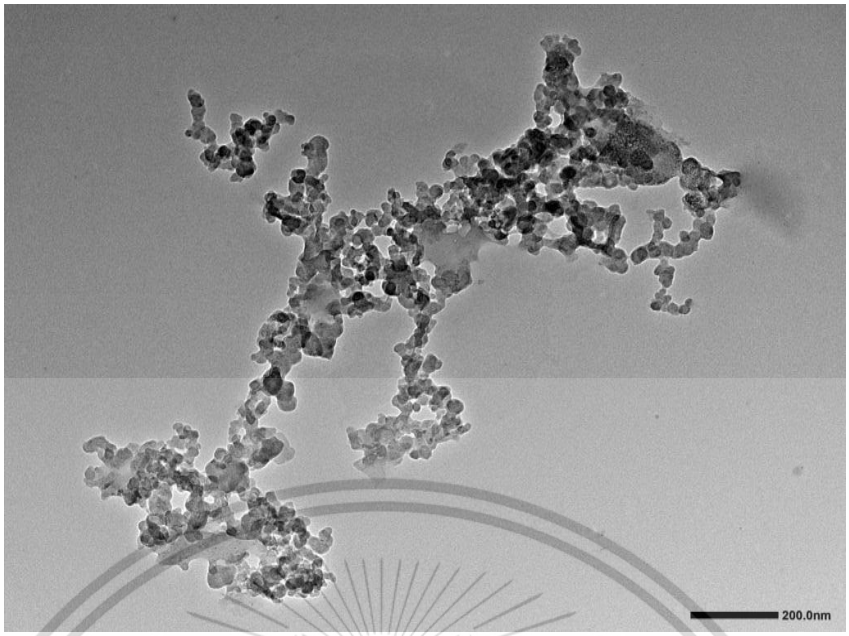

Figure 4.9b TEM image of B100's agglomerated particle

4.5.1 Primary particle's morphology

Figure 4.10a – figure 4.10c show measurement of PM's primary particle size from BE20, B100, and diesel respectively. (**Diesel's particle was also measured as reference results for BE20's and B100's particle analysis**) The measurement applies particle's perimeter approach to determine particle's section area and then to calculate equivalent diameter. Sampling rate is approximately 50-60 per PM types. Figure 4.11a – Figure 4.11d shows measurement result of primary particle's size distribution of fuel BE20, B100, and diesel respectively. B100's particles show size distribution in narrow range compared with BE20's and diesel's particles (Standard deviation of B100's, BE20's, and diesel's particle size is 7.4, 8.6, 8.8 nm, respectively). It means B100's particles are most uniform in size which might relate to uniform fuel molecules (implied from fuel distillation curve Fig. 3.3). For the particle size, average primary particle of **B100** also is smallest **of 27.0 nm**, followed by **BE20 of 29.1 nm** and **Diesel of 29.8nm**.

This material is reserved for educational use only, not allowed for commercial use.
Forbidden to modify the content, and cite the document when use.

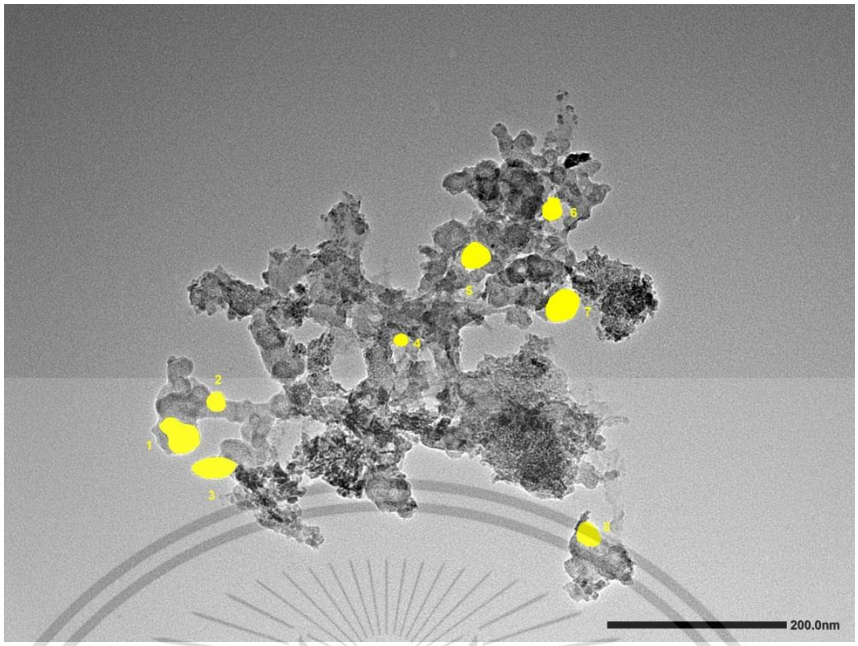

Figure 4.10a Sample of BE20's primary particle's measurement

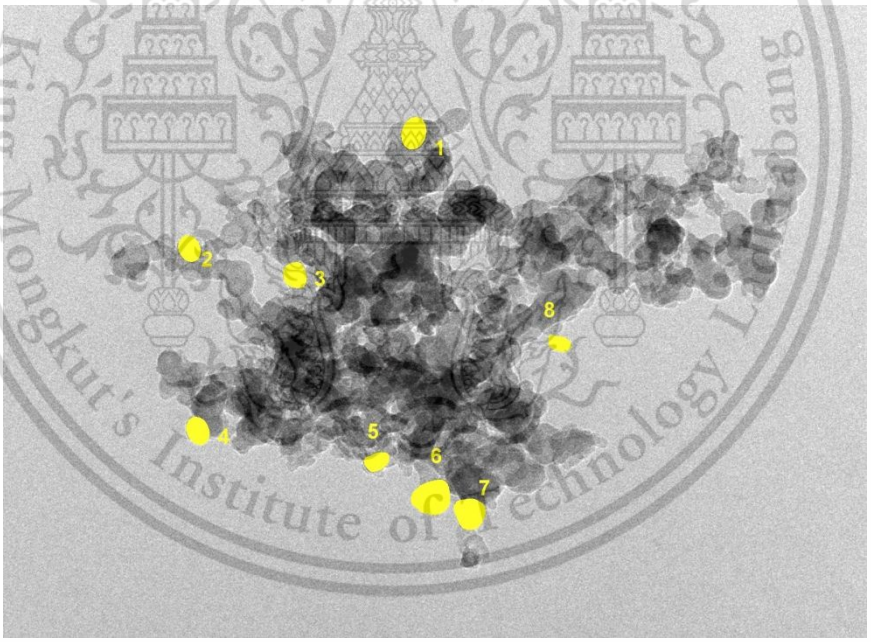

Figure 4.10b Sample of B100's primary particle measurement

This material is reserved for educational use only, not allowed for commercial use.
Forbidden to modify the content, and cite the document when use.

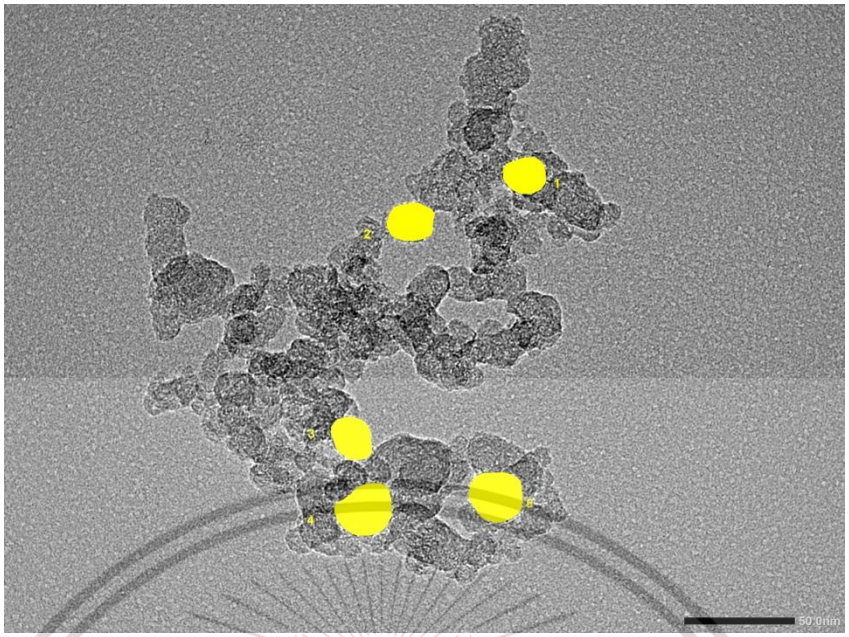

Figure 4.10c Sample of diesel's primary particle's measurement

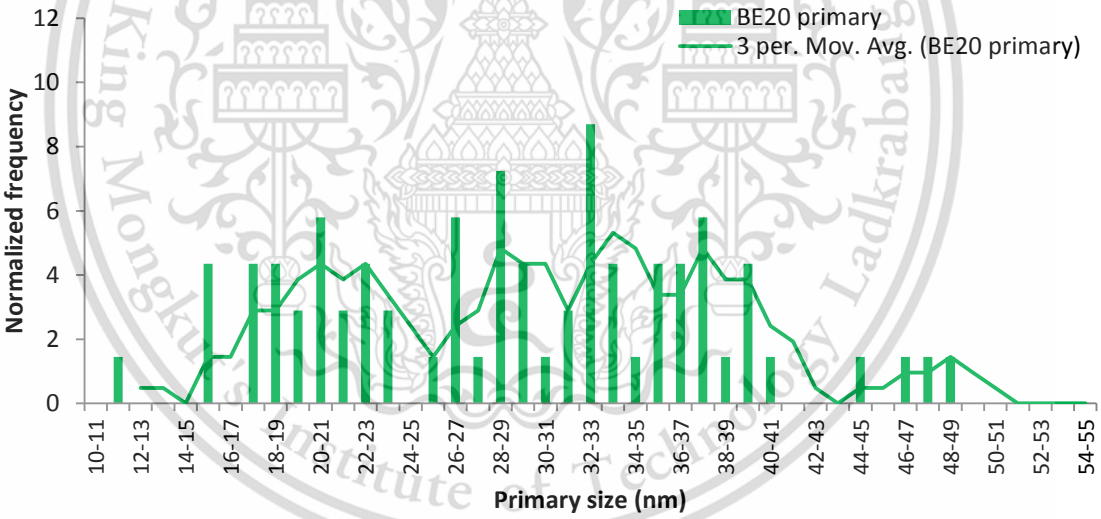

Figure 4.11a BE20's primary particle's size distribution

This material is reserved for educational use only, not allowed for commercial use.
Forbidden to modify the content, and cite the document when use.

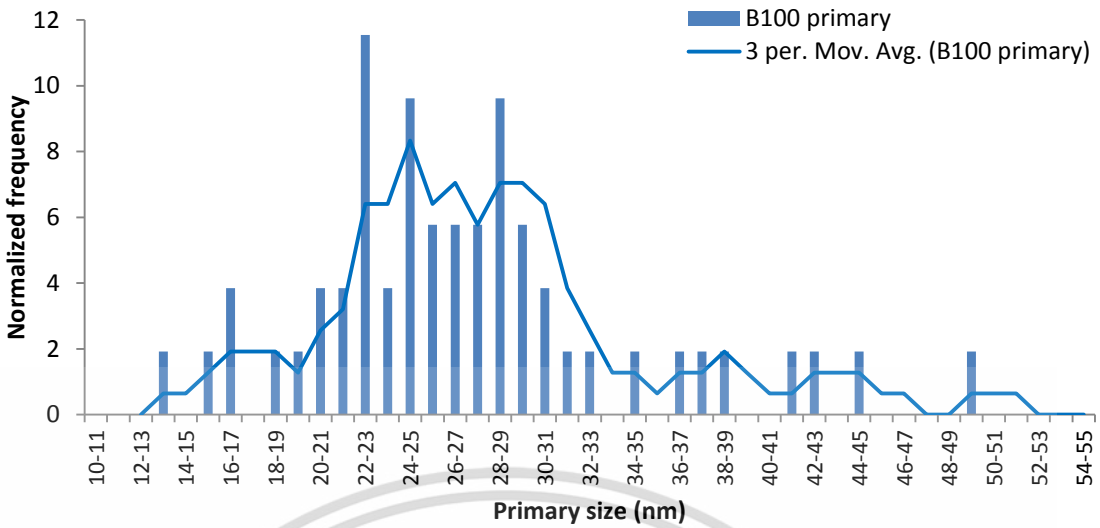

Figure 4.11b B100's primary particle's size distribution

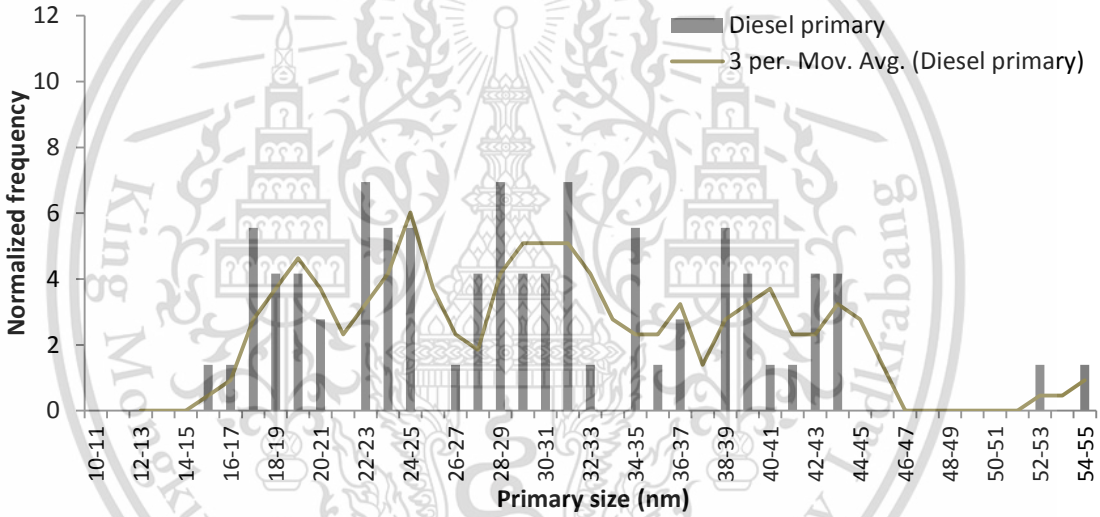

Figure 4.11c Diesel's primary particle's size distribution

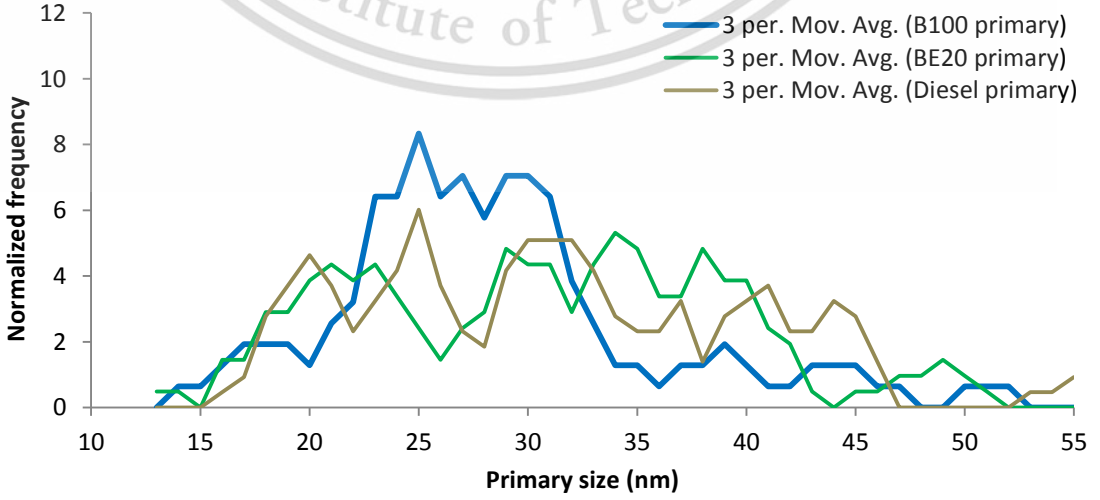

Figure 4.11d Combined fuel's primary particle's size distribution (Moving average)

This material is reserved for educational use only, not allowed for commercial use.
Forbidden to modify the content, and cite the document when use.

Other than the aspect of particle size, further PM characteristics that effect on oxidation reactivity should be investigated. Figure 4.12 propose a conceptual diagram about particle's surface area with different geometry. It is not surprising when **particles become less spherical shapes** tend to have more surface area. As particle shape changes from sphere to octagon to cube, **ratio of perimeter per particle size increases** from 3.14 to 3.57 as well as **ratio of surface area per particle size increases** from 3.14ϕ to 3.90ϕ. This concept then was brought into the investigation of the B100, BE20, and diesel's primary particles. Figure 4.13 represents plots between equivalent diameters of the particles and their perimeters. It is obvious that all particles are not completely spherical because coefficients of the plot or slopes are more than 3.14 or π for all cases. However, the effects of geometry difference cannot be seen obviously. So the different shapes among BE20. B100, diesel's primary particles are not supposed to affect difference in surface area by this investigation.

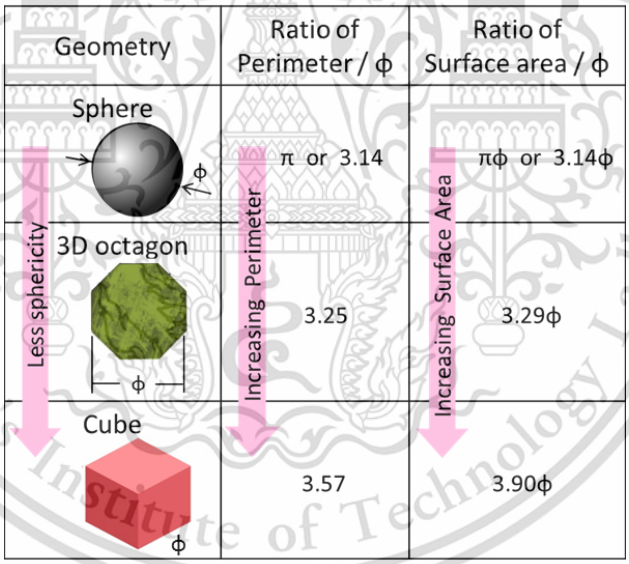

Figure 4.12 Relationship between particle size, perimeter, and surface area for different geometry

This material is reserved for educational use only, not allowed for commercial use.
Forbidden to modify the content, and cite the document when use.

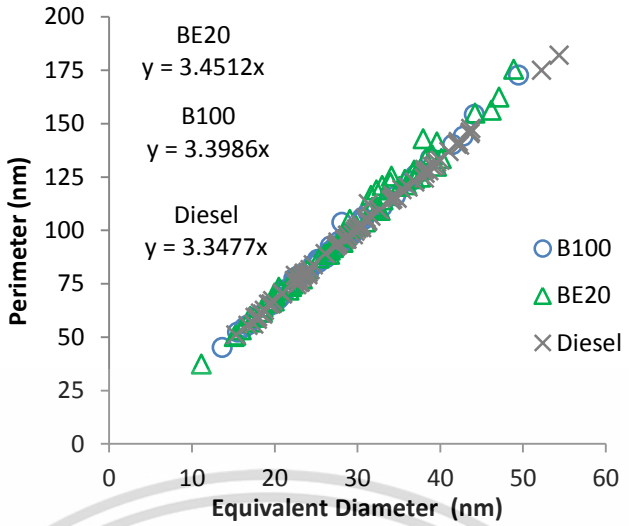

Figure 4.13 Relationship between particle's diameter and perimeter of BE20, B100, and diesel's primary particle

4.5.2 Nanostructure

More insight on particulate matter is necessary to consider in depth to nanostructure level. Figure 4.14 show high magnification TEM images of BE20, B100, and diesel's primary particles or soot particles respectively.

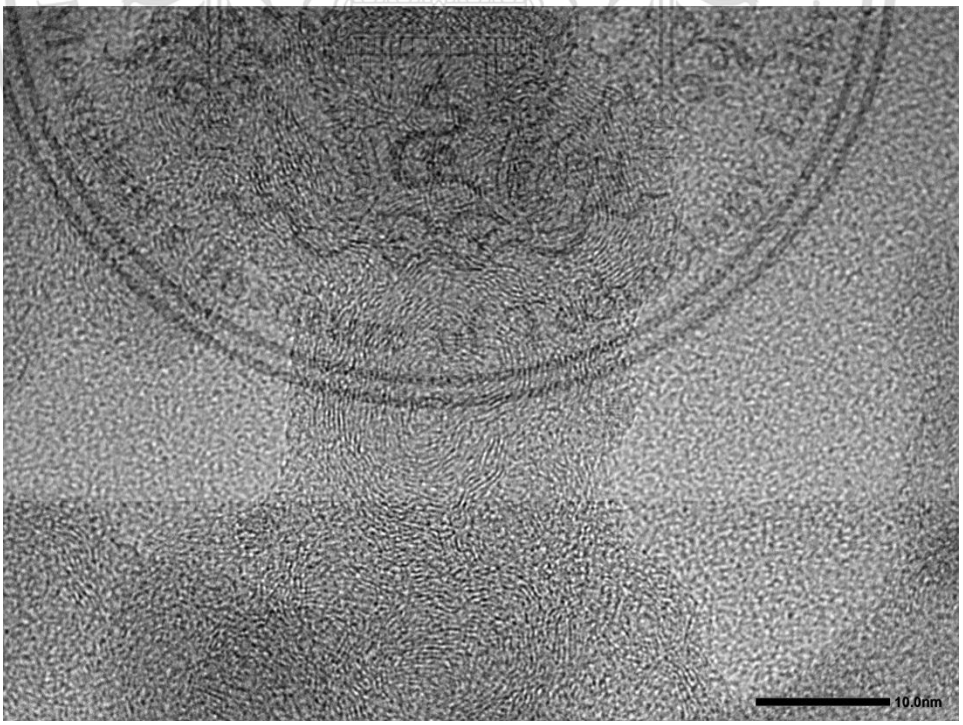

Figure 4.14a BE20's Primary particles

This material is reserved for educational use only, not allowed for commercial use.
Forbidden to modify the content, and cite the document when use.

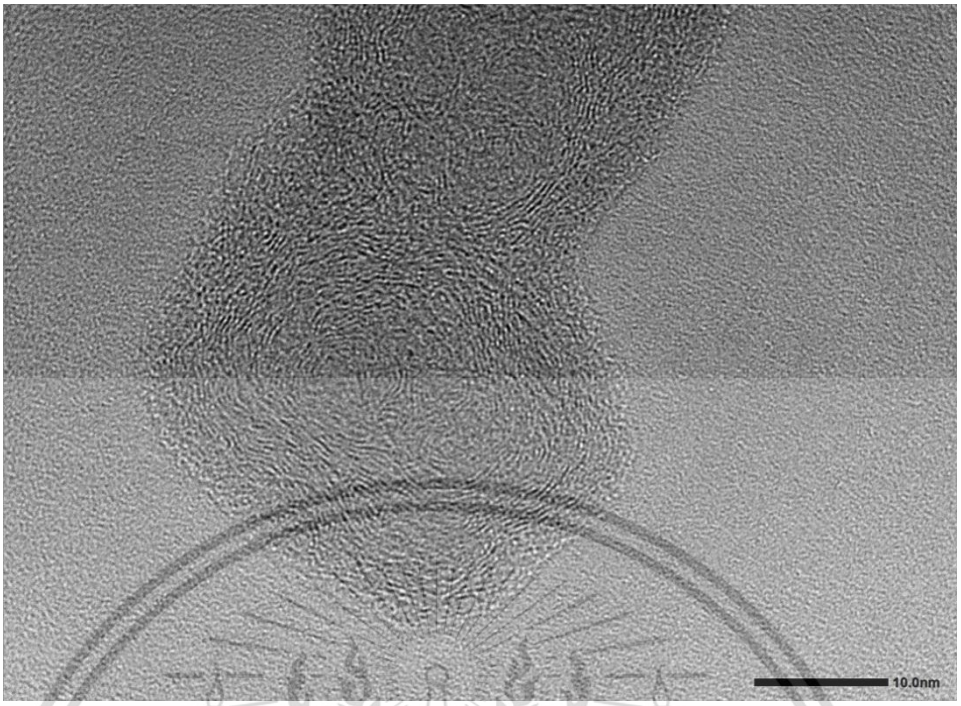

Figure 4.14b B100's Primary particles

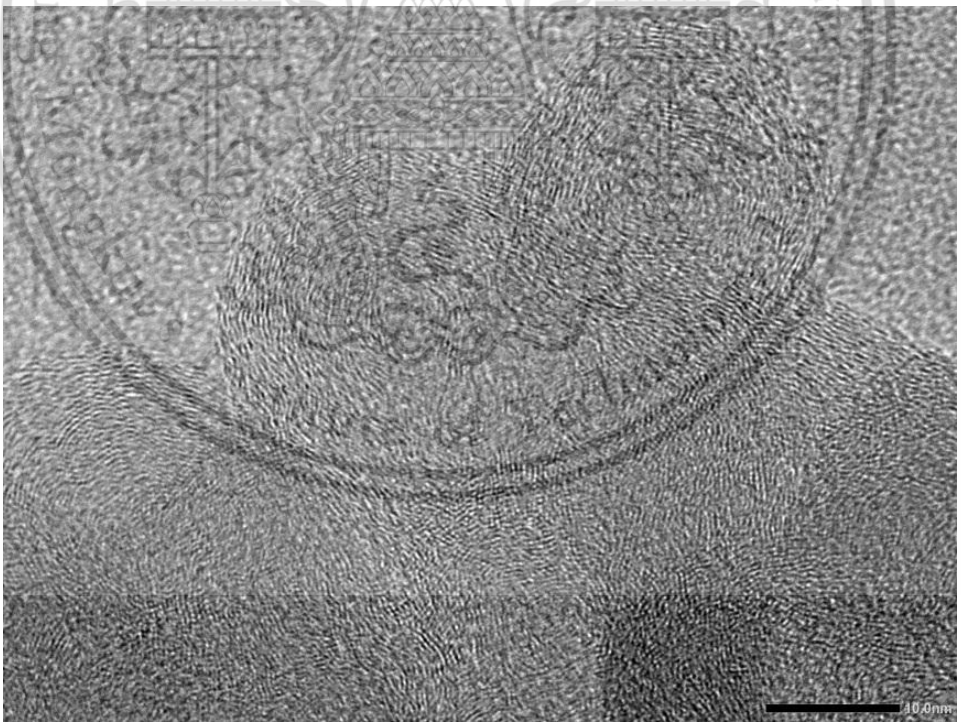

Figure 4.14c Diesel's Primary particles

This material is reserved for educational use only, not allowed for commercial use.
Forbidden to modify the content, and cite the document when use.

In nanostructure level, it is more convenient to refer primary particles as soot particles because we focus on action of carbon on PM characteristics. From the images, it can be seen that soot particles consist of many fringes of carbon. As recalled from the soot model of V. Fernandez-Alos et al. [38] in Fig. 2.26, each fringe, it represents Graphene sheet structure consisting of molecules of hexagon-like carbon - 6 (C-6) as a possible smallest unit. Such molecules are agglomerated into large rings of carbon then become a graphene sheet or carbon platelet. These fringes were processed by image processing method so that they can be quantitatively analyzed. Figure 4.15 show cropped images of BE20, B100, and diesel's soot particle on homogeneous interested areas (approximately 10 nm x 10 nm.). With application of image processing method by software **Image J**, Fig. 4.16a – Fig. 4.16c show black and white images of carbon fringes with noise already filtered. Figure 4.16d – Figure 4.16f show skeletonized images of the black and white images in order that fringe length can be determined quantitatively.

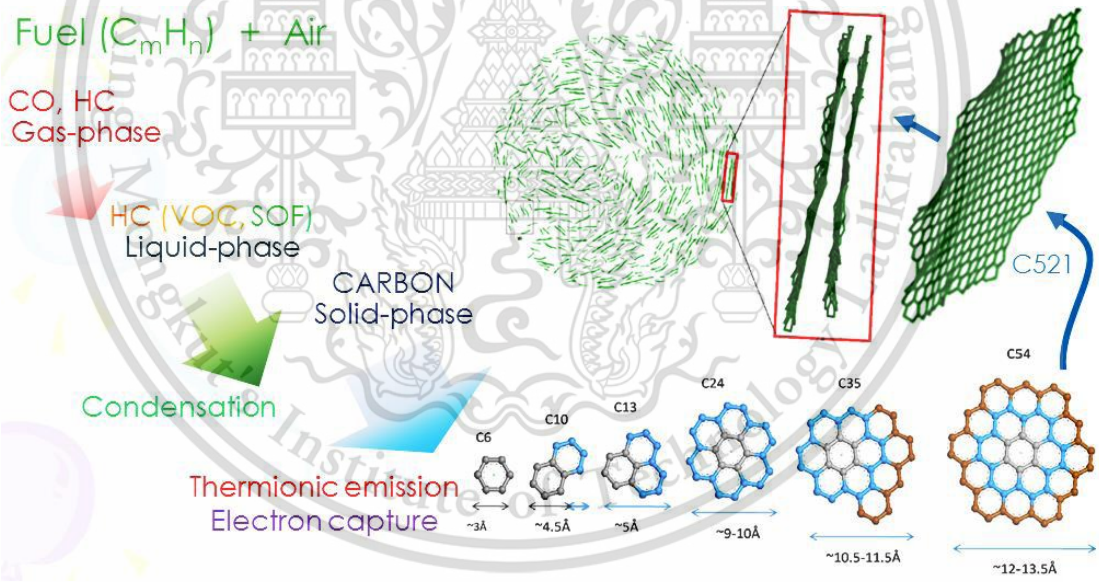

Recalled Figure 2.26 Relationship between number of hexagon rings and carbon atoms in graphene sheet of soot particle [38]

This material is reserved for educational use only, not allowed for commercial use.
Forbidden to modify the content, and cite the document when use.

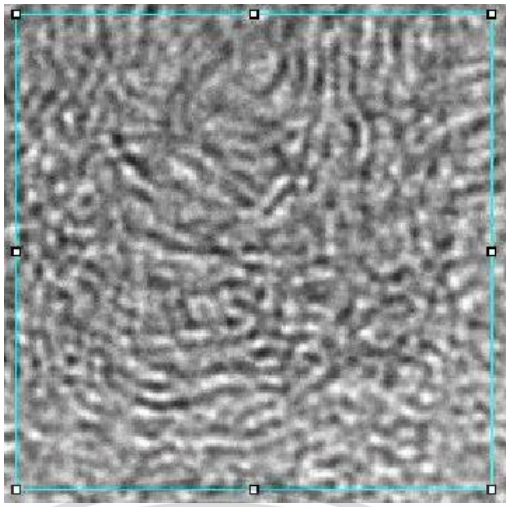

Figure 4.15a BE20's fringe cropped image

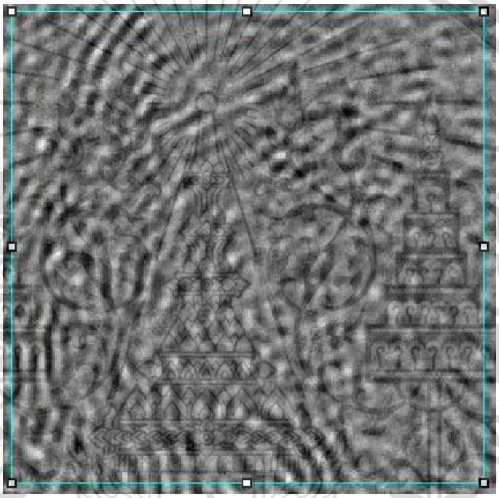

Figure 4.15b B100's fringe cropped image

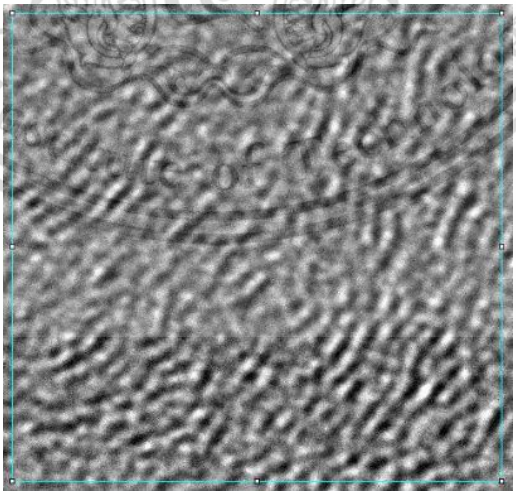

Figure 4.15c Diesel's fringe cropped image

This material is reserved for educational use only, not allowed for commercial use.
Forbidden to modify the content, and cite the document when use.

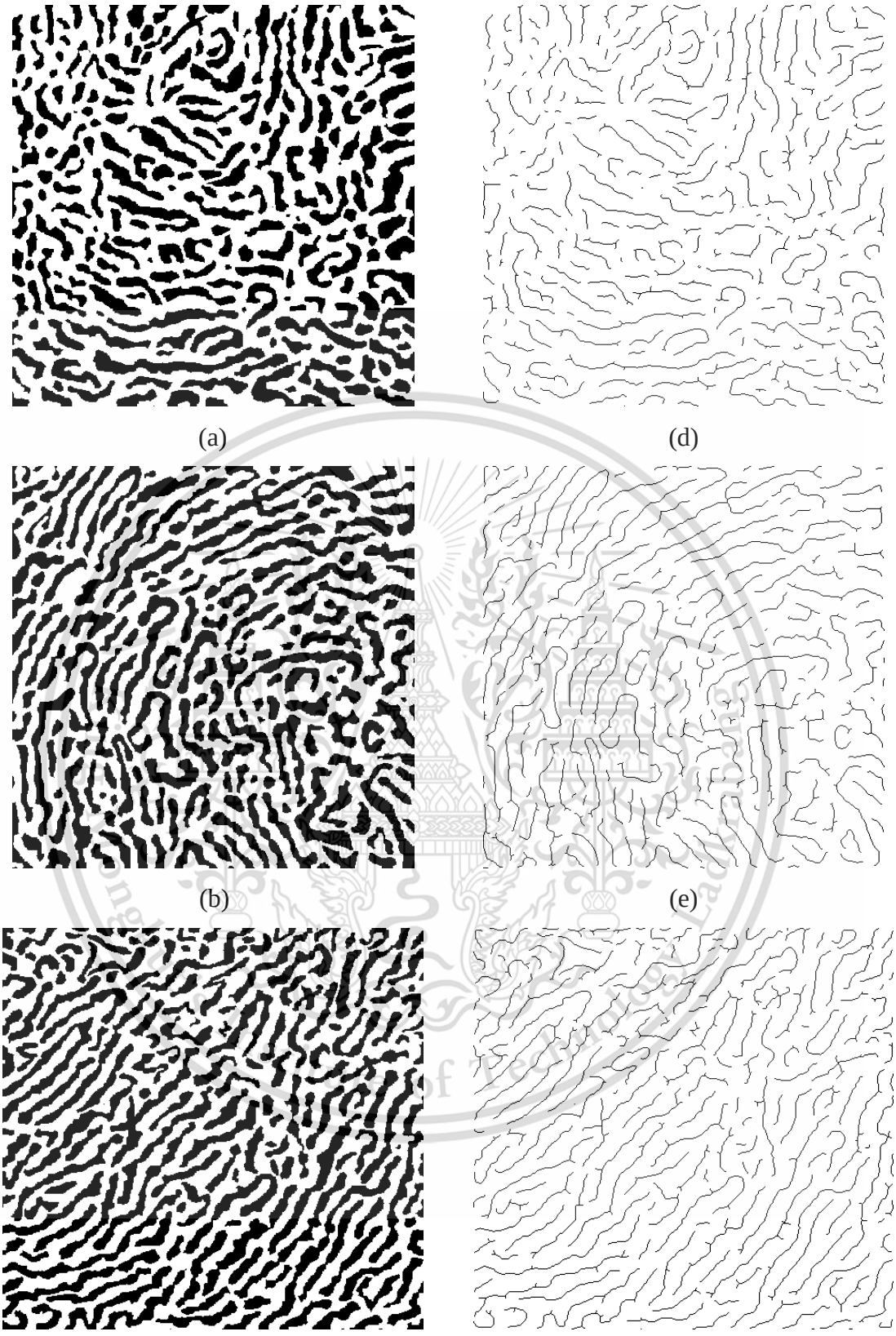

Figure 4.16 Black and white images (a : BE20, b : B100 , c : diesel) and Skeletonized images of carbon fringes (d : BE20, e : B100 , f : diesel)

This material is reserved for educational use only, not allowed for commercial use.
Forbidden to modify the content, and cite the document when use.

From the skeletonized images, scribble lines represent carbon fringes which referred as graphene structure. To understand in detail, insight of carbon atom arrangement in the graphene sheet is necessary to be clarified. According to the conceptual model of Lipkea, the carbon crystallite was assumed that it consists of 2-5 carbon platelets with a pair of graphene sheet. Distance between the graphene sheets is about 0.35–0.36 nm. However, according to the measurement in this research, adjacent skeletonized lines, the distance was found at 0.3 – 0.4 nm. That means the skeletonized images in this case correspond to **1 fringe line per 1 graphene structure**. While longer the line, it has more possibility to contain more number of carbon hexagon rings in the graphene structure.

This concept also agrees with modern transmission electron microscopy. S.Akhtar [22] explained how to interpret TEM image of graphene flakes as shown in Fig. 4.17. The inter-planar spacing between the graphene planes is about 0.335 nm. The graphene layers at a folding become parallel to the incident electron beam in the TEM where each layer exhibits a dark line with ~ 0.335 nm spacing in the high resolution (HR) image.

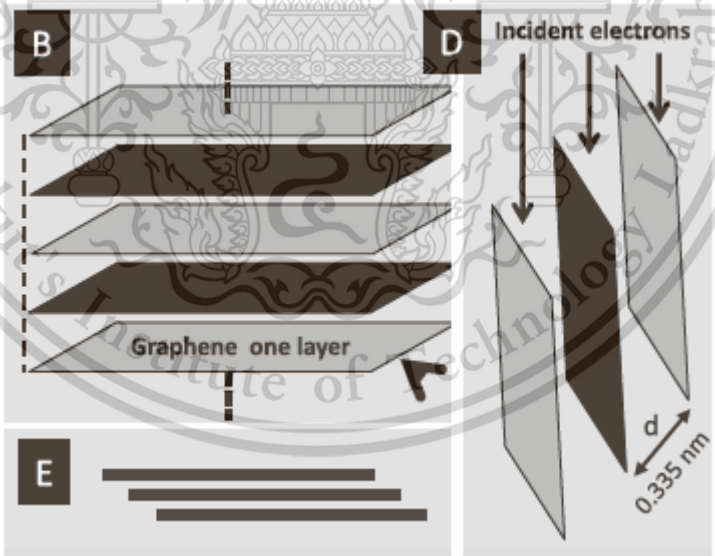

Figure 4.17 Schematic illustration of bulk graphite and one graphene layer [22]

This material is reserved for educational use only, not allowed for commercial use.
Forbidden to modify the content, and cite the document when use.

Figure 4.18a – Figure 4.18d show size distribution of the fringe length from BE20, B100, and diesel's soot particle respectively. **BE20's soot tends to have shortest fringes** compared with B100 and diesel's soot. Most fringes are in the range of 0.4 – 2.0 nm. For B100, most crystallite is under 2.8 nm, while fringes over 3.5nm can be moderately found for diesel. **Average fringe length** of **BE20**, **B100**, and **diesel's** soot are **0.93** nm, **1.35** nm, and **1.45 nm**, respectively.

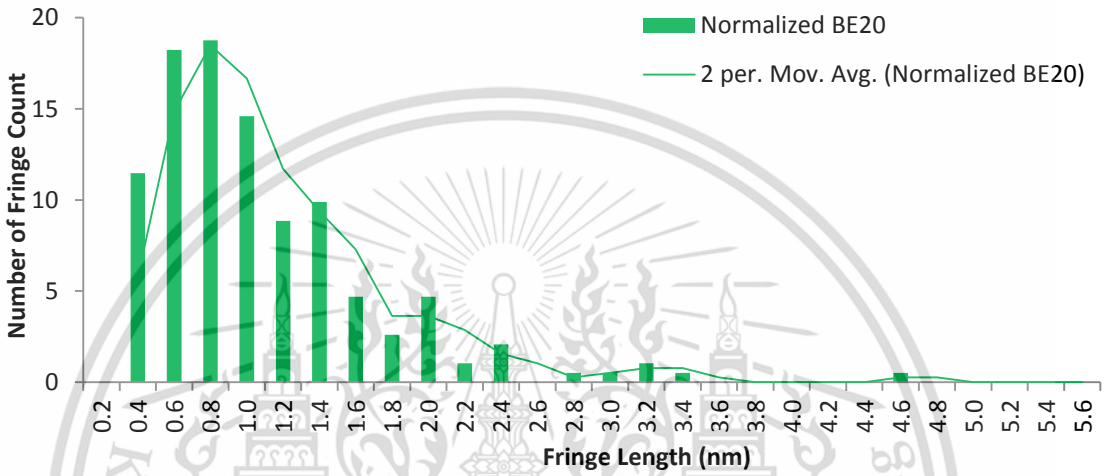

Figure 4.18a BE20's fringe size distribution

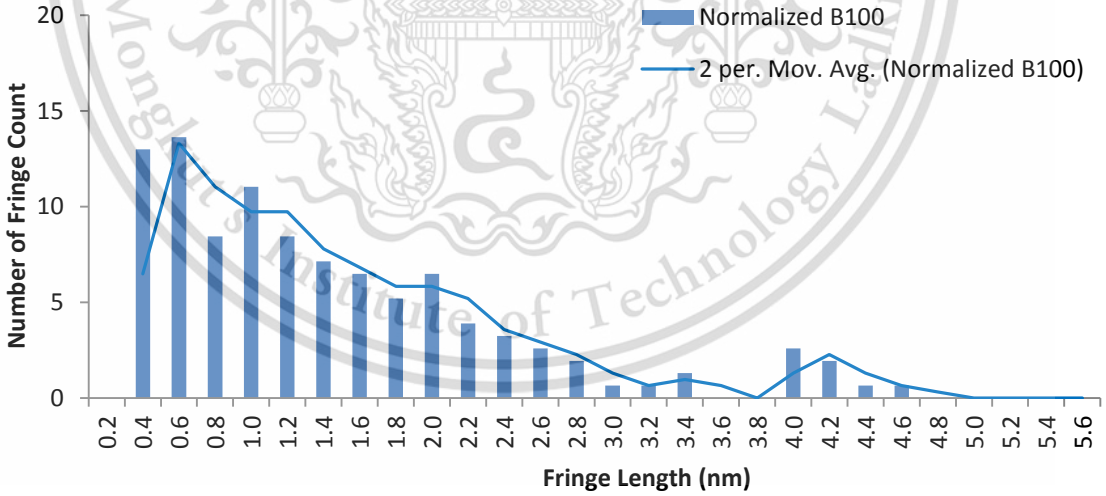

Figure 4.18b B100's fringe size distribution

This material is reserved for educational use only, not allowed for commercial use.
Forbidden to modify the content, and cite the document when use.

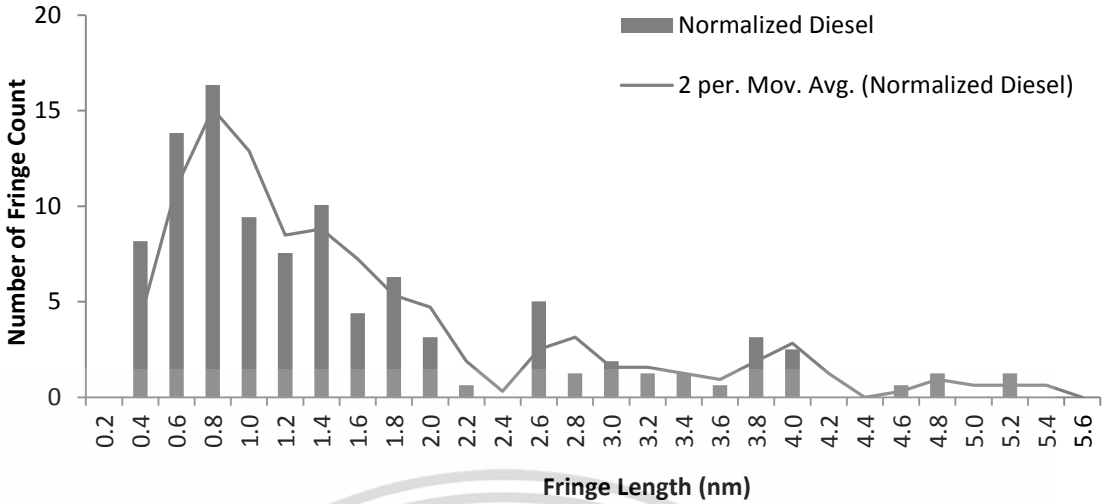

Figure 4.18c Diesel's fringe size distribution

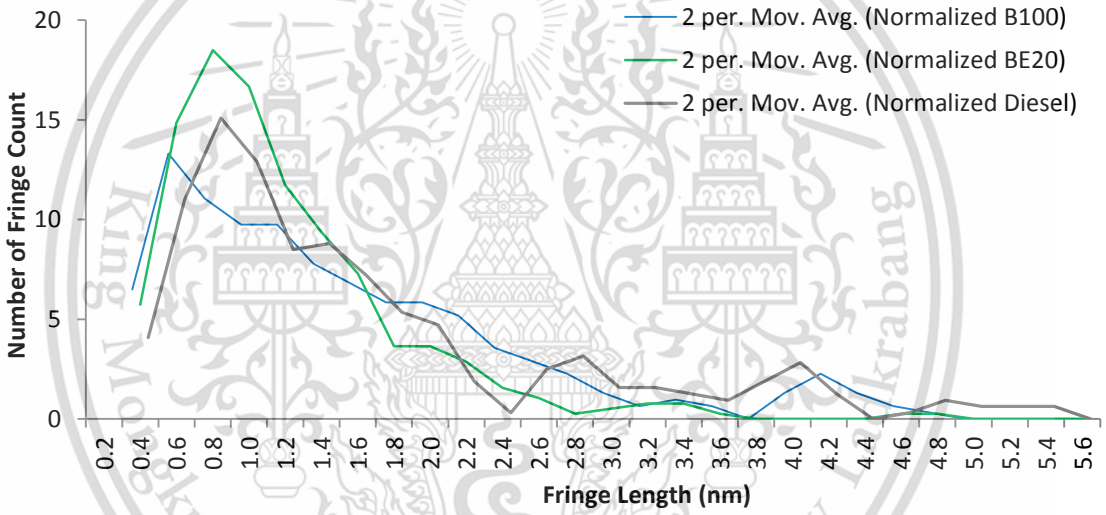

Figure 4.18d Combined fuel's fringe size distribution (Moving average)

As recalled from the soot and char molecular model of V. Fernandez-Alos, carbon atom arrangement model was developed in this research. The model begins with theoretical distance of adjacent carbon atoms in the hexagonal ring of 1.421 A or 0.1421 nm. Therefore, referring simple hexagonal geometry can determine possible minimum crystallite length due to minimum structure of C-6 atoms at approximately 2.6 A or 0.26 nm as shown in Fig. 4.19. As hexagonal structure grows up, dimension of the rings i.e. carbon fringe size can be visualized. Since conceptual graphene sheets are shaped as smooth layer, the skeletonized lines with small branches are out of consideration. Eventually, simulating and gathering enough data of the carbon hexagonal ring structure, **relationships between carbon fringe length** and **number**

This material is reserved for educational use only, not allowed for commercial use.
Forbidden to modify the content, and cite the document when use.

of hexagonal rings and **number of carbon atoms contained in the hexagonal ring** in the corresponding graphene sheet can be predicted as a model shown in Fig. 4.20.

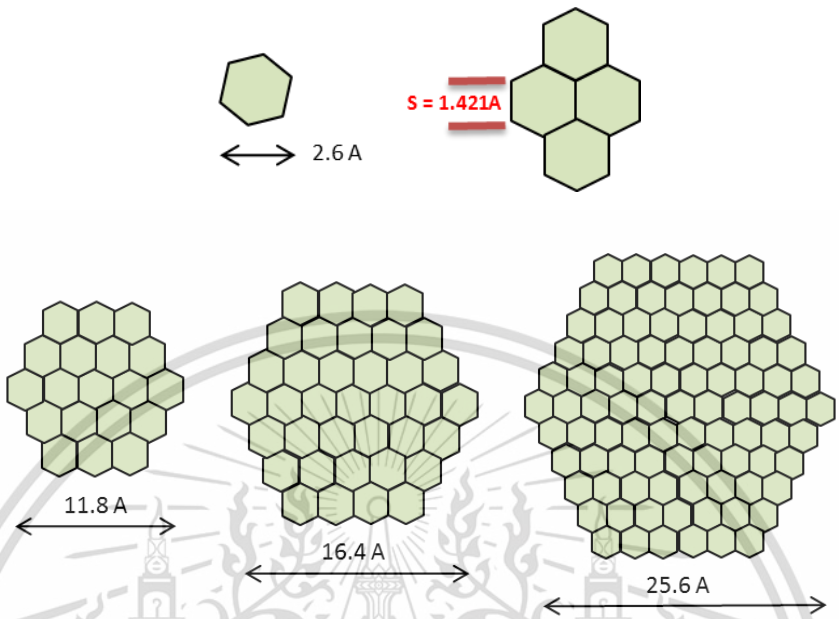

Figure 4.19 Carbon hexagonal ring dimension measurement

Carbon fringe data from the **skeletonized images actually represent a capture of soot particles in two dimensions** i.e. cannot interpret the image in depth dimension. Therefore, to determine carbon atom density, it is necessary to consider another dimension deep into the captured image. **Figure 4.21 propose a model to determine a controlled volume** from the 2-dimension captured image for carbon density estimation. Each graphene sheet is assumed to form a circular sheet referred from V. Fernandez-Alos's [38] because of chemical bonding stability. In order to estimate an accurate controlled volume, the circular graphene sheets are simply transformed into rectangular shape. Integration of all sheets becomes a closed volume which correspond to carbon atom density calculation.

This material is reserved for educational use only, not allowed for commercial use.
Forbidden to modify the content, and cite the document when use.

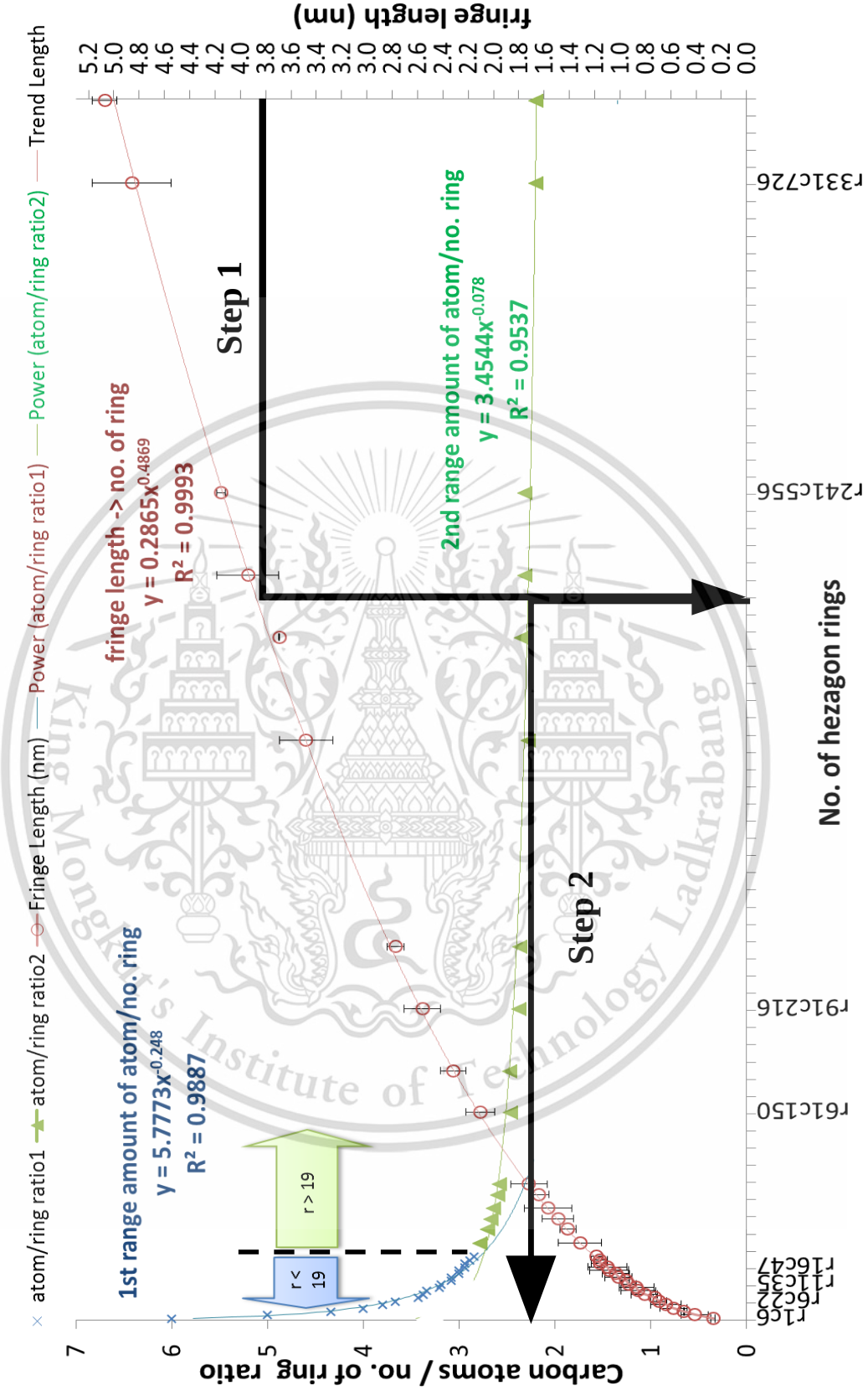

Figure 4.20 Prediction model of carbon fringe length and carbon atom calculation

This material is reserved for educational use only, not allowed for commercial use.
Forbidden to modify the content, and cite the document when use.

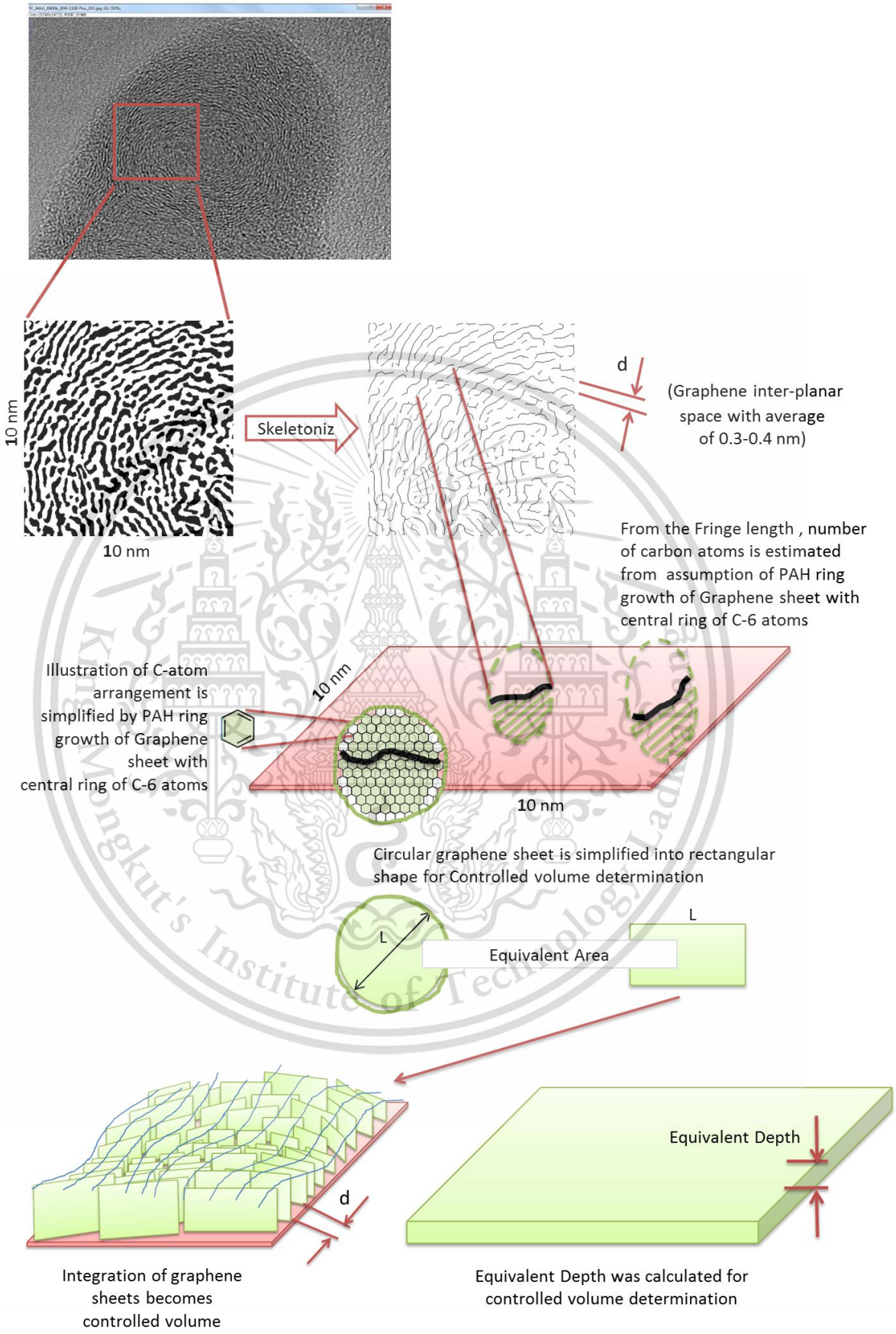

Figure 4.21 Conceptual model of controlled volume for carbon atom density calculation

This material is reserved for educational use only, not allowed for commercial use.

Forbidden to modify the content, and cite the document when use.

Table 4.1 shows calculation results of carbon atom density compared among B100, BE20, and diesel's soot particle. Carbon density of diesel's soot is apparently higher than B100's and BE20's which agrees with the Black and White image from the image processing. Also, all calculation results of soot density are close to commercial products of industrial graphite and carbon black properties.

Table 4.1 Comparison of carbon atom and soot density of BE20, B100, and Diesel soot

Items	BE20	B100	Diesel	Graphite	Carbonblack
Total crystallite length (nm/image)	189.13	208.38	227.45		
Total C atoms	9786.92	14700.46	17695.83		
Control volume (nm^3)	110.86	162.27	171.61		
Carbon atom density (atom/nm^3)	88.28	91.41	100.67		
Soot density (g/cm^3)	**1.76**	**1.82**	**2.01**	1.7-1.8 [a]	1.8 – 2.1 [b]

a : http://www.chemicalbook.com/ProductMSDSDetailCB3109508_EN.htm ;
http://www.inchem.org/documents/icsc/icsc/eics0471.htm

b : Poco Graphite - An Entegris Company

This material is reserved for educational use only, not allowed for commercial use.
Forbidden to modify the content, and cite the document when use.

4.6 Oxidation kinetics

The particulate matter from B100 and BE20 was analyzed by isothermal TGA method to investigate oxidation behavior of the particulate matter. PM mass conversion is plotted with respect to time as shown in Fig. 4.22. Diesel's particulate matter from previous research was also analyzed as reference for this research. Since PM collected from the combustion is not pure soot, it might include some metal wear, humidity, or volatile substance. Therefore, initial TGA data until isothermal temperature reached and the data after steady mass are considered as outliers and then neglected. It can be seen that all graphs have similar trends; that is higher isothermal temperature condition, PM mass reduces faster. Figure 4.23 compares the mass conversion duration from BE20's, B100's, and diesel's PM until 10% mass remained at each isothermal temperature. Obviously, BE20's and B100's PM are oxidized faster and at lower temperature than diesel's PM.

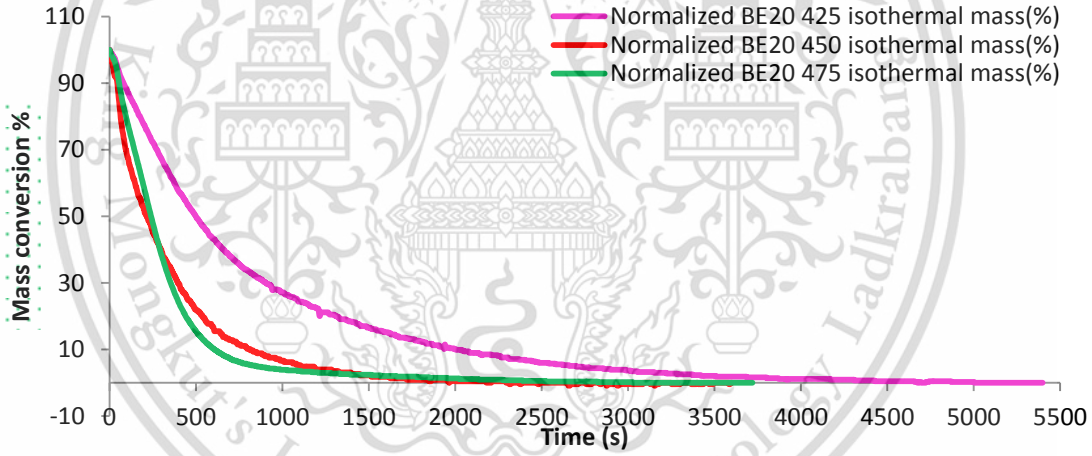

Figure 4.22a Normalized mass conversion of BE20's particulate matter at 425°C, 450°C, and 475°C

This material is reserved for educational use only, not allowed for commercial use.
Forbidden to modify the content, and cite the document when use.

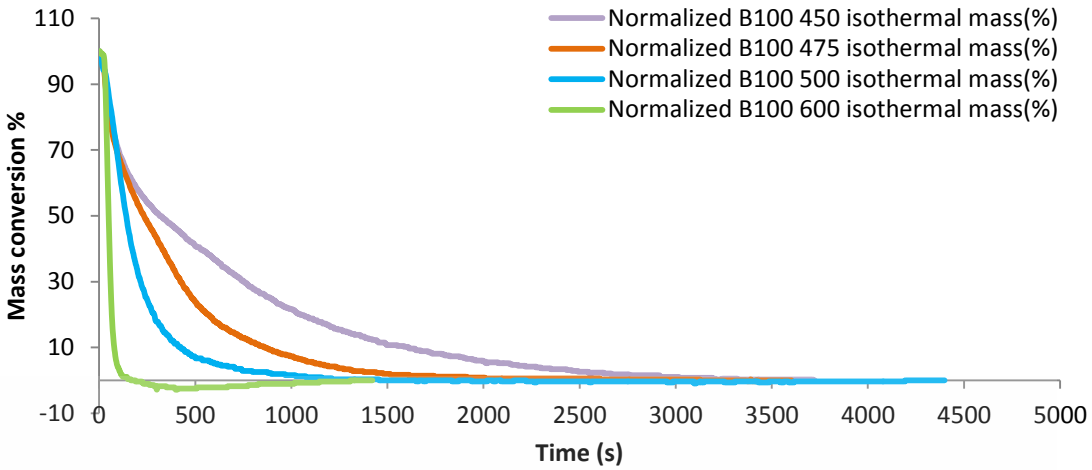

Figure 4.22b Normalized mass conversion of B100's particulate matter at 450°C, 475°C, 500°C, and 600°C

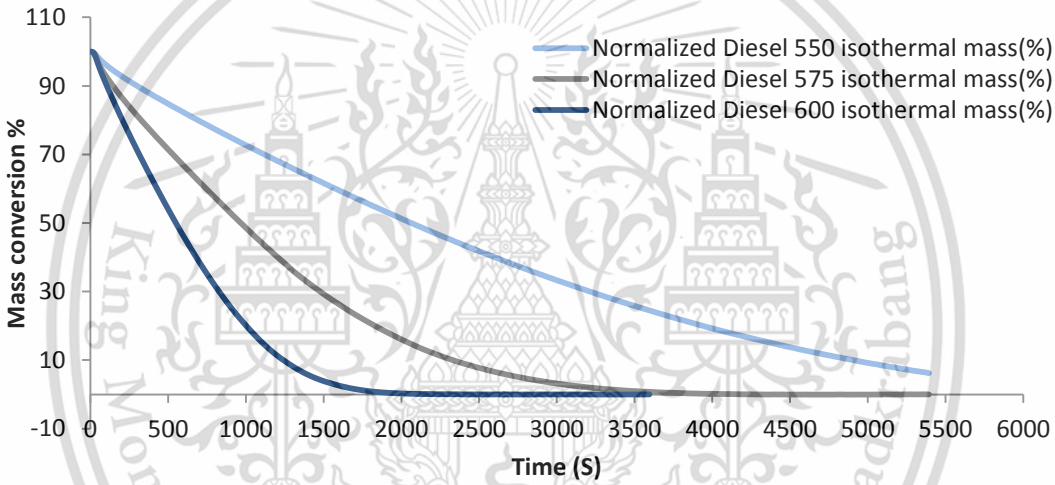

Figure 4.22c Normalized mass conversion of Diesel's particulate matter at 550°C, 575°C, and 600°C

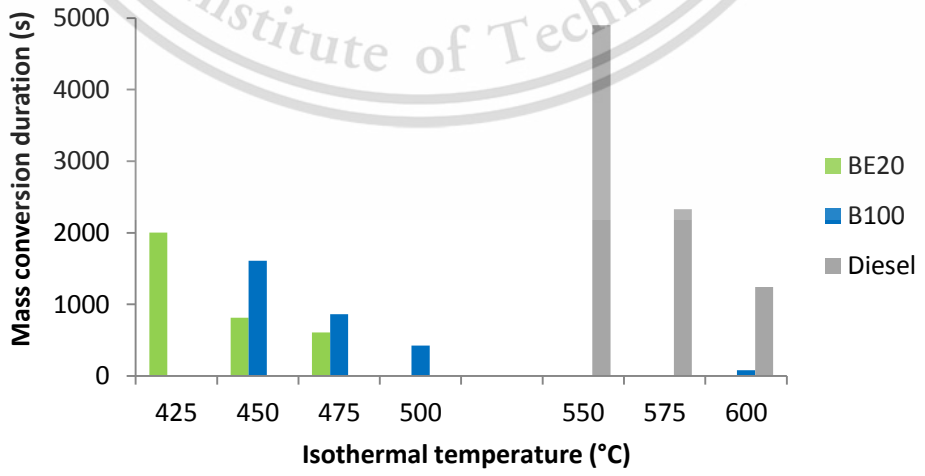

Figure 4.23 Comparison of mass conversion duration of BE20's, B100's, and diesel's PM

This material is reserved for educational use only, not allowed for commercial use.
Forbidden to modify the content, and cite the document when use.

Chemical kinetics of TGA is analyzed by a simple relationship as Eqn.4.1

$$\mathrm{C(PM)} + O_2 \rightarrow CO_2 \tag{4.1}$$

Global chemical reaction rate equation or rate of PM mass conversion is described as relationships as Eqn.4.2

$$\frac{-d[C]}{dt} = kC^n {O_2}^m \tag{4.2}$$

According to the Arrhenius expression form of Eqn. 2.5, rate constant in this research can be expressed as Eqn.4.3

$$k = Ae^{(\frac{-E_a}{RT})} \tag{4.3}$$

Modification of Eqn. 4.2 and Eqn. 4.3 yields Arrhenius linear equation form expressed as Eqn. 4.4

$$\mathbf{ln}\left|\frac{-d[C]}{dt}\right| = -\frac{E_a}{RT} + lnA + n \cdot \mathbf{ln}[C] + m \cdot \mathbf{ln}[O_2] \tag{4.4}$$

where ;

n is order of reaction with respect to [C]

[c] is PM concentration which is equivalent to PM % mass

[O_2] is oxygen concentration

m is order of reaction with respect to [O_2]

k is rate constant which depend on *A* , *Ea* , *R* , *T*

A is particle collision frequency factor

E_a is activation energy

R is gas constant

T is reaction temperature (K)

This material is reserved for educational use only, not allowed for commercial use.
Forbidden to modify the content, and cite the document when use.

4.6.1 Activation energy

Activation energy (E_a) is the minimum energy which is required to initiate and complete a chemical reaction. The lower activation energy means the better reactivity. From the mass conversion graphs (Fig. 4.22), rate of mass conversion was selected within the zone of constant slope for accurate E_a estimation. From the equation form of Eqn. 4.4, it can be simplified as a linear equation form of **Y = m · X + c**. where Y axis is equivalent to ln $\left|\frac{-d[C]}{dt}\right|$, **m is equivalent to** $-\frac{E_a}{R}$, X is equivalent to $\frac{1}{T}$, and C-intercept is responsible for the remaining terms; $lnA + n \cdot \ln[C] + m \cdot \ln[O_2]$. As a result, the data of PM mass conversion rate can be plotted as a graph in Fig.4.24 and activation energy can be calculated as shown in Table 4.2.

Also, results of the activation energy can be interpreted by the mass conversion graphs (Fig. 4.22). E_a of BE20's PM is comparatively low. This is because PM's energy level at temperature of 450°C is high enough to initiate the reaction. Increasing temperature (to 475°C) does not contribute faster reaction. Whereas PM conversion speed for the diesel is much more dependent on temperature i.e. reaction speeds significantly change with different temperatures. Therefore, E_a is comparatively high.

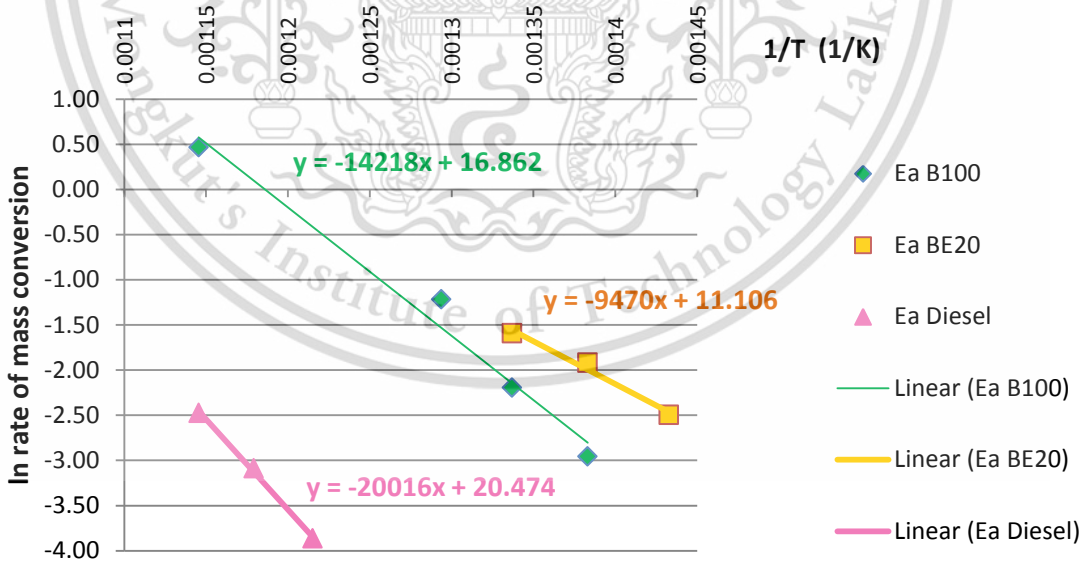

Figure 4.24 Arrhenius plots of B100, BE20, and diesel particulate matter at isothermal TGA condition for E_a determination

This material is reserved for educational use only, not allowed for commercial use.
Forbidden to modify the content, and cite the document when use.

Table 4.2 Calculated activation energy of BE20, B100, and Diesel's PM

	BE20	B100	Diesel
Activation Energy , kJ/mol	78.7	118.2	166.4

4.6.2 Reaction order of particulate matter

Reaction order of particulate matter (*n*) can be obtained similar to the method of activation energy. However, the X-axis becomes *ln* function of decreasing PM mass. **Slope of the graphs directly become n** or reaction order of PM. The plot is shown as Fig.4.25

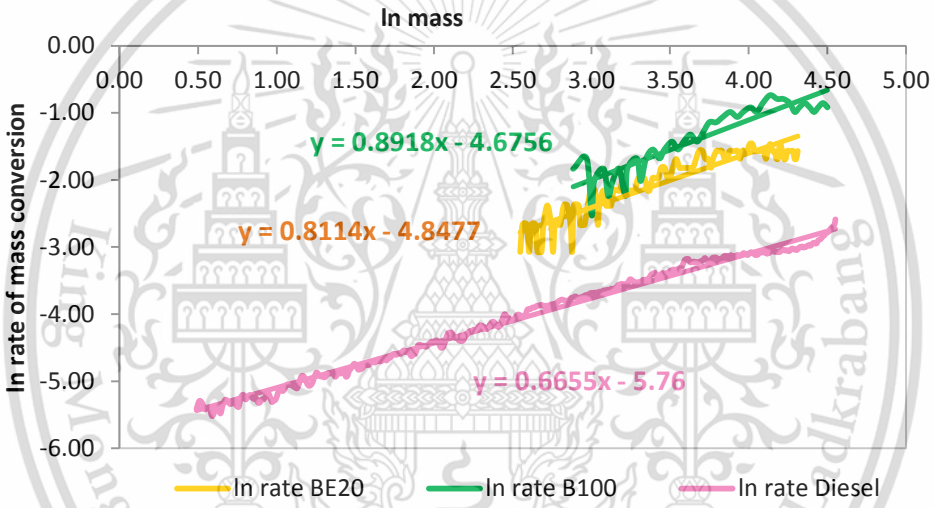

Figure 4.25 Arrhenius plot of B100, BE20, and diesel particulate matter at isothermal TGA condition for Reaction order of PM (*n*)

Table 4.3 Reaction order of BE20, B100, and Diesel's PM

	BE20	B100	Diesel
Reaction order (graph slope)	0.81	0.89	0.67

This material is reserved for educational use only, not allowed for commercial use.
Forbidden to modify the content, and cite the document when use.

4.6.3 Particle collision frequency factor

Particle collision frequency factor (*A*) can be determined by adoption of the n or PM reaction order method. Referred from the Arrhenius linear equation Eqn. 4.4, the collision frequency factor which is represented as a form of ***lnA*** can be calculated from C-intercept.

$$\ln\left|\frac{-d[C]}{ct}\right| = n \cdot \ln[C] + \left[-\frac{E_a}{RT} + m \cdot \ln[O_2] + lnA\right]$$

$$Y = m \quad X + \quad \boldsymbol{c} \tag{4.5}$$

After substituting E_a and T corresponding to the conditions of n value (**m is assumed as 1 and constant O_2 of 21% because air supply in the TGA is constant and considered as over supplied compared with PM sample**) *lnA* can be calculated as summarized in Table 4.4

Table 4.4 Calculated Particle collision frequency factor of BE20, B100, and Diesel's PM

	BE20	B100	Diesel
ln function of Particle collision factor (*ln* A)	4.77	10.67	14.80

This material is reserved for educational use only, not allowed for commercial use.
Forbidden to modify the content, and cite the document when use.

4.6.4 Oxidation kinetics parameter analysis

Recalled from the Arrhenius linear equation of Eqn.4.4, the minus term $-\frac{E_a}{RT}$ slow down the reaction and the plus terms $\boldsymbol{lnA} + \boldsymbol{n} \cdot \mathbf{ln}[\boldsymbol{C}] + \boldsymbol{m} \cdot \mathbf{ln}[\boldsymbol{O_2}]$ boost up the reaction

$$\mathbf{ln}\left|\frac{-d[C]}{dt}\right| = -\frac{E_a}{RT} + \boldsymbol{lnA} + \boldsymbol{n} \cdot \mathbf{ln}[\boldsymbol{C}] + \boldsymbol{m} \cdot \mathbf{ln}[\boldsymbol{O_2}] \qquad \text{(Recalled Eqn. 4.4)}$$

It can be seen that the **collision frequency factor (A) and reaction order (n) try to promote the reaction in a view of physical effect** i.e. to represent how much frequency of the particle collision or as a magnifier terms for the reactant concentration. However, **chemical effect i.e. E_a regulates that the chemical reaction is successful or not**. At **low temperature**, particles have low level of activity. Therefore, physical effects cannot support much to increase the reactivity, whereas **chemical effect** allows reactions which have low Ea to accomplish. On the other hand, at **high temperature**, particles with high energy are easy to overcome E_a. Improvement in **physical effect** i.e. improved chance for particle collision can strongly promote better reactivity. This can be explained as Fig. 4.26. The graph represents BE20 extrapolated plot to higher temperature zone. In the lower temperature zone, conversion rate of BE20's PM is more than B100 and diesel's PM due to lower *Ea*. On the other hand, A and n are the key factors of B100's PM to overcome BE20's mass conversion at higher temperature.

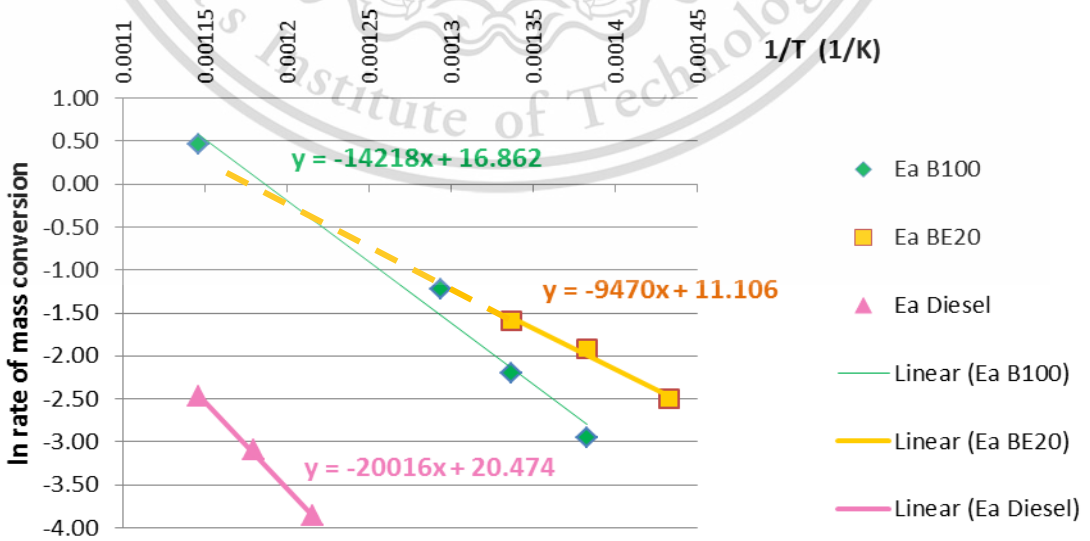

Figure 4.26 Modified Figure 4.23, extrapolated plots of BE20

This material is reserved for educational use only, not allowed for commercial use.
Forbidden to modify the content, and cite the document when use.

4.7 Relationships of oxidation kinetics and particulate matter's morphology and nanostructures

As recalled from the carbon fringe of soot particles, BE20's soot has a trend of shortest fringe length, followed by B100's soot, and diesel's soot has longest fringe. In a viewpoint of Oxidation Kinetics, **Activation energy** of BE20's soot is also lowest, followed by B100 and diesel has highest activation energy as summarized in Table 4.5.

Table 4.5 Relationships between crystallite length and activation energy of BE20, B100, and Diesel's PM

	BE20	B100	Diesel
Fringe length			
Average, nm	**0.93**	**1.35**	**1.45**
Range of 0 – 1 nm	**67%**	45%	45%
Range of 1 – 2 nm	26%	**35%**	33%
Range of 2 – 3 nm	5%	**13%**	11%
Range over 3 nm	2%	7%	**10%**
	Max 4.8 nm	max 5.0 nm	max 5.8 nm
Activation Energy , kJ/mol	78.7	118.2	166.4

The results show agreement with the assumption of J. Hamada et al [43]. For this research, the mechanism can be explained as; hydroxyl (OH-) group in ethanol fuel molecules is a key factor to create much amount of **oxygen (O-) or hydroxyl (OH-)** functional groups **connecting to soot particles** (or graphene sheets as nanostructure level) during soot formation process. These O- or OH- attachments cause the graphene or the crystallites become smaller (**visualized by schematic diagram in Appendix F - Comments and Questions from Thesis Defense - Q3**) as described in Fig. 4.27. This mechanism is supposed to be more effective for biofuel, especially BE20, diesel's fuel molecules have lower oxygen or OH- contents. These O- or OH- contributes to easier initiation of the reaction (i.e. reduced overall activation energy) which agrees with [34].

This material is reserved for educational use only, not allowed for commercial use.
Forbidden to modify the content, and cite the document when use.

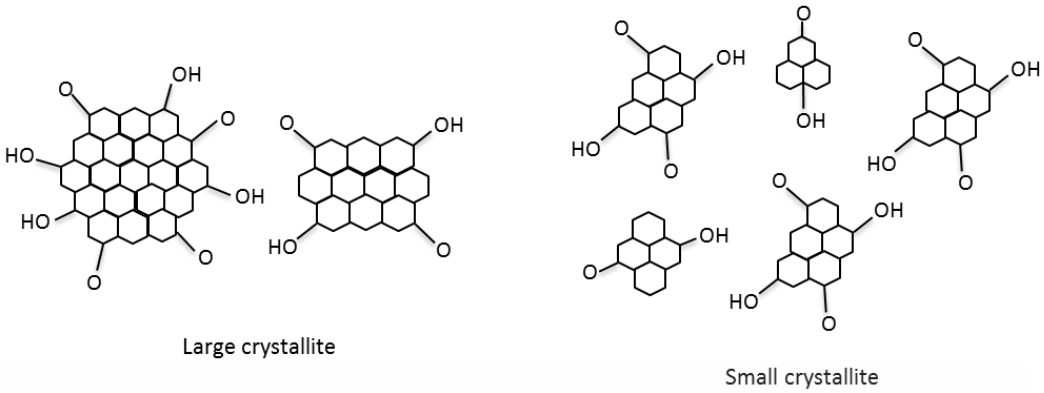

Figure 4.27 Comparison of carbon fringe size in soot particles
Smaller fringes have comparatively higher ratio of O- or OH- per carbon atoms because of more free electrons to capture other substance

Current researches related to explanation of **particle collision frequency factor or A** is likely to represent frequency and direction of collisions between reactant molecules. Referred from the carbon atom density comparison in Table 4.1, the results can be explained with relationships with the particle collision frequency factor. As carbon atom density increases, carbon fringe structure becomes more packed. Hence, there are more chances that oxygen gas molecules collide the active sites (i.e. carbon fringes) to initiate the reaction as illustrated in Fig. 4.28. Detail of dimensional relationships between oxygen molecules and carbon fringe is represented in the **Appendix F - Comments and Questions from Thesis Defense - Q3**. Table 4.6 show carbon atom density of BE20's soot is comparatively lowest. Therefore, *lnA* also becomes lowest compared with B100 and diesel's soot.

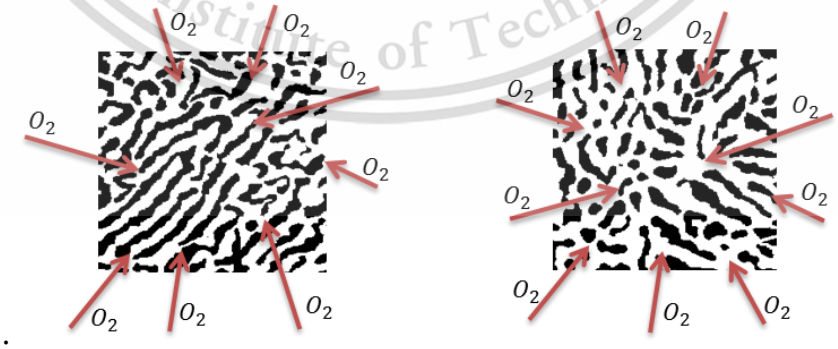

Figure 4.28 Comparison of packed (left: diesel) and loose (right: BE20) Carbon fringe structure of soot particles

This material is reserved for educational use only, not allowed for commercial use.
Forbidden to modify the content, and cite the document when use.

Table 4.6 Relationships between Carbon atom density and particle collision frequency factor *(lnA)* of BE20, B100, and Diesel's PM

	BE20	B100	Diesel
Carbon atom density , atom/nm^3	88.28	91.41	100.67
ln A	4.77	10.67	14.80

According to experimental and modeling study of catalytic diesel soot oxidation [44], K. Leistner explained that global oxidation rate might be formed by taking into account the influence of evolution of surface area as Eqn. 4.6 which is equivalent to the Arrhenius oxidation kinetics models of Eqn. 2.2 ($r = N_t \cdot k(T) \cdot f(p_{O2}, p_{H2O}, \dots)$ and the global chemical equation of Eqn. 4.2 ($\frac{-d[C]}{dt} = kC^n {O_2}^m$)

$$r_j = N_T \cdot k_j(T) \cdot C_{oxidant}^n \tag{4.6}$$

where $\boldsymbol{N_T}$ is defined as the total number of carbon active sites which

$$N_T = Active\ site\ density \cdot S_a \tag{4.7}$$

where S_a is specific surface area which expose to gaseous reactant

$$S_a = S_{a,0} \cdot (1 - X)^{n_x} \tag{4.8}$$

where X is conversion

n_x is reaction order with respect to carbon

Term $\boldsymbol{k_j(T)}$contributes to chemical structure which is supposed to equivalent to *k(T)* in the Arrhenius kinetics model. $\boldsymbol{C_{oxidant}^n}$ is related to reaction order with respect to O_2. For this reason, **reaction order of particulate matter (n)** in this research must be **related to carbon active sites or $\boldsymbol{N_T}$.**

As referred from the **Shrinking core model, $\boldsymbol{n_x}$ = 2/3** was also explained **based on the outer surface area of the carbon particle** which is assumed to be spherical. So, it is reasonable that the reaction order in this research is to be determined at the level of soot particle surface as well. **The total number of carbon active sites** for this research accordingly can be considered as a function of the **product of Carbon Fringe density** and **Soot particle surface area** as illustrated in Fig. 4.28.

This material is reserved for educational use only, not allowed for commercial use.
Forbidden to modify the content, and cite the document when use.

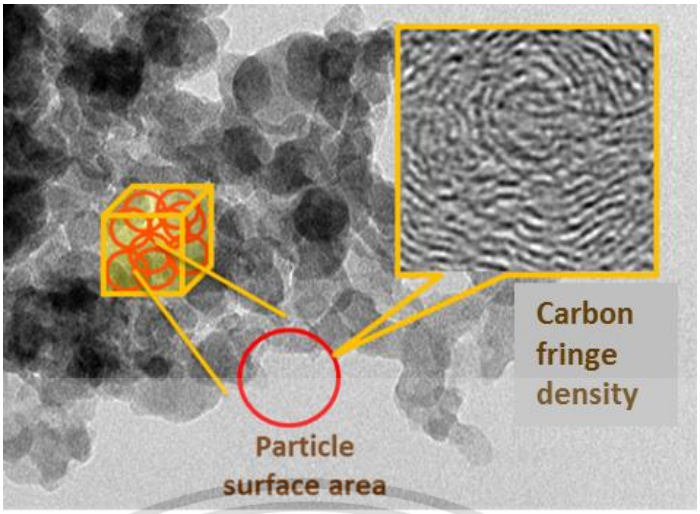

Figure 4.29 Schematics of Total number of carbon active sites or N_T determination on the level of Particle surface and Carbon fringe density

From the results of different soot primary particle's size in section 4.5.1, this effect on different particle surface area based on assumption of circular particles. The surface area of particles can be compared by containing particles in any controlled volume (V) as shown in the Fig. 4.29 as well. Table 4.7 shows the relationships between total particle surface area and the reaction order. B100's particles with maximum surface area conform to the highest value of reaction order.

Table 4.7 Relationships between soot particle surface area and reaction order of BE20, B100, and Diesel's PM

	BE20	B100	Diesel
Primary particle size			
Average, nm	29.1	27.0	29.8
Total particle surface area			
per controlled volume V	0.206V	0.222V	0.201V
Diesel as 100%	107.8%	111.1%	100%
Reaction order of PM	0.81	0.89	0.67

This material is reserved for educational use only, not allowed for commercial use.
Forbidden to modify the content, and cite the document when use.

CHAPTER 5

CONCLUSIONS AND RECOMMENDATIONS

Unique characteristics of ethanol on the aspects of combustion characteristics, PM emission, PM nanostructure, and PM oxidation kinetics were well investigated in this research. A little ratio of ethanol blended on biodiesel results in distinction of engine combustion characteristics and particulate matter properties.

In a viewpoint of combustion, ethanol blended fuel is quite compatible with biodiesel and diesel fuel usage for overall performance except a little performance drop at high speed and more fuel consumption. However, unique fuel properties of ethanol in lower viscosity, higher heat of vaporization, and higher auto ignition temperature effect on better fuel atomization and higher peak of heat release. Moreover, more oxygen content promotes more complete combustion. As a result, Smoke or PM emission from BE20 can be reduced more than 50% compared with base biodiesel combustion.

For PM morphology and nanostructure investigation, there is no obvious difference among appearance, size, and source of PM in agglomerated level, while primary particles hint some difference among BE20, B100, and diesel's soot in the level of carbon fringe. The carbon fringe images derived from the image processing method reveal that one carbon fringe structure might be referred to only one graphene sheet. BE20's soot tends to have smaller carbon fringe of 0.99 nm compared with B100's (1.35 nm) and diesel's (1.45 nm). An adoption of conceptual model about carbon atom arrangement in hexagonal structure can support to find the relationships between the carbon fringe structure and amount of carbon atoms. Accordingly, carbon atom density for each type of soot can be accurately estimated. BE20's soot also shows lowest value of carbon atom density of 88.28 atoms/nm^3.

In the final part, PM oxidation kinetics was investigated. Oxidation parameters of Activation energy, Soot reaction order, and Particle collision frequency factor were determined from soot oxidation by TGA. Considering all parameters together, it is reasonable that diesel's PM is more difficult to oxidize than BE20's and B100's PM.

This material is reserved for educational use only, not allowed for commercial use.

Forbidden to modify the content, and cite the document when use.

Relationships between PM nanostructure and PM oxidation kinetics were also studied. From the analysis, it can be found that smaller carbon fringe structure relates to lower activation energy (E_a) in BE20's soot oxidation by the mechanism of active OH- or O- functional groups. Carbon atom density tends to be a representative of the particle collision frequency factor (A). For the obscure parameter of soot reaction order (n), as referred from Shrinking Core model, it can be comparatively considered as outer surface of the primary particles.

To improve quality in this field of research, there are 3 main aspects should be considered for further improvement. 1) The engine for PM generation should be modified, especially accuracy of fuel injection timing and amount, so that the experimental results at each operating condition can be compared correctly. 2) Other approaches for soot particle size determination should be studied. Currently applied methods yield quite low reliability which is difficult to compare or analyze the results with other researches. 3) TGA experiment should be able to apply with variable oxygen condition. This would result in higher accuracy of oxidation kinetics parameter analysis.

This material is reserved for educational use only, not allowed for commercial use.
Forbidden to modify the content, and cite the document when use.

REFERENCES

1. Energy in Transportation, http://energy4me.org/all-about-energy/energy-technology/energy-in-transportation/
2. Transportation sector energy consumption, https://www.eia.gov/outlooks/ieo/transportation.php
3. J.B. Heywood, Internal Combustion Engine Fundamental, *McGraw-Hill series in Mechanical Engineering*, (1998)
4. Emission standard, https://www.dieselnet.com/standards/eu/ld.php#intro
5. L. Zhu, C.S. Cheung, W.G. Zhang, and Z. Huang, Combustion, performance and emission characteristics of a DI diesel engine fueled with ethanol–biodiesel blends, *Fuel*, 90(5), 1743-1750, (2011), DOI: 10.1016/j.fuel.2011.01.024
6. A. Ramadhas, S. Jayaraj, and M. Chandrasekharan, Use of vegetable oils as I.C. engine fuels - *A review*, *Renewable Energy*, 29, 727-742, (2004), DOI: 10.1016/j.renene.2003.09.008.
7. M. S. Graboski, and R. L. McCormick, Combustion of fat and vegetable oil derived fuels in diesel engines, *Progress in Energy and Combustion Science*, 24(2), pp.125-164, (1998)
8. Office of Energy Efficiency & Renewable Energy, https://energy.gov/eere/energybasics/articles/ethanol-fuel-basics
9. Ethanol-Diesel Blends, https://www.dieselnet.com/tech/fuel_ediesel.php
10. P. Karin, J. Boonsakda, K. Siricholathum, E. Saenkhumvong, C. Charoenphonphanich, and K. Hanamura, Morphology and oxidation kinetics of CI engine's biodiesel particulate matters on cordierite Diesel Particulate Filters using TGA, *International Journal of Automotive Technology*, 18(1), pp.31-40, (2016)
11. K. Siricholathum, P. Karin, C. Charoenphonphanich, K. Hanamura, and N. Chollacoop, Characterization of Biodiesel Particle Emission in Trapping and Regeneration Processes on Cordierite Diesel Particulate Filter, *JSAE/SAE 2015 Small Engine Technologies Conference & Exhibition*, No.2015-32-0821
12. Diesel Engines, http://carenginecooling.blogspot.com/2012/07/diesel-engines-dieselengine-also-known.html
13. Diesel-Engine Management: An Overview, The Bosch Yellow Jackets Edition 2003. Expert Know-How on Automotive Technology. Diesel-Engine

This material is reserved for educational use only, not allowed for commercial use.
Forbidden to modify the content, and cite the document when use.

Management, Published by:© Robert Bosch GmbH, 2003 Postfach 1129, D-73201 Plochingen. Automotive Aftermarket Business Sector, Department of Product Marketing Diagnostics &Test Equipment (AA/PDT5)

14. J. Dec, A Conceptual Model of DI Diesel Combustion Based on Laser-Sheet Imaging*, *SAE Technical Paper,* No.970873, (1997), DOI: 10.4271/970873
15. D. B. Kittelson, Engines and nanoparticles: A review. *J. Aerosol Science*, 29(5-6), 575−588, (1998)
16. Alternative Fuels, https://www.fueleconomy. gov/feg/current.shtml
17. Biofuels, http://www.renewableenergyworld.com/bioenergy/tech/biofuels.html
18. J.V. Gerpen, Biodiesel processing and production, *Fuel Processing Technology*, 2015.86: p. 1097– 1107
19. Ethanol: Formula and Structure, http://study.com/academy/lesson/what-is-ethanol-formula-structure-uses.html
20. Schematics of scanning electron microscopy operation , http://li155-94.members.linode.com/myscope/sem/practice/principles/layout.php
21. Schematics of transmission electron microscopy operation, http://www.hk-phy.org/atomic_world/tem/tem02_e.html
22. S. Akhtar, Transmission Electron Microscopy of Graphene and Hydrated Biomaterial Nanostructures, Uppsala, Acta Universitatis Upsaliensis, (2012)
23. Types of Thermo Gravimetric Analysis TGA, http://pakinfohub.com/types-of-thermo-gravimetric-analysis-tga/
24. Schematics of thermogravimetric analysis operation, https://www.google.co.th/search?q=principles++of+thermogravimetric+analysis+(tga)&biw=1920&bih=979&source=lnms&tbm=isch&sa=X&ved=0ahUKEwjvv5vTlLfNAhWJso8KHcwxBy04ChD8BQgGKAE#imgrc=8yyDqR1PWu02JM%3A
25. K. Cheenkachorn, B. Fungtammasan, Biodiesel as an Additive for Diesohol, *International Journal of Green Energy*, 6(1), pp.57-72, (2009)
26. C.-Y. Lin, K.-H. Wang, The fuel properties of three phase emulsions as an alternative fuel for diesel engines, *Fuel*, 82, pp. 1367-1375, (2003)
27. P. Kwanchareon, A. Luengnaruemitchai, and S. Jai-In, Solubility of a diesel–biodiesel–ethanol blend, its fuel properties, and its emission characteristics from diesel engine, *Fuel*, 86(7-8), pp.1053-1061, (2007)

This material is reserved for educational use only, not allowed for commercial use.
Forbidden to modify the content, and cite the document when use.

28. D.B. Hulwan, and S.V. Joshi, Performance, emission and combustion characteristic of a multicylinder DI diesel engine running on diesel–ethanol–biodiesel blends of high ethanol content, *Applied Energy*, 88(12), pp.5042-5055, (2011)
29. W. Tutak, A. Jamrozik, M. Pyrc, and M. Sobiepański, A comparative study of co-combustion process of diesel-ethanol and biodiesel-ethanol blends in the direct injection diesel engine, *Applied Thermal Engineering*, 117, pp.155-163, (2017)
30. L. Zhu, C.H. Cheung, W. Zhang, and Z. Huang, Combustion, performance and emission characteristics of a DI diesel engine fueled with ethanol–biodiesel blends. *Fuel*, 90(5), pp.1743-1750, (2011).
31. P. Eastwood, Particulate Emissions From Vehicles, Chichester, John Wiley, (2008)
32. M.M. Maricq, Review Chemical Characterization of particulate emissions from diesel engine: A review, *Journal of Aerosal Science*, 2007. 38: p. 1079-1118
33. H. Wang, and M. Frenklach, A detailed kinetic modeling study of aromatics formation in laminar premixed acetylene and ethylene flames, *Combustion and Flame*, 110:173-221
34. O. I. Smith, Fundamentals of soot formation in flames with application to diesel engine particulate emissions, *Progress in Energy and Combustion Science*, 7:275-291
35. P. Karin, Y. Songsaengchan, S. Laosuwan, C. Charoenphonphanich, N. Chollacoop, and K. Hanamura, Physical characterization of biodiesel particle emission by electron microscopy, SAE Technical Papers 2013
DOI: 10.4271/2013-32-9150
36. W. H. Lipkea, J.H. Johnson, and C.T. Vuk, The physical and chemical character of diesel particulate emissions – measurement techniques and fundamental considerations, *Society of Automotive Engineers*, 780108
37. A. Braun, F.E. Huggins, S. Seifert, J. Ilafsky, N. Shah, K.E. Kelly, A. Sharofim, and G.P. Huffman, Size-range analysis of diesel soot with ultra-small angle X-ray scattering, *Combustion and Flame*, 137:63-72, (2004)
38. V. Fernandez-Alos, J. Watson, R. Vander Wal, and J. Mathews, Soot and char molecular representations generated directly from HRTEM lattice fringe images using Fringe3D, *Combustion and Flame*, 158(9), pp.1807-1813, (2011)

This material is reserved for educational use only, not allowed for commercial use.
Forbidden to modify the content, and cite the document when use.

39. K. Yehliu, G. Lilik, R. Vander Wal, C. Sun, and A. Boehman, Impacts of advanced diesel combustion operation on soot nanostructure and reactivity, *International Journal of Engine Research*, 18(5-6), pp.532-542, (2016)
40. A. Williams, S. Black, and R.L. McCormick, Biodiesel Fuel Property Effects on Particulate Matter Reactivity, *6th International Exhaust Gas and Particulate Emissions Forum sponsored by AVL*, Ludwigsburg, Germany, March 9-10, 2010
41. J. Neeft, Kinetics of the oxidation of diesel soot, *Fuel*, 76(12), pp.1129-1136, (1997)
42. P. Karin, J. Boonsakda, K. Siricholathum, E. Saenkhumvong, C. Charoenphonphanich, and K. Hanamura, Morphology and oxidation kinetics of CI engine's biodiesel particulate matters on cordierite Diesel Particulate Filters using TGA, *International Journal of Automotive Technology*, 18(1), pp.31-40, (2016)
43. J. Hamada, K. Nakamura, T. Uenishi, T. Fukuma, J. Kusaka, D. Yamashita, S. Hoshi, and A. Satsuma, Research on internal transfer phenomena of the diesel particulate filter(Sixth report) – A study on the effect of engine operating condition at soot loading on PM structure and the oxidation rate, *2017 JSAE Annual Congress (Spring), Pacifico*, Yokohama, No.20175171
44. K. Leistner, Experimental and Modelling Study of Catalytic Diesel Soot Oxidation, (2012)

This material is reserved for educational use only, not allowed for commercial use.
Forbidden to modify the content, and cite the document when use.

APPENDIX A :

FUEL AND EMISSION STANDARD

A-1 : Diesel fuel

รายละเอียดแนบท้ายประกาศกรมธุรกิจพลังงาน
เรื่อง กำหนดลักษณะและคุณภาพของน้ำมันดีเซล (ฉบับที่ ๕)
พ.ศ. ๒๕๕๔

รายการ	ข้อกำหนด	อัตราสูงต่ำ	น้ำมันดีเซล		วิธีทดสอบ[๔]
			หมุนเร็ว	หมุนช้า	
1	ความถ่วงจำเพาะ ณ อุณหภูมิ 15.6/15.6 *องศาเซลเซียส* (Specific Gravity at 15.6/15.6 °C)	ไม่ต่ำกว่า และ	0.81	-	ASTM D 1298
		ไม่สูงกว่า	0.87	0.920	
2	จำนวนซีเทน (Cetane Number) หรือ				ASTM D 613
	ดัชนีซีเทน (Calculated Cetane Index)				ASTM D 976
	ก่อนวันที่ 1 มกราคม พ.ศ. 2555	ไม่ต่ำกว่า	47	45	
	ตั้งแต่วันที่ 1 มกราคม พ.ศ. 2555 เป็นต้นไป	ไม่ต่ำกว่า	50	45	
3	ความหนืด (Viscosity, *เซนติสโตกส์* (*cSt*))				ASTM D 445
	3.1 ณ อุณหภูมิ 40 *องศาเซลเซียส* (at 40 °C)	ไม่ต่ำกว่า และ	1.8	-	
		ไม่สูงกว่า	4.1	8.0	
	หรือ				
	3.2 ณ อุณหภูมิ 50 *องศาเซลเซียส* (at 50 °C)	ไม่สูงกว่า	-	6.0	
4	จุดไหลเท (Pour Point, *องศาเซลเซียส* (°C))	ไม่สูงกว่า	10	16	ASTM D 97
5	กำมะถัน (Sulphur, *ร้อยละโดยน้ำหนัก* (%wt.))				
	ก่อนวันที่ 1 มกราคม พ.ศ. 2555	ไม่สูงกว่า	0.035	1.5	ASTM D 4294
	ตั้งแต่วันที่ 1 มกราคม พ.ศ. 2555 เป็นต้นไป	ไม่สูงกว่า	0.005	1.5	ASTM D 2622
6	การกัดกร่อนแผ่นทองแดง (Copper Strip Corrosion)	ไม่สูงกว่า	หมายเลข 1	-	ASTM D 130
7	เสถียรภาพต่อการเกิดปฏิกิริยาออกซิเดชัน (Oxidation Stability, *กรัม/ลูกบาศก์เมตร* (g/m^3))	ไม่สูงกว่า	25	-	ASTM D 2274
8	กากถ่าน (Carbon Residue, *ร้อยละโดยน้ำหนัก* (%wt.))	ไม่สูงกว่า	0.05	-	ASTM D 189
9	น้ำและตะกอน (Water and Sediment, *ร้อยละโดยปริมาตร* (%vol.))	ไม่สูงกว่า	0.05	0.3	ASTM D 2709
10	เถ้า (Ash, *ร้อยละโดยน้ำหนัก* (%wt.))	ไม่สูงกว่า	0.01	0.02	ASTM D 482

(ต่อ -๒-)

This material is reserved for educational use only, not allowed for commercial use.
Forbidden to modify the content, and cite the document when use.

รายการ	ข้อกำหนด		อัตราสูงต่ำ	น้ำมันดีเซล		วิธีทดสอบ[1/]
				หมุนเร็ว	หมุนช้า	
11	จุดวาบไฟ (Flash Point,	*องศาเซลเซียส* ($^{\circ}C$)	ไม่ต่ำกว่า	52	52	ASTM D 93
12	การกลั่น (Distillation,	*องศาเซลเซียส* ($^{\circ}C$)				ASTM D 86
	อุณหภูมิของส่วนที่กลั่นได้โดยปริมาตรในอัตราร้อยละเก้าสิบ (90% recovered)		ไม่สูงกว่า	357	-	
13	โพลีไซคลิก อะโรมาติก ไฮโดรคาร์บอน (Polycyclic Aromatic Hydrocarbon,	*ร้อยละโดยน้ำหนัก* *% wt.)*				ASTM D 2425
	ก่อนวันที่ 1 มกราคม พ.ศ. 2555		-	-	-	
	ตั้งแต่วันที่ 1 มกราคม พ.ศ. 2555 เป็นต้นไป		ไม่สูงกว่า	11	-	
14	สี (Colour)			-		
	14.1 ชนิดของสี (Hue)			เหลือง	น้ำตาล	
	14.2 ความเข้มของสี (Intensity)		ไม่ต่ำกว่า	-	4.5	ASTM D 1500
			และ ไม่สูงกว่า	4.0	7.5	
15	ไบโอดีเซลประเภทเมทิลเอสเตอร์ของกรดไขมัน (Methyl Ester of Fatty Acid,	*ร้อยละโดยปริมาตร* *%vol.)*	ไม่ต่ำกว่า และ ไม่สูงกว่า	3 5	-	EN 14078
16	คุณสมบัติการหล่อลื่น รอยขีดข่วน (Lubricity , Wear Scar	*ไมโครเมตร* *(μm)*	ไม่สูงกว่า	460	-	CEC F – 06 - 96
17	สารเติมแต่ง (ถ้ามี) (Additive)		ให้เป็นไปตามที่ได้รับความเห็นชอบจากอธิบดีกรมธุรกิจพลังงาน			

หมายเหตุ 1/ วิธีทดสอบอาจใช้วิธีอื่นที่เทียบเท่าก็ได้ แต่ในกรณีที่มีข้อโต้แย้งให้ใช้วิธีที่กำหนดในรายละเอียดแนบท้ายนี้

This material is reserved for educational use only, not allowed for commercial use.
Forbidden to modify the content, and cite the document when use.

A-2 : Biodiesel fuel

รายละเอียดแนบท้ายประกาศกรมธุรกิจพลังงาน

เรื่อง กำหนดลักษณะและคุณภาพของไบโอดีเซลประเภทเมทิลเอสเตอร์ของกรดไขมัน

พ.ศ. ๒๕๕๒

รายการ	ข้อกำหนด		อัตราสูงต่ำ		วิธีทดสอบ [1]
1	เมทิลเอสเตอร์ (Methyl Ester,	*ร้อยละโดยน้ำหนัก % wt.)*	ไม่ต่ำกว่า	96.5	EN 14103
2	ความหนาแน่น ณ อุณหภูมิ 15 °ซ (Density at 15 °C,	*กิโลกรัม/ลูกบาศก์เมตร kg/m ^{3})*	ไม่ต่ำกว่า และ ไม่สูงกว่า	860 900	ASTM D 1298
3	ความหนืด ณ อุณหภูมิ 40 °ซ (Viscosity at 40 °C,	*เซนติสโตกส์ cSt)*	ไม่ต่ำกว่า และ ไม่สูงกว่า	3.5 5.0	ASTM D 445
4	จุดวาบไฟ (Flash Point,	*องศาเซลเซียส °C)*	ไม่ต่ำกว่า	120	ASTM D 93
5	กำมะถัน (Sulphur,	*ร้อยละโดยน้ำหนัก %wt.)*	ไม่สูงกว่า	0.0010	ASTM D 2622
6	กากถ่าน (ร้อยละ 10 ของกากที่เหลือจากการกลั่น) (Carbon Residue , on 10 % distillation residue,	*%wt)*	ไม่สูงกว่า	0.30	ASTM D 4530
7	จำนวนซีเทน (Cetane Number)		ไม่ต่ำกว่า	51	ASTM D 613
8	เถ้าซัลเฟต (Sulphated Ash,	*ร้อยละโดยน้ำหนัก %wt.)*	ไม่สูงกว่า	0.02	ASTM D 874
9	น้ำ (Water,	*ร้อยละโดยน้ำหนัก wt.)*	ไม่สูงกว่า	0.050	EN ISO 12937
10	สิ่งปนเปื้อนทั้งหมด (Total Contaminate,	*ร้อยละโดยน้ำหนัก %wt.)*	ไม่สูงกว่า	0.0024	EN 12662
11	การกัดกร่อนแผ่นทองแดง (Copper Strip Corrosion)		ไม่สูงกว่า	หมายเลข 1	ASTM D 130
12	เสถียรภาพต่อการเกิดปฏิกิริยาออกซิเดชั่น ณ อุณหภูมิ 110 องศาเซลเซียส (Oxidation Stability at 110 °C,	*ชั่วโมง hours)*	ไม่ต่ำกว่า	10	EN 14112

(ต่อ-2-)

This material is reserved for educational use only, not allowed for commercial use.
Forbidden to modify the content, and cite the document when use.

รายการ	ข้อกำหนด		อัตราสูงต่ำ		วิธีทดสอบ [1/]
13	ค่าความเป็นกรด (Acid Value ,	*มิลลิกรัมโปตัสเซียมไฮดรอกไซด์/กรัม mg KOH/g)*	ไม่สูงกว่า	0.50	ASTM D 664
14	ค่าไอโอดีน (Iodine Value ,	*กรัมไอโอดีน/ 100 กรัม g Iodine / 100 g)*	ไม่สูงกว่า	120	EN 14111
15	กรดลิโนเลนิกเมทิลเอสเตอร์ (Linolenic Acid Methyl Ester ,	*ร้อยละโดยน้ำหนัก %wt.)*	ไม่สูงกว่า	12.0	EN 14103
16	เมทานอล (Methanol,	*ร้อยละโดยน้ำหนัก %wt.)*	ไม่สูงกว่า	0.20	EN 14110
17	โมโนกลีเซอไรด์ (Monoglyceride	*ร้อยละโดยน้ำหนัก %wt.)*	ไม่สูงกว่า	0.80	EN 14105
18	ไดกลีเซอไรด์ (Diglyceride ,	*ร้อยละโดยน้ำหนัก %wt)*	ไม่สูงกว่า	0.20	EN 14105
19	ไตรกลีเซอไรด์ (Triglyceride ,	*ร้อยละโดยน้ำหนัก %wt)*	ไม่สูงกว่า	0.20	EN 14105
20	กลีเซอรีนอิสระ (Free glycerin ,	*ร้อยละโดยน้ำหนัก %wt.)*	ไม่สูงกว่า	0.02	EN 14105
21	กลีเซอรีนทั้งหมด (Total glycerin,	*ร้อยละโดยน้ำหนัก %wt.)*	ไม่สูงกว่า	0.25	EN 14105
22	โลหะกลุ่ม 1 (โซเดียมและโปแตสเซียม) (Group I metals (Na+K),	*มิลลิกรัม/กิโลกรัม mg/kg)*	ไม่สูงกว่า	5.0	EN 14108 และ EN 14109
	โลหะกลุ่ม 2 (แคลเซียมและแมกนีเซียม) (Group II metals (Ca+Mg),	*มิลลิกรัม/กิโลกรัม mg/kg)*	ไม่สูงกว่า	5.0	pr EN 14538
23	ฟอสฟอรัส (Phosphorus,	*ร้อยละโดยน้ำหนัก %wt.)*	ไม่สูงกว่า	0.0010	ASTM D 4951
24	สารเติมแต่ง (ถ้ามี) (Additive)		ให้เป็นไปตามที่ได้รับความเห็นชอบจากอธิบดีกรมธุรกิจพลังงาน		

หมายเหตุ 1/ วิธีทดสอบอาจใช้วิธีอื่นที่เทียบเท่าก็ได้ แต่ในกรณีที่มีข้อโต้แย้งให้ใช้วิธีที่กำหนดในรายละเอียดแนบท้ายนี้

This material is reserved for educational use only, not allowed for commercial use.
Forbidden to modify the content, and cite the document when use.

A-3 : Thailand emission standards for small diesel engine vehicle

ประกาศกระทรวงอุตสาหกรรม

ฉบับที่ ๔๓๕๔ (พ.ศ. ๒๕๕๔)

ออกตามความในพระราชบัญญัติมาตรฐานผลิตภัณฑ์อุตสาหกรรม

พ.ศ. ๒๕๑๑

เรื่อง กำหนดมาตรฐานผลิตภัณฑ์อุตสาหกรรม

รถยนต์ขนาดเล็กที่ใช้เครื่องยนต์แบบจุดระเบิดด้วยการอัด เฉพาะด้านความปลอดภัย : สารมลพิษจากเครื่องยนต์ ระดับที่ 7

หน่วยเป็น g/km

ประเภทรถยนต์	มวลอ้างอิง (kg)	คาร์บอนมอนอกไซด์	ออกไซด์ของไนโตรเจน	ไฮโดรคาร์บอนรวมกับออกไซด์ของไนโตรเจน	สารมลพิษอนุภาค
รถยนต์นั่ง มวลเต็มอัตราบรรทุกไม่เกิน 2 500 kg	-	0.50	0.25	0.30	0.025
รถยนต์นั่งมวลเต็มอัตราบรรทุกเกิน 2 500 kg หรือรถยนต์บรรทุกและรถยนต์นั่งที่ดัดแปลงมาจากรถยนต์บรรทุกที่มีมวลเต็มอัตราบรรทุกไม่เกิน 3 500 kg	ไม่เกิน 1 305	0.50	0.25	0.30	0.025
	เกิน 1 305 แต่ไม่เกิน 1 760	0.63	0.33	0.39	0.04
	เกิน 1 760	0.74	0.39	0.46	0.06

This material is reserved for educational use only, not allowed for commercial use.
Forbidden to modify the content, and cite the document when use.

APPENDIX B :

FUEL TEST REPORT

B-1 : CHN analysis

CHN Analysis Result No. 591110-1025

Sample	น้ำมันพื้นฐานดีเซล
Sample Owner	Park Watanawongskorn
Objective	To quantitate percentages of C, H and N elements.
Instrument	CHNS/O Analyzer (Thermo Scientific™ FLASH 2000)
Method	Gaseous products freed by pyrolysis in high-purity oxygen and were chromatographically separated by elution development with quantitatively detected by thermal conductivity detector.
Analysis Date	November 1, 2016

Result

Sample No.	Sample Name		%Carbon	%Hydrogen	%Nitrogen
591110 1025_1	DIESEL	(1)	82.91	13.60	0.00
		(2)	83.64	13.85	0.00
		average	**83.28**	**13.73**	**0.00**
591110 1025_2	B100	(1)	73.88	12.33	0.00
		(2)	75.18	12.60	0.00
		average	**74.53**	**12.47**	**0.00**
591110 1025_3	HVO	(1)	82.12	15.18	0.00
		(2)	81.81	15.07	0.00
		average	**81.97**	**15.13**	**0.00**
591110 1025_4	HSD	(1)	83.17	13.33	0.00
		(2)	83.04	13.46	0.00
		average	**83.11**	**13.40**	**0.00**
591110 1025_5	HSD HN	(1)	82.94	13.61	0.00
		(2)	82.76	13.48	0.00
		average	**82.85**	**13.55**	**0.00**

Amporn Eongprakornkeaw

(Miss. Amporn Eongprakornkeaw)

Analyst

Sunan R.

(Mrs. Sunan Rangseekansong)

Chief Scientist

King Mongkut's Institute of Technology Ladkrabang

This material is reserved for educational use only, not allowed for commercial use.
Forbidden to modify the content, and cite the document when use.

B-2 : Heating value

ผลการวิเคราะห์ค่าพลังงานความร้อนด้วยเครื่อง Bomb Calorimeter AC - 500

โดยศูนย์เครื่องมือวิจัยวิทยาศาสตร์และเทคโนโลยี จุฬาลงกรณ์มหาวิทยาลัย

ตัวอย่าง : น้ำมันเชื้อเพลิง

รหัสงาน : 590411-1175

เจ้าของตัวอย่าง : ภาคย์ วัฒนวงศกร

สถาบันเทคโนโลยีพระจอมเกล้าเจ้าคุณทหารลาดกระบัง

ชื่อตัวอย่าง	ค่าความร้อน (cal/g)		
	วัดครั้งที่ 1	วัดครั้งที่ 2	ค่าเฉลี่ย
E100	6776.0	6756.4	6766.2
B100	9483.8	9396.7	9440.3
HSD	10920.6	10942.8	10931.7
HSD-HN	10855.9	10882.2	10869.1
DIESEL	10981.8	11077.6	11029.7

นางอารี ลิ่มนิรันดร

เจ้าหน้าที่วิเคราะห์

This material is reserved for educational use only, not allowed for commercial use.
Forbidden to modify the content, and cite the document when use.

B-3 : Auto ignition temperature (Diesel)

FOCUSLAB™ Fluid & Oil Analysis Technology

ISO 9001 : 2008 Certified

Customer Code	: 20010	Sample Information	
Customer Name	: KMITL	Unit ID / Sample Information Identification	: Diesel / Fuel Oil
Address	: 3 Moo 2, Chalongkrung Road Ladkrabang Bangkok 10520	Oil Type/Viscosity	: not given
Test Code	: 62100		

Test Report Sample No 369208

Test Description	Test Method	Unit	Test Result	Limit
Auto Ignition	ASTM E 659	C	288	-

Note : The result(s) issued in this report only reflected the analysis of the sample(s) submitted.
Test Result Data Interpretation is not available .
Limit of test parameters are not available .

Tested and Issued By

Kanjana K.
Lab Technologist

Approved and Authorised by

Somchai J.
Machine Lubricant Analyst

This material is reserved for educational use only, not allowed for commercial use.
Forbidden to modify the content, and cite the document when use.

B-4 : Auto ignition temperature (Biodiesel)

FOCUSLAB™ Fluid & Oil Analysis Technology

ISO 9001 : 2008 Certified

Customer Code : 20010
Customer Name : KMITL
Address : 3 Moo 2, Chalongkrung Road
Ladkrabang Bangkok 10520

Test Code : 62100

Sample Information

Unit ID / Sample Information Identification : B100 Fuel Oil

Oil Type/Viscosity : not given

Test Report Sample No 369205

Test Description	Test Method	Unit	Test Result	Limit
Auto Ignition	ASTM E 659	C	294	-

Note : The result(s) issued in this report only reflected the analysis of the sample(s) submitted.
Test Result Data Interpretation is not available .
Limit of test parameters are not available .

Tested and Issued By

Kanjana K.
Lab Technologist

Approved and Authorised by

Somchai J.
Machine Lubricant Analyst

This material is reserved for educational use only, not allowed for commercial use.
Forbidden to modify the content, and cite the document when use.

APPENDIX C :

CARBON HEXAGONAL STRUCTURE

No. of Carbon ring	Carbon ring Shape	No. of Carbon atoms	Possible plate length			Remark :	
			Dim.	parameter	value		
1		6	①	2S cos30	2.461244	s =	1.42
			②	2S	2.842000	s cos30 =	1.23062
			③			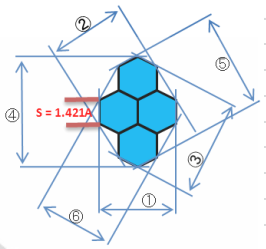	
			④				
			⑤				
			⑥				
				Average	2.651622		
2		10	①	4S cos30	4.922488		
			②	3.5S	4.973500		
			③	3S cos30	3.691866		
			④	2S	2.842000		
			⑤	same as Dim3			
			⑥	same as dim2			
				Average	4.107464		
3		13	①	4S cos30	4.922488	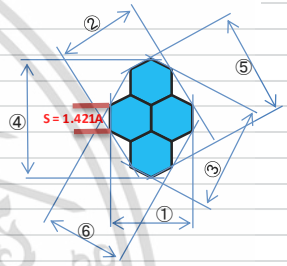	
			②	3.5S	4.973500		
			③	same as dim1			
			④				
			⑤				
			⑥				
				Average	4.947994		
4		16	①	4S cos30	4.922488		
			②	3.5S	4.973500		
			③	5S cos30	6.153110		
			④	5S	7.105000		
			⑤	same as dim3			
			⑥	same as dim2			
				Average	5.788525		
5	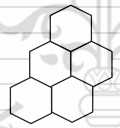	19	①	5S cos30	6.153110		
			②	5S	7.105000		
			③	6S cos30	7.383733		
			④	same as dim2			
			⑤	same as dim1			
			⑥	3.5S	4.973500		
				Average	6.403836		
6	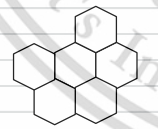	22	①	6S cos30	7.383733		
			②	5S	7.105000		
			③	same as dim1			
			④	5S	7.105000		
			⑤	5S cos30	6.153110		
			⑥	same as dim4			
				Average	6.936711		
7	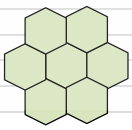	24	①	6S cos30	7.383733		
			②	5S	7.105000		
			③	same as dim1			
			④	same as dim2			
			⑤				
			⑥				
				Average	7.244366		
8	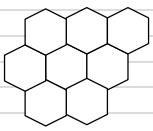	27	①	7S cos30	8.614355		
			②	6.5S	9.236500		
			③	samw as dim1			
			④	5S	7.105000		
			⑤	6S cos30	7.383733		
			⑥	same as dim4			
				Average	8.084897		

This material is reserved for educational use only, not allowed for commercial use.
Forbidden to modify the content, and cite the document when use.

No. of Carbon	Carbon ring Shape	No. of Carbon	Possible plate length			Remark :
			Dim.	parameter	value	
9	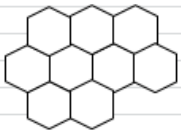	30	①	8S cos30	9.844977	
			②	6.5S	9.236500	
			③	7S cos30	8.614355	
			④	5S	7.105000	
			⑤	6S cos30	7.383733	
			⑥	6.5S	9.236500	
				Average	8.570177	
10	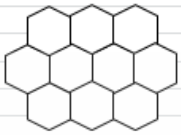	32	①	8S cos30	9.844977	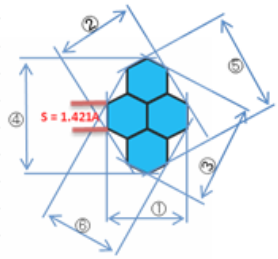
			②	6.5S	9.236500	
			③	7S cos30	8.614355	
			④	5S	7.105000	
			⑤	same as dim3		
			⑥	same as dim2		
				Average	8.700208	
11	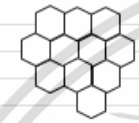	35	①	8S cos30	9.844977	
			②	6.5S	9.236500	
			③	7S cos30	8.614355	
			④	6.5S	9.236500	
			⑤	8S cos30	9.844977	
			⑥	6.5S	9.236500	
				Average	9.335635	
12		37	①	8S cos30	9.844977	
			②	6.5S	9.236500	
			③	8S cos30	9.844977	
			④	6.5S	9.236500	
			⑤	same as dim3		
			⑥	same as dim2		
				Average	9.540738	
13		40	①	8S cos30	9.844977	
			②	8S	11.368000	
			③	9S cos30	11.075599	
			④	6.5S	9.236500	
			⑤	8S cos30	9.844977	
			⑥	6.5S	9.236500	
				Average	10.101092	
14		42	①	9S cos30	11.075599	
			②	8S	11.368000	
			③	9S cos30	11.075599	
			④	6.5S	9.236500	
			⑤	8S cos30	9.844977	
			⑥	6.5S	9.236500	
				Average	10.306196	

No. of Carbon	Carbon ring Shape	No. of Carbon	Possible plate length			Remark :
			Dim.	parameter	value	
15	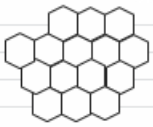	45	①	10S cos30	12.306221	
			②	8S	11.368000	
			③	9S cos30	11.075599	
			④	6.5S	9.236500	
			⑤	8S cos30	9.844977	
			⑥	8S	11.368000	
				Average	10.866549	
16	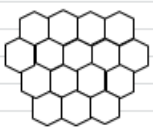	47	①	10S cos30	12.306221	
			②	8S	11.368000	
			③	9S cos30	11.075599	
			④	6.5S	9.236500	
			⑤	same as dim3		
			⑥	same as dim2		
				Average	10.996580	

This material is reserved for educational use only, not allowed for commercial use.
Forbidden to modify the content, and cite the document when use.

No. of Carbon	Carbon ring Shape	No. of Carbon	Possible plate length			Remark :
			Dim.	parameter	value	
17	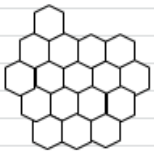	50	①	10S cos30	12.306221	
			②	8S	11.368000	
			③	9S cos30	11.075599	
			④	8S	11.368000	
			⑤	10S cos30	12.306221	
			⑥	8S	11.368000	
				Average	11.632007	
18	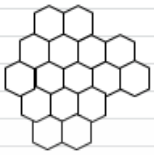	52	①	10S cos30	12.306221	
			②	8S	11.368000	
			③	9S cos30	11.075599	
			④	8S	11.368000	
			⑤	10S cos30	12.306221	
			⑥	8S	11.368000	
				Average	11.632007	
19	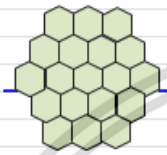	54	①	10S cos30	12.306221	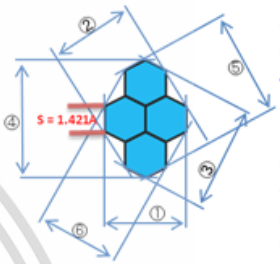
			②	8S	11.368000	
			③	same as dim1		
			④	same as dim2		
			⑤			
			⑥			
				Average	11.837110	
23		64	①	12S cos30	14.767465	
			②	9.5S	13.499500	
			③	11S cos30	13.536843	
			④	8S	11.368000	
			⑤	10S cos30	12.306221	
			⑥	9.5S	13.499500	
				Average	13.162922	
27		73	①	12S cos30	14.767465	
			②	9.5S	13.499500	
			③	12S cos30	14.767465	
			④	9.5S	13.499500	
			⑤	same as dim3		
			⑥	same as dim2		
				Average	14.133483	
30		80	①	13S cos30	15.998087	
			②	11S	15.631000	
			③	13S cos30	15.998087	
			④	9.5S	13.499500	
			⑤	12S cos30	14.767465	
			⑥	9.5S	13.499500	
				Average	14.898940	
33	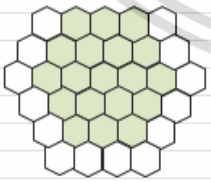	87	①	14S cos30	17.228709	
			②	11S	15.631000	
			③	13S cos30	15.998087	
			④	9.5S	13.499500	
			⑤	13S cos30	15.998087	
			⑥	11S	15.631000	
				Average	15.664397	
37	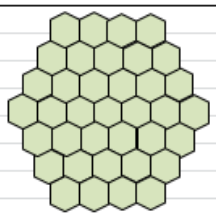	96	①	14S cos30	17.228709	
			②	11S	15.631000	
			③	same as dim1		
			④	same as dim2		
			⑤			
			⑥			
				Average	16.429855	

This material is reserved for educational use only, not allowed for commercial use.
Forbidden to modify the content, and cite the document when use.

No. of Carbon	Carbon ring Shape	No. of Carbon	Possible plate length			Remark :
			Dim.	parameter	value	
40	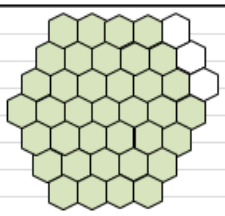	103	①	15S cos30	18.459331	
			②	12.5S	17.762500	
			③	15S cos30	18.459331	
			④	11S	15.631000	
			⑤	14S cos30	17.228709	
			⑥	11S	15.631000	
				Average	17.195312	
61	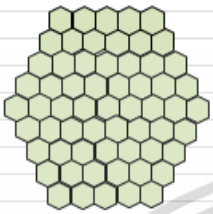	150	①	18S cos30	22.151198	
			②	14S	19.894000	
			③	same as dim1		
			④	same as dim2		
			⑤			
			⑥			
				Average	21.022599	
73	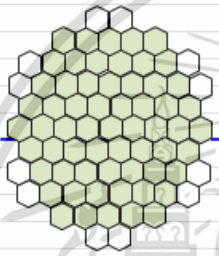	180	①	18S cos30	22.151198	
			②	17S	24.157000	
			③	same as dim1		
			④	same as dim2		
			⑤			
			⑥			
				Average	23.154099	
91	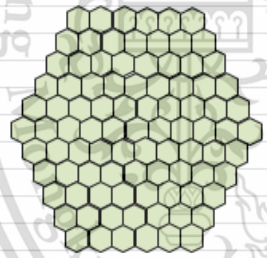	216	①	22S cos30	27.073686	
			②	17S	24.157000	
			③	same as dim1		
			④	same as dim2		
			⑤			
			⑥			
				Average	25.615343	
109	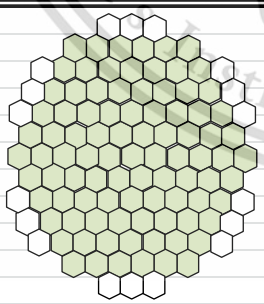	258	①	22S cos30	27.073686	
			②	20S	28.420000	
			③	same as dim1		
			④	same as dim2		
			⑤			
			⑥			
				Average	27.746843	

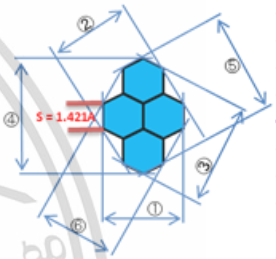

This material is reserved for educational use only, not allowed for commercial use.
Forbidden to modify the content, and cite the document when use.

No. of Carbon	Carbon ring Shape	No. of Carbon	Possible plate length			Remark :
			Dim.	parameter	value	
169	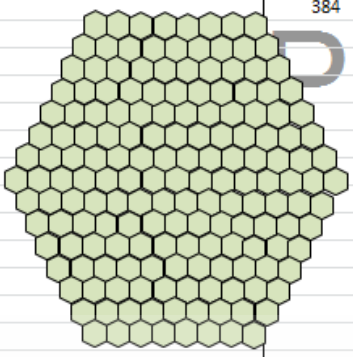	384	①	30S cos30	36.918663	
			②	23S	32.683000	
			③	same as dim1		
			④	same as dim2		
			⑤			
			⑥			
				Average	34.800831	
199	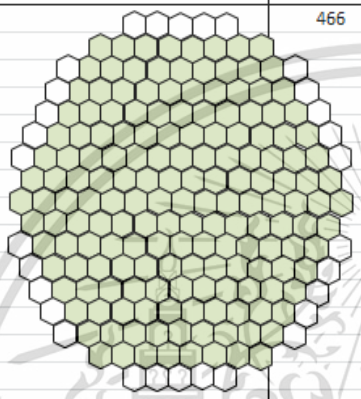	466	①	30S cos30	36.918663	
			②	26S	36.946000	
			③	same as dim1		
			④	same as dim2		
			⑤			
			⑥			
				Average	36.932331	
217	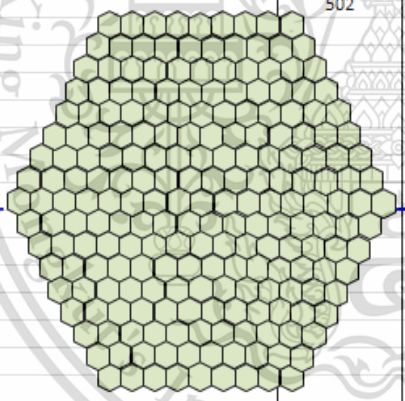	502	①	34S cos30	41.841151	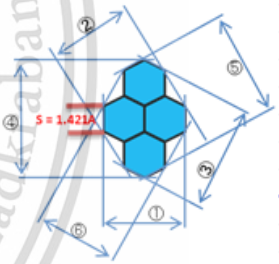
			②	26S	36.946000	
			③	same as dim1		
			④	same as dim2		
			⑤			
			⑥			
				Average	39.393576	
241	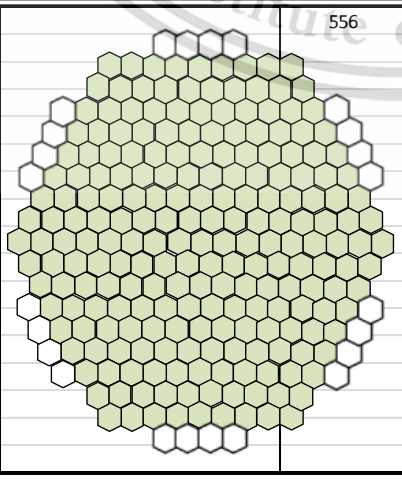	556	①	34S cos30	41.841151	
			②	29S	41.209000	
			③	same as dim1		
			④	same as dim2		
			⑤			
			⑥			
				Average	41.525076	

This material is reserved for educational use only, not allowed for commercial use.
Forbidden to modify the content, and cite the document when use.

No. of Carbon	Carbon ring Shape	No. of Carbon	Possible plate length			Remark :
			Dim.	parameter	value	
331	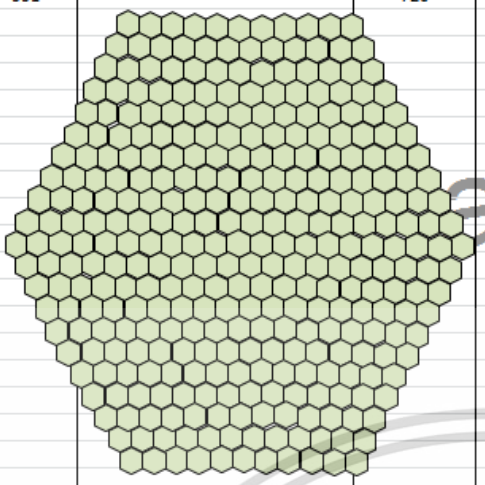	726	①	42S cos30	51.686128	
			②	32S	45.472000	
			③	same as dim1		
			④	same as dim2		
			⑤			
			⑥			
				Average	48.579064	
355	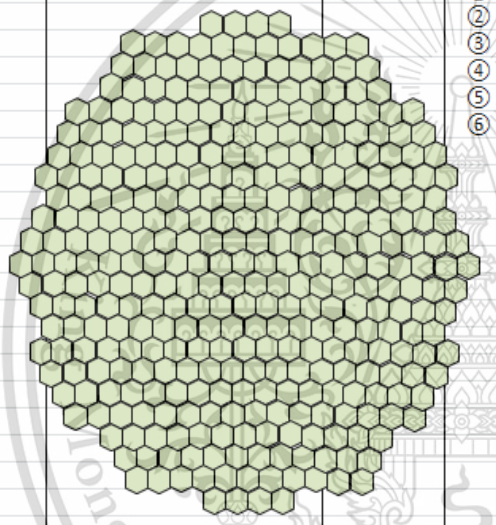	780	①	42S cos30	51.686128	
			②	35S	49.735000	
			③	same as dim1		
			④	same as dim2		
			⑤			
			⑥			
				Average	50.710564	

age 5

Mongkut's Institute of Technology Ladkrabang

This material is reserved for educational use only, not allowed for commercial use.
Forbidden to modify the content, and cite the document when use.

APPENDIX D :

TGA EXPARIMENTAL DATA

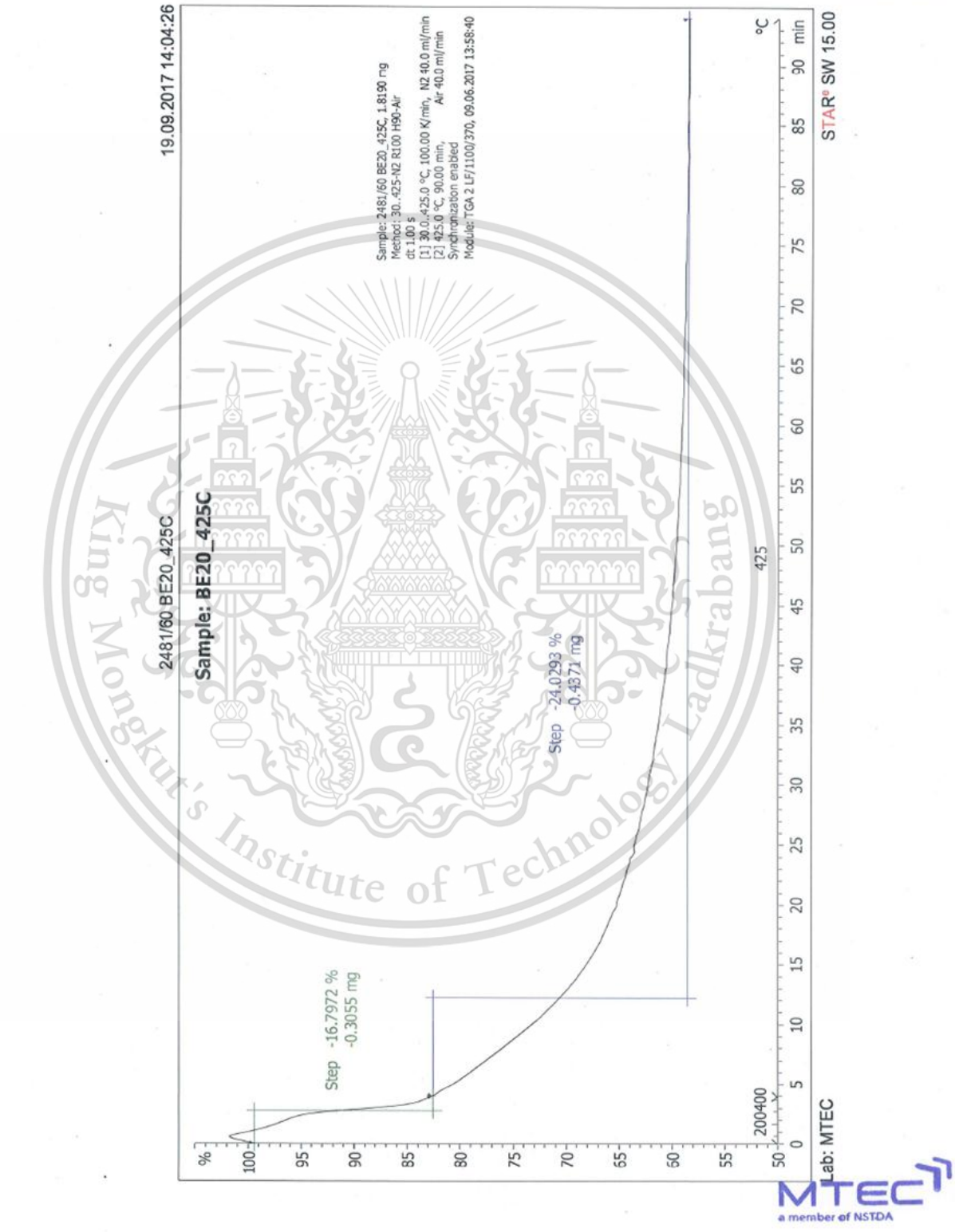

This material is reserved for educational use only, not allowed for commercial use.
Forbidden to modify the content, and cite the document when use.

This material is reserved for educational use only, not allowed for commercial use.
Forbidden to modify the content, and cite the document when use.

This material is reserved for educational use only, not allowed for commercial use.
Forbidden to modify the content, and cite the document when use.

This material is reserved for educational use only, not allowed for commercial use.
Forbidden to modify the content, and cite the document when use.

This material is reserved for educational use only, not allowed for commercial use.
Forbidden to modify the content, and cite the document when use.

This material is reserved for educational use only, not allowed for commercial use.
Forbidden to modify the content, and cite the document when use.

This material is reserved for educational use only, not allowed for commercial use.
Forbidden to modify the content, and cite the document when use.

This material is reserved for educational use only, not allowed for commercial use.
Forbidden to modify the content, and cite the document when use.

APPENDIX E :

PUBLICATIONS

This material is reserved for educational use only, not allowed for commercial use.
Forbidden to modify the content, and cite the document when use.

講演番号	168

文献番号	20175168

Impact of Diesel Engine Combustion Characteristics on Particulate Matter's Morphology and Nanostructure from Ethanol-blended Biodiesel

Park Watanawongskorn[1)*], Preechar Karin[1)], Chinda Charoenphonphanich[2)], Jiramed Boonsakda[1)], Katsunori Hanamura[3)], and Nuwong Chollacoop[4)]

1) International College, King Mongkut's Institute of Technology Ladkrabang, Chalongkrung Rd., Ladkrabang, Bangkok, 10520, Thailand (E-mail: park.wa@gmail.com)
2) Faculty of engineering, King Mongkut's Institute of Technology Ladkrabang
3) Department of Mechanical Engineering, Tokyo Institute of Technology
4) National Metal and Materials Technology Center, National Science and Technology Development Agency

ABSTRACT: Many biodiesel researchers have been revealed that biodiesel plays a key role in Particulate Matter (PM) reduction due to impact of effective oxygen function compared with diesel fuel. To reduce further PM emission, oxygenated fuel such as ethanol could be one of possible options. This research focused on effects of ethanol on PM's quantity and morphology by blending with biodiesel. The PM quantity from engine operation was inspected altogether with PM's nanostructure by SEM and TEM technique. Results from this research could be utilized for Diesel Particulate Filter development for ethanol-blended biodiesel fuel.

KEY WORDS: Heat engine, Particulate Matter(PM), Diesel engine, Ethanol, Biodiesel

1. INTRODUCTION

Diesel engines are considered as one of the highest thermal efficiency engines among internal combustion engines (ICE)[(1)]. However, a major disadvantage is particulate matter (PM) emission which is harmful to human body and environment.

Biofuels, such as biodiesel or ethanol, have been often discussed as alternatives for diesel fuel replacement since they are obtained from renewable sources and their benefits in emission reduction. Biodiesel consists of alkyl monoesters of fatty acids derived from vegetable oil or animal fats. Due to its similar physical properties to diesel fuel, there is no need to modify the engine when the engine is fueled with the blends[(2-4)]. Ethanol is a low cost oxygenated fuel with high oxygen content. Use of ethanol in diesel fuel can contribute significant reduction of particulate matter (PM) emission for motor vehicles[(5)]. However, its considerable weakpoint is miscibility with diesel fuel. Kraipat et al.[(6)] studied about an emulsifier needed to homogenize the blend and found that biodiesel could be a good agent. The three-phase diagram showed that less than ten percent of biodiesel by volume fraction promote stability of the mixture.

In terms of engine performance and emission, many researchers have investigated effects of biodiesel-ethanol-diesel fuel on diesel engines. B. Prbakaran et al.[(7)] investigated effects of ethanol addition to biodiesel by blending with the maximum blend ratio of 50% ethanol. Operated with a single-cylinder diesel engine, brake thermal efficiency of the blends was similar to diesel base fuel. There was a decrease of nitrogen oxides and smoke emission, while maximum heat release rate and maximum pressure for the blends at higher load were increased. Prashant et al.[(8-9)] conducted investigations of a 4-cylinder diesel engine powered by diesel-ethanol blend. They showed that ignition delay increased for 40% ethanol fraction at low load. However, with higher load, ignition delay was found to be decreasing. The peak pressure rise was increasing at all cases. Darratray Bapu Hulwan et al.[(5)] studied performance, emission, and combustion characteristics of a multicylinder diesel engine from diesel-ethanol-biodiesel blends. The experiment was conducted with adjustable injection-timing fuel system. The report showed that at high ethanol blend ratio it is necessary to advance injection timing due to limited Cetane index. At high ratio of ethanol, smoke reduced remarkably at medium and high load for both low and high engine speed. An according research from Lei Zhu et al.[(2)] showed a test of ethanol-biodiesel blended fuel in a 4-cylinder diesel engine. They found that ethanol-biodiesel blends caused increase in maximum pressure and heat release rate and retarded further far away from top dead center.

Diesel particulate matters consist of a solid fraction and a soluble organic fraction (SOF). Primary particles of the PMs, composed of carbon and metallic ash, are coated with SOF and sulfate. The mean diameter of primary particles is usually in the range of 20-80 nm. Agglomerated particles are an assembly of primary particles and aggregates whose total surface area does not differ appreciable from the sum of specific surface areas of primary particles. Agglomerated particle size is normally 80-300 nm[(1,10)]. Scanning Electron Microscope (SEM) and Transmission

This material is reserved for educational use only, not allowed for commercial use.
Forbidden to modify the content, and cite the document when use.

Electron Microscope (TEM) observation of PMs have been conducted by several researchers[11]. A primary soot particle has two distinct parts; an inner core and an outer shell[12-13]. Generally, a primary particle from ICE has only one core with concentric fringe pattern which is hard to be distinguished as inner core or outer shell. Some primary particles were found to have a hollow interior and the outer shell exhibiting evidence of graphitization, with a higher crystalline than the non-hollowed particles[12,14]. Size distributions of diesel engine's PMs have been categorized as PM10, diameter (D) < 10 micron; fine particles, D < 2.5 micron; ultrafine particles, D < 0.1 micron; and nanoparticles, D < 0.05 micron or 50 nm.[12,15].

According to some recent researches about PM's quantity and morphology from biodiesel combustion, results showed that PM's quantity and average primary nanoparticle sizes have some relationships with engine speed and engine load. Biodiesel's PMs emitted about half in quantity and a little smaller in primary particle size, compared with diesel's PMs[12]. As a result of biodiesel and ethanol's benefits mentioned as above, especially ethanol combustion characteristics, the aim of this research is to study effects of combustion characteristics on PM's quantity emission, morphology, and nanostructure, by using ethanol-blended biodiesel fuel. Base biodiesel fuel was compared with a fraction of ethanol blended with biodiesel. The test was performed on a conventional diesel engine. PM quantity and morphology were investigated by an opacity smoke meter and electron microscopy for better understanding.

2. EXPERIMENTAL SETUP AND METHOD

2.1 Engine and Combustion Analyzer setup

The experiment was carried out on a 1-cylinder natural aspirated, direct injection, displacement of 709 cm^3 , compression ratio of 18:1, diesel engine. Fuel injection system was not modified. Engine specification was represented in Table1. The engine was coupled with an eddy-current dynamometer and a control system to adjust engine speed and engine load as shown in Fig. 1. Fuel supply system was set with a weight scale to measure fuel consumption. Exhausted gas temperature was measured at the exhausted port by a thermocouple.

Table 1
Engine specification.

Items	Details
Engine type	1-cylinder, Natural aspirated, Direct injection, Compression Ignition
Bore x Stroke	97mm x 96mm
Displacement	709cm^3
Compression ratio	18:1
Rated power	9.2kW @ 2400rpm
Injection timing	19° CA bTDC
Injection pressure	22MPa

For parameter analysis in the combustion chamber, pressure versus crank angle data were measured by a piezoelectric sensor

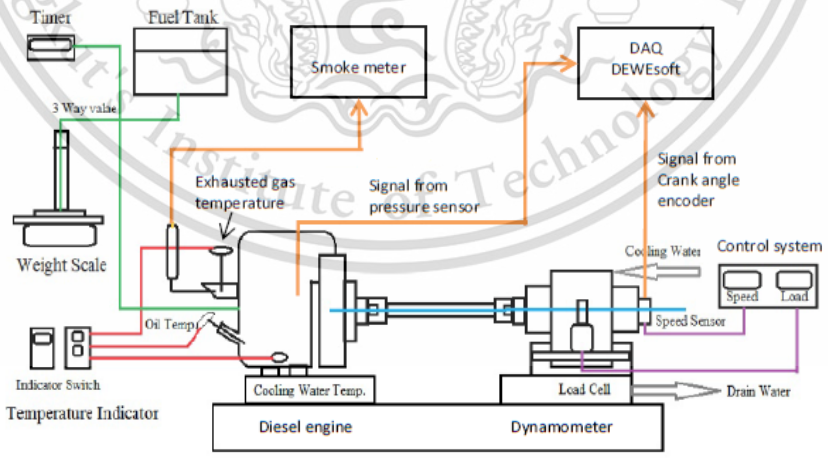

Fig. 1 Schematic diagram of experimental set up

This material is reserved for educational use only, not allowed for commercial use.
Forbidden to modify the content, and cite the document when use.

(Kistler 6052C31, 250Bar, sensitivity: ±0.5%) and a crank angle encoder (CA-RIE-360, resolution: 360 pulses/rev.). Signals of the cylinder pressure were recorded with one-degree resolution of crank angle. For further statistical analysis, two hundred engine cycles were recorded with three repeats. The pressure signals then were amplified with the data acquisition equipment (DEWESoft SIRIUSi-HS-CA) to obtain heat release rate, $dQ_n/d\Theta$ which can be estimated by deriving the formula in Reference[10].

$$\frac{dQn}{d\theta} = \frac{\gamma}{\gamma - 1} p \frac{dV}{d\theta} + \frac{\gamma}{\gamma - 1} V \frac{dp}{d\theta} \quad (1)$$

Here γ is the ratio of specific heats, Cp/Cv. An appropriate range for γ for diesel heat release analysis is 1.3–1.35. The wall heat transfer and blow by losses are not considered to find the heat released due to combustion of fuel inside cylinder. This helps to eliminate additional approximation in the analysis of heat release.

PM's quantity was measured by an opacity diesel smoke meter (OKUDA DSM-240, 0-100%, ±3% accuracy) which optically evaluate soot collected on paper filters by light reflection method.

2.2 Experimental fuel

The fuels used in this experiment include biodiesel (B100) and ethanol-biodiesel blend. The blended fuels contain 10% and 20% by weight of ethanol, and are identified as BE10 and BE20 respectively. The biodiesel was produced from palm-olein (B100-TIS2313-2549). The ethanol was used as Anhydrous ethanol 99.8%. Base fuels properties are shown in Table 2. For the blended fuel, properties of calorific value, heat of evaporization, carbon content, hydrogen content, oxygen content, stoichiometric air-fuel ratio, and density were estimated by interpolation and calculation.

2.3. Experimental method

Engine performance curve, brake specific fuel consumption (BSFC), brake thermal efficiency (BTE), and exhausted gas temperature (EGT) were measured to see overview effects of ethanol compared with biodiesel. In-cylinder pressure and net heat release rate from selected engine operating conditions were then recorded to see combustion characteristics.

PM's quantity was measured at the exhausted port as well as PM powder was collected by using an in-house metal-net particle collector to investigate morphology and nanostructures by using scanning electron microscopy (FE-SEM: Hitachi SU5000), and transmission electron microscopy(TEM: JEOL JEM-2100Plus)

Table 2
Fuel properties.

Properties	Biodiesel	Ethanol	BE10	BE20
Chemical formula	$C_{14.9}H_{29.9}O_{1.9}$	C_2H_6O	-	-
Cetane index	66.1	8.0	-	-
Calorific Value (kJ/kg)	39525	28329	38405	37285
Heat of evaporization (kJ/kg)	300	840	354	408
Viscosity @ 40°C (mm^2/s)	4.5	1.2	-	-
Carbon (% mass)	74.5	52.2	72.3	70.0
Hydrogen (% mass)	12.5	13.0	12.5	12.6
Oxygen (% mass)	13.0	34.8	15.2	17.4
Stoichiometric Air fuel ratio	12.3	9.0	11.9	11.6
Density @ 25°C (kg/m^3)	875.3	789.0	866.7	858.0

3. RESULTS AND DISCUSSION

3.1 Engine performance

The engine performance curve of biodiesel and ethanol blended biodiesel is plotted in Fig. 2. Engine load decreases as increasing engine speed for all fuels. The ethanol blended fuel produces lower load due to lower calorific value as well as lower stoichiometric air-fuel ratio i.e. leaner combustion compared with biodiesel. The engine load shows significant drop at higher speed and more ethanol blended ratio.

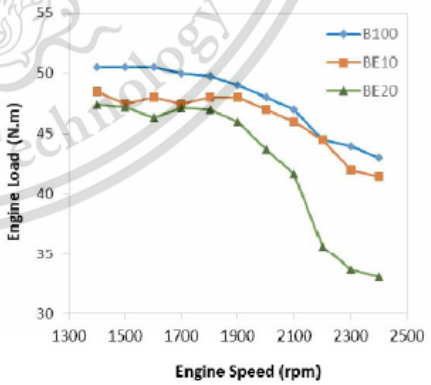

Fig. 2 Engine performance curve

This material is reserved for educational use only, not allowed for commercial use.
Forbidden to modify the content, and cite the document when use.

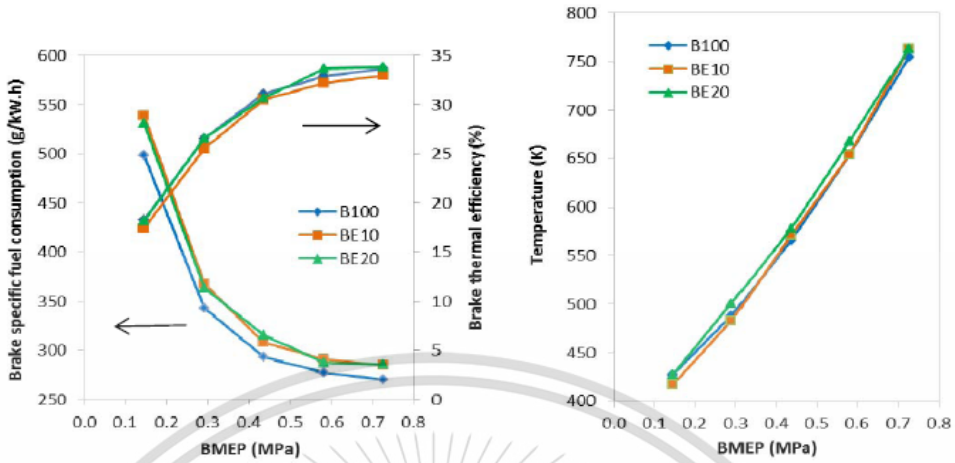

Fig. 3 Brake specific fuel consumption, Brake thermal efficiency, and Exhausted gas temperature at engine speed of 2000 rpm

3.2 Brake specific fuel consumption (BSFC), Brake thermal efficiency (BTE), and Exhausted gas temperature (EGT)

Brake specific fuel consumption (BSFC), Brake thermal efficiency (BTE), and Exhausted gas temperature (EGT) are shown in Fig. 3. BSFC of the ethanol blended fuels, are higher than that of biodiesel at all load conditions due mainly to the lower calorific value of ethanol. Thus, the amount of fuel supply into the engine must be greater. The trend shows decrease in the BSFC as the engine load increase. It can be explained as; when the engine load increases, combustion temperature which is implied from the rise of EGT increases as well. Reactivity of fuel and oxygen activates conversion of combustion heat to mechanical work much more than amount of energy from the fuel input. That is why the BSFC decreases as the engine load increases.

BTE plots show that as the engine load increases, the engine produces more thermal efficiency for all fuels. The BTE of BE20 and B100 is close to each other because the higher BSFC of BE20 compensates its lower calorific value, compared with B100.

3.3 Combustion characteristics

In-cylinder pressure variation with respect to crank angle are shown in Fig. 4a and heat release rate in Fig. 4b. The engine load was varied in the range of 0.2 MPa, 0.4 MPa, and 0.6 MPa at constant engine speed of 2400 rpm. Peak pressures of all fuels increase with the increasing engine load. Considering at the ethanol blended fuels, at low load of 0.2MPa, the peak pressure occurs after the biodiesel's peak for 10 to 15 crank angle degrees. At the low load condition, low combustion temperature causes ethanol blended fuel which has higher heat of evaporization as well as low cetane index delays in start of combustion. Therefore, the peak pressure occur further away from top dead center. At higher engine load, the increase of combustion temperature cause better fuel vaporization which leads to less combustion delay in the ethanol blended fuel and the peak pressures increase as well.

Heat release rate plots show that combustion processes of all fuels start with premixed combustion phase followed by diffusion combustion phase. At low engine load, the fuel with more ethanol content which is BE20 has more significant ignition delay which effects on retarded premixed combustion phase, while a higher peak of the heat release can be observed. The reason is that low temperature in the low load condition causes the ethanol blended fuel need more time for fuel atomization due to higher heat of vaporization of ethanol as explained above. After enough fuel atomization and mixing with oxygen, rapid combustion produces high peaks of heat release rate as shown in the Fig. 4b. However, at the higher engine load, higher combustion temperature make better fuel vaporization and fuel atomization as well. There is reduction in retarded combustion for the ethanol blended fuels as well as stronger premixed combustion leads to higher peak of heat release rate. Although the ethanol blended fuels have more delay in premixed combustion, their combustion processes tends to finish earlier than biodiesel which agrees with a little lower EGT in Fig. 3. That means the diffusion combustion time for the ethanol blend is reduced since better fuel atomization, mixing, and more oxygen content in the fuels promote more complete combustion.

This material is reserved for educational use only, not allowed for commercial use.
Forbidden to modify the content, and cite the document when use.

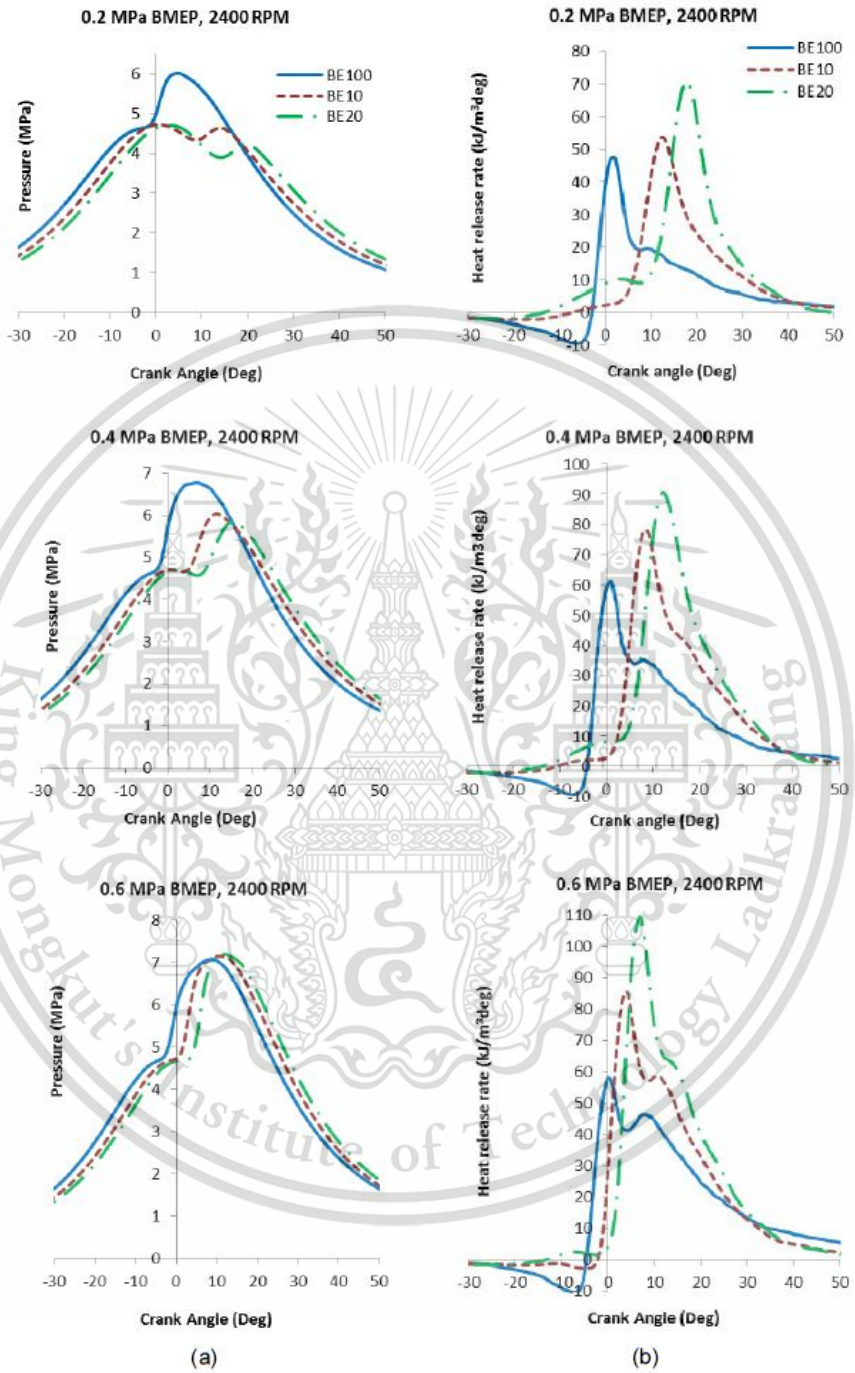

Fig. 4 (a) In-cylinder pressure, (b) Heat release rate versus crank angle at engine speed of 2400 rpm

This material is reserved for educational use only, not allowed for commercial use.
Forbidden to modify the content, and cite the document when use.

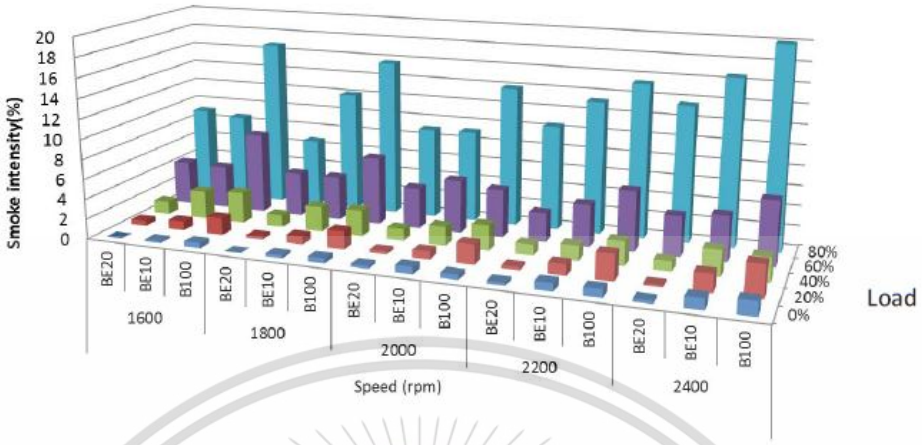

Fig. 5 Smoke intensity

3.4 PM's quantity emission

Figure 5 shows measurement results of smoke intensity which is an indirect method to estimate PM's quantity. The intensity is strongly dependent on the engine load. The more engine load, the greater smoke intensity due to more fuel supply for combustion. The ethanol blended fuels produce less smoke than the biodiesel at almost all engine operating conditions because retarded combustion characteristics provide enough time for fuel atomization and high peak of heat relaease tends to promote better fuel-oxygen's reactivity.

3.5 PM's morphology and nanostructure

Morphology and nanostructure of the PM were investigated by electron microscopy. Some PM's types were found on the paper filters such as fine particles or PM 2.5, D < 2.5 micron, and ultrafine particles, D < 100 nm. Fig. 6 shows a sample of a fine particle from BE10 fuel.

SEM images of biodiesel's and BE20's agglomerated particles are presented in Fig. 7 and Fig. 8 respectively. Biodiesel's agglomerated particles tends to gather densely on the paper filter, compared with BE20's agglomerated particles.

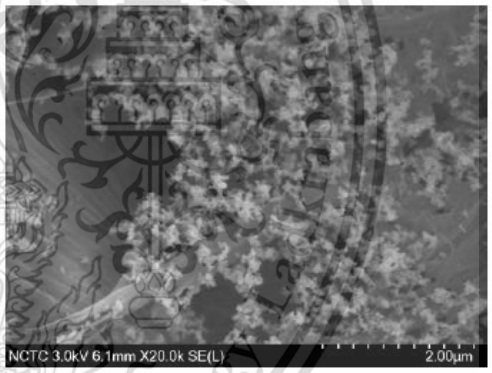

Fig. 7 SEM image of biodiesel's agglomerated particles on paper filter at 0.6 MPa and 2000 rpm

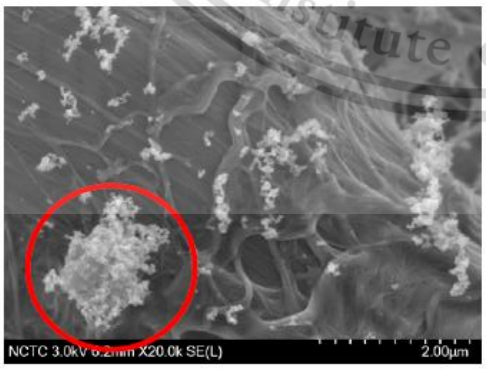

Fig. 6 SEM image of BE10's PM 2.5 at 0.6 MPa and 2000 rpm

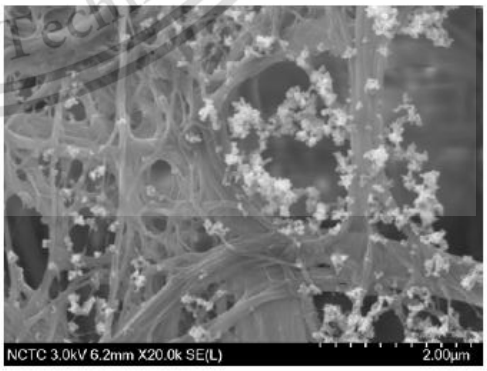

Fig. 8 SEM image of BE20's agglomerated particles on paper filter at 0.6 MPa and 2000 rpm

This material is reserved for educational use only, not allowed for commercial use.
Forbidden to modify the content, and cite the document when use.

Visualized by TEM images, each agglomerated paticle consists of many uniformed primary nanoparticles. Figure 9 and Figure 10 show TEM image of biodiesel's and BE20's agglomerated particle in the engine condition of 0.6 MPa load and 2000 rpm. respectively. It can befound that average size of the agglomerated particles has no significant difference among biodiesel's and ethanol blended biodiesel's PM.

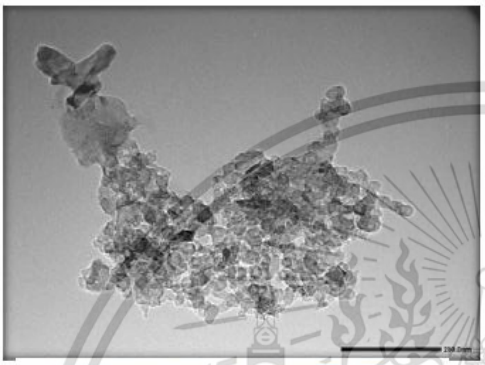

Fig. 9 TEM image of biodiesel's agglomerated particles at 0.6 MPa and 2000 rpm

Fig. 10 TEM image of BE20's agglomerated particles at 0.6 MPa and 2000 rpm

Moreover, primary nanoparticles of biodiesel's and ethanol blended's PM was observed with further TEM's magnification so that inner core and outer shell of the primary nanoparticles can be clearly seen. Figure 11 and Figure 12 show TEM image of biodiesel's and BE20's primary nanoparticle respectively. Morphology of biodiesel's primary particle has clear cut and smooth contour compared with ethanol's. Carbon crystallite traces are also clear. While contour of BE20's primary nanoparticle is not smooth and appears incomplete spherical form. It is possible that PM's oxidation from ethanol blended fuel's combustion is stronger around primary particles compared with biodiesel fuel.

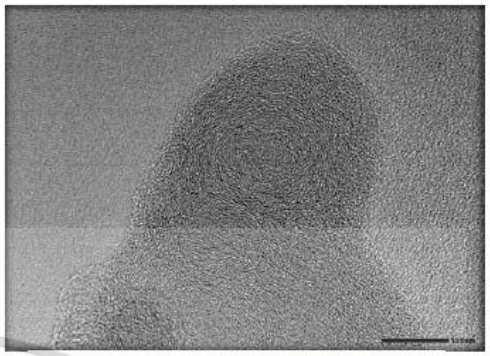

Fig. 11 TEM image of biodiesel's primary particle at 0.6 MPa and 2000 rpm

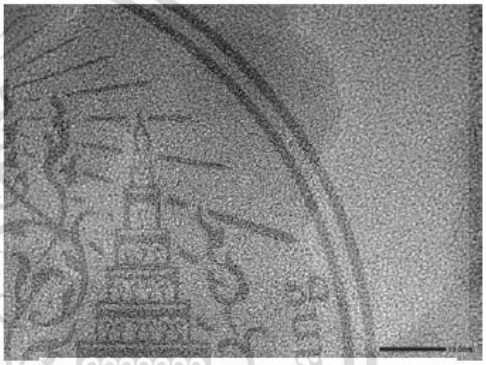

Fig. 12 TEM image of BE20's primary particle at 0.6 MPa and 2000 rpm

4. CONCLUSION

The research started with a review of physical fuel properties in order to forecast combustion behavior of the ethanol-blended biodiesel. Then the engine performance test was conducted. Ethanol blended fuel contributed higher BSFC since the nature of lower calorific value compared with biodiesel while BTE has no significant difference. Combustion analysis showed a considerable delayed combustion of the ethanol blended fuel due to lower cetane index and more heat of evaporization. As a result of ignition delay, fuel have more preparation for better atomization leading to rapid premixed combustion with high peak of heat release rate. Early finish in diffusion combustion phase also emphasizes the rapid combustion behavior of the ethanol blended fuel. Combustion behaviors might effect on PM's quantity reduction. However, opacity smoke meter is not the most accurate way to measure PM's quantity since some PM particles that covered by hydrocarbon cannot be detected by the smoke meter.

This material is reserved for educational use only, not allowed for commercial use.
Forbidden to modify the content, and cite the document when use.

PM's morphology and nanostrucuture were successfully investigated by SEM and TEM techniques. Nanostructure of agglomerated particles has no significant difference among biodiesel and ethanol blended biodiesel. However, there were trails of incomplete morphology of BE20's primary nanoparticle. These can be implied that ethanol blended fuel has more potential in PM's oxidation reactivity.

ACKNOWLEDGEMENT

The authors gratefully acknowledge the academic support from Thailand Advanced Institute of Science and Technology and Tokyo Institute of Technology (TAIST-Tokyo Tech) by National Science and Technology Development Agency (NSTDA) and the financial support from Thailand Graduate Institute of Science and Technology (TGIST), Thailand Research Fund(TRF), and KMITL International College.

REFERENCES

(1) Preechar Karin, Hiroshi Oki, Katsunori Hanamura, Chinda Charoenphonphanich, Nanostructures and Oxidation Kinetics of Diesel Particulate Matters, The Second TSM International Conference on Mechanical Engineering, 19-21 October, 2011, Krabi

(2) Zhu, L., Cheung, C., Zhang, W., & Huang, Z. (2011). Combustion, performance and emission characteristics of a DI diesel engine fueled with ethanol–biodiesel blends. Fuel, 90(5), 1743-1750. doi:10.1016/j.fuel.2011.01.024

(3) Ramadhas AS, Jayaraj S, Muraleedharan C. Use of vegetable oils as I.C. enginefuels – a review. Renew Energy 2004; 29:727–42.

(4) Graboski MS, McCormick RL. Combustion of fat and vegetable oil derived fuelsin diesel engines. Prog Energy Combust Sci 1998;24:125–64

(5) Hulwan, Dattatray Bapu, and Satishchandra V. Joshi. "Performance, emission and combustion characteristic of a multicylinder DI diesel engine running on diesel–ethanol–biodiesel blends of high ethanol content." Applied Energy 88, no. 12 (2011): 5042-055. doi:10.1016/j.apenergy.2011.07.008.

(6) Kraipat Cheenkachorn, Monpilai H.Narasingha, Jutahawan Pupakornnopparut , Biodiesel as an Additive for Diesohol, Asian Journal on Energy and Environment, 2006, 7(01), 267-276, ISSN 1513-4121

(7) Prbakaran, B., and Dinoop Viswanathan. "Experimental investigation of effects of addition of ethanol to bio-diesel on performance, combustion and emission characteristics in CI engine." Alexandria Engineering Journal (2016)

(8) Tutak, W., Jamrozik, A., Pyrc, M., & Sobiepański, M. (2017). A comparative study of co-combustion process of diesel-ethanol and biodiesel-ethanol blends in the direct injection diesel engine. Applied Thermal Engineering, 117, 155-163. doi:10.1016/j.applthermaleng.2017.02.029

(9) G.K. Prashant, D.B. Lata, P.C. Joshi, Investigations on the effect of ethanol blend on the combustion parameters of dual fuel diesel engine, Appl. Therm. Eng. 96 (2016) 623–631.

(10) Heywood, J.B. (1998). Internal Combustion Engine Fundamental, McGraw-Hill series in mechanical engineering, Singapore.

(11) Karin, P., Borhanipour, M., Songsaengchan, Y., Laosuwan, S., Charoenphonphanich, C., Chollacoop, N., & Hanamura, K. (2015). Oxidation kinetics of small CI engine's biodiesel particulate matter. International Journal of Automotive Technology, 16(2), 211-219. doi:10.1007/s12239-015-0023-4

(12) Karin, P., Boonsakda, J., Sirichola thum, K., Saenkhumvong, E., Charoenphonphanich, C., & Hanamura, K. (2016). Morphology and oxidation kinetics of CI engine's biodiesel particulate matters on cordierite Diesel Particulate Filters using TGA. International Journal of Automotive Technology, 18(1), 31-40. doi:10.1007/s12239-017-0003-y

(13) Ishiguro, T., Takatori, Y. and Akihama, K. (1997). Microstructure of diesel soot particles probed by electron microscopy: First observation of inner core and outer shell. Combustion and Flame 108, 1, 231–234.

(14) Vander Wal, R. L., Yezerets, A., Currier, N. W., Kim, D. H. and Wang, C. H. (2007). HRTEM study of diesel soot collected from diesel particulate filters. Carbon 45, 1, 70–77.

(15) Kittelson, D. B. (1998). Engines and nanoparticles: A review. J. Aerosol Science 29, 5-6, 575–588.

This material is reserved for educational use only, not allowed for commercial use.

Forbidden to modify the content, and cite the document when use.

This material is reserved for educational use only, not allowed for commercial use.
Forbidden to modify the content, and cite the document when use.

JSAE 20179094 / SAE 2017-32-0094

Impact of Biodiesel on Small CI Engine Combustion Behavior and Particle Emission Characteristic

Preechar Karin, Park Watanawongskorn, Jiramed Boonsakda
Eakkawut Saenkhumvong, Sippakorn Rungsritanapaisan, Settavit Srivarocha
Chinda Charoenphonphanich
King Mongkut's Institute of Technology Ladkrabang

Nuwong Chollacoop
National Science and Technology Development Agency

Katsunori Hanamura
Tokyo Institute of Technology

Copyright © 2017 SAE Japan and Copyright © 2017 SAE International

ABSTRACT

Diesel engines are high thermal efficiency because of high compression ratio but produce high concentration of particulate matter (PM) because of direct injection fuel diffusion combustion. PM must be removed from the exhaust gas to protect human health. This research describes biodiesel engine performance, efficiency and combustion behavior using combustion pressure analyzer. It was clearly observed that PM emitted from CI engines can be reduced by using renewable bio-oxygenated fuels. The morphology and nanostructure of fossil fuel and biofuel PMs were investigated by using a Scanning electron microscopy (SEM) and Transmission electron microscopy (TEM). The morphology of biodiesel and diesel doesn't have much different in the viewpoint of particulate matter trapping using DPF micro surface pores. The agglomerated ultrafine particles and primary nanoparticles sizes of diesel and biodiesel engine's PM are approximately 50-500 nm and 20-50 nm, respectively. The primary particle of biodiesel engine's PM is smaller than that of fossil diesel. The average of diesel and biodiesel PM's carbon platelets is in the range of 0.2-5.2 nm.

INTRODUCTION

Diesel engines are considered as one of the highest thermal efficiency engines among internal combustion engines (ICE) [1]. However, a major disadvantage is particulate matter (PM) emission which is harmful to human body and environment. Biofuels, such as biodiesel or ethanol, have been often discussed as alternatives for diesel fuel replacement since they are obtained from renewable sources and their benefits in emission reduction. Biodiesel consists of alkyl monoesters of fatty acids derived from vegetable oil or animal fats. Due to its similar physical properties to diesel fuel, there is no need to modify the engine when the engine is fueled with the blends [2-4]. In terms of engine performance and emission, many researchers have investigated effects of biodiesel fuel on diesel engines. M.M. Hasan *et al.* [5] investigated effects of biodiesel by blending with the maximum blend ratio of 30% biodiesel. Operated with a single-cylinder diesel engine, brake thermal efficiency of the blends was similar to diesel base fuel. There was a decrease of nitrogen oxides and smoke emission, while maximum heat release rate and maximum pressure for the blends at higher load were increased. Mohanad *et al.* [6-7] conducted investigations of a 4-cylinder diesel engine powered by rapeseed biodiesel blend. They showed that ignition delay increased for higher cetane number. Sakthivel *et al.* [8] studied performance, emission, and combustion characteristics of a diesel engine, injection timing is a major parameter that sensitively affects the engine performance, emission and durability. The brake thermal efficiency for B20 was higher compared to diesel in the entire load. The ignition delay and combustion duration were shorter for biodiesel than diesel which results in lower heat release rate, peak pressure and rate of pressure rise. Retardation of injection timing caused decrease in emission and combustion parameters like Oxides of Nitrogen (NO_x), Hydrocarbon (HC) and Carbon Monoxide (CO), peak pressure, ignition delay, combustion duration and heat release rate which increased with advancement in injection timing. An according research from Guven *et al.* [9] showed that biodiesel blends caused decrease in maximum pressure and heat release rate and retarded further far away from top dead center.

Diesel particulate matters consist of a solid fraction and a soluble organic fraction (SOF). Primary particles of the PMs, composed of carbon and metallic ash, are coated with SOF and sulfate. The mean diameter of primary particles is usually in the range of 20-80 nm. Agglomerated particles are an assembly of primary particles and surface area does not differ appreciable from the sum of specific surface areas of primary particles. Agglomerated particle size is normally 80-300 nm [10]. Scanning Electron Microscope (SEM) and Transmission Electron Microscope (TEM) observation of PMs have been conducted by several researchers [11]. A

This material is reserved for educational use only, not allowed for commercial use.
Forbidden to modify the content, and cite the document when use.

primary soot particle has two distinct parts; an inner core and an outer shell [12-13]. Generally, a primary particle from ICE has only one core with concentric fringe pattern which is hard to be distinguished as inner core or outer shell [14]. Size distributions of diesel engine's PMs have been categorized as PM10, diameter (D) < 10 micron; fine particles, D < 2.5 micron; ultrafine particles, D < 0.1 micron; and nanoparticles, D < 0.05 micron or 50 nm. [15].

METHODOLOGY

Table 1. Engine specification.

Items	Details
Engine type	1-cylinder, Natural aspirated, Direct injection, Compression Ignition Engine
Bore x Stroke	97 mm x 96mm
Displacement	709 cm3
Compression ratio	18:1
Rated power	9.2 kW @ 2400 rpm
Injection timing	19° CA bTDC
Injection pressure	22 MPa

Table 2. Fuel properties.

Properties	Diesel	Biodiesel
Chemical formula	$C_{14.2}H_{28}$	$C_{14.9}H_{29.9}O_{1.9}$
Carbon (% mass)	85.1	74.5
Hydrogen (% mass)	14.0	12.5
Oxygen (% mass)	0.9	13.0
Auto ignition temp (°C)	288	294
Calorific value (kJ/kg)	46,180	39,525
Heat of vaporization (kJ/kg)	250	300
Viscosity @ 40°C (mm^2/s)	3.0	4.5
Density @ 25°C (kg/m^3)	844.8	875.3
Stoichiometric air fuel ratio	14.7	12.3
Distillation (°C)		
T10	214.3	336.2
T30	250.3	339.7
T50	281.5	341.4
T70	312.5	345.4
T90	352.3	351.2

The experiment was carried out on a 1-cylinder natural aspirated, direct injection, displacement of 709 cm3, compression ratio of 18:1, diesel engine. Fuel injection system was not modified (mechanical fuel injection system). Engine specification was represented in Table 1. The engine was coupled with an eddy-current dynamometer and a control system to adjust engine speed and engine load. Fuel supply system was set with a weight scale to measure fuel consumption. For parameter analysis in the combustion chamber, pressure versus crank angle data were measured by a piezoelectric sensor (Kistler 6052C31, 250Bar, sensitivity: ±0.5%) and a crank angle encoder (CA-RIE-360, resolution: 360 pulses/rev.). Signals of the cylinder pressure were recorded with one-degree resolution of crank angle. For further statistical analysis, two hundred engine cycles were recorded with three repeats. The pressure signals then were amplified with the data acquisition equipment (DEWESoft SIRIUSi-HS-CA) to obtain heat release rate.

The fuels used in this research include commercial diesel and biodiesel (B100). The commercial diesel contains approximately 5% biodiesel due to the regulation while the biodiesel was produced from palm-olein (B100-TIS2313-2549). Fuels properties are shown in Table 2. Biodiesel is more homogeneous molecules which shown by vaporize temperature. It is very narrow and very high around 610 to 620 Kelvin. This implies that biodiesel has higher heat of vaporization. Engine performance curve, brake specific fuel consumption (BSFC) and brake thermal efficiency (BTE) were measured to see overview effects of biodiesel compared with commercial diesel. In-cylinder pressure, net heat release rate, and accumulative heat release from selected engine operating conditions were then recorded to see combustion characteristics.

PM's quantity was measured by an opacity diesel smoke meter (OKUDA DSM-240, 0-100%, ±3% accuracy) which optically evaluate soot collected on paper filters by light reflection method. PM powder was collected by using an in-house metal-net particle collector to investigate morphology and nanostructures by using scanning electron microscopy (FE-SEM: Hitachi SU5000), and transmission electron microscopy (TEM: JEOL JEM-2100Plus)

RESULTS AND DISCUSSION

Combustion Characteristics

The engine performance curve of diesel and biodiesel is plotted in Fig. 1 (a). Engine load decreases as increasing engine speed for all fuels. Brake specific fuel consumption (BSFC) and Brake thermal efficiency (BTE) are shown in Fig. 1 (b) and (c), respectively. BSFC of the biodiesel are higher than that of diesel at all load conditions due mainly to the lower calorific value. Thus, the amount of fuel supply into the engine must be greater. The trend shows decrease in the BSFC as the engine load increase. It can be explained as; when the engine load increases, combustion temperature which is implied from the rise of Exhaust gas temperature (EGT) as shown in Fig. 1 (d) increases as well. Reactivity of fuel and oxygen activates conversion of combustion heat to mechanical work much more than amount of energy from the fuel input. That is why the BSFC decreases as the engine load increases. BTE plots show that as the engine load increases, the engine produces more thermal efficiency for both fuels. The BTE of biodiesel is higher than diesel at all load condition because the fuel properties such as more oxygen fraction could promote complete combustion which biodiesel could reach optimum BTE at less load compared with diesel.

This material is reserved for educational use only, not allowed for commercial use.
Forbidden to modify the content, and cite the document when use.

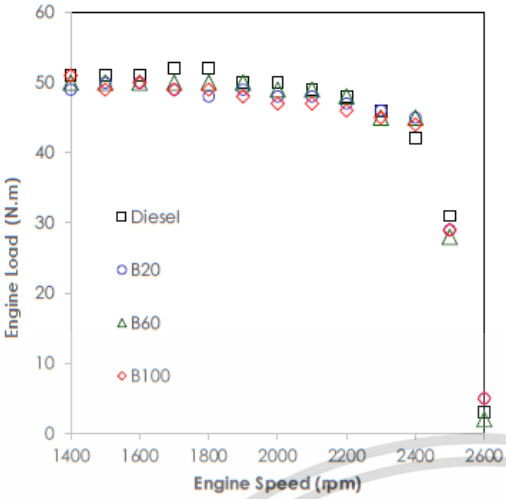

(a) Engine performance

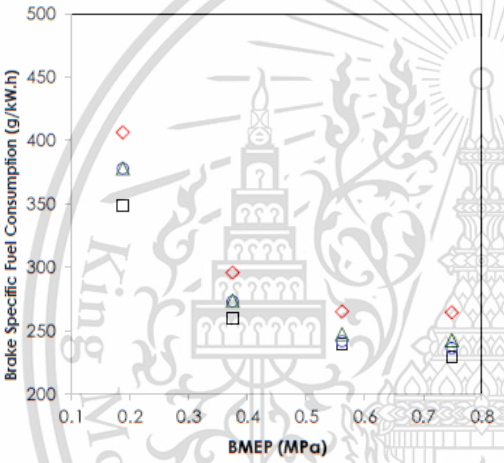

(b) Fuel consumption

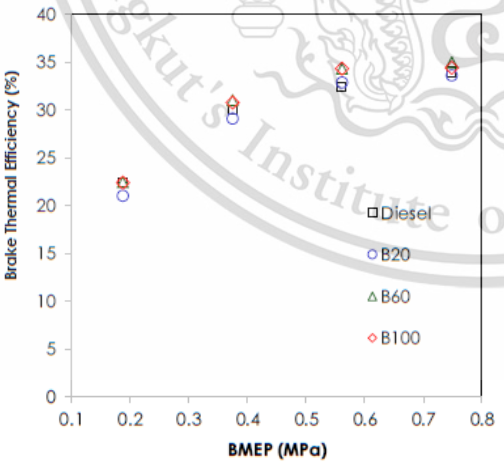

(c) Brake thermal efficiency

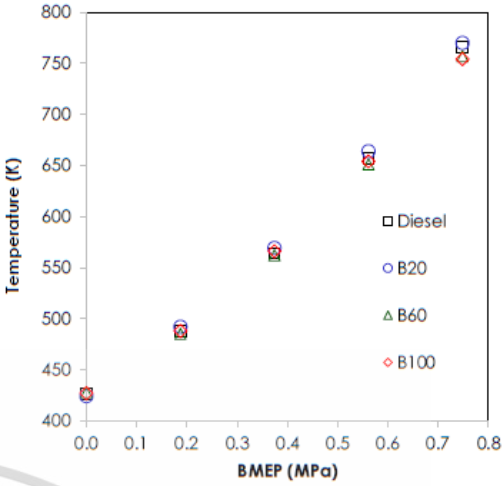

(d) Exhaust gas temperature

Figure 1. (a) Engine performance, (b) Brake specific fuel consumption (BSFC), (c) Brake thermal efficiency (BTE), and (d) Exhaust gas temperature (EGT) at the engine speed of 2000 rpm.

In-cylinder pressure variation with respect to crank angle is shown in Fig. 2, and heat release rate in Fig. 3. The engine load was varied in the range of 0.2 MPa, 0.4 MPa, and 0.6 MPa at constant engine speed of 2400 rpm. Peak pressures of all fuels increase with the increasing engine load. Considering the biodiesel at 0.2 MPa and 0.4 MPa BMEP load, the pressure rises of biodiesel before reaching peak pressure occurs prior to the diesel. This is the effect of higher oxygen fraction in fuel promote faster combustion. At higher engine load, the increase of combustion temperature cause better fuel vaporization for both fuels, so there is no significant in pressure rise with respect to crank angle.

Heat release rate plots show that combustion processes of all fuels start with ignition delay, premixed combustion phase, and followed by diffusion combustion phase. At same start of injection of 19° CA bTDC in the condition of 0.2 MPa and 0.4 MPa BMEP load, biodiesel has shorter ignition delay, while a higher peak of the heat release can be observed on diesel on all load conditions. From fuel properties of biodiesel, density and auto ignition temperature was negative impact with shorter ignition delay, so oxygen fraction is that mainly effects of shorter ignition delay than diesel fuel. The reason is that low temperature in the low load condition with higher oxygen fraction causes the biodiesel start combustion earlier. However, longer ignition delay in diesel causes enough fuel atomization and mixing with oxygen, so it produces higher peaks of heat release rate. In addition, it is also well-known that the high bulk modulus of the biodiesel makes the injection timing earlier in the case of mechanical injection system, which may advance the auto-ignition timing.

This material is reserved for educational use only, not allowed for commercial use.
Forbidden to modify the content, and cite the document when use.

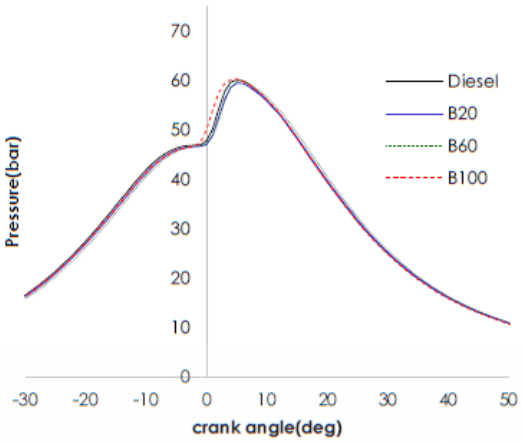

(a) 0.2 MPa BMEP

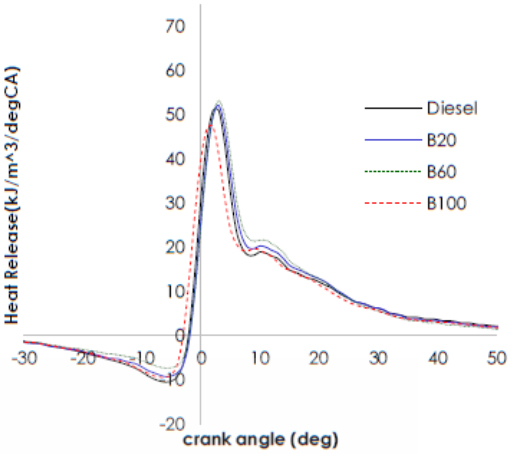

(a) 0.2 MPa BMEP

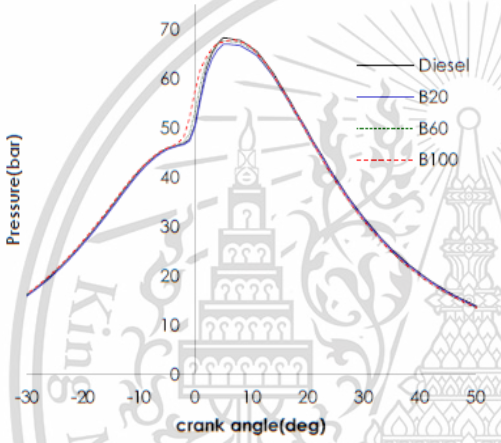

(b) 0.4 MPa BMEP

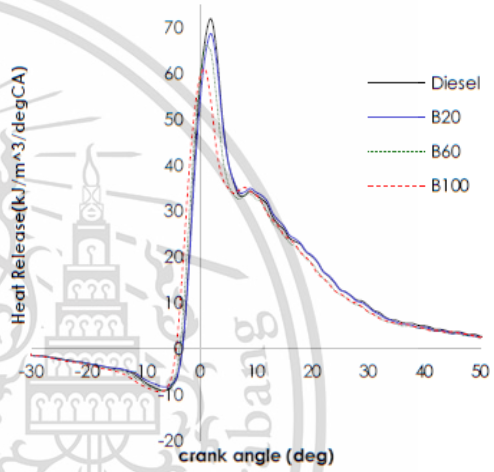

(b) 0.4 MPa BMEP

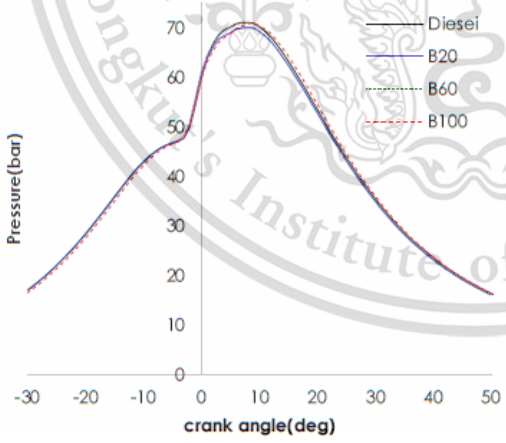

(c) 0.6 MPa BMEP

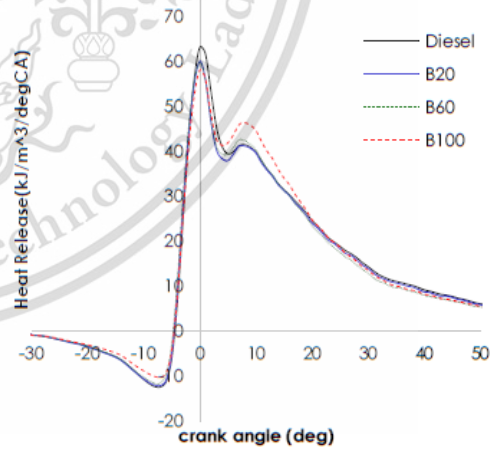

(c) 0.6 MPa BMEP

Figure 2. In-cylinder pressure versus crank angle at engine speed of 2400 rpm, (a) 0.2 MPa BMEP, (b) 0.4 MPa BMEP and (c) 0.6 MPa BMEP.

Figure 3. Heat release rate versus crank angle at engine speed of 2400 rpm, (a) 0.2 MPa BMEP, (b) 0.4 MPa BMEP and (c) 0.6 MPa BMEP.

SETC2017

This material is reserved for educational use only, not allowed for commercial use.
Forbidden to modify the content, and cite the document when use.

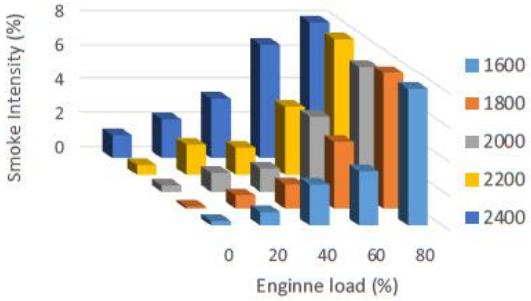

(a) Diesel engine's particulate matter

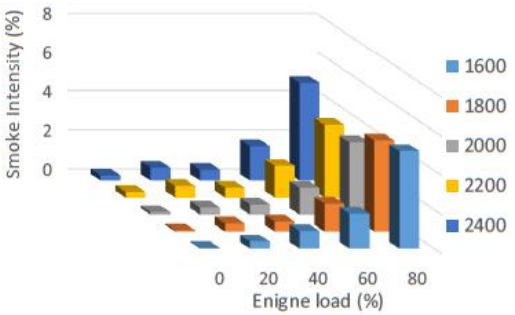

(d) B100 engine's particulate matter

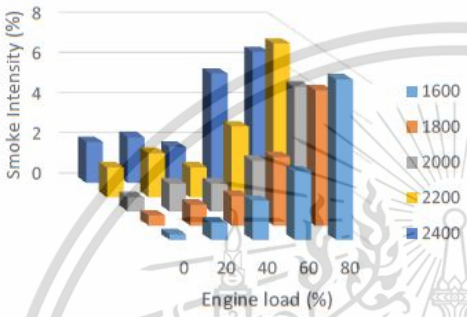

(b) B20 engine's particulate matter

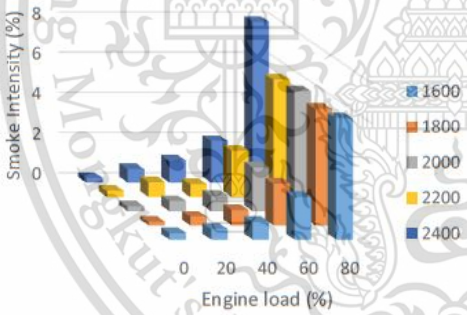

(c) B60 engine's particulate matter

Figure 4. Quantity of (a) diesel (b) B20 (c) B60 and (d) B100 engine's PM using opacity smoke meter in each engine load and engine speed operation condition.

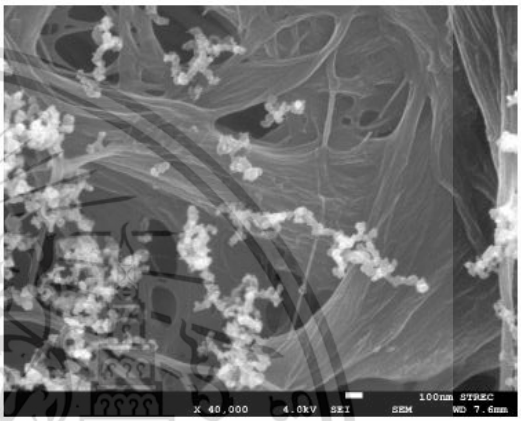

Figure 5. SEM image of diesel engine's fine particle emission in the condition of 80% load engine operation.

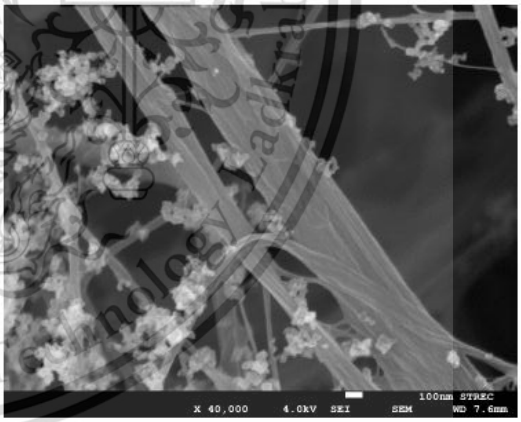

Figure 6. SEM image of B100 engine's fine particle emission in the condition of 80% load engine operation.

This material is reserved for educational use only, not allowed for commercial use.
Forbidden to modify the content, and cite the document when use.

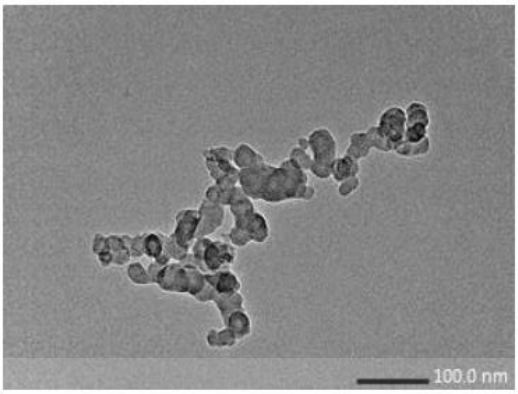

Figure 7. TEM image of diesel ultrafine particle emission in condition 80% load operation.

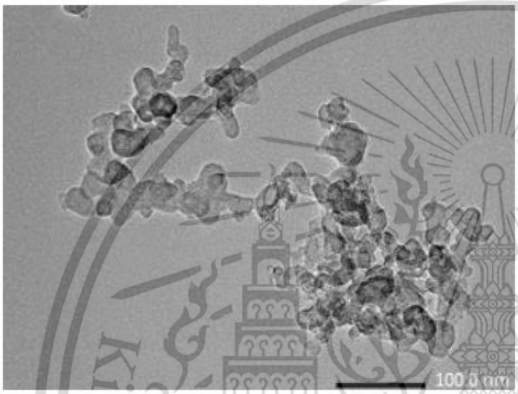

Figure 8. TEM image of B100 ultrafine particle emission in condition 80% load operation.

Particle Emission Characteristics

Figure 4 shows measurement results of smoke intensity which is an indirect method to estimate PM's quantity. The intensity is strongly dependent on the engine load. The more engine load, the greater smoke intensity due to more fuel supply for combustion. In this research, much amount of particle was used to determine the integrity of combustion process. The biodiesel produces less smoke than the diesel at almost all engine operating conditions because oxygenated fuel promote more complete combustion and better fuel-oxygen's reactivity.

Morphology and nanostructure of the PM were investigated by electron microscopy. Some PM's types were found on the paper filters such as fine particles and ultrafine particles. Ultrafine particles of diesel and biodiesel engine's PM consist of many single nanoparticles. Figure 5 and 6 show fine particle of diesel and biodiesel in the condition of 80% (engine torque of 38 Nm) load engine operation, respectively.

Agglomerated ultrafine particles of diesel and biodiesel engine's PM was also clearly observed using TEM as shown in Fig. 7 and 8, respectively. The average agglomerated ultrafine particle diameter size are in the range of 50-500 nm. Primary nanoparticles of diesel and biodiesel engines was also clearly observed using TEM as shown in Fig. 9 and 10, respectively. The average primary nanoparticle diameter size are in the range of 20-50 nm. Each carbon platelet in the inner core and outer shell of primary nanoparticle was also clearly observed by TEM.

Moreover, TEM image is used for numerate platelet number that aggregate layered in the particle. Each of platelet is consisted properly by carbon atom from incomplete combustion product. Figures 11, 12 and 13 are the images of original 10 nm^2 focused area, after post processing of two colors and after post processing of skeleton carbon platelet length estimation of diesel fuel. Figures14, 15 and 16 are the images of original 10 nm^2 focused area, after post processing of two colors and after post processing of skeleton carbon platelet length estimation of biodiesel, respectively. From the skeleton images, the carbon platelets inside the PM were measured by image processing program. The skeleton carbon platelets, which have 1-unit pixel width for each platelet, were measured for the white area in the image to be a carbon platelet length. The estimated of platelet sizes distribution in each condition are shown in Fig.17 and 18. The average of diesel and B100 PM carbon platelets is in the range of 0.2-5.2 nm.

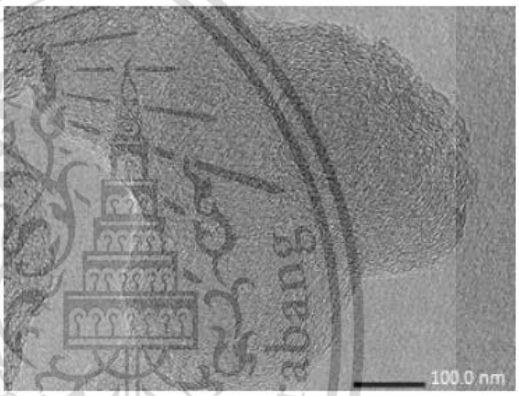

Figure 9. TEM image of diesel primary nanoparticle emission in condition 80% load operation.

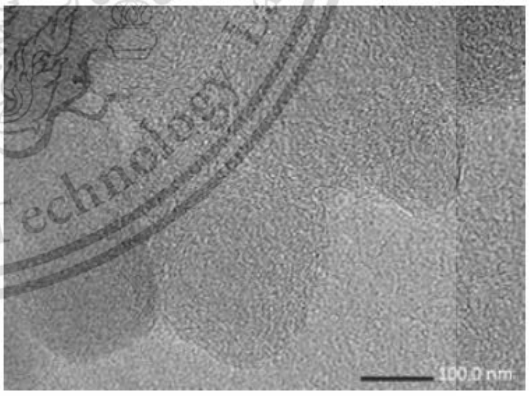

Figure 10. TEM image of B100 primary nanoparticle emission in condition 80% load operation.

This material is reserved for educational use only, not allowed for commercial use.
Forbidden to modify the content, and cite the document when use.

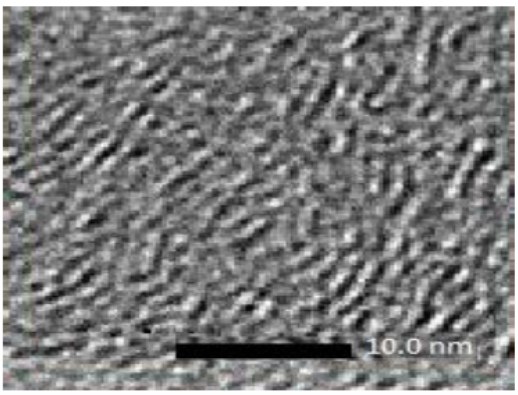

Figure 11. TEM images of engine 80% load operation diesel single PMs.

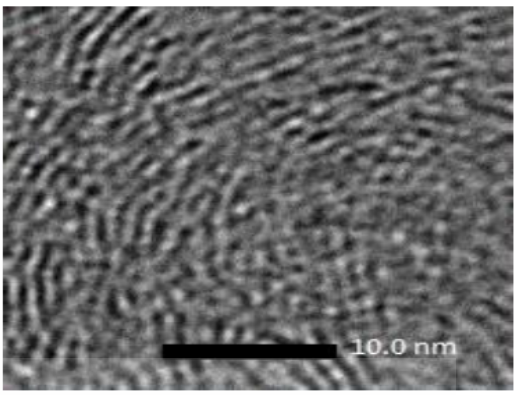

Figure 14. TEM images of engine 80% load operation B100 single PMs.

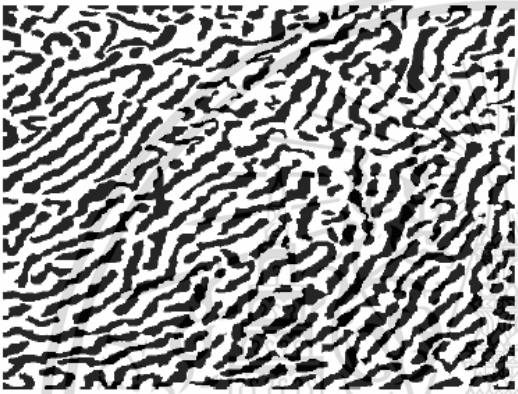

Figure 12. Two colors TEM images post process of engine 80% load operation diesel single PMs 10nm^2 focused area.

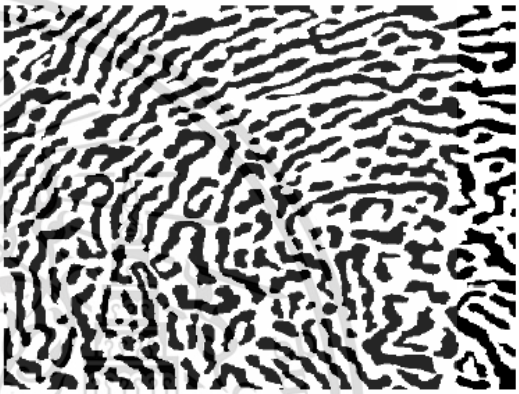

Figure 15. Two colors TEM images post process of engine 80% load operation B100 single PMs 10nm^2 focused area.

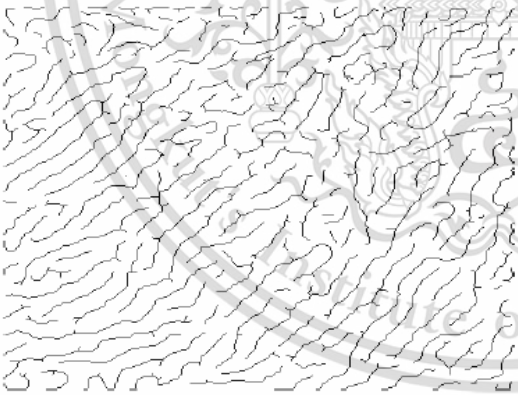

Figure 13. Skeleton TEM images post process of engine 80% load operation diesel single PMs 10nm^2 focused area.

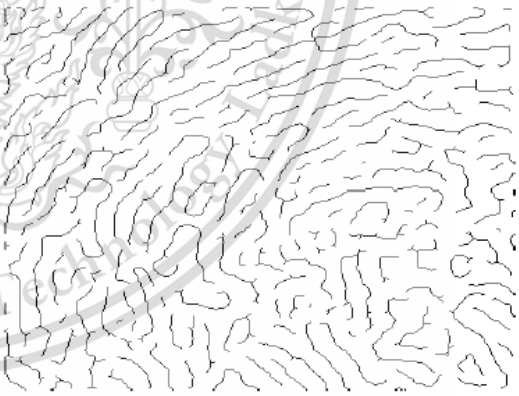

Figure 16. Skeleton TEM images post process of engine 80% load operation B100 single PMs 10nm^2 focused area.

This material is reserved for educational use only, not allowed for commercial use.
Forbidden to modify the content, and cite the document when use.

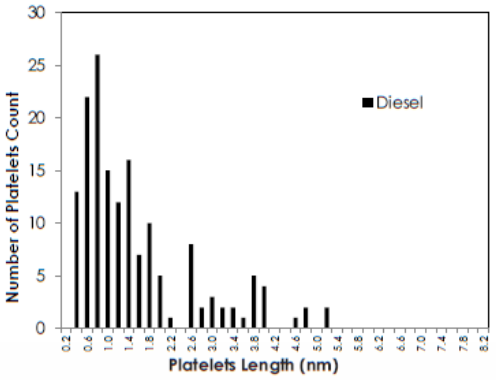

Figure 17. Platelet sizes distribution of diesel PM's carbon platelets.

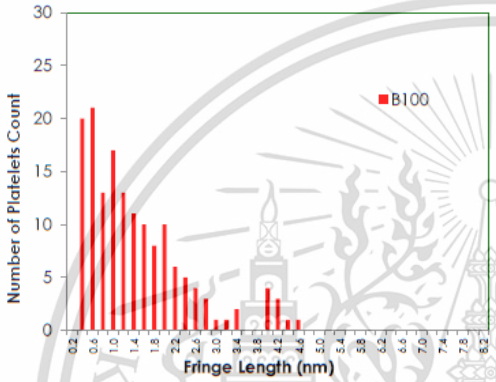

Figure 18. Platelet sizes distribution of B100 PM's carbon platelets.

CONCLUSIONS

The amount of particulate matter emitted from CI engine depend on several variables. The result shows the parameter which has the highest effect on PM quantity is engine load, concentration of biodiesel and engine speed respectively. When increase concentration of biodiesel in fuel, PM reduce because oxygen concentration in fuel increase. Higher concentration of oxygen makes more complete combustion and higher thermal efficiency. The quantities of particulate matter emitted from biodiesel engine are approximately a half of diesel engine's particulate matter. Morphology of CI engine's PM10, PM2.5, ultrafine particle and nanoparticle was characterized using SEM and TEM successfully. The morphology of biodiesel and conventional diesel doesn't have much different in the viewpoint of particulate matter trapping using DPF micro surface pores.

REFERENCES

1. J. B. Heywood, Internal Combustion Engine Fundamental, *McGraw-Hill series in mechanical engineering*, Singapore, (1998).

SETC2017

2. L. Zhu, C. Cheung, W. Zhang, and Z. Huang, Combustion, performance and emission characteristics of a DI diesel engine fueled with ethanol–biodiesel blends. *Fuel*, 90 (5), 1743-1750, (2011).
3. A. S. Ramadhas, S. Jayaraj and C. Muraleedharan, Use of vegetable oils as I.C. engine fuels – a review. *Renew Energy*, 29, 727–42, (2004).
4. M. S. Graboski and R. L. McCormick, Combustion of fat and vegetable oil derived fuels in diesel engines. *Prog Energy Combust Sci*, 24, 125–64, (1998).
5. M.M. Hasan and M.M. Rahman, Performance and emission characteristics of biodiesel–diesel blend and environmental and economic impacts of biodiesel production, *Renewable and Sustainable Energy Reviews*,74, 938–948, (2017).
6. M. Aldhaidhawi, R. Chiriac and V. Badescu, Ignition delay, combustion and emission characteristics of Diesel engine fueled with rapeseed biodiesel. *Renewable and Sustainable Energy Reviews,* 73, 178-186, (2017).
7. G.K. Prashant, D.B. Lata and P.C. Joshi, Investigations on the effect of ethanol blend on the combustion parameters of dual fuel diesel engine, *Applied Thermal Engineering*. 96, 623–631, (2016).
8. G. Sakthivel and N. Saravanan and M. Ilangkumaran, Influence of injection timing on performance, emission and combustion characteristics of a DI diesel engine running on fish oil biodiesel, *Energy*, 116, 1218-1229, (2016).
9. G. Gonca and E. Dobrucali, Theoretical and experimental study on the performance of a diesel engine fueled with diesel-biodiesel blends, *Renewable Energy*, 93, 658-666, (2016).
10. P. Karin, H. Oki, K. Hanamura and C. Charoenphonphanich, Nanostructures and Oxidation Kinetics of Diesel Particulate Matters, *Journal of Research and Applications in Mechanical Engineering*, 1(2), 3-8, (2012).
11. P. Karin, M. Borhanipour, Y. Songsaengchan, S. Laosuwan, C. Charoenphonphanich, N. Chollacoop and K. Hanamura, Oxidation kinetics of small CI engine's biodiesel particulate matter. *International Journal of Automotive Technology*, 16(2), 211-219, 2015.
12. P. Karin, J. Boonsakda, K. Siricholathum, E. Saenkhumvong, C. Charoenphonphanich and K. Hanamura, Morphology and oxidation kinetics of CI engine's biodiesel particulate matters on cordierite Diesel Particulate Filters using TGA. *International Journal of Automotive Technology*, 18(1), 31-40, (2017).
13. T. Ishiguro, Y. Takatori and K. Akihama, Microstructure of diesel soot particles probed by electron microscopy: First observation of inner core and outer shell. *Combustion and Flame* 108(1), 231−234, (1997).
14. R. L. Vander Wal, A. Yezerets, N. W. Currier, D. H. Kim and C. H. Wang, HRTEM study of diesel soot collected from diesel particulate filters, *Carbon,* 45(1), 70−77, (2007).
15. D. B. Kittelson, Engines and nanoparticles: A review. *J. Aerosol Science*, 29(5-6), 575−588, (1998).

ACKNOWLEDGMENTS

The authors gratefully acknowledge the support from Bangchak Corporation Public Co., Ltd., FOCUSLAB Ltd., Thailand Research Fund (TRF), KMITL and NSTDA.

This material is reserved for educational use only, not allowed for commercial use.
Forbidden to modify the content, and cite the document when use.

APPENDIX F:

COMMENTS AND QUESTIONS FROM THESIS DEFENSE

Comments and Questions from Thesis Defense

Topic :

Characterization of Morphology, Nanostructure, and Oxidation Kinetics of Biofuel Particulate Matters

Date :

30 November 2017

Place :

NSTDA Rangsit 2 (Thailand)

and

Tokyo Institute of Technology (Japan)

Examiners :

Asst. Prof. Dr. Chinda Charoenphonphanich (KMITL)

Asst. Prof. Dr. Preechar Karin (KMITL)

Prof. Dr. Katsunori Hanamura (Tokyo Tech)

Dr. Nuwong Chollacoop (NSTDA)

Dr. Manida Tongroon (NSTDA)

Student :

Park Watanawongskorn

This material is reserved for educational use only, not allowed for commercial use.
Forbidden to modify the content, and cite the document when use.

Q1) Uncertainty of Carbon Fringe in "2D TEM images → 3D calculation" is not included. How to be sure that the model is correct. Some factor is needed for 3D calculation. (Prof. Dr. Hanamura and Dr. Nuwong)

From 2D TEM image to 3D Calculation, there are 6 main factors contributing to Carbon atom and soot density estimation as following and details of each factors are described in Table1.

1. Fringe properties
2. Fringe population
3. Fringe size
4. Fringe shape
5. Fringe space
6. Calculation model

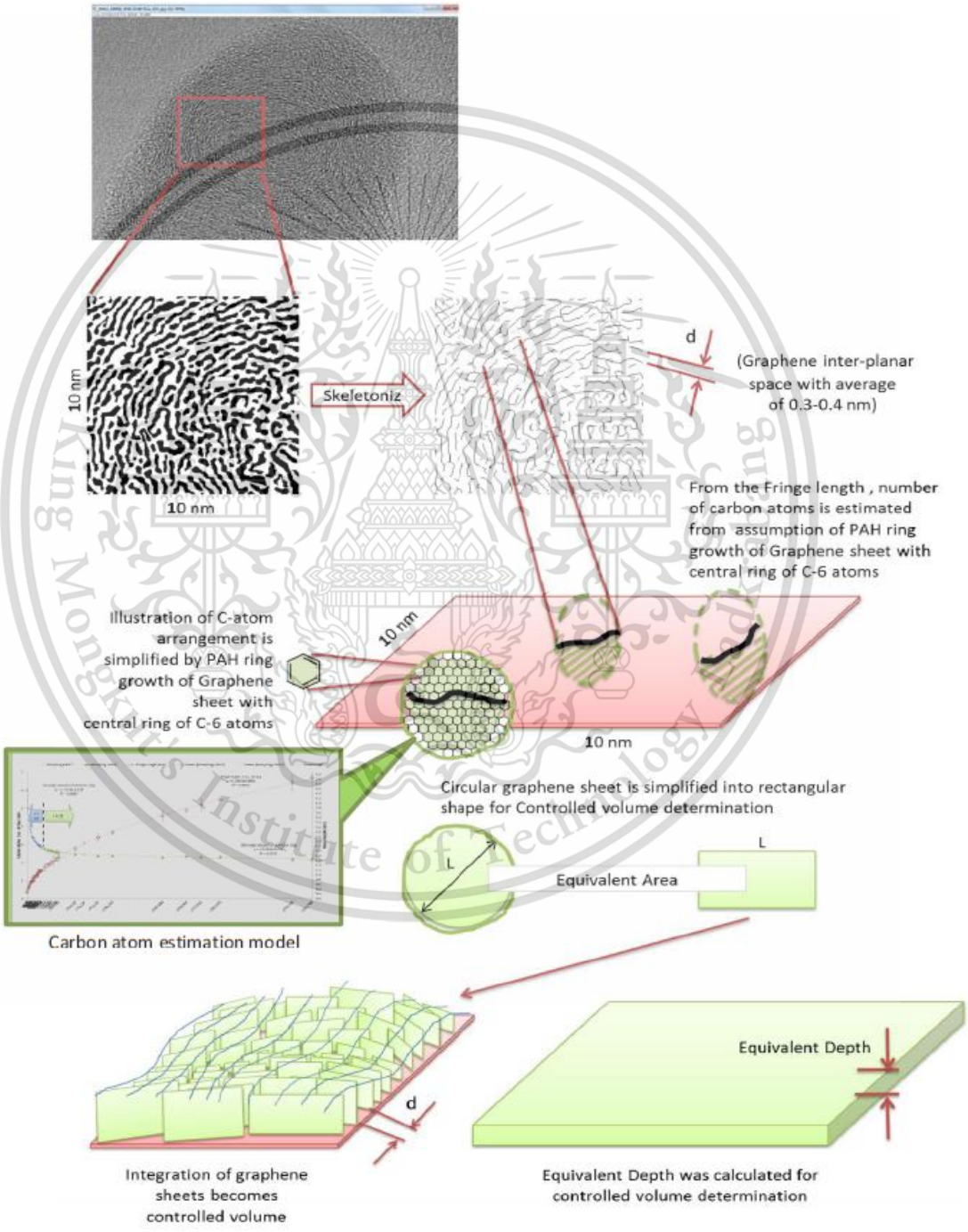

Fig. 1 Procedure for carbon atom and soot density estimation

This material is reserved for educational use only, not allowed for commercial use.
Forbidden to modify the content, and cite the document when use.

Table 1 _ Factors to carbon atom and soot density estimation

Factors	Possible Uncertainty due to the factors	Really Considered as uncertainty??	How to verify?	Amount of uncertainty			
				Over Estimation	Quantity	Under Estimation	Quantity
Fringe Properties	Carbon fringes might not be Graphite structures	No	**Compare Carbon fringe VS Graphite structure properties** A. Soot elemental component is Carbon → same as Graphite B. TEM Observation with electron scattering curve • Onion-like subunits (Ishiguro et al)  • Parallel sheets perpendicular to soot particle's radius **Confirmed by electron scattering curve VS Porod's law (Braun's Paper)** 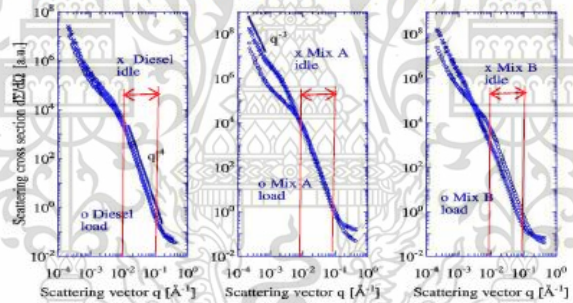 " Sharp e^- density transition found in soot primary particle zone (q of 0.01 - 0.1)" → This sharp e^- density transition mostly occurs in "Parallel structure" 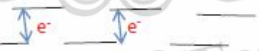 Carbon allotropes which has unique Parallel sheet structure is "Graphite" 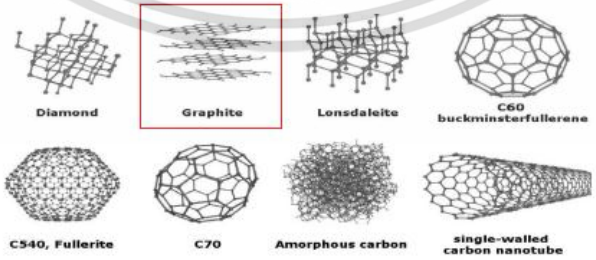 C. Electrical conductivity				

Factors	Possible Uncertainty due to the factors	Really Considered as uncertainty??	How to verify?	Amount of uncertainty			
				Over Estimation	Quantity	Under Estimation	Quantity
Fringe Population	Uncleared fringe poplation on TEM images 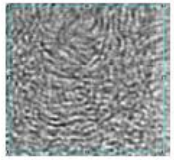	Yes	By considering TEM Mechanism 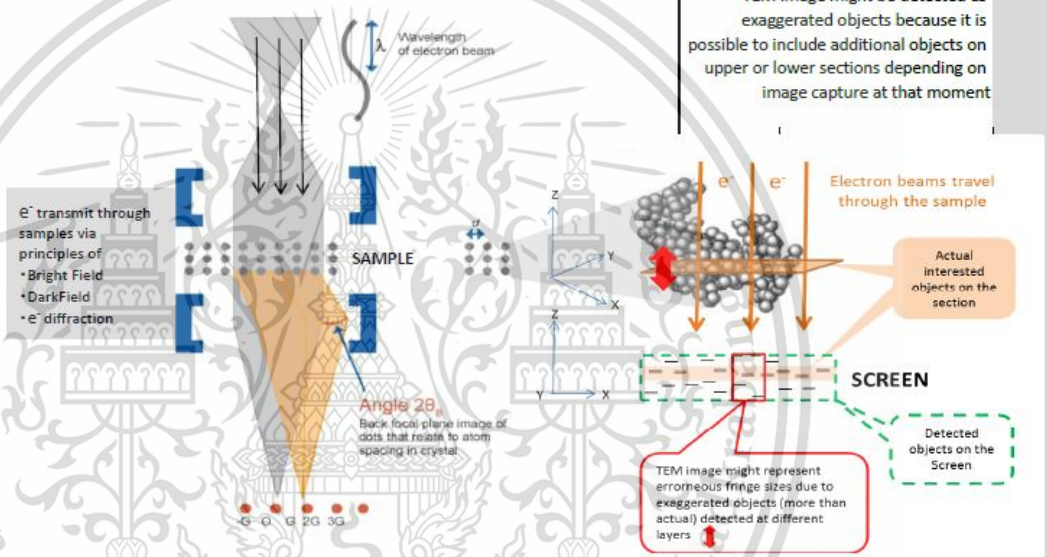	Yes	TEM image might be detected as exaggerated objects because it is possible to include additional objects on upper or lower sections depending on image capture at that moment		
Fringe Size	Image J processing Error in extraction of Black and White image 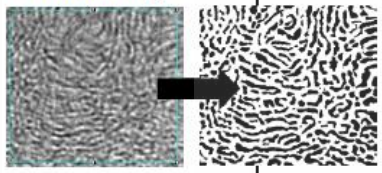	Yes	Check and estimate error of Black and White image extraction	Yes	Fringe Length error Approximately 3 - 10 pixels with scale of 46 pixels/nm length → **Error in Fringe size of 0.065 nm to 0.217 nm**	Yes	Fringe Length error Approximately 3 - 10 pixels with scale of 46 pixels/nm length → **Error in Fringe size of 0.065 nm to 0.217 nm**
Fringe Size	Fringe sizes from TEM observation are not reliable (Observation ≠ Actual object)	No	Compare with Experimental results Proved by P. Parent et al. (France Paper) L_s from TEM images range : 2.5 nm ~ 3.66 nm L_s from Ramen experiment - Equation range : 2.6 nm ~ 3.06 nm				

King Mongkut's Institute of Technology

Factors	Possible Uncertainty due to the factors	Really Considered as uncertainty??	How to verify?	Amount of uncertainty			
				Over Estimation	Quantity	Under Estimation	Quantity
Fringe Size	Fringe sizes from TEM observation are not reliable	No	Compare average results with Other researchers @ similar fuel/combustion Ethelyne+Butanol in Flame burners : 0.79 nm ~ 1.26 nm Diesel soot with unknown treatments : 0.4 nm ~ 2.0 nm Post-flame gases by FT : 1.5 nm ~ 2.0 nm Jet engine by HRJ and JP-8 : 0.8 nm ~ 1.15 nm 2.5L Diesel engine : 0.97 nm Small diesel engine by Yutthana KMITL : 1.5 nm ~ 2.0 nm **PARK'S DIESEL ENGINE :** 0.93 ~ 1.45 nm				
Fringe Shape	Carbon fringe sheets might not be circular shape as applied in prediction model 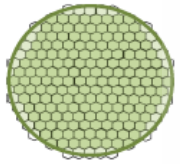	Yes	So far, none of researchers can predict exact shape of graphite sheets	Yes	Carbon fringe might be measured at largest dimension → Estimation results might be exaggerated 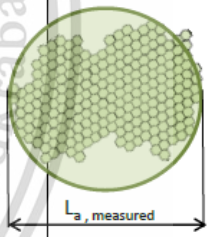	Yes	Carbon fringe might be measured at smallest dimension →Estimation results might be under estimated 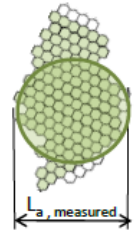
Fringe Space	Adjacent fringe space from TEM observation is not reliable	No	Compare with Experimental results from other researchers Proof by France Paper with TEM diffraction Adjacent fringe space or d_{002} **spacing :** 0.36 nm ~ 0.37 nm 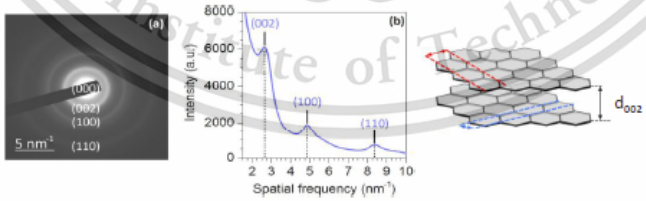 Proof by Braun Paper with X-ray density method Adjacent fringe space or d_{002} **spacing :** 0.372 nm **Park's TEM observation** Adjacent fringe space or d_{002} **spacing :** 0.3 nm ~ 0.4 nm				

Factors	Possible Uncertainty due to the factors	Really Considered as uncertainty??	How to verify?	Amount of uncertainty			
				Over Estimation	Quantity	Under Estimation	Quantity
Calculation Model	Calculation Model cannot correspond to all Fringe sizes correctly **See attached calculation sheet **	Yes	Investigate all possible Fringe size and compare with results from the calculation model at each cases of hexagonal ring structures 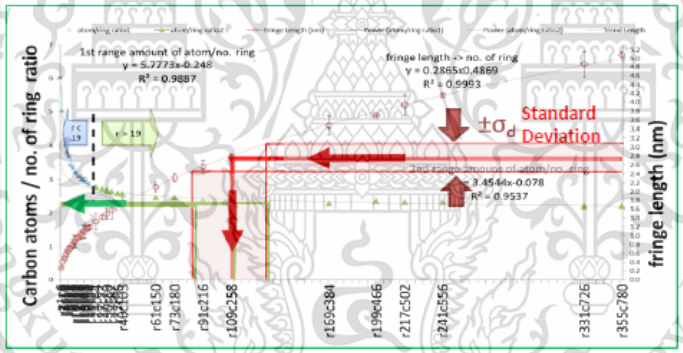	Yes	Standard deviation of Fringe size at all cases of hexagonal rings with respect to the model's equation, σ_d = **0.1023** nm To consider practical uncertainty , select Fringe size tolerance of $3\sigma_d$. **Carbon atom density** at upper tolerance or due to Fringe with oversize **(+3σd)** can be **+24.64%** **more than nominal value**	Yes	Standard deviation of Fringe size at all cases of hexagonal rings with respect to the model's equation, σ_d = **0.1023** nm To consider practical uncertainty , select Fringe size tolerance of $3\sigma_d$. **Carbon atom density** at lower tolerance or due to too small Fringe size **(-3σd)** can be **-19.41%** **less than nominal** value

King Mongkut's Institute of Technology Ladkrabang

Calculation sheet : Error estimation of the calculation model

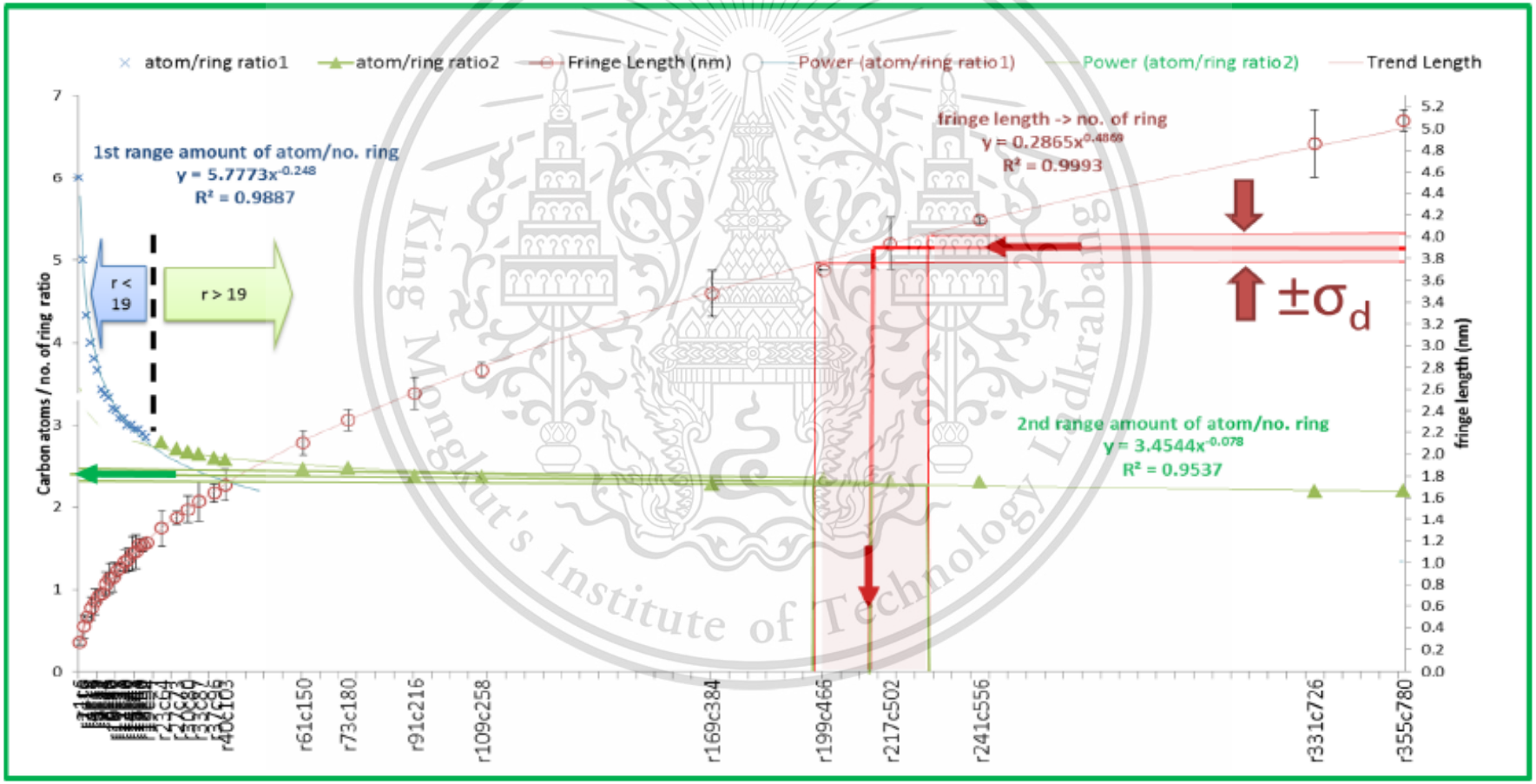

From the relationship of Fringe length and Hexagonal rings, $L_{regression} = 0.2895 \times (\text{no. of ring})^{0.4869}$ and all cases of possible fringe length wrt each hexagonal rings, calculation is shown below

Only error from the model

Standard deviation of $L_{regression}$, σ_d 0.1023 nm

Including error from extraction of Black and White images with 0.065 - 0.217 nm

Total tolerance , σ_t = = SQRT($(3\sigma_d)^2$+0.217^2) 0.3759 nm

Range all counted data (nm)	% wrt all fuels		Min estimation (-3 σ_d)	@Mode calculation	Max estimation (+3 σ_d)	Range all counted data (nm)	% wrt all fuels		Min estimation (-σ_t)	@Mode calculation	Max estimation (+ σ_t)
			limit @ 0.265 possible smallest 1						limit @ 0.265 possible smallest 1		
range 0-0.6	25.5	Fringe length	ring 0.3248		0.6317	range 0-0.6	25.5	Fringe length	ring 0.3248		0.7007
		no. ring =						**no. ring =**			
		(L / 0.2865)^(1 / 0.4869)	0.8520	1.2939	5.0728			(L / 0.2865)^(1 / 0.4869)	0.8520	1.2939	6.2759
		C / no. ring ratio						C / no. ring ratio			
		< 19 ring :						< 19 ring :			
		C ratio = 5.7773*x^(-0.248)	6.0115	5.4196	3.8621			C ratio = 5.7773*x^(-0.248)	6.0115	5.4196	3.6635
		> 19 ring :						> 19 ring :			
		C ratio = 3.4544*x^(-0.078)						C ratio = 3.4544*x^(-0.078)			
		Carbon atoms	5.1215	7.0127	19.5917			**Carbon atoms**	5.1215	7.0127	22.9920
		Equivalent graphene height						**Equivalent graphene height**			
		Circle area/fringe length	0.2081	0.2551	0.4961			Circle area/fringe length	0.2081	0.2551	0.5503
		product						product			
		height * length	0.0552	0.0829	0.3134			height * length	0.0552	0.0829	0.3856
range 0.6-1.2	34.5	Fringe length	0.4371	0.7440	1.0509	range 0.6-1.2	34.5	Fringe length	0.3681	0.7440	1.1199
		no. ring =						**no. ring =**			
		(L / 0.2865)^(1 / 0.4869)	2.3811	7.0990	14.4293			(L / 0.2865)^(1 / 0.4869)	1.6735	7.0990	16.4415
		C / no. ring ratio						C / no. ring ratio			
		< 19 ring :						< 19 ring :			
		C ratio = 5.7773*x^(-0.248)	4.6589	3.5533	2.9801			C ratio = 5.7773*x^(-0.248)	5.0847	3.5533	2.8852
		> 19 ring :						> 19 ring :			
		C ratio = 3.4544*x^(-0.078)						C ratio = 3.4544*x^(-0.078)			
		Carbon atoms	11.0934	25.2247	43.0009			**Carbon atoms**	8.5091	25.2247	47.4366
		Equivalent graphene height						**Equivalent graphene height**			
		Circle area/fringe length	0.3433	0.5843	0.8254			Circle area/fringe length	0.2891	0.5843	0.8795
		product						product			
		height * length	0.1501	0.4347	0.8674			height * length	0.1064	0.4347	0.9850
range 1.2-1.8	18.3	Fringe length	0.8995	1.2064	1.5133	range 1.2-1.8	18.3	Fringe length	0.8305	1.2064	1.5823
		no. ring =						**no. ring =**			
		(L / 0.2865)^(1 / 0.4869)	10.4831	19.1571	30.5137			(L / 0.2865)^(1 / 0.4869)	8.8989	19.1571	33.4384
		C / no. ring ratio						C / no. ring ratio			
		< 19 ring :						< 19 ring :			
		C ratio = 5.7773*x^(-0.248)	3.2258					C ratio = 5.7773*x^(-0.248)	3.3596		
		> 19 ring :						> 19 ring :			
		C ratio = 3.4544*x^(-0.078)		2.7438	2.6460			C ratio = 3.4544*x^(-0.078)		2.7438	2.6271
		Carbon atoms	33.8169	52.5631	80.7377			**Carbon atoms**	29.8969	52.5631	87.8471
		Equivalent graphene height						**Equivalent graphene height**			
		Circle area/fringe length	0.7065	0.9475	1.1885			Circle area/fringe length	0.6523	0.9475	1.2427
		product						product			
		height * length	0.6355	1.1431	1.7986			height * length	0.5418	1.1431	1.9663

Range all counted data (nm)	% wrt all fuels		Min estimation (-3 σ_d)	@Mode calculation	Max estimation (+3 σ_d)
range 1.8-2.4	10.0	Fringe length	1.9716	2.2785	2.5854
		no. ring =			
		(L / 0.2865)^(1 / 0.4869)	52.5369	70.7141	91.6677
		C / no. ring ratio			
		< 19 ring :			
		C ratio = 5.7773*x^(-0.248)			
		> 19 ring :			
		C ratio = 3.4544*x^(-0.078)	2.5362	2.4781	2.4284
		Carbon atoms	133.2419	175.2335	222.6056
		Equivalent graphene height			
		Circle area/fringe length	1.5485	1.7895	2.0306
		product			
		height * length	3.0530	4.0774	5.2498
range 2.4-3.0	5.2	Fringe length	2.2506	2.5575	2.8644
		no. ring =			
		(L / 0.2865)^(1 / 0.4869)	68.9472	89.6476	113.1418
		C / no. ring ratio			
		< 19 ring :			
		C ratio = 5.7773*x^(-0.248)			
		> 19 ring :			
		C ratio = 3.4544*x^(-0.078)	2.4830	2.4326	2.3889
		Carbon atoms	171.1925	218.0787	270.2795
		Equivalent graphene height			
		Circle area/fringe length	1.7676	2.0087	2.2497
		product			
		height * length	3.9782	5.1371	6.4440
range 3.0-3.6	2.5	Fringe length	2.9551	3.2620	3.5689
		no. ring =			
		(L / 0.2865)^(1 / 0.4869)	120.6226	147.7615	177.7310
		C / no. ring ratio			
		< 19 ring :			
		C ratio = 5.7773*x^(-0.248)			
		> 19 ring :			
		C ratio = 3.4544*x^(-0.078)	2.3770	2.3396	2.3062
		Carbon atoms	286.7146	345.7069	409.8778
		Equivalent graphene height			
		Circle area/fringe length	2.3209	2.5620	2.8030
		product			
		height * length	6.8586	8.3571	10.0037

Range all counted data (nm)	% wrt all fuels		Min estimation (-σ_t)	@Mode calculation	Max estimation (+ σ_t)
range 1.8-2.4	10.0	Fringe length	1.9026	2.2785	2.6544
		no. ring =			
		(L / 0.2865)^(1 / 0.4869)	48.8320	70.7141	96.7605
		C / no. ring ratio			
		< 19 ring :			
		C ratio = 5.7773*x^(-0.248)			
		> 19 ring :			
		C ratio = 3.4544*x^(-0.078)	2.5507	2.4781	2.4182
		Carbon atoms	124.5541	175.2335	233.9841
		Equivalent graphene height			
		Circle area/fringe length	1.4943	1.7895	2.0847
		product			
		height * length	2.8431	4.0774	5.5337
range 2.4-3.0	5.2	Fringe length	2.1816	2.5575	2.9334
		no. ring =			
		(L / 0.2865)^(1 / 0.4869)	64.6779	89.6476	118.8077
		C / no. ring ratio			
		< 19 ring :			
		C ratio = 5.7773*x^(-0.248)			
		> 19 ring :			
		C ratio = 3.4544*x^(-0.078)	2.4954	2.4326	2.3798
		Carbon atoms	161.3947	218.0787	282.7349
		Equivalent graphene height			
		Circle area/fringe length	1.7134	2.0087	2.3039
		product			
		height * length	3.7381	5.1371	6.7581
range 3.0-3.6	2.5	Fringe length	2.8861	3.2620	3.6379
		no. ring =			
		(L / 0.2865)^(1 / 0.4869)	114.9118	147.7615	184.8569
		C / no. ring ratio			
		< 19 ring :			
		C ratio = 5.7773*x^(-0.248)			
		> 19 ring :			
		C ratio = 3.4544*x^(-0.078)	2.3860	2.3396	2.2991
		Carbon atoms	274.1757	345.7069	425.0061
		Equivalent graphene height			
		Circle area/fringe length	2.2668	2.5620	2.8572
		product			
		height * length	6.5422	8.3571	10.3940

Range all counted data (nm)	% wrt all fuels		Min estimation (-3 σ_d)	@Mode calculation	Max estimation (+3 σ_d)
range 3.6-4.2	2.3	Fringe length	3.6485	3.9554	4.2623
		no. ring =			
		(L / 0.2865)^(1 / 0.4869)	185.9681	219.5220	255.9361
		C / no. ring ratio			
		< 19 ring :			
		C ratio = 5.7773*x^(-0.248)			
		> 19 ring :			
		C ratio = 3.4544*x^(-0.078)	2.2980	2.2685	2.2415
		Carbon atoms	427.3609	497.9839	573.6802
		Equivalent graphene height			
		Circle area/fringe length	2.8655	3.1066	3.3476
		product			
		height * length	10.4549	12.2877	14.2685
range 4.2-4.8	1.0	Fringe length	4.4826	4.7895	5.0964
		no. ring =			
		(L / 0.2865)^(1 / 0.4869)	283.8451	325.1992	369.4431
		C / no. ring ratio			
		< 19 ring :			
		C ratio = 5.7773*x^(-0.248)			
		> 19 ring :			
		C ratio = 3.4544*x^(-0.078)	2.2235	2.2000	2.1782
		Carbon atoms	631.1226	715.4419	804.7323
		Equivalent graphene height			
		Circle area/fringe length	3.5206	3.7617	4.0027
		product			
		height * length	15.7816	18.0165	20.3994
range 4.8-5.4	0.6	Fringe length	4.5048	4.8117	5.1186
		no. ring =			
		(L / 0.2865)^(1 / 0.4869)	286.7446	328.3077	372.7613
		C / no. ring ratio			
		< 19 ring :			
		C ratio = 5.7773*x^(-0.248)			
		> 19 ring :			
		C ratio = 3.4544*x^(-0.078)	2.2217	2.1984	2.1767
		Carbon atoms	637.0643	721.7449	811.3942
		Equivalent graphene height			
		Circle area/fringe length	3.5381	3.7791	4.0202
		product			
		height * length	15.9385	18.1842	20.5778

Range all counted data (nm)	% wrt all fuels		Min estimation (-σ_t)	@Mode calculation	Max estimation (+ σ_t)
range 3.6-4.2	2.3	Fringe length	3.5795	3.9554	4.3313
		no. ring =			
		(L / 0.2865)^(1 / 0.4869)	178.8201	219.5220	264.5140
		C / no. ring ratio			
		< 19 ring :			
		C ratio = 5.7773*x^(-0.248)			
		> 19 ring :			
		C ratio = 3.4544*x^(-0.078)	2.3051	2.2685	2.2357
		Carbon atoms	412.1928	497.9839	591.3850
		Equivalent graphene height			
		Circle area/fringe length	2.8114	3.1066	3.4018
		product			
		height * length	10.0633	12.2877	14.7340
range 4.2-4.8	1.0	Fringe length	4.4136	4.7895	5.1654
		no. ring =			
		(L / 0.2865)^(1 / 0.4869)	274.9485	325.1992	379.7844
		C / no. ring ratio			
		< 19 ring :			
		C ratio = 5.7773*x^(-0.248)			
		> 19 ring :			
		C ratio = 3.4544*x^(-0.078)	2.2290	2.2000	2.1735
		Carbon atoms	612.8616	715.4419	825.4787
		Equivalent graphene height			
		Circle area/fringe length	3.4665	3.7617	4.0569
		product			
		height * length	15.2997	18.0165	20.9552
range 4.8-5.4	0.6	Fringe length	4.4359	4.8117	5.1876
		no. ring =			
		(L / 0.2865)^(1 / 0.4869)	277.8011	328.3077	383.1499
		C / no. ring ratio			
		< 19 ring :			
		C ratio = 5.7773*x^(-0.248)			
		> 19 ring :			
		C ratio = 3.4544*x^(-0.078)	2.2272	2.1984	2.1721
		Carbon atoms	618.7217	721.7449	832.2209
		Equivalent graphene height			
		Circle area/fringe length	3.4839	3.7791	4.0743
		product			
		height * length	15.4542	18.1842	21.1360

Range all counted data (nm)	% wrt all fuels		Min estimation (-3 σ_d)	@Mode calculation	Max estimation (+3 σ_d)
range 5.4-6.0	0.1	Fringe length	5.4302	5.7371	6.0440
		no. ring =			
		(L / 0.2865)^(1 / 0.4869)	420.8526	471.1598	524.3851
		C / no. ring ratio			
		< 19 ring :			
		C ratio = 5.7773*x^(-0.248)			
		> 19 ring :			
		C ratio = 3.4544*x^(-0.078)	2.1562	2.1373	2.1195
		Carbon atoms	907.4453	1007.0098	1111.4508
		Equivalent graphene height			
		Circle area/fringe length product	4.2648	4.5059	4.7469
		height * length	23.1588	25.8506	28.6903
		Average Carbon atoms	61.5490	81.5300	108.3620
		Interest area , A			
		Average Height of Fringe	1.4820	1.5819	1.6868
		Interest Volume	1.4820A	1.5819A	1.6868A
		Density, Carbon atoms / nm^3	**41.531/A**	**51.5393/A**	**64.2412/A**
			-19.41%	0	+24.64%

Range all counted data (nm)	% wrt all fuels		Min estimation (-σ_t)	@Mode calculation	Max estimation (+ σ_t)
range 5.4-6.0	0.1	Fringe length	5.3612	5.7371	6.1129
		no. ring =			
		(L / 0.2865)^(1 / 0.4869)	409.9480	471.1598	536.7485
		C / no. ring ratio			
		< 19 ring :			
		C ratio = 5.7773*x^(-0.248)			
		> 19 ring :			
		C ratio = 3.4544*x^(-0.078)	2.1606	2.1373	2.1157
		Carbon atoms	885.7447	1007.0098	1135.5894
		Equivalent graphene height			
		Circle area/fringe length product	4.2107	4.5059	4.8011
		height * length	22.5743	25.8506	29.3488
		Average Carbon atoms	57.5840	81.5300	114.9886
		Interest area , A			
		Average Height of Fringe	1.4652	1.5819	1.7178
		Interest Volume	1.4652A	1.5819A	1.7178A
		Density, Carbon atoms / nm^3	**39.3011/A**	**51.5393/A**	**66.9395/A**
			-23.74%	0	+29.88%

From the Table1, it can be seen that uncertainty which affects carbon atom estimation are **"Unclear Fringe population on TEM images", "Image J processing error", "Unpredictable Fringe shape", and "Uncertainty from calculation model"**

However, the **uncertainty that cannot be estimated** comes from
1) Mechanism on TEM image acquisition
2) Unpredictable Fringe shape

For the **uncertainty that can be estimated**,
1) **Fringe length** uncertainty from Image processing method : 0.065 nm to 0.217 nm
2) **Fringe length** uncertainty from Calculation model : Std. deviation = 0.1023 nm

Combination of the Fringe length uncertainty yields the **uncertainty of carbon atom density in the range of : up to 23.74% lower or 29.88% greater** than nominal value compared with the calculation model. (See attached calculation sheet)

King Mongkut's Institute of Technology Ladkrabang

This material is reserved for educational use only, not allowed for commercial use.
Forbidden to modify the content, and cite the document when use.

Q2) Fringe length scale in the presentation material page 39 is not accurate. (Dr. Nuwong)

Fringe length scale presented in the reseach was 0.2nm resolution , while other researchers measured at 0.1 nm resolution.

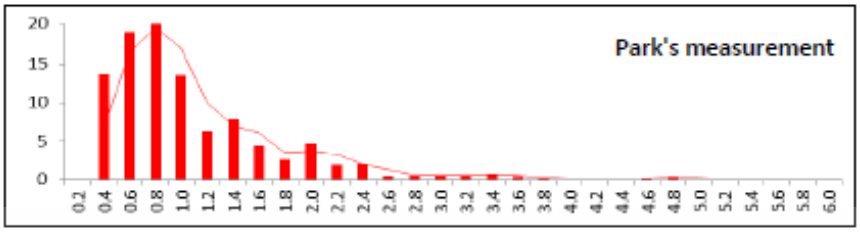

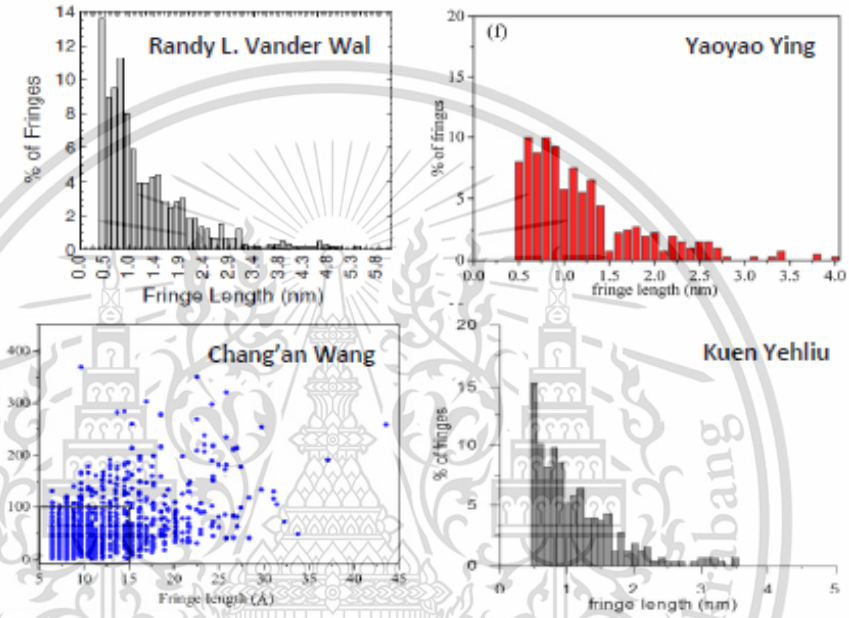

However, after adjustment to 0.1 nm resolution, results yields similar trends with previous measurement (0.2 nm resolution) among each fuel type, while BE20 fringes are dominant at smaller size, B100 at medium size, and Diesel fringes can be found at 5.2 and 5.8 nm.

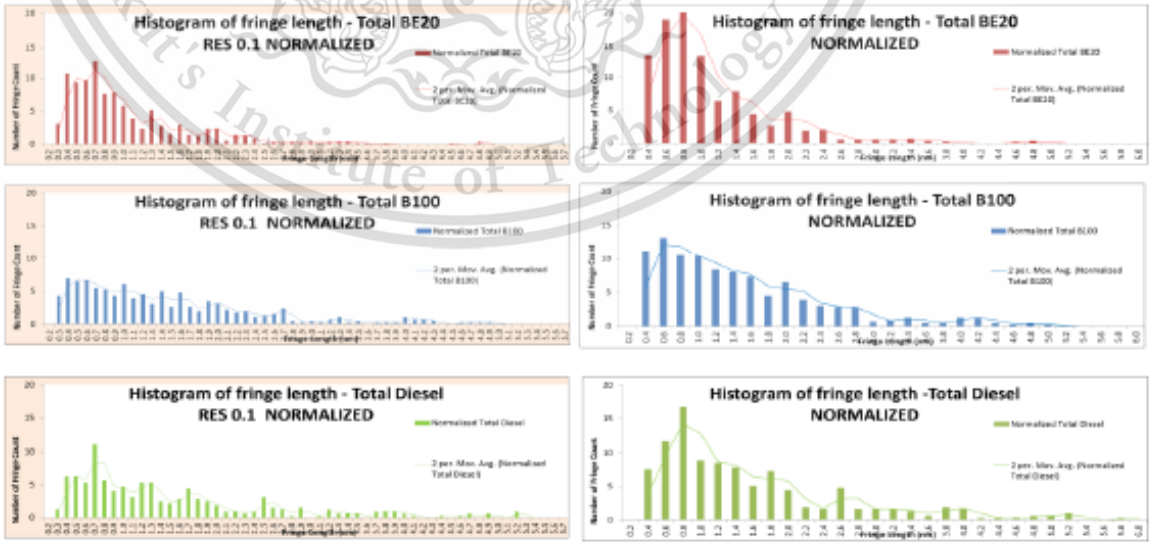

This material is reserved for educational use only, not allowed for commercial use.
Forbidden to modify the content, and cite the document when use.

Q3) According the location of oxygen molecules/atoms on soot in oxidation process, explain dimensional relationships of oxygen molecules/atoms and carbon fringe. (Prof. Dr. Hanamura)

Schematic diagrams of -O, -OH on carbon fringe at soot formation, and O_2 penetrating through carbon fringe at soot oxidation from the presentation material are shown below

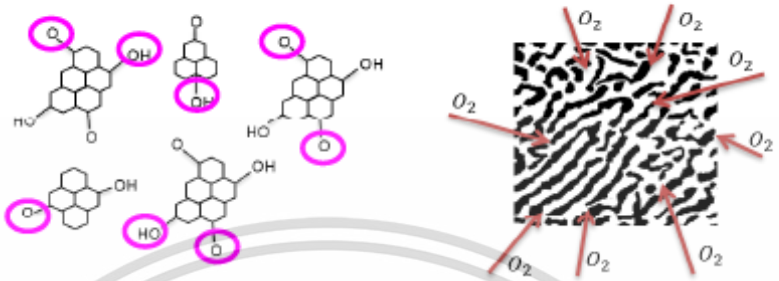

Dimensional relationships of -O, -OH, and carbon fringe should be described with consideration of the terms "Covalent bond distance or Bond length" and "Van der waal Radius"

"Covalent Bond Distance" or Bond Length is defined by the internuclear distance between two covalently bonded atoms. "Van der Waals Radius" is defined as half of the internuclear separation of two non-bonded atoms of the same element on their closest possible approach .

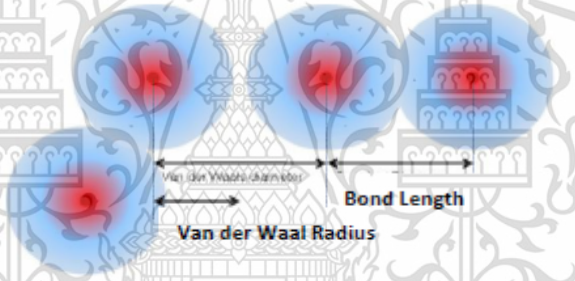

Fig. 3.1 Schematics of Van der Waal Radius and Bond Length[1]

Table 3.1 Van-der-Waals Radius and Bond Length [2],[3]

		Picometre
Van der Waal Radius	H	120
	C	170
	O	152
Bond Length	O-H	96
	O=O	132-146
	C-O	143

Fig. 3.2 Schematics of Element and Bonded element sizes according to Van der Waal Radius and Bond Length (**True dimensional scale**)

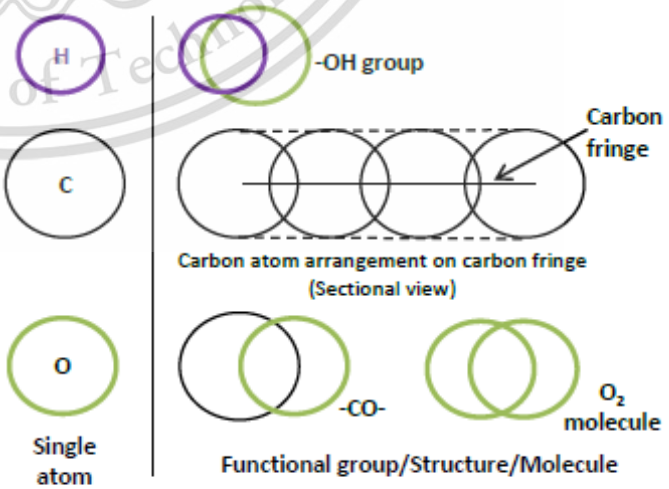

This material is reserved for educational use only, not allowed for commercial use.
Forbidden to modify the content, and cite the document when use.

Fig. 3.3 Schematic diagram of -O or -OH location on carbon fringe at soot formation (sectional view)

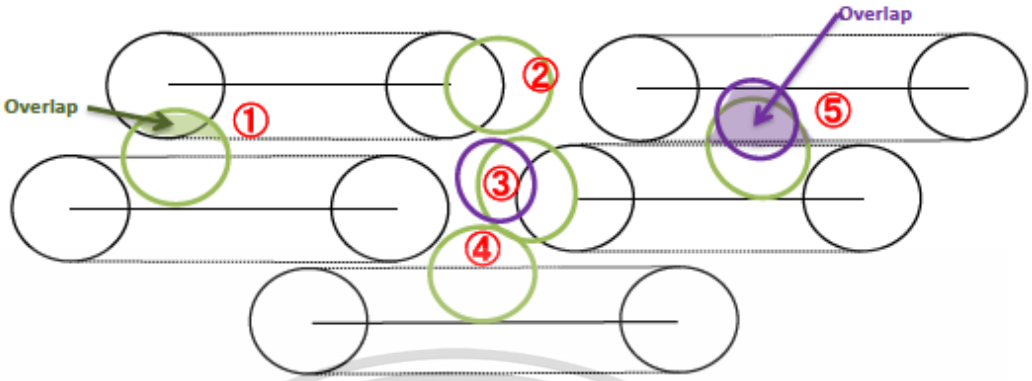

From the experimental result in the thesis, carbon fringe space was found at 0.3-0.4 nm. According to the space limit, -O or -OH is difficult to interfere between carbon fringe layers as shown on ① and ⑤. Therefore, -O or -OH can be found on edge portions of the carbon fringe as shown on space ② and ③ (This is true when there is adequate space between edge portion of the carbon fringe e.g. more than 0.5 nm) However, -O or -OH can be connected to middle portion of carbon fringe if there is enough space on edge portion of adjacent fringes as shown on ④.

Fig. 3.4 Schematic diagram of O_2 molecule penetration through carbon fringe at soot oxidation (Sectional view)

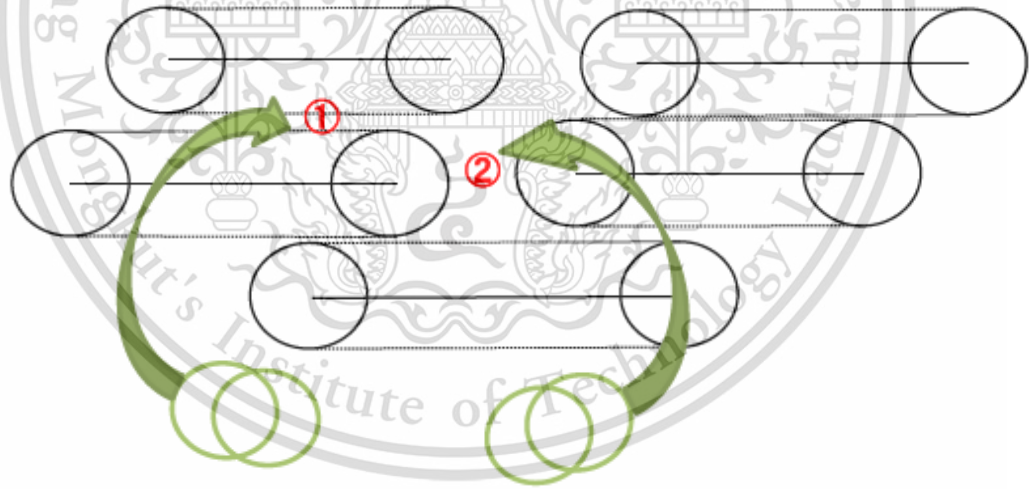

Referring Fig. 2.3, oxygen molecules are easier to penetrate carbon fringes through inner core of primary particles via path ② because of more space. Moreover, oxidizing agents such as -O or -OH are located at the fringe edge portions. As a result, oxidation tends to occur at the edges of carbon fringe.

[1] https://chem.libretexts.org/Core/Physical_and_Theoretical_Chemistry/Chemical_Bonding/Fundamentals_of_Chemical_Bonding/Covalent_Bond_Distance%2C_Radius_and_van_der_Waals_Radius

[2] http://www.crystalmaker.com/support/tutorials/crystalmaker/atomic-radii/index.html

[3] https://archive.org/stream/Chemistry_10th_Edition_Raymond_Chang#page/n9/mode/2up

This material is reserved for educational use only, not allowed for commercial use.
Forbidden to modify the content, and cite the document when use.

Q4) Need more review of Activation Energy from Diesel and Biodiesel soot oxidation
(Prof. Dr. Hanamura and Dr. Nuwong)

Activation energy values of Diesel and Biodiesel soot are compared in the table below. It can be seen that experimental results in this research are not significant different from other researchers.

Researcher	Experimental condition	Activation energy (kJ/mol)
Diesel soot		
Park (This Thesis)	Small diesel engine	**166**
Karin P.[1]	Small diesel engine	153-165
Isabel C. Jaramillo[2]	Flame burner	136-142
Aleksey Yezerets[3]	Filtered by DPF with catalyst	146
Kyeong O. Lee[4]	TGA with NO_2,CO_2,O_2 as reactant	154-159
Hwan S. Chong[5]	Light duty diesel engine	148-149
Biodiesel soot		
Park (This Thesis)	Small diesel engine	**118**
Karin P.[1]	Small diesel engine	147-157
X.J. Man[6]	4.3L Diesel engine with wide Torque range	77.8-114
J. Rodríguez-Fernandez[7]	Filtered by DPF both charge and regenerative mode	84-117

[1] 10. P. Karin, J. Boonsakda, K. Siricholathum, E. Saenkhumvong, C. Charoenphonphanich, and K. Hanamura,
[2] https://doi.org/10.1016/j.combustflame.2014.04.016
[3] https://doi.org/10.1016/j.cattod.2003.08.003
[4] https://doi.org/10.1016/j.proci.2012.06.121
[5] Hwan S. Chong , Suresh K. Aggarwal , Kyeong O. Lee , Seung Y. Yang & Heeje Seong (2013) Experimental Investigation on the Oxidation Characteristics of Diesel Particulates Relevant to DPF Regeneration, Combustion Science and Technology, 185:1, 95-121
[6] https://doi.org/10.1016/j.egypro.2015.02.020
[7] 10.1021/ef200194m

This material is reserved for educational use only, not allowed for commercial use.
Forbidden to modify the content, and cite the document when use.

Q5) Calculate Particle Collision Frequency Factor or Pre-exponential Factor A and compare with the values of other gaseous chemical reaction (Prof. Dr. Hanamura)

Pre-exponential factor values for some gas phase reactions vary from $1.99*10^5$ to 10^{12} as shown in Table1 and Table2.

Table 1. Some gas phase reactions and their observed and calculated logarithmic values of Arrhenius frequency factors (A).[1]

Reaction	Log A, mole-1 s Observed	A
$NO + O_3 \rightarrow NO_2 + O_2$	11.9	$1.47*10^5$
$NO_2 + F_2 \rightarrow NO_2F + F$	12.2	$1.99*10^5$
$NO_2 + CO \rightarrow NO + CO_2$	13.1	$4.89*10^5$
$2ClO \rightarrow Cl_2 + O2$	10.8	$4.90*10^4$
$2NOCl \rightarrow 2NO + Cl_2$	13.0	$4.42*10^5$
$NO + Cl_2 \rightarrow NOCl + Cl$	12.6	$2.97*10^5$

Table 2. Experimental rate constants compared to the ones predicted by collision theory for gas phase reactions [2]

Reaction	A (Azra frequency factor)
$2ClNO \rightarrow 2Cl + 2NO$	$9.4\ 10^9$
$2ClO \rightarrow Cl_2 + O_2$	$6.3\ 10^7$
$H_2 + C_2H_4 \rightarrow C_2H_6$	$1.24\ 10^6$
$Br_2 + K \rightarrow KBr + Br$	10^{12}

For soot oxidation reaction, researchers also figured out the Pre-exponential Factor, A as shown in Table3. It can be seen that A values for Diesel soot in this research are not significant different from other researchers

Table 3 Comparison of Pre-exponential Factor, A for soot oxidation reaction

Researcher	Experimental condition	Pre-exponential Factor , A
Isabel C. Jaramillo[3]	Flame burner (Diesel)	$7.40*10^2$
	Flame burner (Butanol)	$2.67*10^2$
Hwan S. Chong[4]	Light duty diesel engine	$4.34*10^6$ - $4.54*10^5$
Congwei Mei[5]	Carbon black with MoO_3 catalyst	$6.47*10^3$ - $8.88*10^6$
John P. A. Neeft[6]	Printex-U carbon black	$1.26*10^7$ - $1.87*10^7$
Park (This Thesis)	Small diesel engine	
	Diesel @TGA Air(O_2 = 21%)	**$2.67*10^6$** (lnA=14.80)
	Biodiesel @TGA Air(O_2 = 21%)	**$4.32*10^4$** (lnA=10.67)
	BE20 @TGA Air(O_2 = 21%)	**$1.18*10^2$** (lnA=4.77)

[1]D. R. Herschbach, H. S. Johnston, K. S. Pitzer and R. E. Powell, "Comparison of the Arrhenius Frequency Factors (A) of Some Gas-Phase Reactions," Journal of Chemistry Physics, Vol. 25, 1956, p. 73.
[2] https://en.wikipedia.org/wiki/Collision_theory
[3] https://doi.org/10.1016/j.combustflame.2014.04.016
[4] Hwan S. Chong , Suresh K. Aggarwal , Kyeong O. Lee , Seung Y. Yang & Heeje Seong (2013) Experimental Investigation on the Oxidation Characteristics of Diesel Particulates Relevant to DPF Regeneration, Combustion Science and Technology, 185:1, 95-121
[5] MEI, Congwei et al. Optimized Heating Rate and Soot-catalyst Ratio for Soot Oxidation over MoO3 Catalyst. Bulletin of Chemical Reaction Engineering & Catalysis, [S.l.], p. 408-414, oct. 2017. ISSN 1978-2993
[6] https://doi.org/10.1016/S0016-2361(97)00119-1

This material is reserved for educational use only, not allowed for commercial use.
Forbidden to modify the content, and cite the document when use.

Q6) Verify relationships between Nanostructure and Oxidation Kinetics of the Biodiesel(B100) PM that generated from different engines, **engine A and engine B.** (Dr. Nuwong)

From the research conclusion, soot Nanostructure and Oxidation Kinetics are numerically related as shown on below table.

Table 1 — Nanostructure | Oixdation Kinetics

Soot Type	BE20	B100	B100	Diesel
Engine Type	B	A	B	A
Avg carbon fringe length (nm)	0.93	1.23	1.35	1.45
Activation Energy (kJ/mol)	78.7	101.3	118.2	166.4
Carbon fringe density(atom/nm^3)	88.28	88.40	91.41	100.67
Frequency factor				
calculated as **lnA**	4.77	7.39	10.67	14.8
calculated as **A**	1.18E+02	1.63E+03	4.32E+04	2.67E+06
Primary particle size	29.08	27.96	27.03	29.82
Soot Reaction order (n_{carbon})	0.81	0.78	0.89	0.66

B100 soot properties from both Engine A and Engine B shows that the results comply with explanation in this research; as carbon fringe size is smaller, activation energy is reduced because soot oxidation is activated by attachment of -O, -OH, or other active radicals. As lighter carbon fringe density, lower collision opportunity, i.e. collision frequency factor reduces. As soot particle become smaller, soot reaction order tends to increase due to more particle surface.

With overall comparison among all soot types, BE20-B100-Diesel, almost Nanostructure and Oxidation Kinetics properties of all soots also conform with the above explanation , while B100 results are in the middle of BE20 and Diesel, except properties of primary particle size and reaction order. A possible cause might come from difficulty in reflection of accurate particle size to actual particle surfaces since particle geometry cannot 100% conform spherical shape as shown below (particle surface was estimated based on spherical geometry).

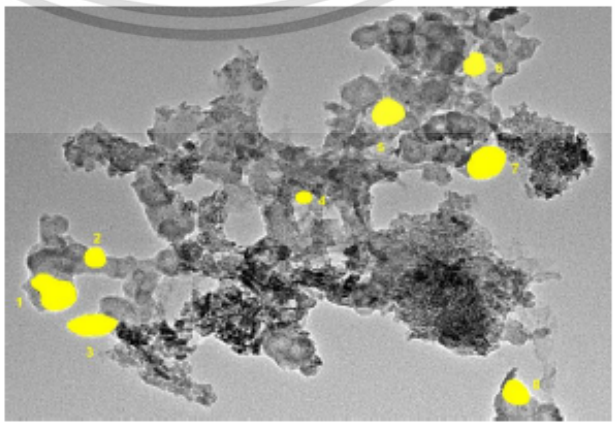

This material is reserved for educational use only, not allowed for commercial use.
Forbidden to modify the content, and cite the document when use.

Q7) Verify oxygen content and OH- functional group existence in biofuel's soot (Prof. Dr Hanamura and Dr. Chinda)

According to the mechanism of O- , OH- functional groups attachment on carbon fringe structure of biofuel's soot particles (especially BE20) which induce to lower soot activation energy in biofuel PM, Oxygen content was verified with the Labtest results as shown below. (Also refer attached Labtest report)

Operated by **Engine B**	BE20	B100	Diesel
Fuel's oxygen content	17.4%	13.0%	0.9%
Soot's oxygen content	17.97%	17.94%	7.11%

Oxygen content of biofuel's soot is apparently higher than Diesel soot. However,oxygen content from BE20 is curiously a little higher than that of B100's. Unfortunately, there is a limitation to further verification due to limited PM sample for the CHNS/O analysis.

To verify -OH functional group existence in BE20's soot particles, FT-IR analysis was performed as shown below.

Scientific Equipment Center , PSU.

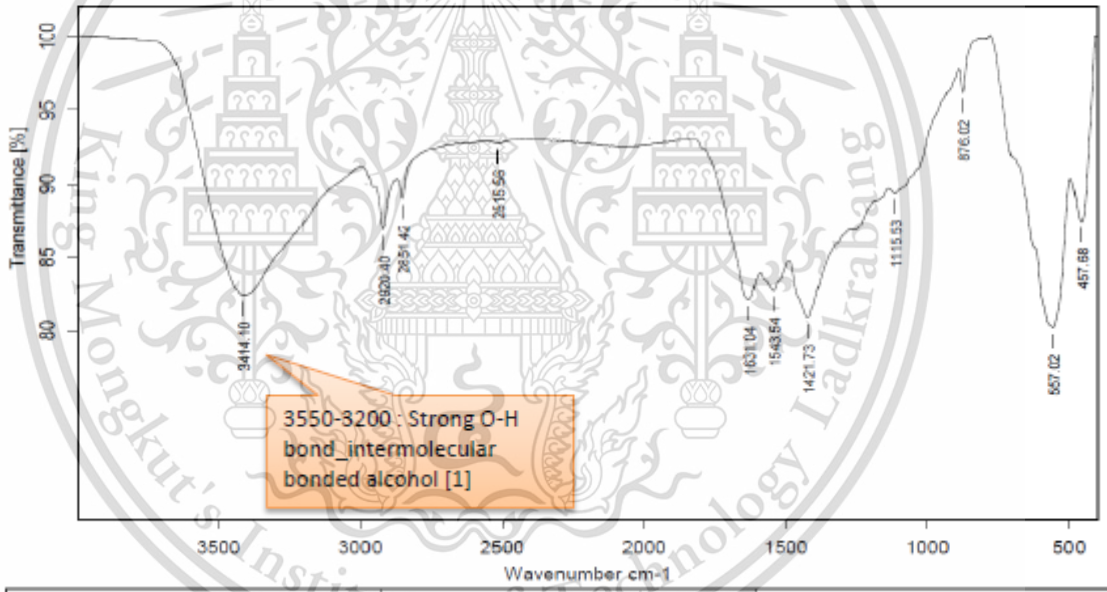

Sample : Soot	Frequency Range :4000-400 cm-1	Measured on : 28/12/2560	
File name : 5415PARK	Resolution : 4	Instrument : Vertex70	Sample Scans : 64
Analyst : Supornrat Maneechot	Zerofilling : 2	Acquisition Mode Double Sided,Forward-Backward	

FT-IR Spectroscopy

From the results of CHNS/O and FT-IR analysis, it might be concluded that -OH radical is a key factor for BE20 soot to support the reduction of soot activation energy.

[1] https://chem.libretexts.org/Reference/Reference_Tables/Spectroscopic_Parameters/Infrared_Spectroscopy_Absorption_Table

This material is reserved for educational use only, not allowed for commercial use.
Forbidden to modify the content, and cite the document when use.

ศูนย์เครื่องมือวิทยาศาสตร์
มหาวิทยาลัยสงขลานครินทร์ วิทยาเขตหาดใหญ่

ชั้น 1 อาคารบริหารวิชาการรวม อ.หาดใหญ่ จ.สงขลา 90110
โทรศัพท์ 074-286904-7 โทรสาร 074-212813 อีเมล sec-all@group.psu.ac.th เว็บไซต์ http://www.sec.psu.ac.th

วิสัยทัศน์: เป็นองค์กรภาครัฐที่เติบโตด้วยความมุ่งมั่นสู่การเป็นองค์กรที่มีสมรรถนะสูง
และยั่งยืนจากการให้บริการทดสอบด้วยเครื่องมือวิจัยทางวิทยาศาสตร์

F-RES-003 ฉบับที่ 11 บังคับใช้ 08/05/60

รายงานผลการทดสอบ

เลขที่รายงาน:	R0021/61	หน้า:	1/1
เลขที่ใบขอใช้บริการฯ:	S422/60	วันที่รับตัวอย่าง:	25 ธันวาคม 2560
ชื่อและที่อยู่ลูกค้า:	นายภาคย์ วัฒนวงศกร วิทยาลัยนานาชาติ สถาบันเทคโนโลยีพระจอมเกล้าเจ้าคุณทหารลาดกระบัง ถนนฉลองกรุง เขตลาดกระบัง กรุงเทพ 10520		
ผู้ทดสอบ:	นางสาวทรงสุดา พรหมทอง		
วันที่ทำการทดสอบ:	27-28 ธันวาคม 2560		
วิธีการทดสอบ:	In-house method refer to WI-RES-CHNS/O-002		
เครื่องมือทดสอบ:	CHNS/O Analyzer, Flash 2000, ThermoScientific, Italy		
เทคนิคการทดสอบ:	Dynamic Flash Combustion		
สภาพตัวอย่าง:	ผงเขม่า, น้ำมัน HVO		
รายละเอียดตัวอย่าง:	เขม่า, น้ำมัน HVO	จำนวน:	4 ตัวอย่าง

ผลการทดสอบ:

ที่	ชื่อตัวอย่าง	หน่วย	ผลการทดสอบ±SD			
			ไนโตรเจน	คาร์บอน	ไฮโดรเจน	ออกซิเจน
1	เขม่า ตัวอย่าง 1	%wt.	ไม่ทดสอบ	ไม่ทดสอบ	ไม่ทดสอบ	17.97
2	เขม่า ตัวอย่าง 2	%wt.	ไม่ทดสอบ	ไม่ทดสอบ	ไม่ทดสอบ	17.94
3	เขม่า ตัวอย่าง 3	%wt.	น้อยกว่า 0.01	77.55 ± 0.01	0.68 ± 0.03	7.11 + 0.08
4	น้ำมัน HVO	%wt.	น้อยกว่า 0.01	81.88 ± 0.42	14.39 ± 0.07	1.80 ± 0.02

- ข้างอิงข้อมูลดิบ sever2\raw data\CHNSO_2000data_2560\5422-60.PDF, SD= Standard deviation, LOQ= ขีดจำกัดการทดสอบปริมาณเท่ากับ 0.01% wt.
- ตัวอย่างที่ 1 และ 2 ทดสอบเฉพาะ Oxygen 1 ซ้ำ, ตัวอย่างที่ 4 ของแต่ละวิทดสอบ 2 ซ้ำ

(นางรุสนี กุลวิจิตร)
หัวหน้าฝ่ายบริการเครื่องมือวิจัยทางวิทยาศาสตร์
5 มกราคม 2561

หมายเหตุ รายงานผลการทดสอบนี้มีผลเฉพาะกับตัวอย่างที่นำมาทดสอบเท่านั้น และรายงานผลการทดสอบนี้ต้องไม่ถูกทำสำเนาเพียงบางส่วน ยกเว้นทำทั้งฉบับ โดยไม่ได้รับความยินยอมเป็นลายลักษณ์อักษรจากทางศูนย์เครื่องมือวิทยาศาสตร์

This material is reserved for educational use only, not allowed for commercial use.
Forbidden to modify the content, and cite the document when use.

ศูนย์เครื่องมือวิทยาศาสตร์
มหาวิทยาลัยสงขลานครินทร์ วิทยาเขตหาดใหญ่

ชั้น 1 อาคารบริหารวิชาการรวม อ.หาดใหญ่ จ.สงขลา 90110
โทรศัพท์ 074-286904-7 โทรสาร 074-212813 อีเมล sec-all@group.psu.ac.th เว็บไซต์ http://www.sec.psu.ac.th

วิสัยทัศน์: เป็นองค์กรภาครัฐที่เติบโตด้วยความมุ่งมั่นสู่การเป็นองค์กรที่มีสมรรถนะสูง
และยั่งยืนจากการให้บริการทดสอบด้วยเครื่องมือวิจัยทางวิทยาศาสตร์

F-RES-003 ฉบับที่ 11 บังคับใช้ 08/05/60

รายงานผลการทดสอบ

เลขที่รายงาน:	R0018/61	หน้า:	1/1
เลขที่ใบขอใช้บริการ:	5415/60	วันที่รับตัวอย่าง:	25 ธันวาคม 2560
ชื่อและที่อยู่ลูกค้า:	นายภาคย์ วัฒนวงศกร วิทยาลัยนานาชาติ สถาบันเทคโนโลยีพระจอมเกล้าเจ้าคุณทหารลาดกระบัง ถนนฉลองกรุง เขตลาดกระบัง กรุงเทพฯ 10520		
ผู้ทดสอบ:	นางสาวสุทธรัตน์ มณีโชติ		
วันที่ทำการทดสอบ:	28 ธันวาคม 2560		
วิธีการทดสอบ:	อ้างถึง WI-RES-FTIR2-001		
เครื่องมือทดสอบ:	Fourier Transform Infrared Spectrometer, Vertex70, Bruker, Germany		
เทคนิคการทดสอบ:	Pellet KBr		
สภาพตัวอย่าง:	ผงเขม่า		
รายละเอียดตัวอย่าง:	เขม่า	จำนวน:	1 ตัวอย่าง

ผลการทดสอบ:

ลำดับที่	ชื่อตัวอย่าง
1	เขม่าตัวอย่าง 1

แสดงดังสเปกตรัมที่แนบและอ้างถึงไดเรกทอรี: 5415PARK

(นางรุสนี กูลวิจิตร)
หัวหน้าฝ่ายบริการเครื่องมือวิจัยทางวิทยาศาสตร์
3 มกราคม 2561

หมายเหตุ รายงานผลการทดสอบนี้มีผลเฉพาะกับตัวอย่างที่นำมาทดสอบเท่านั้น และรายงานผลการทดสอบนี้ต้องไม่ถูกทำสำเนาเพียงบางส่วน ยกเว้นทำทั้งฉบับ โดยไม่ได้รับความยินยอมเป็นลายลักษณ์อักษรจากทางศูนย์เครื่องมือวิทยาศาสตร์

This material is reserved for educational use only, not allowed for commercial use.
Forbidden to modify the content, and cite the document when use.

Scientific Equipment Center , PSU.

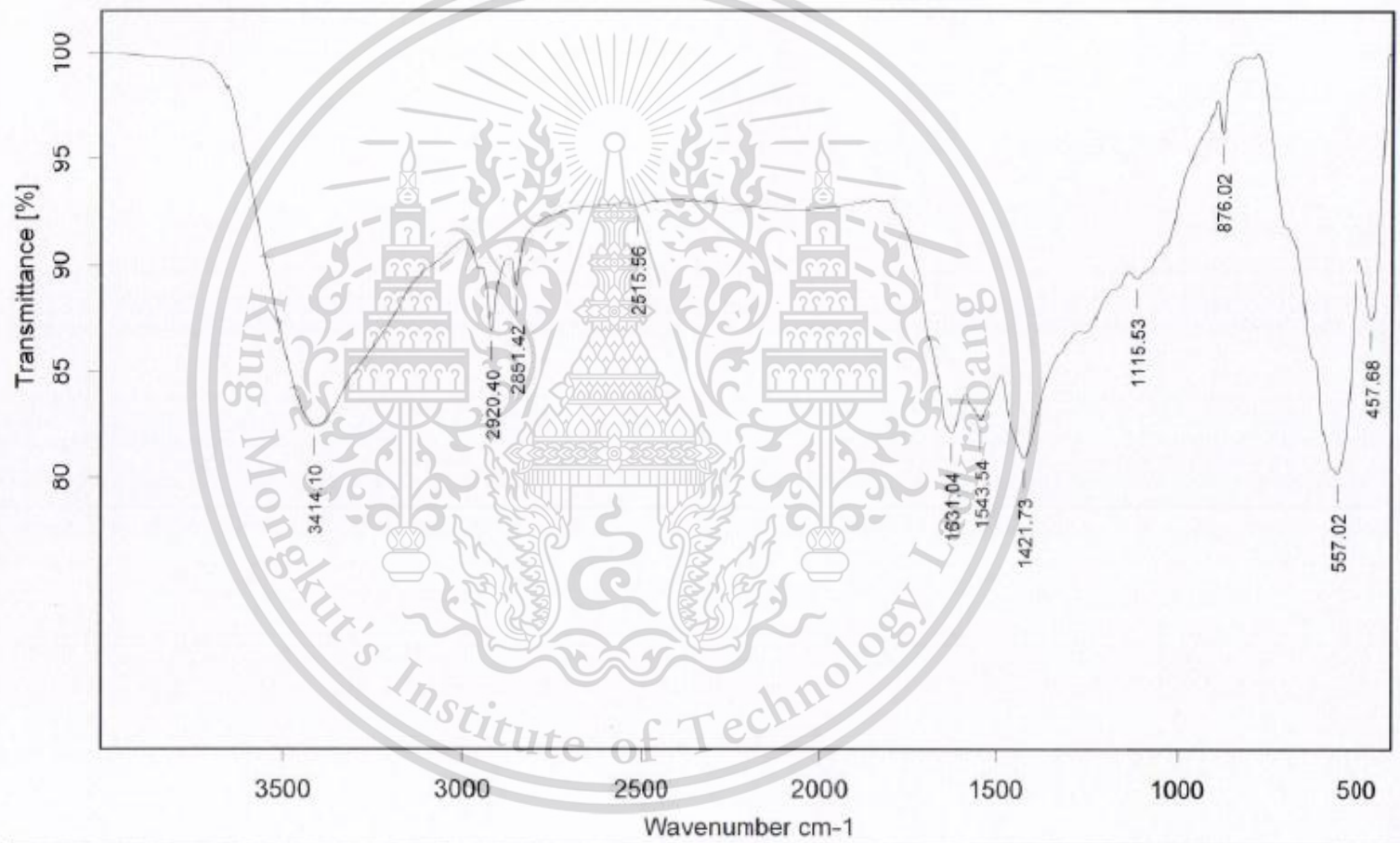

Sample : Soot	Frequency Range :4000-400 cm-1	Measured on : 28/12/2560	
File name : 5415PARK	Resolution : 4	Instrument : Vertex70	Sample Scans : 64
Analyst : Supornrat Maneechot	Zerofilling : 2	Acquisition Mode Double Sided,Forward-Backward	

FT-IR Spectroscopy

King Mongkut's Institute of Technology Ladkrabang

Q8) How to link the results of combustion characteristics to PM properties. However, combustion characteristics should not be explained based on experimental Heat Release data because of limitation in experimental equipment(fuel injection system) (Dr. Chinda and Dr. Manida)

This research methodology start from combustion of Diesel, Biodiesel, and Bio-ethanol fuel at different engine operating conditions and to see effects of Combustion characteristics, PM emission quantity, and PM nanostructure/Oxidation Kinetics as shown below.

However, the relationships of PM nanostructure and Oxidation Kinetics were studied only at specific engine conditions. Therefore, it is more approprite to consider relationships among Combustion characteristics - PM emission quantity - Fuel properties.

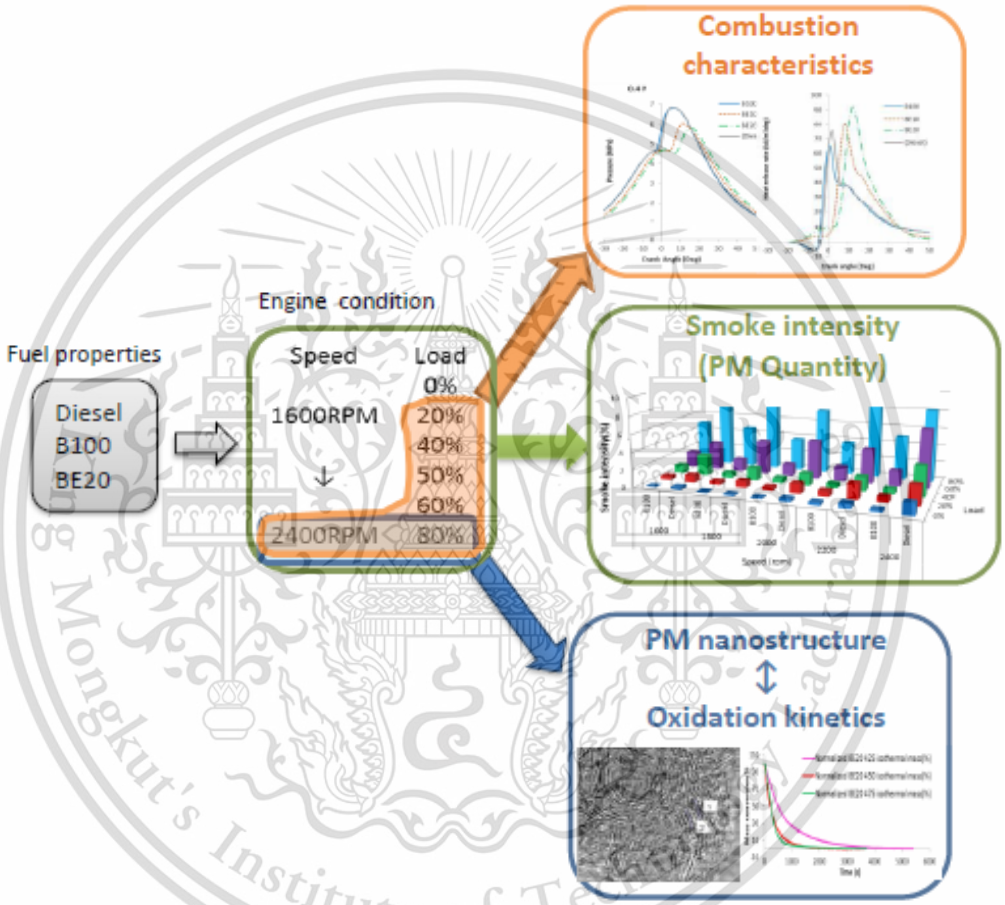

Combustion characteristics from the experiment is straightforward to load conditions. At more load conditions, more fuel supply tends to generates more combustion pressure as well as higher heat release rate in the combustion chamber. Referred from Willard W. Pulkrabek[1], Fig. 1 show air-fuel vapor zone around the injector tip. Zone A and B which is too rich to burn and rich combustible zone are mostly expected in soot generation.

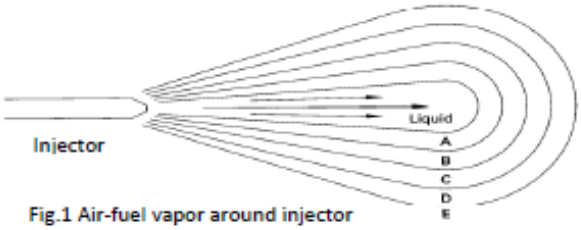

Fig.1 Air-fuel vapor around injector

This material is reserved for educational use only, not allowed for commercial use.
Forbidden to modify the content, and cite the document when use.

Therefore, more PM or soot generation is contributed by more combustion pressure and higher heat release in the combustion chamber.

For the aspect of fuel properties on amount of PM generation, combustion processes after fuel injection can be classified as following steps. Each process is also affected by diferent fuel properties.[1]

1) **Atomization** : Higher fuel viscosity, more difficult to atomize
2)**Vaporization** : More heat of vaporization, more difficult for fuel vaporization
3) ~~**Mixing** :~~ Not affected by fuel properties
4) **Sef-ignition** : Higher auto-ignition temperature, more ignition delay
5) Combustion : Air-fuel ratio or higher oxygen content, easier for combustion

Table 1 compares fuel properties which affect PM generation or PM reduction among BE20, B100, and diesel fuel

● : PM generation ○ : PM reduction

Fuel properties	Heat of vaporization	Oxygn content	Auto ignition temperature	Viscosity	Heating value
BE20	● High	○ High	○ High	○ Low	● Low
B100	○ Low	○ Medium-High	● Medium-low	● High	● Medium-low
Diesel	○ Low	● Low	● Low	● Medium-high	○ High

According to the experimental result, smoke intensity reduction in BE20 should be contributed by the **fuel properties of more oxygen content, higher auto ignition temperature, and lower fuel viscosity.**

[1] Willard W. Pulkrabek, University of Visconsin - Platterville, Engineering Fundamentals of the Internal Combustion Engine, 2nd Edition.

This material is reserved for educational use only, not allowed for commercial use.
Forbidden to modify the content, and cite the document when use.

AUTHOR BIOGRAPHY

Author: Mr. Park Watanawongskorn
Degree: Master of Automotive Engineering
Place of Birth: Bangkok,Thailand

Undergraduate and Graduate Education:

Master of Engineering in Automotive Engineering,
King Mongkut's Institute of Technology Ladkrabang, Bangkok,

Bachelor of Engineering in Mechanical Engineering ,
Sirindhorn International Institute of Technology, Thammasat University, Bangkok

Major: Automotive Engineering

Presentations and Publications:

[1] Park Watanawongskorn, Preechar Karin, Chinda Charoenphonphanich, Jiramed Boonsakda, Katsunori Hanamura, and Nuwong Chollacoop "Impact of Diesel Engine Combustion Characteristics on Particulate Matter's Morphology and Nanostructure from Ethanol-blended Biodiesel", 2017 JSAE Annual Congress (Spring) in Pacifico Yokohama, May 24-26 2017, Japan

[2] Preechar Karin, Park Watanawongskorn, Jiramed Boonsakda, Eakkawut Saenkhumvong, Sippakorn Rungsritanapaisan, Settavit Srivarocha, Chinda Charoenphonphanich, Nuwong Chollacoop, and Katsunori Hanamura "Impact of Biodiesel on Small CI Engine Combustion Behavior and Particle Emission Characteristics", The 21rd Small Engine Technology Conference (SETC), November 17-19, 2017, Jakarta, Indonesia.

This material is reserved for educational use only, not allowed for commercial use.
Forbidden to modify the content, and cite the document when use.